AD-A248 645

9101-07 (2)

NONCONTACT CHARACTERIZATION OF PV DETECTOR ARRAYS

DTIC
S ELECTE D
APR 1 5 1992
C

Final Report

November 1987 - June 1990

on Contract #DAAB0787CF105

Center for Night Vision
and Electro-Optics
Fort Belvoir, VA

STATEMENT A
Approved for public release;
Distribution Unlimited

LORAL
Infrared & Imaging Systems
2 Forbes Road
Lexington, MA 02173

92-07288

92 3 23 056

NONCONTACT CHARACTERIZATION OF PV DETECTOR ARRAYS

Final Report

November 1987 - June 1990

on Contract #DAAB0787CF105

Center for Night Vision and Electro-Optics Fort Belvoir, VA

Statement A per telecon Michael Gremn
Center for Night Vision and Electro-
Optics AMSEL-RD-NV-IRT
FT Belvoir, VA 22060
NWW 4/14/92

Accession For
NTIS GRA&I ☑
DTIC TAB ☐
Unannounced ☐
Justification
By
Distribution/
Availability Codes
Dist | Avail and/or Special
A-1

LORAL
Infrared & Imaging Systems

2 Forbes Road
Lexington, MA 02173

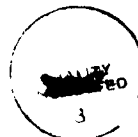

Contents

1 **INTRODUCTION** 1-1

2 **TEST TECHNIQUE OVERVIEW** 2-1

3 **OPEN CIRCUIT DIODE RESPONSE ANALYSIS** 3-1
3.1 INTRODUCTION 3-1
3.2 PHOTOGENERATED CARRIER CONCENTRATIONS AND QUANTUM EFFICIENCY 3-2
3.3 BACKGROUND INFLUENCE AND CONSTRAINTS 3-5
3.4 PHOTOVOLTAGES 3-6
3.5 STEADY STATE EXCESS CARRIER CONCENTRATIONS 3-10
3.6 EXCESS CARRIER FREQUENCY RESPONSE 3-11
3.7 DISCUSSION OF PHOTO INDUCED RoA APPROACHES 3-12
3.8 CAPACITANCE COUPLED RoA MEASUREMENTS 3-12

4 **SUMMARY OF TEST TECHNIQUES INVESTIGATED** 4-1
4.1 CAPACITANCE COUPLED TESTING 4-1
4.2 ELECTRON BEAM TESTING 4-2
4.3 SAW INVESTIGATIONS 4-3
4.4 OPTICAL TESTING 4-4
4.5 UV PROBING 4-5

5 **SUMMARY AND RECOMMENDATIONS** 5-1
5.1 DISCUSSION 5-1
5.2 RECOMMENDATIONS 5-2

Appendices

A **CAPACITANCE COUPLED TESTING** A-1
B **ELECTRON BEAM TESTING** B-1
C **SAW TESTING** C-1
D **OPTICAL TESTING** D-1
E **UV PROBING** E-1

SECTION 1
INTRODUCTION

Testing of (HgCd)Te photodiode arrays prior to connection to the multiplexer readout electronics has to date not been possible. In order to be of value for large area arrays diode testing must not disturb the sensitive electrical contacts typically made up of very soft indium bumps. The objective of the program was to develop and demonstrate a fast, reliable nondestructive technique for non contact; impedance measurement in LWIR HgCdTe PV detector arrays. Five different types of non contact diode evaluation technique were explored.

Three of the 5 test techniques examined were investigated in some detail; these techniques were based on **Capacitance Coupling, Electron Beam** and **SAW** diode probing. The C-coupled and E-beam test approaches included both technique analysis and measurements on diodes. The SAW investigations were only analytical. The possibilities of several types of **Optical** test approach were also analytically evaluated. A very small effort was devoted to fifth test approach based on **UV** probing and some preliminary promising results were obtained on several resistors.

Section 2 of this report provides an overview of all the techniques surveyed. Section 3 provides a theoretical basis for diode response analysis to optical and electrical stimuli. This section aids in the theoretical understanding of some of the test approaches selected. Section 4 summarizes the results of the test techniques investigated. Section 5 summarizes our conclusions and provides short and long term recommendations for non destructive FPA testing. The detailed discussions of the test approaches are presented in the Appendices.

A significant part of the work was spent on E-beam and SAW investigations. The E-beam work was performed by Dr. David Schaefer at Honeywell SSED in Minneapolis (now at Monolithic Sensors in Rolling Meadow, Illinois). The SAW investigations were carried out by Dr. Stanley Reible of Micrilor Associates in Wakefield, Massachusetts and Professor Abraham Bers of MIT, Cambridge, Massachusetts. The very preliminary UV probe evaluations were performed by Mr. Joseph Patterson of Ultraprobe, Laguna Hills, California. The Capacitance Coupled and Optical test techniques were investigated at Loral Infrared & Imaging Systems.

SECTION 2
TEST TECHNIQUE OVERVIEW

Several diode impedance test techniques allow current flow through the diode without requiring physical contact to the diode frontside metallization. Diode impedances are deduced from $\delta V/ \delta I$ measurements in these non contact test approaches which include E-beam probing, UV probing and Tunnelling Current probing. All other test techniques except for the lateral Photovoltage technique rely on some measure of the **free charge changes** produced by externally induced diode perturbations.

The LWIR diode test approaches examined were principally directed at testing the common LWIR p-on-n structure. In this structure diode perturbations such as those produced by optical pumping will change the total number of carriers by two different means; first by junction space charge or depletion width modulation and secondly by excess carrier population in the diffusion regions. For the n-side we can write $\Delta n_{total} = n\Delta d + d\Delta n(x)$, where n is the electron concentration and d is the neutral n-side thickness which can be effectively modulated by modulating the depletion width. All the test techniques not based on external current flow, except for the Lateral Photovoltage technique, depend in some measure on either the junction depletion modulation $n\Delta d$ or, and the integrated effect of the excess charge modulations $d\Delta n(x)$ in the diffusion region.

For good LWIR diodes at 77K the depletion modulation will generally dominate over the diffusion modulation. Table 2.1 shows all the test approaches that appear possible, at least in principle, and the simplest form of diode RoA correlation to the measured probing parameter, e.g., transmission, photoluminescence etc. C_j denotes the junction capacitanceper unit area near zero bias. The test techniques can be grouped into 5 types.

Table 2-1. Possible Diode Impedance Test Techniques Grouped Into 5 Types

TEST APPROACH	STIMULUS	MEASUREMENT & CORRELATION
1. ***I-V Type Approaches***		
E-beam	Primary electrons	$\delta V/\delta I = Ro$
UV	UV photons	$\delta V/\delta I = Ro$
Tunnelling Probe (Not investigated)	Quasi contact	$\delta V/\delta I = Ro$
2. ***Optical Approaches***		
Photoluminescence	Pump beam	Steady emission & (RoA) T_{base} Time constant & (RoA) Cj
Optically Modulated Absorption (Transmission mode)	Pump + probe ~ Eg	Steady modulation & (RoA) Cj Time constant & (RoA) Cj
Optically Modulated Absorption (Transmission mode)	Pump + probe < Eg	Steady modulation & (RoA) Cj Time constant & (RoA) Cj
3. ***Optical & Electrical Approaches***		
Lateral Photovoltage	Pump beam scan from edge-to-edge	Not Ro measure except for near short.
Photoconductivity	Pump beam	Steady Modulation & (RoA) Time constant & (RoA) Cj
4. ***SAW based Approaches***		
SAW Charge readout	Non linear EM field interaction (~1 μm IDT-to-FPA separation)	SAW attenuation & (RoA) Cj transient
SAW RF Probe	Non linear EM field interaction (~10 μm IDT-to-FPA separation)	SAW attenuation & (RoA) Cj transient
5. ***Capacitance Coupled***		
C-Coupled	Step voltage by close proximity capacitance probe	Current transient & (RoA) Cj

NOTE: All correlations involving the junction (RoA) Cj parameter apply only if this is much longer than the base layer lifetime.

SECTION 3
OPEN CIRCUIT DIODE RESPONSE ANALYSIS

This section provides the theoretical basis for evaluating several contactless diode impedance test techniques.

3.1 INTRODUCTION

Diode impedance Ro evaluation approaches can be divided into two broad categories, these are:

Electron Transport and Direct Ro = $\partial V/\partial I$ Type Measurements

The test approaches included here are:

- Physical Probe Contact
- Tunnelling Contact
- E-beam induced secondary electron emission
- UV induced electron emission

Diode Excitation and Contactless Probe Monitoring

With this kind of approach some form of contactless stimulation of the diode is provided and the diode response is monitored and then analyzed to reveal Ro. The stimulation can either cause space charge transient modulations such as provided by capacitance coupling or SAW, or it can be photoinduced resulting in photocurrents, photovoltages. In all these cases the space charge modulations are accompanied by changes in the carrier concentrations in the p and n layers. The response property being monitored may be a voltage, current, conductivity or absorption change or photoluminescence. The measurements may be steady state or transient.

The second category of indirect measurements requires a fundamental understanding of diode physics to enable the test techniques investigated to be properly evaluated. Since the background radiation flux level is very important in all measurements, the analyses will include the background as a steady state effect. The total response in the diode properties can then be expressed as the sum of a

steady state and a modulated effect. The modulated effect considered will be a periodic harmonic stimulation at frequency ω rather than a transient. The following expressions will be used to denote steady state and modulated variables:

$Q(t)$	=	$Q_o + \tilde{Q}e^{i\omega t}$	Photon Flux
$J_{diff}(t)$	=	$J_{odiff} + \tilde{J}e^{i\omega t}$	Diffusion currents
$V(t)$	=	$V_o + \tilde{V}\, e^{i\omega t}$	Photovoltages
$\Delta n(t)$	=	$\Delta n_o + \Delta\tilde{n}^{\,i\omega t}$	Excess minority carriers
			($\Delta n \equiv$ electrons or holes)
		$\eta_o, \eta(\omega)$	Quantum efficiencies

For convenience the photon flux Q here represents the absorbed flux with reflection losses already taken into account.

3.2 PHOTOGENERATED CARRIER CONCENTRATIONS AND QUANTUM EFFICIENCY

The diode model that will be used is the common LWIR p-on-n structure shown below. We start by developing the model for photogenerated carriers using optical pumping from either the p-side or n-side.

Δn, D, τ and L_o denote the excess minority concentration, diffusion coefficient, lifetime and the steady state diffusion length. The symbol Δn will be generally used to refer to **either** excess electron or hole minority carriers. The material parameter subscripts have been omitted to allow for generality depending on which side is optically pumped. For simplicity surface recombination is neglected here although it has been included in analysis detailed elsewhere. [1]

If α is the absorption coefficient, the generation rate of excess carriers is $G(x,t) = \alpha\,\tilde{Q}\,e^{-\alpha x}e^{i\omega t}$. The continuity equation for the diffusing photogenerated carriers is then

$$\frac{\partial \Delta n_{ph}(x,t)}{\partial t} = G(x,t) - \frac{\Delta n_{ph}(x,t)}{\tau} + D\frac{\partial^2 \Delta n_{ph}(x,t)}{\partial x^2}, \qquad (3.1)$$

1. "Optical Evaluation of LWIR HgCdTe p-on-n double layers", IRIS Materials Group Meeting, Monterey, CA, August 12, 1989

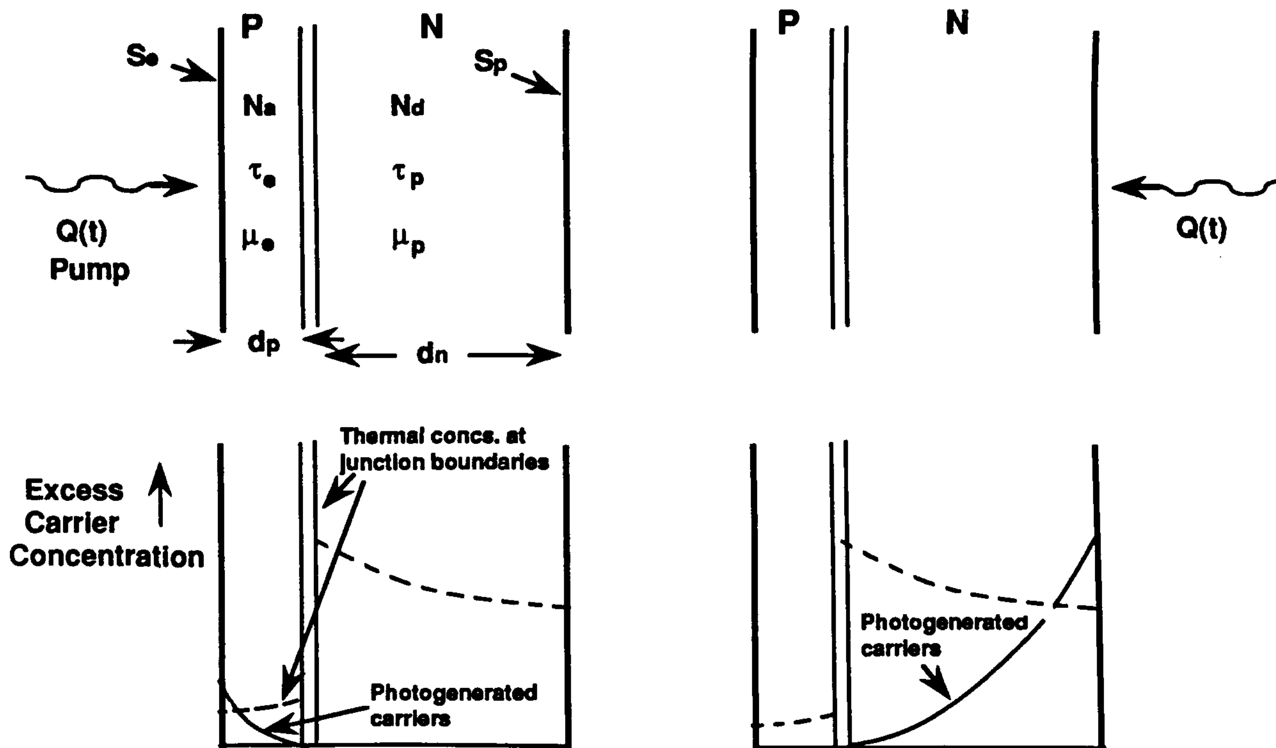

Figure 3-1. Schematic of Excess Photogenerated Carriers Diffusing to the Junction. Broken lines represent excess carrier profiles in steady state equilibrium with the junction photovoltage. X-axis origins will be referenced from the side being pumped (x = o) i.e. p-layer surface or n-side/substrate interface.

which leads to an excess carrier profile given by

$$\Delta\tilde{n}_{ph}(x,t) = \frac{\alpha\tilde{Q}\ \tau}{\alpha^2 L_o^2 - i\omega\tau - 1}\left[\left(\frac{(A+iB)\,e^{-\alpha d} + \alpha L_o e^{d/L}}{(A+iB)\,e^{d/L} + (A+iB)\,e^{-d/L}}\right)e^{-x/L} + \left(\frac{(A+iB)\,e^{-\alpha d} - \alpha L_o e^{-d/L}}{(A+iB)\,e^{d/L} + (A+iB)\,e^{-d/L}}\right)e^{x/L} - e^{-\alpha x}\right] e^{i\omega t}, \tag{3.2}$$

where $d = d_p$ for frontside pumping, $d = dn_n$ for backside pumping and the low frequency ($\omega\tau << 1$) diffusion length $L_o = \sqrt{D\tau}$, while at high frequencies

$$L = \frac{L_o}{A+iB}, \quad \text{where } A + iB = (1 + i\omega\tau)^{1/2}, \quad A^2, B^2 = (\sqrt{1+\omega^2\tau^2} \ \pm\ 1)/2.$$

The expression for $\Delta\tilde{n}_{ph}(x,t)$ can be considerably simplified if a short wavelength pump source is used. It is generally preferable to use shorter wavelength pump radiation for several reasons. First, wider EO and AO modulation bandwidths can be used for transient or frequency response analysis. Secondly,

individual detector illumination due to lower diffraction limitations is possible. Thirdly, diode response analysis will be shown to be much easier when the frontside quantum efficiency at short wavelengths is close to unity and the photocurrent diffusion times to the junction are short enough to be negligible, so that this frequency response is flat even when $\omega\tau > 1$.

Around 1 μm wavelengths (close to Nd, He-Ne and GaAs laser lines) the absorption coefficients of LWIR HgCdTe is approximately 2×10^4 cm^{-1} and αd, αL_o are both much greater than unity for either frontside or backside pumping. Under these conditions equation 3.2 simplifies to

$$\Delta\tilde{n}_{ph}(x,t) = \frac{\tilde{Q}\tau}{L_o(A+iB)}\left[\frac{\mathrm{Sinh}(d-x)/L}{\mathrm{Cosh}(d/L)}\right]e^{i\omega t}. \qquad (3.3)$$

The integrated excess carrier concentration on the pumped side is then given by:

$$\Delta\tilde{n}_{ph}(t) = \frac{\tilde{Q}\tau}{(1+i\omega\tau)}\left(\frac{\mathrm{Cosh}(d/L)-1}{\mathrm{Cosh}(d/L)}\right). \qquad (3.4)$$

The frequency dependent quantum efficiency $\eta(\omega)$ can be determined from:

$$\tilde{J}e^{i\omega t} = \eta(\omega)q\tilde{Q}e^{i\omega t} = -qD\frac{\partial\Delta\tilde{n}_{ph}(x,t)}{\partial x}\bigg|_{x=d}$$

then $$\eta(\omega) = 1/\mathrm{Cosh}(d/L) \qquad (3.5)$$

For p-side pumping $d/L = d_p/L_{eo}$ and since $d_p/L_{eo} \sim 1/50$ the quantum efficiency will be close to 1, and the frequency response very flat even when $\omega\tau>1$. For n-side pumping, typically with $0.5 \lesssim d_n/L_{po} \lesssim 2$, the steady state quantum efficiency will be somewhat less than 1. When $\omega\tau$ becomes significant $\eta(\omega)$ will rolloff in a complicated way.

3.3 BACKGROUND INFLUENCE AND CONSTRAINTS

Excessive background illumination of a diode will cause an erroneous interpretation of diode impedance in the open circuit condition. Figure 3-2 illustrates the problem.

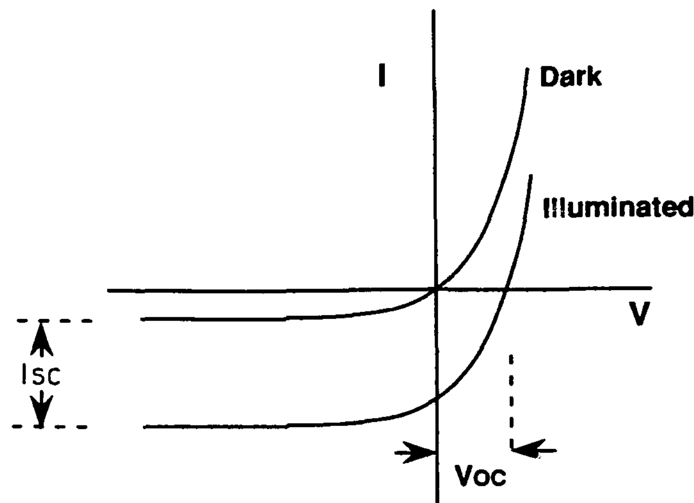

Figure 3-2. Effect of Background Flux

In the open circuit condition the photocurrent must equal the forward current since the net current must be zero. This current balance will occur at a photovoltage V_0 where the dynamic impedance RA will be less than for the non-illuminated zero bias case. The possible problem of an erroneous RoA measurement is circumvented in contact I-V measurements by using a low impedance external circuit current path which forces the junction to be operated near zero bias.

The steady state background effect on diode impedance can be easily determined when diffusion current dominates. If the junction voltage $V(t) = V_0 + \tilde{V}e^{i\omega t}$ and $e\tilde{V}/kT \lesssim 1$ the excess minority carrier concentrationsΔn (electrons or holes)on either side of the junction can be expressed as (n_{po} or p_{no}) x [exp (eV(t)/kT) - 1] giving

$$\Delta n(t) = (n_{po} \text{ or } p_{no}) \exp(eV_0/kT) - 1] + (n_{po} \text{ or } p_{no}) \exp(eV_0/kT) \frac{e\tilde{V}}{kT} e^{i\omega t} \quad (3.6)$$

$$= \Delta n_0 + \Delta \tilde{n} e^{i\omega t},$$

where the Δn_0 and $\Delta \tilde{n}$ represent the steady state and modulated components at the depletion edges. Balancing the steady state photo and diffusion currents.

$$e\eta_o Q_o = J_{sat}\left(\exp(eV_o/kT) - 1\right) = (kT/eRoA)\left(\exp(eV_o k/T) - 1\right)$$

provides a measure of V_O given by

$$Vo = (kT/e)\,Ln\left((1 + e\eta_o Q_o RoA/(kT/e))\right) \tag{3.7}$$

Low background conditions can now be defined as those under which RA is effectively RoA. These conditions are met when $e\eta_o\, Q_o(RoA)/(kT/e) \ll 1$. For LWIR Ro testing at 77 K this constraint effectively translates to

$$Q_o \ll 10^{17}/(RoA)\ \text{photons/cm}^2-\text{s}. \tag{3.8}$$

3.4 PHOTOVOLTAGES

The response time in the rise or fall of the junction photovoltage is limited by how fast electrons and holes can diffuse into or out of the space charge regions and the net generation or recombination rates of excess carriers which are related to the carrier lifetime. The excess carrier concentrations associated with a modulated photovoltage $\tilde{V}$ will be denoted by $\Delta\tilde{n}_{th}(x,t)$ to denote thermal equilibrium values.

The solutions to $\Delta\tilde{n}_{th}(x,t)$ are obtained using the same continuity equation used for photogenerated carriers except that in this case the generation term G(x,t) has been dropped, i.e.,

$$\frac{\partial \Delta n_{th}(x,t)}{\partial t} = \frac{\Delta n_{th}(x,t)}{\tau} + \frac{D\partial^2 \Delta n_{th}(x,t)}{\partial x^2}.$$

The minority carrier concentration $\Delta\tilde{n}_{th}\, e^{i\omega t}$ at the junction boundary is given by equation 3.6. After simplifying for negligible surface recombination we obtain

$$\Delta\tilde{n}_{th}(x,t) = \frac{\text{Cosh}(x/L)}{\text{Cosh}(d/L)}\Delta\tilde{n}e^{i\omega t} \tag{3.9}$$

The modulated n-side diffusion current is then given by

$$\tilde{J}_{ndiff} e^{i\omega t} = - \ (+e) D_p \frac{\partial \Delta \tilde{n}_{th}}{\partial x} (x, t) |_{x = d_n} \quad (3.10)$$

and
$$\frac{1}{RA_{ndiff}} = \frac{1}{RA_{n\infty}} \text{Tanh}\left(d_n (1 + i\omega\tau_p)^{1/2} / L_{po}\right) (1 + i\omega\tau_p)^{1/2}$$

with a similar expression for the p-side.

The total concentration of excess carriers as a function of time is found by integrating equation 3.9 when

$$\Delta \tilde{n}_{th}(t) = L \ \text{Tanh}(d/L) \Delta \tilde{n} e^{i\omega t} \quad (3.11)$$

The amplitude of the modulated photovoltage $\tilde{V}$ is determined by balancing the photocurrent minus the capacitive loading of the junction (capacitance Cj Farads/unit area) with the modulated diffusion currents and other remaining types of leakage current J_r such as g-r currents

$$e\tilde{Q}\eta(\omega) - C_j \frac{dV(t)}{dt} = \tilde{J}_{ndiff} + \tilde{J}_{pdiff} + \tilde{J}_r \ , \quad (3.12)$$

Further analysis of equation 3.12 depends on the steady state *open circuit* voltage. Since generally $J_{ndiff} >> J_{pdiff}$ the p-side diffusion current will be neglected. Two cases are now considered.

Case 1. Diffusion Current Dominates

The case when J_r is negligible invariably applies to high background fluxes when $eV_o/kT>1$; it may also apply at low photogeneration levels. Substituting equation 3.10 into 3.12 gives

$$e\tilde{Q}\eta(\omega) \ - \ i\varpi C_j \tilde{V}(\omega) = \frac{1}{RA_{n\infty}} \text{Tanh}\left(d_n (1 + i\omega\tau_p)^{1/2} / L_{po}\right) (1 + i\omega\tau_p)^{1/2} \tilde{V}(\omega) \quad (3.13)$$

The photovoltage frequency response $\tilde{V}$ (w) rolloff can be related to the low frequency amplitude $\tilde{V} = e\eta_o (RA)_n \tilde{Q}$ when wt<<1. When wt $\tilde{>}$ 1, equation 3.13 has simple solutions only for the cases when d_n/L_p« 1 or dn/L_p>> 1. Then

$$\underset{(d_n/L_{po} \ll 1)}{\tilde{V}(\omega)} = \frac{\tilde{V}}{[1 + \omega^2 (\tau_p + \tau_{RC})^2]^{1/2}} \quad (3.14)$$

$$\tilde{V}(\omega)_{(d_n/L_{po}>>l)} = \frac{\tilde{V}}{\left|(1 + i\omega\tau_p)^{1/2} + i\omega\tau_{RC}\right|} \tag{3.15}$$

where $\tau_{RC} = (RA)_n C_j$.

The expressions for V(ω) can be physically understood in the following way. In both cases the rise of the photovoltage depends not only on supplying photocurrent to modulate the space charge width, but also on increasing the number of excess carriers in equilibrium with the photovoltage. Thus, the junction characteristics of RoA and C_j associated with storing or leaking charges are intimately tied up with the carrier lifetime τ.

The difference between the thick and thin base region cases can now be recognized. When the diode structure is thin there is a negligible delay between photogenerated carriers ending up either in the space charge region or the base layer. Both the space charge and diffusion regions can take up excess carriers. Therefore, the effect of ending up in either is invisible in the frequency response and the total effective time constant $\tau_{eff} = \tau_p + \tau_{RC}$.

In the thick diode case the junction modulations are more loosely coupled to the excess carrier modulations further removed from the junction. If the diode RoA is high and most of the photogenerated carriers end up modulating the space charge, their will be little difference in the photovoltage frequency response rolloff between the thin and thick diode cases. However, if the RoA is so low that most of the modulation is in the number of excess carriers in the n-region the frequency response rolloff will be more complicated as indicated by equation 3.15.

Case 2 Low Background (eV_o/kT, $e\tilde{V}/kT<1$)

In this case diffusion current does not necessarily dominate the leakage current, and the remaining leakage current term J_r in equation 3.12 must be retained. Assuming that for small biases $\tilde{J}_r = \tilde{V}/(R_oA)_r$ the current balance equation is now

$$e\tilde{Q}\eta(\omega)e^{i\omega t} - C_j\frac{dV(t)}{dt} = \frac{(1+i\omega\tau_p)^{1/2}}{(RoA)_{n\infty}}\text{Tanh}\left(d_n(1+i\omega\tau_p)^{1/2} / L_{po}\right)\tilde{V}(\omega)e^{i\omega\tau} + \frac{\tilde{V}(\omega)e^{i\omega}}{(RoA)_r} \quad (3.16)$$

The photovoltage response for the thin diode ($d_n/L_p \ll 1$) if $\omega\tau p \ll$ l is then

$$\tilde{V}(\omega) = \frac{\tilde{V}}{(1+\omega^2\tau_{RC}^2)^{1/2}} \quad (3.17)$$

where $\frac{1}{RoA} = \frac{1}{(RoA)_{n\infty}} + \frac{1}{(RoA)_r}$, $\tau_{RC} = (RoA)C_j$, $\tilde{V} = e\eta_o\tilde{Q}(RoA)$.

When $d_n/L_p >> 1$ the general form of the photovoltage response is much more complicated and does not lead to a simple pole rolloff.

It is important to note the similarities and differences in optical and capacitively induced modulations of a diode structure. A step voltage pulse applied to an electrode capacitively coupled (capacitance C_p) to the p-layer will result in transient diode currents, and charge and junction voltage modulations. These modulations will last for only a short time depending on τ_{RC} and τ before collapsing to the same state as before the pulse while a charge C_pV is delivered to the surface of the p-layer. As in the photovoltage response τ_{RC} and τ cannot be separated in a thin diode structure. By contrast the photovoltage response experiences similar transients, but in this case when $\omega\tau << 1$ the spare charge modulations remain sustained by the steady photocurrent. In addition, in providing forward currents to balance the photocurrent, the diode experiences an increase in the minority carrier concentrations associated with the photovoltage.

3.5 STEADY STATE EXCESS CARRIER CONCENTRATIONS

Modulations in the excess carrier concentration induced by low Q_0, $\tilde{Q}$ levels can be related to diode impedances. The total concentration of excess carriers $\Delta n(t)$ per unit area can be expressed as the sum of photogenerated carriers and thermally generated carriers. In addition, excess carriers are introduced by the modulation of the space charge width; this contribution is treated later. For the moment the sum of Δn_{th} and Δn_{ph} is obtained by combining equations 3.4, 3.6 and 3.11 in the low frequency and low Q_0, $\tilde{Q}$ limits giving

$$\Delta\tilde{n} = \mathrm{Tanh}(d/L_o)\ L_o\ p_{no} e^{\frac{eV_o}{kT}} \left(\frac{e\tilde{V}}{kT}\right) + \tilde{Q}\tau\left(\frac{\mathrm{Cosh}\ (d/L_o) - 1}{\mathrm{Cosh}(d/L_o)}\right)$$

$$= \eta_o \tilde{Q}\tau \left[\frac{(RoA)}{(RoA)_{diff}} + (\mathrm{Cosh}(d/L_o) - 1)\right] \qquad (3.18)$$

$$\Delta n_{th} \qquad\qquad \Delta n_{ph}$$

where the following relations have been used: $p_{no} = n_i^2/N_d$, $\tilde{V} = e\eta_o(RoA)\tilde{Q}$, $\eta_o = 1/\mathrm{Cosh}(d/L_o)$, $L_o = \sqrt{D\tau}$, $\mu/D = e/kT$, $1/(RoA)_{n\infty} = (en_i^2/N_d)(\mu_p kT/\tau_p)^{1/2}$, $1/(RoA)_{diff} = \mathrm{Tanh}\ (d/L_o)/(RoA)_{n\infty}$.

Equation 3.18 shows that the thickness of the pumped side layer determines the relative magnitude of the two excess carrier contributions. The expression simplifies considerably when frontside/p-side pumping is used and $d_p/L_{eo} \ll$ l. In this case:

$$\Delta\tilde{n}_{front\ pumped} = \tilde{Q}\tau_p \left[\frac{RoA}{(RoA)_{diff}}\right] \qquad (3.19)$$

It is interesting to note here that when the diode impedance is dominated by diffusion currents, i.e. $RoA = (RoA)_{diff}$, then $\Delta\tilde{n} = \tilde{Q}\tau_p$. This is the same result that would be obtained if the p-region and space charge region were removed.

The ratio $(RoA)/(RoA)_{diff}$ can be recognized as the portion of excess carriers that end up recombining in the base layer. The other carriers recombine through undesireable processes directly across the junction. In this respect the impedance ratio may be considered as a figure of merit with a maximum possible value of unity.

The effect of a modulation of the space charge region will now be included. The decrease in space charge width as the junction photovoltage increases can be recognized as an increase in the n-region thickness which also produces additional carriers. The excess carrier contribution from the space charge modulations is simply given by $C_j\tilde{V}/e = \eta o C_j(RoA)\tilde{Q}$. The total low frequency carrier modulation for frontside pumping with $\eta o = 1$ is now

$$\Delta\tilde{n} = \tilde{Q}\tau_p\left[\frac{RoA}{(RoA)_{diff}} + \frac{\tau_{RC}}{\tau_p}\right] \qquad (3.20)$$

3.6 EXCESS CARRIER FREQUENCY RESPONSE

Monitoring the excess carrier frequency response in response to a modulated photogenerating source $\tilde{Q}e^{i\omega t}$ can provide a measure of the junction impedance. The following develops the expression for this response. Again, we use the simplest front side pumped configuration where $\eta(\omega) = \eta o = 1$. From equations 3.11 and 3.20 the total modulated response at high frequencies is given by

$$\Delta\tilde{n}(\omega) = \frac{L_{po}}{(1 + i\omega\tau_p)^{1/2}} \mathrm{Tanh}\left(\frac{d_n(1 + i\omega\tau_p)^{1/2}}{L_{po}}\right)\Delta\tilde{n} + C_j\tilde{V}(\omega)/e$$

where $\Delta\tilde{n} = p_{no}(e\tilde{V}/kT)$ at low backgrounds. Then if $d_n/L_{po}, \varpi\tau_p << 1$, and using equation 3.14

$$\Delta\tilde{n}(\omega) = \left[\frac{RoA}{(RoA)_{diff}} + \frac{\tau_{RC}}{\tau_p}\right] \frac{\tilde{Q}\tau_p}{(1 + \omega^2\tau_{eff}^2)^{1/2}} \qquad (3.21)$$

where $\tau_{eff} = \tau_p + \tau_{RC}$

Typically the p-on-n structure exhibits junction capacitance values of around $C_j = 6 \times 10^{-8}$ F/cm^2.

A good value for an LWIR diode RoA product at 77 K is RoA ~ 100 ohm cm^2 when $\tau_{RC} = (RoA)C_j \approx$ 6 µs; a value considerably higher than the typical 1 µs expected from an optimally doped base layer. In such cases with $\tau_{RC}/\tau >> 1$ the total excess carrier response is dominated by the space charge response where

$$\Delta \tilde{n}(\omega) = \frac{\tilde{Q}\tau_{RC}}{(1 + \omega^2 \tau_{RC}^2)^{1/2}}$$

A similar result will apply in a thick diode if RoA is high.

3.7 DISCUSSION OF PHOTO INDUCED RoA TEST APPROACHES

Table 3.1 summarizes all the changes in p-on-n diode parameters resulting from low flux level optical pumping. Experimental design and diode RoA measurement sensitivity issues, based on several different test approaches, are discussed in Section 4.

3.8 CAPACITANCE COUPLED R_0A MEASUREMENTS

Low frequency capacitance coupled measurements of diode photovoltages have the simplest theoretical basis for data interpretation. With frontside pumping at a known flux level $\tilde{Q}$ and a quantum efficiency near unity, the photovoltage $\tilde{V}(\omega)$ provides a direct measure of (RoA). Backside pumping provides a measure of η_o(RoA).

The photovoltage frequency response rolloff can provide a measure of RoA when $\tau_{RC} >> \tau$ and C_j is known. When $\tau_{RC} \sim \tau$, τ_{RC} is difficult to determine. One means of circumventing this difficulty would be to make another frequency response evaluation at a higher photovoltage bias when the RA product and, therefore, τ_{RC} would be significantly reduced so that $\tau_{RC} << \tau$. The two sets of measurements might then be used to determine both τ and τ_{RC}.

Table 3-1. Summary of P-on-n Diode Parameter Responses to a Modulated Photo Flux $\tilde{Q}^{i\omega t}$ using Either Front/p-side or Back/n-side Optical Pumping

PARAMETER	PUMPED SIDE	LOW FREQUENCY VALUES	NORMALIZED RESPONSE WHEN $d_n/L_{po}<<1$ or $\tau_{rc}/\tau>>1$	MEASUREMENT APPROACHES
Quantum Efficiency	Front	1	Flat	--
	Back	$Cosh^{-1}(d_n/L_{po})$	Complex	
Photovoltage ($\lambda_{pump} \sim 1\ \mu m$)	Front	$e\tilde{Q}(RoA)$	$\frac{1}{(1+\omega^2(\tau_p+\tau_{RC})^2)^{1/2}}$	Capacitance Coupled
	Back	$e\eta_o\tilde{Q}\ (RoA)$	Generally complex	
Excess free carriers in n layer	Front	$\tilde{Q}\tau_p\left[\frac{(RoA)}{(RoA)_{diff}}+\frac{\tau_{RC}}{\tau_p}\right]$	$\frac{1}{(1+\omega^2(\tau_p+\tau_{RC})^2)^{1/2}}$	Optical or Conductivity modulation
	Back	$\eta_o\tilde{Q}\tau_p\left[\frac{RoA}{(RoA)_{diff}}+\frac{\tau_{RC}}{\tau_p}+(\cosh(d/L)-1)\right]$	Generally complex	

SECTION 4
SUMMARY OF TEST TECHNIQUES

Five techniques for non contact diode evaluation were explored. The results of each of the investigations are summarized below. The detailed reports are given in the Appendix section.

4.1 CAPACITANCE COUPLED TESTING

Capacitance coupled testing offers the potential for rapid, non contact measurements of medium and long wavelength photodiode arrays. Zero bias resistance, responsivity, and junction capacitance (Cj) can be measured on each element in the array. The measurements are entirely electrical and can be completely described with a simple electrical model. During the first phase of this program, the electrical model was developed and tested using a silicon diode at room temperature. The electrical parameters (Ro and Cj) of this diode were similar to those expected for a typical long wavelength mercury cadmium telluride detector at 80 degrees Kelvin. The results of this first phase of the program in monthly progress report number 12, is reprinted in Appendix A-1 of this report.

In the second phase of the program, we designed, built, and tested a prototype C-coupled test setup to determine the feasibility of a production test station using the capacitance coupled approach. Although we found no fundamental problems with our prototype tester, we were unable to demonstrate testing of real diodes due to a number of practical difficulties with our prototype setup. We also discovered that we had overestimated the maximum available probe capacitance and underestimated the stray capacitances. We concluded that the implementation of a production test station would present a number of difficult engineering challenges.

In addition to the practical difficulties of implementing a capacitance coupled tester, there are a number of difficulties associated with any non-contact test method. These problems are analyzed in Section 3 of this report. The two effects which are expected to cause the most trouble are the requirement for testing at a low background flux, and the effects of the diffusion capacitance. The low background requirement significantly complicates the design of the tester. The diffusion capacitance, under certain conditions, can be large enough to substantially reduce the accuracy of the C-coupled testing, as explained in Appendix A-1.

Enhanced Capacitance Coupled Testing

Several research papers on capacitance microscopy appeared during the course of this program. The techniques used have the potential for bypassing most of the problems we encountered with our experimental setup. If we were to sense the photovoltage only, as suggested in Section 3, and use these more sophisticated capacitance techniques, a capacitance coupled tester would probably be feasible. More details of the enhanced techniques are discussed in Appendix A-1.

Non-Destructive Contact Probing

As part of the checkout procedure for our capacitance coupled prototype, we implemented a "light touch" contact test using most of the same electronics. This test method is feasible due to the very short test time required to measured Ro and photocurrent with a direct contact (about 100μs), together with the very precise positioning possible with the piezoelectric transducer. A preliminary probe lifetime test was conducted with favorable results. More details of this method are given in Appendix A-1.

4.2 ELECTRON BEAM TESTING

An E-beam probe system designed for probing VLSI circuit voltages was used to investigate the possibility of contactlessly measuring HgCdTe diode I-V characteristics. Most of the effort spent in this investigation was focussed on developing the test technique. Dynamic impedance measurements of 400 MΩ were eventually obtained on an MWIR diode. Analysis suggested 1 MΩ LWIR diode impedances could be made with instrumentation that is optimized for this task.

Several major shortcomings of the test instrumentation and test methodology used were identified. First, the secondary electron emission from the diode metallization was found to be unstable. This was still a problem even after procedures had been developed to interleave the calibration and test procedures with each ΔI, ΔV data test and calibration sequence completed within about 100 ms. Secondly, the SE detector appeared to have an inadequate temporal and voltage resolution response. Thirdly, the conflict between a sufficiently large electron beam aperture for focussing and scanning could not be reconciled with the requirement for low LWIR backgrounds below around 10^{15} photons/cm^2-s.

Although there does not appear to be a fundamental limit to the E-beam approach, it was evident that several **significant** instrument problems and limitations needed to be addressed **prior** to undertaking any I-V type measurements. It is felt that effort to address the instrument problems would most likely best be undertaken in an environment specializing in E-beam systems.

4.3 SAW INVESTIGATIONS

Two different SAW approaches to diode evaluation were examined in terms of both experimental design and theoretical analysis. The two approaches are referred to as the **Charge Store Readout** and the **RF Probe**. In either approach all diodes can be charged simultaneously with a short electrical impulse properly applied across an air gap, or by optical pumping. Biasing in the **Charge Store Readout** process can also be accomplished through the convolution of oppositely directed pulses to produce a spatially varying stored charge pattern. The SAW summary section of Appendix C illustrates the two techniques and the charging processes. The diode discharge is monitored with SAW readout pulses which experience a degree of modulation proportional to the amount of stored charge left on the diodes. The charging and discharge monitoring processes in the SAW techniques are similar to the processes involved in the Capacitance Probing Technique.

Analysis indicated that the "Charge Store Readout" approach provides the best S/N resolution. However for HgCdTe diodes the approach has two serious drawbacks. First, a very close and uniform piezoelectric-diode separation of no more than 1 micron must be maintained. Secondly, the best spatial probing resolution is typically a minimum of two or three diodes. Although some signal processing can probably be performed to effectively gain better spatial resolution this approach can be difficult and not always that convenient. In addition, while electronic means can be used for one dimensional line scanning of diode elements with a one dimensional SAW probe, mechanical stepping is required along the second axis. Such stepping, subject to a one micron gap constraint is expected to be very difficult.

To circumvent the spacing problem a SAW RF probe concept based on a non-linear process was conceived. In this case semiconducting GaAs with a weak linear piezoelectric effect is used to provide a SAW path into delineated implanted highly doped regions which can provide a strong nonlinear acousto-electric fields at the sum and difference frequency. The much longer spatially distributed polarization

fields that can be located opposite the diodes will now decay with distance from the surface of the probe much more slowly than the rapid spatially varying linearly produced SAW fields. In this way the gap spacing can be realized to about 10 microns. A method of evaluating all diodes in a mosaic array by part mechanical and part electronic stepping may thus be possible.

While individual diodes with dimensions as small as 35 microns could now be individually evaluated, the S/N ratio for each diode would be only approximately equal to 1 for a line scan covering 10 diodes. Signal averaging would therefore be required to improve the measurements.

In summary, only the RF probe approach may be capable of addressing diode array test requirements since only this technique provides tolerable probe/sample proximity constraints and adequate spatial resolution. However, the RF probe approach is only a concept at this time, and a one man year effort would first be required to first demonstrate this concept and up to a 5 man year effort to fully develop a practical measurement instrument.

4.4 OPTICAL TESTING

Optical pumping of diodes generates and modulates the electron and hole distributions in a way which depends partly on the diode impedance. Unfortunately the very low pumping fluxes required, the small diode areas and the low optical absorption cross-sections and photoluminescence efficiencies all conspire to make purely optical test approaches impossible or at best very difficult candidates for LWIR diode impedance testing.

Other combined optical-electrical techniques for diode testing were also considered. Analysis showed that the lateral photovoltage or induced current measurements cannot distinguish between good and poor diodes unless the diode impedances are drastically low. Furthermore, it would be impossible to extract the small modulation signal from a single diode surrounded by thousands of other diodes subjected to the same background.

A similar setup to that used for lateral measurements may however be able to use the larger base layer photoconductivity modulations; these modulations can be simply related to the diode impedance in good diodes. However, the ability to extract the photoconductivity signal from a single diode in an FPA

will again largely depend on the FPA configuration including the location of the base layer grounds; some of the grounds may be left floating during the non destructive testing.

4.5 UV PROBING

Diode impedance measurements based on UV stimulated Photocurrents and voltage probing appears to be quite feasible if photon energies above the diode passivation layer absorption edge are used. This condition should avoid the formation of trapping states at the passivation layer/HgCdTe interface and therefore diode impedance degradation.

UV probe measurements on resistors with resistance values in the 10^8 - 10^9 Ω range typical of MWIR diodes were demonstrated in a non-optimized commercial UV probing instrument. The UV source in these measurements was a filtered high pressure Hg lamp in which a small part of the lamp emission was focused to an area of 100 μm in diameter providing a photocurrent of approximately 1 nA.

The only major drawback in the present application appears to be the necessary expensive investment in a CW UV ion laser. Currently, these lasers are the only sources of CW radiation around 250 nm which can provide sufficient photo-current from a region well within the diode metallization area. However, it is quite likely that other much cheaper, smaller and more reliable UV lasers will be available within the next few years to make the UV probing approach quite attractive.

SECTION 5
SUMMARY AND RECOMMENDATIONS

5.1 DISCUSSION

Eleven diode impedance test approaches were identified in Section 2 of this report and these were grouped into five technical approach types. All of these approaches were examined except for the tunneling approach. The eleven approaches can be categorized into three fundamentally different generic types. Test approaches in the first group can be described as "I-V type" approaches wherever there is some net electron transport across the diode. The Electron beam, UV probing and Tunnelling probe test approaches all fall into the I-V type test group. The second group of test approaches can be described as "Charge Modulation" approaches. In this case an electromagnetic field or optical radiation source generates or redistributes electrons and holes in the diode. The magnitude and transient response of these charge modulation effects, differently monitored in the various approaches, is then related to the diode impendance and other parameters. Lateral Photovoltage or Photocurrent measurements may be separately categorized as a third category.

All the charge modulation test approaches have the drawback that unless RoA $\gtrsim$ 100 Ω cm^2 data interpretation of RoA is difficult. As the RoA decreases the steady and transient modulations start to become more dependent on the diffusion capacitance in addition to the junction capacitance. This fundamental limitation compounded with the other findings of insufficient test sensitivity, diode spatial resolution limitations and/or practical implementation restrictions disqualifies all the charge modulation approaches as candidate test techniques except possibly the photoconductivity based test approach.

The lateral photovoltage or photocurrent techniques are eliminated from the list of candidate techniques since they do not provide a measure of RoA except in very special cases.

A large effort was spent on investigating the E-beam approach. Although some high impedance 400 MΩ measurements were made, the approach suffered from several severe test system problems. These problems may, or may not be resolved with a dedicated effort focussed on solving some fundamental instrument problems.

Only the UV photocurrent and voltage probing approach appears to have a realistic possibility of succeeding as a non contact and accurate diode impedance test approach. A drawback seen in the UV technique is the present cost of CW UV laser sources. However, for the long range planning it should be noted that it is likely that alternate CW UV solid state lasers will probably be commercially available within the next 5 years.

5.2 RECOMMENDATIONS

The investigations in this program included some very light direct probe contact I-V tests performed as an outfall of the C-coupled technique evaluation. The results of this light direct contact testing were promising. The light force contact test approach is recommended for automation and immediate implementation.

Longer term investigations should be continued on two possible test techniques. First the possibility of using space charge modulated photoconductivity should be analyzed for the most common focal plane configurations. Alternate ground configurations may be evaluated so long as these do not significantly impact the FPA process or array performance. Secondly, investigation should be continued in UV probing because this approach appears to have the best potential of meeting all the non destructive test requirements.

APPENDIX A
CAPACITANCE TESTING

APPENDIX A
CAPACITANCE COUPLED PROTOTYPE TESTER

Figure A-1 shows a block diagram of the prototype system. The system includes electronics for closed loop control of the probe to sample spacing while making simultaneous detector measurements. The signal from the capacitance coupled probe is amplified by a preamplifier and postamplifier. This signal can then be analyzed as outlined in this appendix to determine the detector parameters. The same signal is also sent to a phase sensitive detector which extracts the amplitude of the square wave test signal. The output of the phase sensitive detector is a DC voltage whose amplitude represents the probe capacitance. This voltage is then amplified by an error amplifier and transducer power amplifier and used to drive a piezoelectric transducer, thus completing the feedback loop.

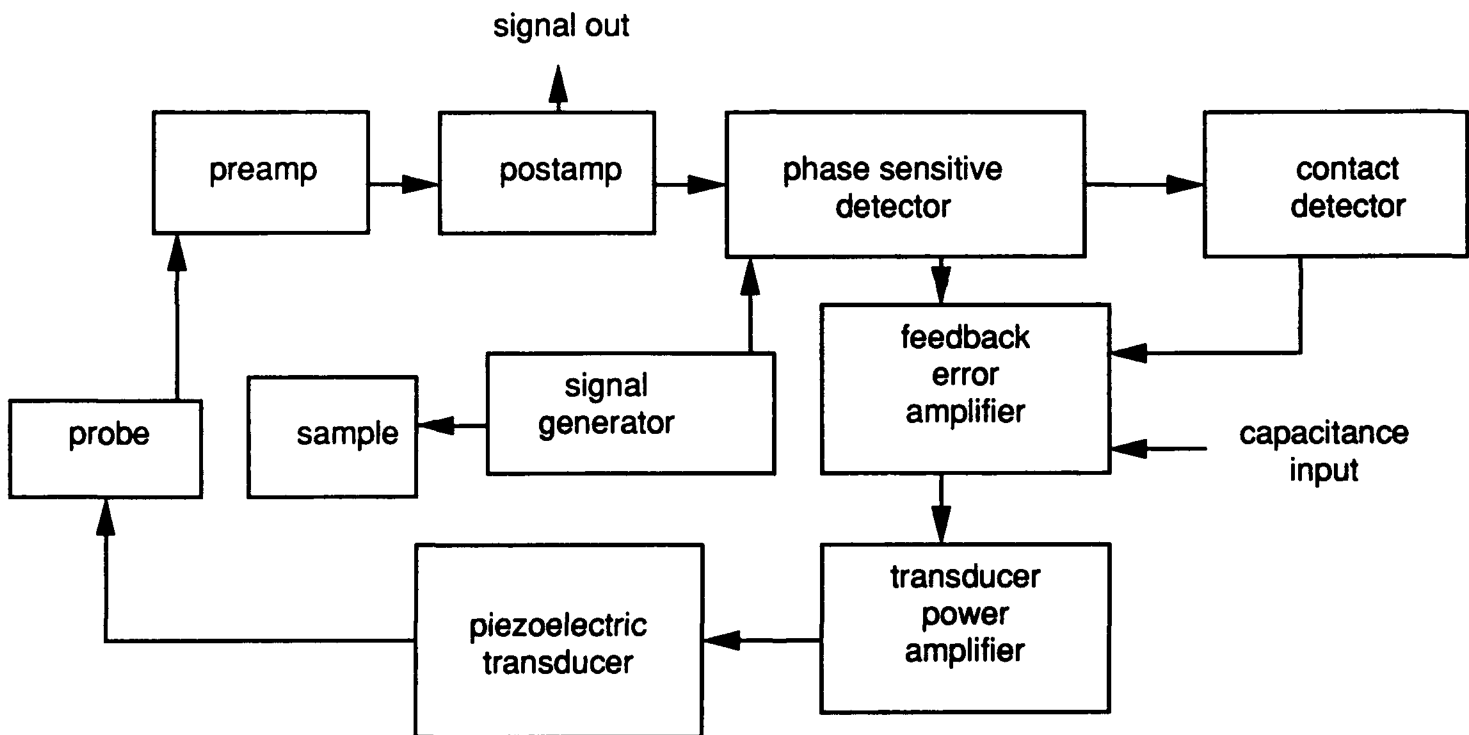

Figure A-1. C-Coupled Electronics Block Diagram

We spent a good deal of effort ensuring that each of the blocks in this diagram work as intended. Detailed schematics of the electronics are included. The preamplifier noise was measured and found to be as predicted. The phase sensitive detector and error amplifier worked as intended. The power amplifier was specifically designed for a bandwidth (100 kHz) and slew rate (0.5 V/μs) good enough so that the prop-

erties of the power amplifier would not affect the overall feedback loop. We selected a standard piezoelectric transducer with a rated displacement of 45 μm with 100 Volts input. This relatively low voltage allowed for a simple power amplifier design and significantly reduced the safety requirements of the system.

As an example of the signal levels involved, the capacitance of a 1 mil diameter probe spaced 1μm above a detector pad is less than 5 pF. For a typical detector signal of 5 mV and an effective preamplifier input capacitance of 5 pF, the signal voltage available at the preamplifier is 5 μV and the signal current at a frequency of 1 kHz is about 0.1 pA. Although these numbers are larger than the fundamental preamplifier noise, these signal levels are very small.

A.1 LOOP BANDWIDTH

At the beginning of the project, we anticipated that the performance of the tester would be determined mostly by the properties of the feedback loop. A high bandwidth in the feedback loop would result in very accurate position control of the probe to sample spacing even in the presence of the stray mechanical vibrations which are always present. Accurate Z-axis control would allow for a small probe to sample spacing, which would improve the signal to noise ratio and minimize the effect of stray capacitance on the measurement accuracy. Therefore, our efforts after the electronics were completed and checked out centered on maximizing the loop bandwidth.

Our first loop bandwidth measurements indicated an effective bandwidth of about 50 Hz (we estimated that about 1 kHz bandwidth would be required). We were able to identify the limiting element in the feedback loop as the probe mount, which was not sufficiently stiff, and consequently added a time delay to the loop and limited the maximum obtainable bandwidth.

We then redesigned the probe assembly, as shown in Figures A-2 and A-3. The outer probe shield is soldered into a small stainless steel collar which is bolted to the piezoelectric transducer. The top of the probe is wired with a short flexible connection to the preamplifier, which is mounted to the (stationary) body of the transducer. The stiffness of this assembly appeared to be sufficient for a 1 kHz loop bandwidth.

When we tried to increase the loop bandwidth, however, we found that the loop was still not stable. We traced this instability to microphonic (piezoelectric) signals generated in the probe and preamplifier

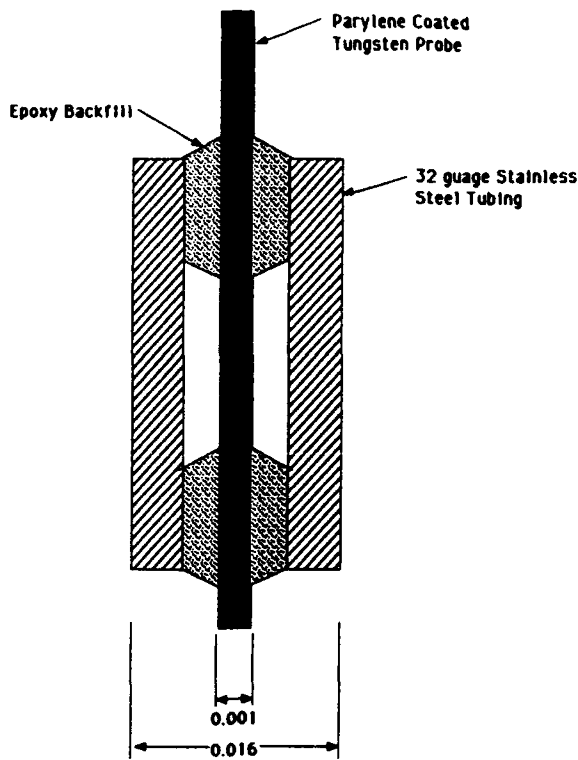

Figure A-2. Shielded Probe Design

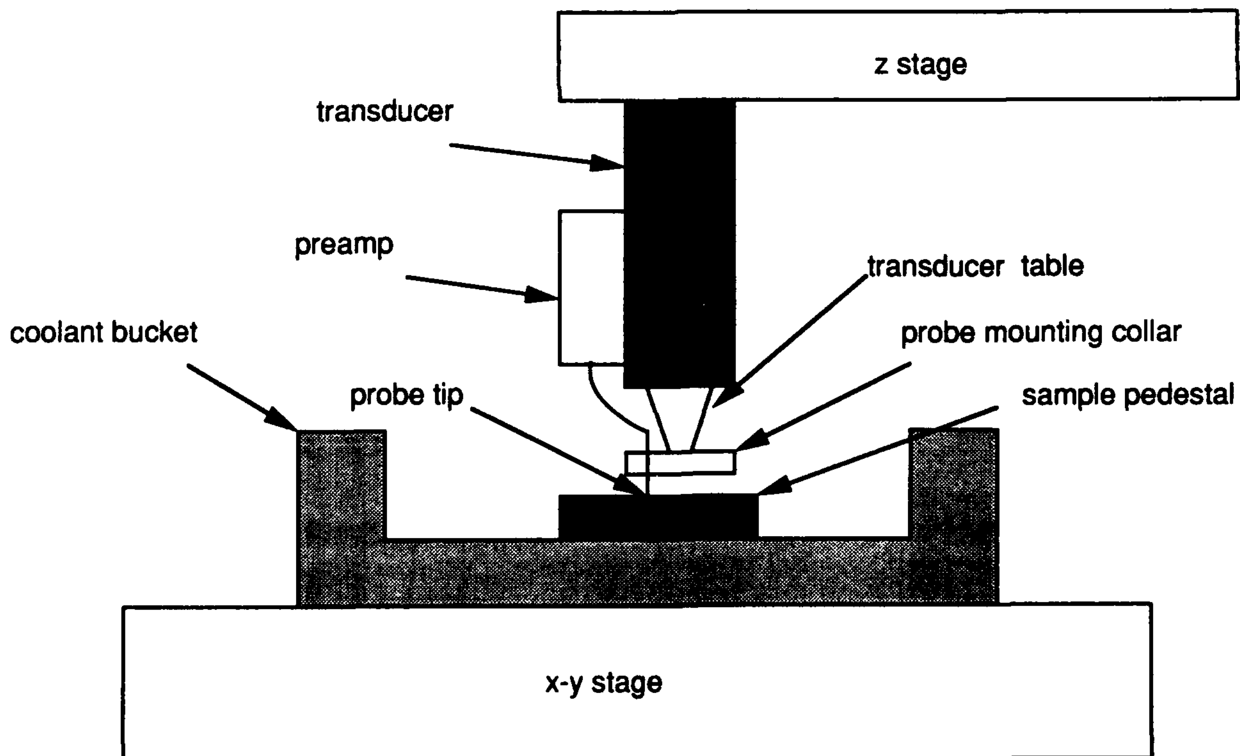

Figure A-3. C-Coupled Mechanical System

assembly. Although these signals are rejected by the phase sensitive detector circuit, the rejection is not perfect due to residual unbalance in the circuit.

We then reduced the stray signals by eliminating unnecessary insulators from the preamplifier/probe assembly. We adjusted the phase sensitive detector for best balance to maximize rejection of stray signals. The bandwidth of the loop could then be increased to about 200 Hz, still well below the mechanical limit. The loop behavior was very difficult to understand at this point. It appeared that the stray signals were still limiting the loop stability at high bandwidths, due to interaction between the mechanical system resonances and the phase sensitive detector. The loop stability varied dramatically with small changes in the measurement frequency, for example.

During the evaluation of the loop stability, we discovered that if the probe actually contacted the sample, the electronics overloaded, with the result that the probe was fully extended by the feedback loop. The undesirable behavior resulted in the destruction of several probes. We then added a circuit which detected the overload and bypassed the main loop, full retracting the probe. This circuit proved essential when attempting actual detector measurements.

Since we had exhausted all the options for increasing the loop bandwidth, we then proceeded with the evaluation.

A.2 EVALUATION WITH LONG WAVE FOCAL PLANE

The next phase of the evaluation was the attempt to measure signal from a real focal plane array. We mounted an insulated bucket to hold liquid nitrogen underneath the probe assembly and procured a sample detector array mounted in an IC package. Figure A-3 shows a diagram of the system front end.

At this point we also reconsidered our analysis of the maximum available probe capacitance. Since the capacitance of two parallel plates is inversely proportional to the spacing, the capacitance should become infinite as the spacing is reduced. We had neglected, however, the effects of surface roughness of the plates (in this case, the probe and the diode contact). Since a very small surface area is involved, we realized that the capacitance would still be finite when the plates touch, and would not be much larger than the parallel plate capacitance at a spacing equal to the peak surface variation. Along the same lines, we had underestimated the effect of stray capacitance from the body of the probe. Even though the spacing

from the probe body to the rest of the array is large, this is more than compensated for by the larger areas involved.

The first problem with the setup was to align the probe to the detector indium bumps. Unfortunately, the probe shield was much larger than the bump size, preventing visual alignment. We then attempted alignment by looking for signals in the feedback loop; the increased height of the indium bumps should show up as a correction signal in the feedback loop. At best, however, it was difficult to distinguish this signal from the random vibrations of the test setup. Mounting the system in a vibration isolated environment would have allowed alignment by this method.

We then attempted to measure a detector by pouring liquid nitrogen into the bucket. We prepared a "clamshell" cold shield which could be folded around the detector array, leaving a small hole for the probe assembly. We found that the microphonics induced by the boiling nitrogen were much larger than those we observed when the system was warm. There was then no change for alignment or measurement of detector signals.

To avoid this problem, it would be necessary to use gas cooling in a vibration isolated environment. At this point, we terminated the experiments and considered other options as discussed below.

A.3 FURTHER OPTIONS

At the point we terminated the experiments, it was clear that developing a capacitance coupled tester along the lines we were pursuing would be a long, difficult, and expensive task. The need for rapid, nondestructive testing of large diode arrays remains, however, and so we investigated two alternatives, non-destructive contact probing and more sophisticated capacitance coupled systems. We feel that the non-destructive contact probing is the method of choice, provided only that problems with the probe lifetime and cleanliness can be managed. The more sophisticated capacitance coupled approaches are suggested by work from IBM on capacitance microscopy.

A.3.1 NON-DESTRUCTIVE CONTACT PROBING

As we worked to develop the capacitance coupled prototype, it became clear that with the piezoelectric transducer, it was possible to control the probe with extremely high precision. One of the experiments

we performed in the checkout of the system was to implement a simple electronic circuit which lowered the probe at a constant velocity of about 1 cm/s (10 μm/ms). When contact with the detector was detected, a scope trigger signal was retracted at the highest possible velocity. The 100 μs measurement time is more than adequate to measure both Ro and Ri with reasonable precision.

During the measurement time, the probe continues to enter the indium detector pad at the same velocity, penetrating to a total depth of 1μm. Since the indium detector contact is about 10 μm deep, this type of contact will barely disturb the bulk of the indium. Even repeated contacts to the same element should cause a barely observable deformation of the indium contact.

The problems we foresee with this approach are: lifetime of the probe, and open or faulty contacts. A vendor of a similar "light touch" probing system performed a test to determine if typical probes would be contaminated or otherwise degraded by thousands of such tests. The results showed mostly that the vendor's system was not properly detecting contact, and the probe was being driven completely through the indium test sheet. In spite of this mistreatment, the probe appeared to survive the test with no problems.

The second problem, of no contact due to an open detector or other mechanical problems, is more difficult to handle. We propose a computer controlled tester which measures the average height of bumps which have been successfully contacted and uses this information to limit the excursion when no contact is found. A force limiting spring or force sensor as part of the probe assembly might also serve to limit array damage when no electrical contact is detected.

LORAL IRIS has successfully operated a cold probe station for about 10 years in the production of photoconductive arrays. Only limited cold shielding is necessary for contact measurements, since the response and Ro measurements can be performed even with a substantial background flux. Considering all the factors, the non-destructive contact probing is the method of choice of further work.

A.3.2 ENHANCED CAPACITANCE COUPLED TESTING

As part of this project, we obtained several research reports on related topics, including scanning tunneling microscopy, atomic force microscopy, and capacitance microscopy. We were especially interested in the electronics associated with capacitance microscopy, since the reported sensitivity of 10^{-22}F/Hz$^{1/2}$ was about 100 times better than obtainable with our capacitance coupled setup.

After reading the reports carefully, we decided that the capacitance sensor used (it was originally developed for the unsuccessful RCA videodisk project) incorporated a UHF tuned circuit. The signal to noise ratio would then be improved by the Q of the tuned circuit; a Q of 100 is readily obtainable.

The other interesting feature of the capacitance microscope was the use of dC/dZ technique: the probe to sample spacing was varied at a high frequency, and only the component of the capacitance which varied at the modulation frequency was used. This approach rejected all the 1/f noise of the capacitance sensor, as well as signals due to capacitance not directly at the probe tip. Thus, the probe would not require shielding, and could be visually aligned if needed.

The problem with these techniques is that it is not obvious how to perform the Ro measurement using the dC/dZ signal. It seems likely, therefore, that only measurements of diode photovoltage would be available, and that dV/dZ technique would be needed to ensure that the signal being measured was indeed coming from the capacitance at the probe tip.

The general tone of the published reports is that there are remarkable techniques available for making measurements with small, non-contacting probes. Further assessment of these techniques is justified if the non-destructive contact probing proves to be much more difficult than currently anticipated.

(Remainder of this Appendix (A-1) is an excerpt from the 12th monthly report of this contract.

A.4 C-COUPLED

During September, the planned C-coupled demonstration using measurements on silicon diodes was completed. The time domain behavior of the system was found to be much simpler to analyze than the frequency domain analysis previously reported. A new preamplifier was designed, built and used for the measurements. The measurements agree with conventional measurements on the same device. A block diagram of equipment for an automatic test system was generated. These developments confirm the earlier conclusion that capacitance probe diode measurements are feasible, and that the performance of an automatic tester will be limited mostly by the positioning of the probe.

A.4.1 PREAMPLIFIER DESIGN AND PERFORMANCE

Figure A-4 is a simplified schematic of the new preamplifier. It incorporates a low noise, high bandwidth operational amplifier with a discrete FET matched pair input buffer for very low input current. The input device is a Siliconix U423, designed for very high input impedance amplifiers. This configuration is also called "current sensitive" or "charge sensitive", since the output voltage of the amplifier is proportional to either current or charge at the input, depending on the feedback element used.

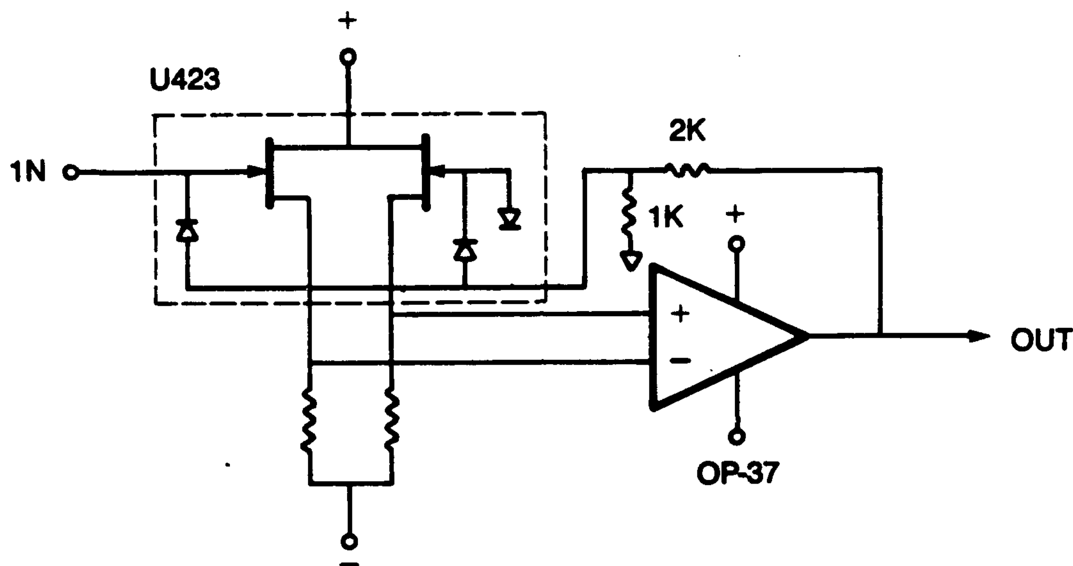

Figure A-4. Simplified Preamplifier Schematic

The novel aspect of this amplifier is the feedback element used. The integrated substrate to gate diode of the U423 forms the feedback element. This diode behaves as capacitor of about 3 pF in parallel with about 10^{12} Ohms. It was chosen as the feedback element because of the difficulty of obtaining components of this value, and to minimize parasitics. A divide by 3 in the feedback loop increases the total gain by a factor of 3. The amplifier behaves as if the feedback capacitor were about 1 pF. The bandwidth obtained from the preamplifier is about 5 MHz; it should therefore be usable with diode junction time constants as low as 300 ns. (An Ro as low as 10^5 Ohms with a junction capacitance of 3 pF, for example).

The amplifier behaves as a charge sensitive amplifier over the frequency range of about 1Hz to its upper bandwidth limit of about 5MHz. Below about 0.1 Hz, the effective resistance of the feedback element causes the amplifier to behave as a current sensitive amplifier. This allows for the leakage current of the input device to be accommodated, and sets an upper limit on the junction time constant that can be conveniently measured of about 0.1 second. (An Ro as high as 3×10^{10} Ohms with a 3pF junction capacitance).

The amplifier output noise was measured as about 50 nV per root Hz over most of the frequency range. Expressed as charge referred to the input, this is 5×10^{-20} coulombs per root Hz. This value is very close to the expected value based on the U423 noise voltage of 10 to 15 nV per root Hertz (from the manufacturer's data sheet) and a total stray capacitance of 3 to 5 pF at the input. The noise at frequencies the conclusion that mechanical properties of the test setup are very important.

Expressing the amplifier noise in terms of charge is convenient because the equivalent noise voltage of a tester can then be simply determined from the fundamental relation:

$$V = Q/C \tag{1}$$

For example, with a probe capacitance of 10^{-14} F, the effective input noise voltage is 5×10^{-6} V per root Hz. That is, a voltage measurement accurate to about 5 microvolts can be made in about 1 second; a measurement accurate to about 50 microvolts can be made in about 10 ms. The voltage accuracy required for diode measurements is related to kT/q, which is about 7 mV at 80 K. This amplifier will then provide a signal-to-noise ratio of about 100:1 with a 10 ms measurement time with a probe capacitance of 10^{-14} F. This calculation agrees very well with the estimates presented earlier in the program.

If desired, the input transistor of the amplifier can be mounted some distance away from the remainder of the circuitry. This would allow the device to be purchased as a bare chip, and wire bonded into a probe assembly. The noise of this device is expected to decrease with temperature, reaching a minimum at about 150 K. It might ultimately be practical to incorporate a small heater into the probe assembly to maintain this temperature. Alternately, the transistor can be located for enough away from the probe tip to be maintained at room temperature without significantly degrading the amplifier noise.

A.4.2 TIME DOMAIN MEASUREMENTS

The original concept of capacitance probe testing was the realization that a voltage change on, for example, a diode contact pad will include a charge on an adjacent electrode. The charge sensitive amplifier converts this induced charge to an output voltage. (In this case, the ratio is 1 volt out =

10^{-12} coul. in.) The amplifier output voltage is now directly proportional to the diode voltage. The ratio is Cp/Ca. With a probe capacitance of 10^{-14} F, the output voltage is.01 times the diode voltage. As mentioned above, a typical photovoltage of about 5 mV can be measured with about 1% accuracy in 10 ms with the new preamplifier.

In addition to the photovoltage, a measurement of the device Ro is needed. This measurement can be obtained by biasing the diode and then measuring the rate at which the voltage discharges into Ro. The time constant of this discharge is just the product of the diode Ro and the junction capacitance. More generally, for larger voltages, the rate of change of diode voltage is equal to the diode current divided by the junction capacitance. Thus, if the junction capacitance can be determined, the complete I-V characteristics, including Ro, can be determined.

Figure A-5 shows an equivalent circuit for the device under test, including junction capacitance, Ro, probe capacitance, and the preamplifier. When a fast rising pulse is applied to the diode common, a charge is applied to the preamplifier through the probe capacitance. The same charge necessarily appears across the diode junction, since the probe and junction are electrically in series. After several junction time constants, the voltage across the diode is 0 and the amplifier charge has increased to equal the product of the applied voltage step and the probe capacitance. Since the magnitude of the voltage step is known, the value of probe capacitance is simply calculated. Once the probe capacitance is known, the change in voltage across the diode, and thus the diode junction capacitance, can be calculated. The junction time constant is then determined from the junction voltage decay time constant, and Ro is then calculated. The waveforms and formulas involved are shown in Figure A-6.

The time domain analysis here is mathematically equivalent to the frequency domain analysis presented earlier in the program. The time domain analysis is easier to understand, and it is also simpler to

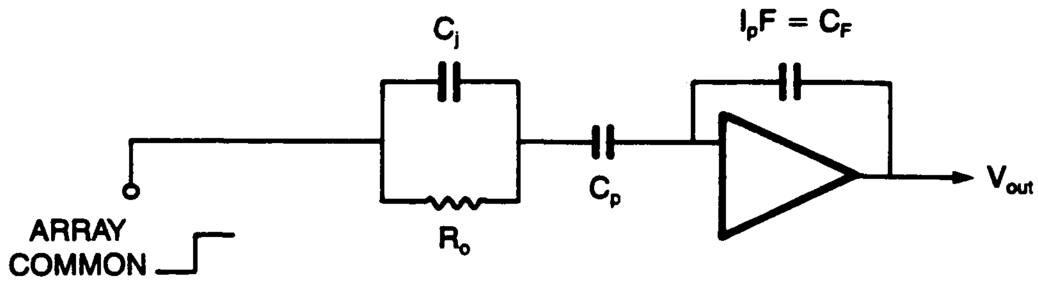

Figure A-5. Test Equivalent Circuit

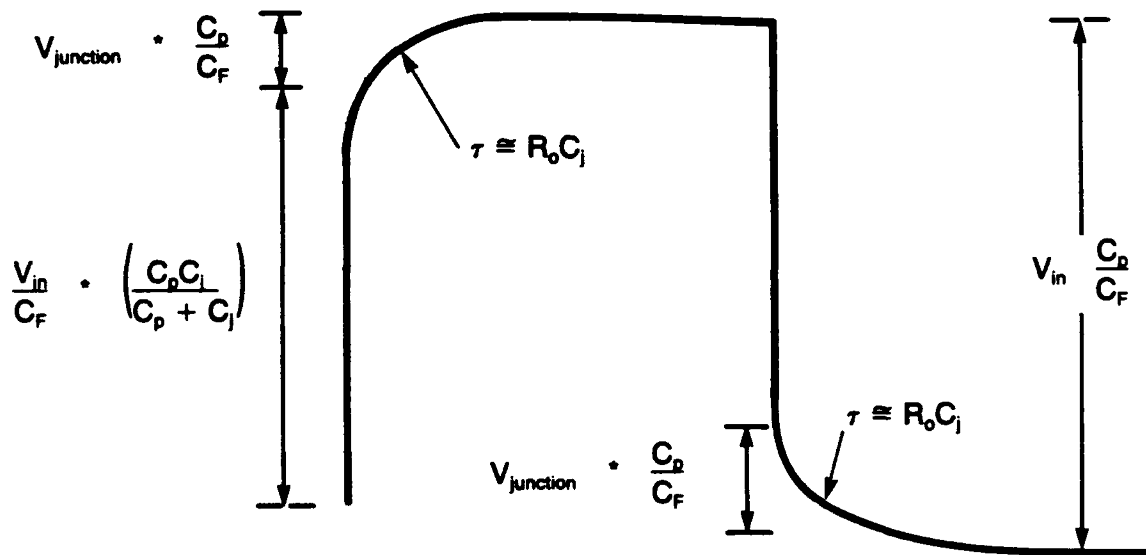

Figure A-6. Theoretical Measurement Waveform

include nonlinear effects into the analysis. In addition, the equipment needed to perform a time domain analysis is readily available.

A.4.3 MEASUREMENT RESULTS

Figures A-7 to A-15 show sample waveforms with a IN5711 diode, including photovoltage measurement. This diode was used because it has electrical properties at room temperature which are similar to those expected of long wave detectors at 80 K. It has an Ro of about 15 MOhms, and a junction capacitance of about 1.6 pF. In addition, it is in a glass package which allows for generation of photocurrent. With a high intensity lamp source, we were able to generate a photovoltage as large as 100 mV with this device. The I-V characteristics of this diode are shown in Figure A-7 (not illuminated) and Figure A-8 (illuminated).

Figure A-9 shows a capacitance coupled impedance measurement. Note that all the predicted features of the theoretical curve are present. Figures A-10 and A-11 are expanded versions of the data of Figure A-9 (using the capability of the digital storage scope). Shown on the Figures are the actual measurement sequence: the probe capacitance is determined from the measured output voltage and the known input voltage and preamplifier capacitance. (The effective amplifier capacitance in the figures has been adjusted for a postamplifier gain of 100). The voltage step and rise time at the top and bottom of the waveform are then used to calculate the junction capacitance and Ro. The values computed in the Figures are within about 20% of the values measured on similar devices using conventional equipment.

The probe capacitance for these measurements was about 6.3×10^{-14}F. This value was chosen to swamp strays in the test setup and to simulate the ratio of strays to probe capacitance which we expect with an array sized probe. The resulting signal-to-noise ratio is very large, as can be seen from the photographs. The signal-to-noise ratio of a smaller probe capacitance was simulated by reducing the input voltage. The signal-to-noise ratio was then enhanced by averaging 64 sweeps with a digital oscilloscope. The results, shown in Figures A-10 and A-11, are exactly as expected. Even with 64 averages at a pulse rate of 2 kHz, the total measurement time is still only 32 ms.

Figure A-12 shows the change in diode resistance with illumination level. Figure A-13 shows an impedance measurement made with a large input voltage. Notice that the forward bias time constant is very small, while the reverse bias curve shows a linear, rather than exponential, shape. Figure A-14 shows

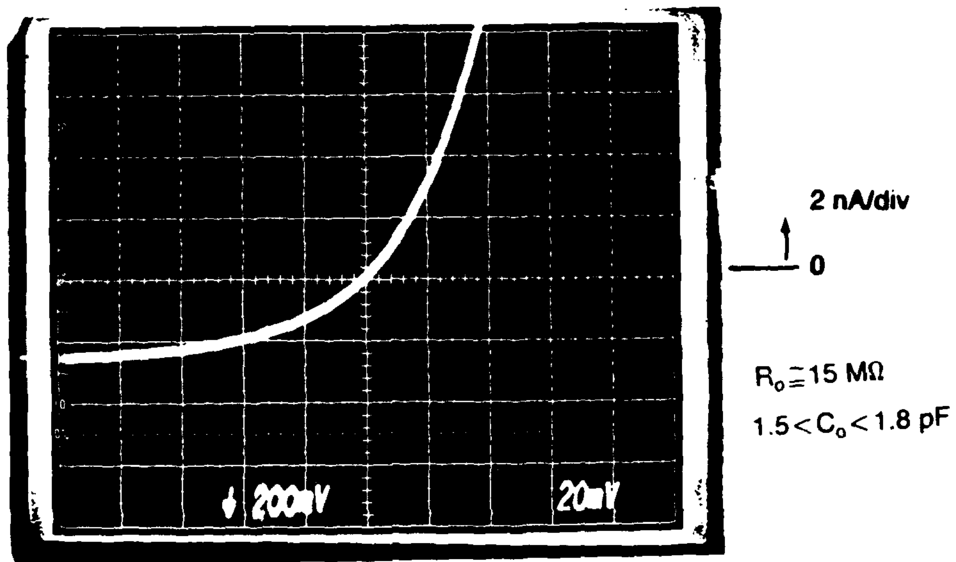

0 → 20 mV/div

Figure A-7. Contact Measurement of IN5711 Silicon Diode I-V -Dark

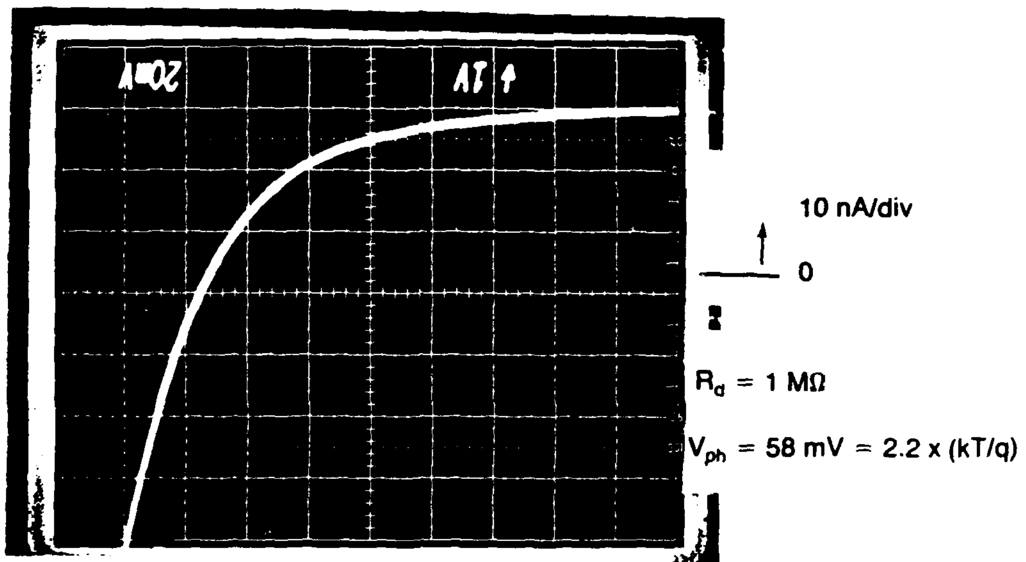

0 → 20 mV/DIV

Figure A-8. Contact Measurement of IN5711 Silicon Diode I-V -Illuminated

dt = 167.1 μS

dV = 313 mV

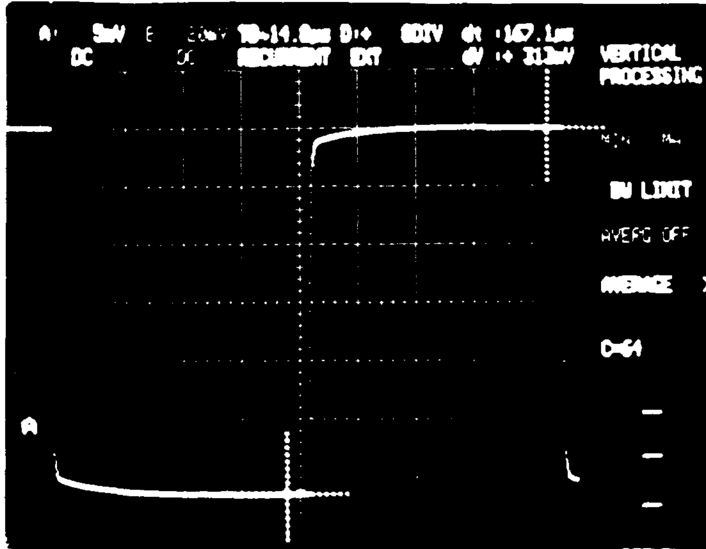

$5 \times 10^{-16}\ \frac{\text{COULOMB}}{\text{DIV}}$

$C_F = 10^{-14}$ F

$V_{in} = 50$ mV

$C_P = C_F \frac{V_o}{V_{in}} = 63$ fF

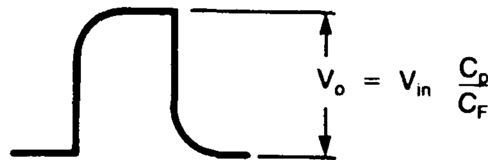

Figure A-9. C-Coupled Output Waveform Step Height Used to Measure Probe Capacitance Cp

dt = 160.5 μS

dV = 15.1 mV

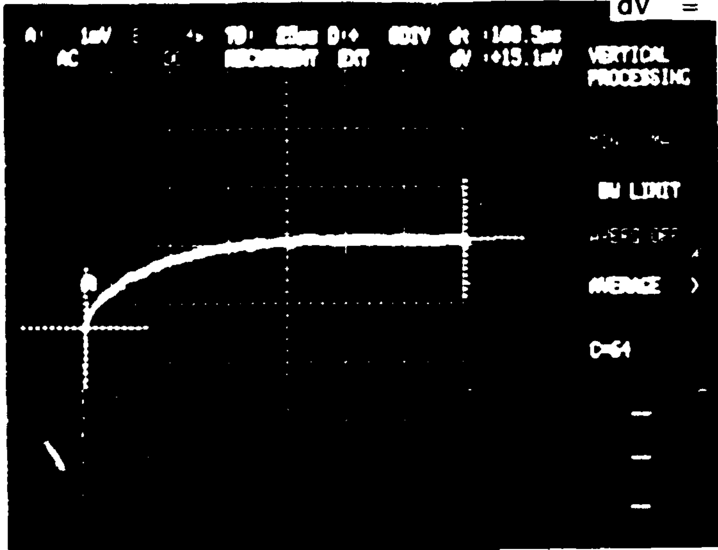

$$C_j = C_P \frac{V_o}{\Delta V} = 1.3\text{ pF}$$

DIODE VOLTAGE V_j

$$= \Delta V \frac{C_F}{C_P} = 24\text{ mV}$$

dt = 23.63 μS

dV = 9.77 mV

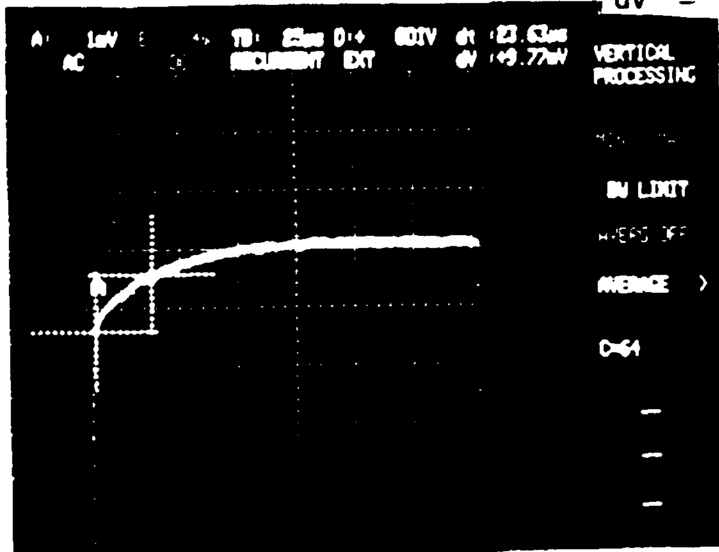

$$R_o = \frac{dt}{C_j} = 18\text{ M}\Omega$$

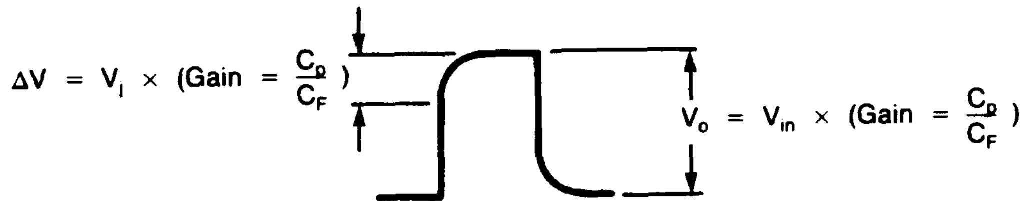

Figure A-10. Ro, Cj and Vj Values Extracted from Expanded Waveform (Upper)

dt = 160.6 μS

dV = -13.7 mV

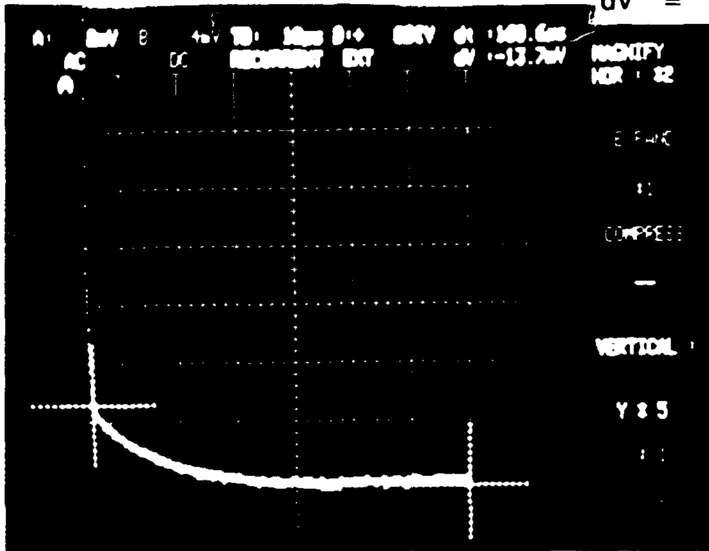

$$C_j = C_P \frac{V_o}{\Delta V} = 1.4 \text{ pF}$$

DIODE VOLTAGE

$$= dV \frac{C_F}{C_P} = 2.2 \text{ mV}$$

dt = 24.50 μS

dV = -8.79 mV

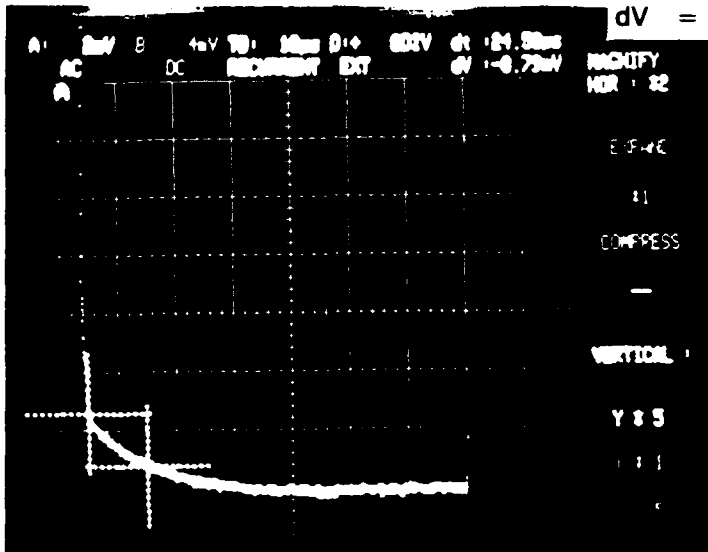

$$R_o = \frac{dt}{C_j} = 17.5 \text{ M}\Omega$$

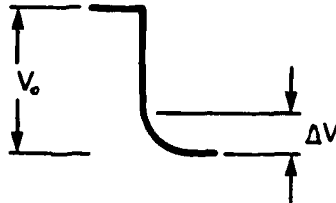

Figure A-11. Ro, Cj and Vj Values Extracted from Expanded Waveform (Lower)

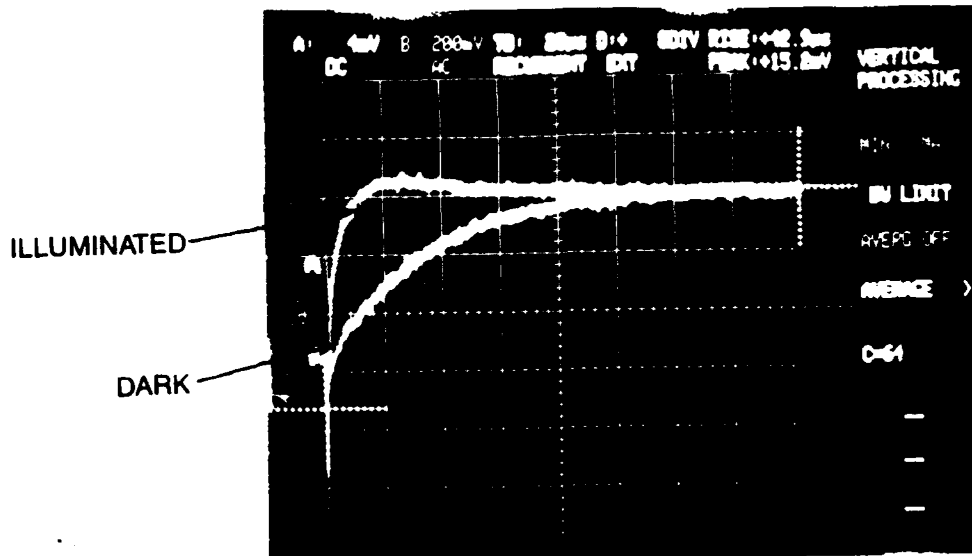

Figure A-12. Expected Time Constant Reduction Due to Illumination

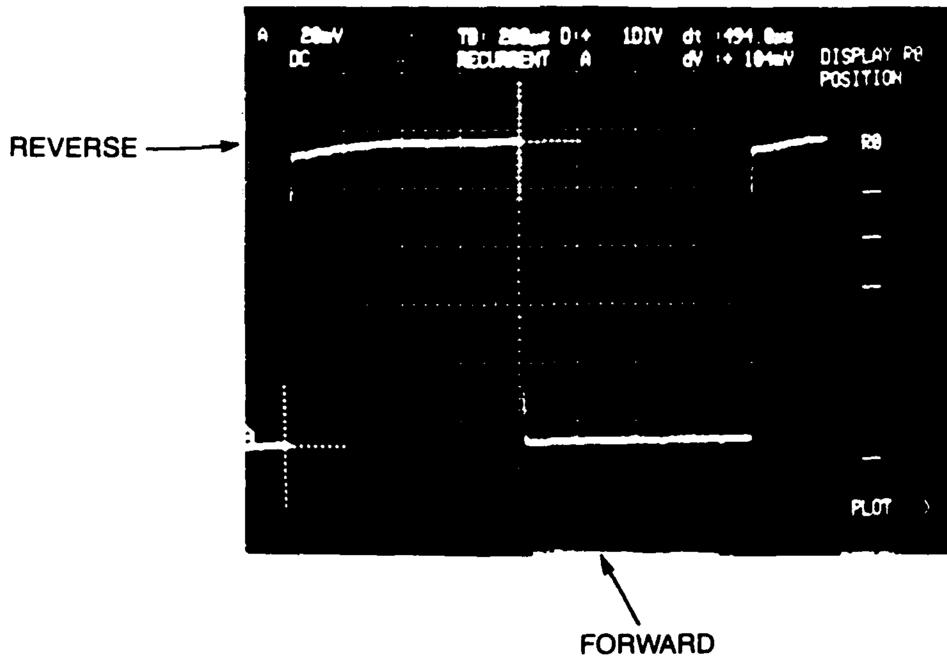

Figure A-13. Asymmetry in C-Coupled Output Waveform Observed Due to Nonlinearities of Diodes at High Bias

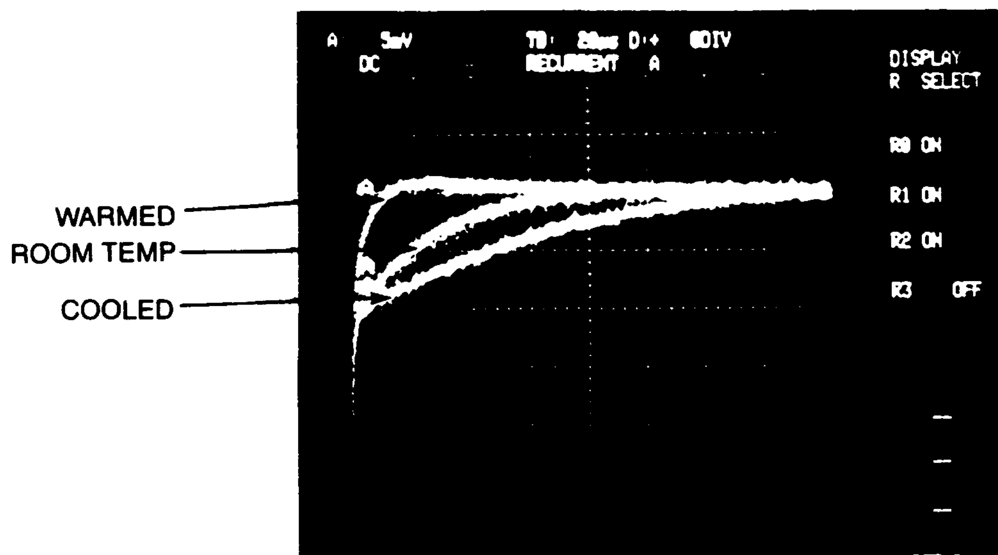

Figure A-14. Expected Variation of Ro with Temperature observed

the change in time constant Ro with temperature. The temperature was changed with cold nitrogen gas and a hot air gun. Figure A-15 shows direct and capacitance coupled photovoltage measurements. For this photograph, the gain of the capacitance coupled setup was adjusted to match the gain of the direct measurement. As expected, the waveforms are practically identical.

A.4.4 EQUIPMENT NEEDED FOR AUTOMATIC TESTING

The photographs of the screen of the averaging digital oscilloscope demonstrates that, as expected, the signal-to-noise ratio can be improved simply by averaging multiple scans of the preamplifier output. This type of equipment is available from a number of manufacturers and is readily interfaced to computers. The calculations would be performed as above, except that a least squares analysis would be used with the averaged data to optimize the accuracy of the parameters.

Another problem which is simplified by the use of time domain measurements is that of active probe positioning. The probe can be positioned by controlling the peak-to-peak amplitude of the amplifier output to give a particular probe capacitance. As long as the bandwidth of the probe position servo loop is lower

10 mV
DIV

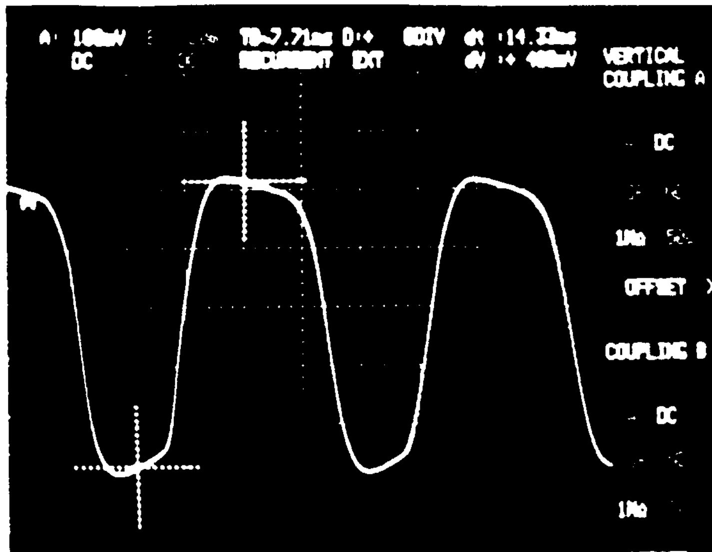

C-COUPLED
MEASUREMENT

7.7 mS/DIV

10 mV
DIV

DIRECT CONTACT
MEASUREMENT

7.7 mS/DIV

Figure A-15. Direct and C-Coupled Photo Voltage Measurement

than the pulse repetition frequency, no interference between the probe positioning and the electrical measurements should occur. Notice that the signal-to-noise ratio involved in measuring the probe capacitance is much larger than for measuring diode parameters; the probe positioning should be very accurate. Measurements at lower frequencies could still be performed by allowing for the effects of positioning servo on the amplifier output waveform.

APPENDIX B
ELECTRON-BEAM TESTING

NONCONTACT CHARACTERIZATION OF PV DETECTORS AND ARRAYS

Final Report

1 November 1987 - 31 October 1988

on Contract #DAAB0787CF105

Center for Night Vision and Electro-Optics Fort Belvoir, VA

LORAL
Infrared & Imaging Systems

2 Forbes Road
Lexington, MA 02173

TABLE OF CONTENTS

(directed to input this manually)

SECTION	TITLE	PAGE
1	INTRODUCTION	
2	APPROACH AND SYSTEM MODIFICATIONS	
	2.1 Principles of Voltage Probing by Secondary Electron Energy Analysis	
	2.2 Applied Beam Technology IL-200 Voltage-Probing Scanning Electron Microscope	
	2.3 Schemes for Current Control and Device Voltage Measurement	
	2.4 Impedance Measurement Process and Test Controller Development	
	2.5 Cold Stage and Cold Radiation Shielding	
	2.6 Vacuum Configuration and Measurement	
3	RESULTS AND DISCUSSION	
	3.1 Control of Primary Current	
	3.2 Control of Impressed Current	
	3.3 IV Measurements on MWIR Photodiode	
	3.4 Effects of Cold Shielding on Secondary Electron Collection and Energy Analysis	
	3.5 Measurement of Noise and Systematic Error	
4	CONCLUSIONS	
5	SUMMARY	
6	APPENDICES	

SECTION 1
INTRODUCTION AND SUMMARY

Screening of photovoltaic detector arrays at the wafer level can provide benefit to the production process at a point where handling of a large number of arrays is relatively straightforward. It provides more immediate feedback to the wafer-level portion of the array fabrication process than other tests which occur later in the production process, and eliminates the cost of hybridization of arrays which are already out of spec at the wafer level

This report summarizes the results and conclusions from a 12-month investigation of the electron beam approach to non-contact, non-destructive electrical measurements of photodiode arrays at the wafer level for the purpose of wafer-level screening. The general principles of the method are described, as well as the particular details of the feasibility tests which were carried out in a voltage-probing electron beam system which was originally developed and sold commercially, but modified to some extent for this investigation. The particular results of the feasibility tests are presented and discussed, and general conclusions are given concerning the overall feasibility of the electron beam approach, some particular strengths and weaknesses of the method as it was tried in this work. A summary of the investigations and recommendations are presented at the end of this report.

Statement of the Problem

At present there are no effective techniques for 100% screening of PV detector arrays at the wafer level in a production setting. Available methods for measuring detector characteristics at the wafer level either pose the risk of damage to detector elements (such as mechanical probing) or commit arrays to a readout or interface structure (TRO or DID structure). Voltage-probing scanning electron microscope technology, on the other hand, is potentially capable of rapidly measuring detector characteristics on an element-by-element basis in a totally non-contacting, non-destructive manner.

Voltage-probing electron microscopy is being increasingly used in applications requiring non-contact, non-destructive electrical characterization of signals in integrated circuits. However, unique modifications of the technique are needed for impedance measurements on photodiode arrays because the devices to be tested are isolated from any hard contact means of biasing and thus totally passive.

SECTION 2
APPROACH AND EXPERIMENTAL METHODS

2.1 PRINCIPLE OF VOLTAGE PROBING BY ENERGY ANALYSIS OF SECONDARY

Electron Emission

Changes in the voltage of a sample can be sensed and measured in a non-contact, non-destructive manner by analysis of the energy distribution of the secondary electrons (SE's) generated by an electron beam incident on the sample surface. A series of typical SE energy distributions is shown in Figure 2-1. The distribution is typically about 20 eV wide with a peak at about 5 eV.

The basic effect used to sense and measure sample voltage changes is a uniform shift of the SE energy spectrum to higher or lower energies due to acceleration or deceleration of SE's as they move away from the vicinity of a sample surface biased away from ground potential. The various curves in the top half of Figure 2-1 show this effect; for positive or negative voltage changes the distribution moves to lower or higher energies, respectively.

A retarding field energy analyzer used in a voltage-probing SEM acts as a high pass SE energy filter, allowing only those SE's with a kinetic energy greater than a certain threshold value to pass through to the SE detector. The threshold kinetic energy value is determined by the voltage set on the retarding grid of the analyzer. This grid is identified in Figure 2-2, and the high pass energy filtering action illustrated. A useful quantity for description and analysis of the technique is the ratio of the SE currents incident on and transmitted by the analyzer, which is its transmission T. Any changes in the sample voltage result in a change in analyzer transmission due to the shift in SE energy distribution, which in turn modulates the SE detector output. This kind of modulation also occurs to some extent in a conventional SEM where it is known as voltage contrast. The specific adaptations in a voltage-probing SEM are designed to enhance the sensitivity and reproducibility of this effect so that it may be used for quantitative measurements.

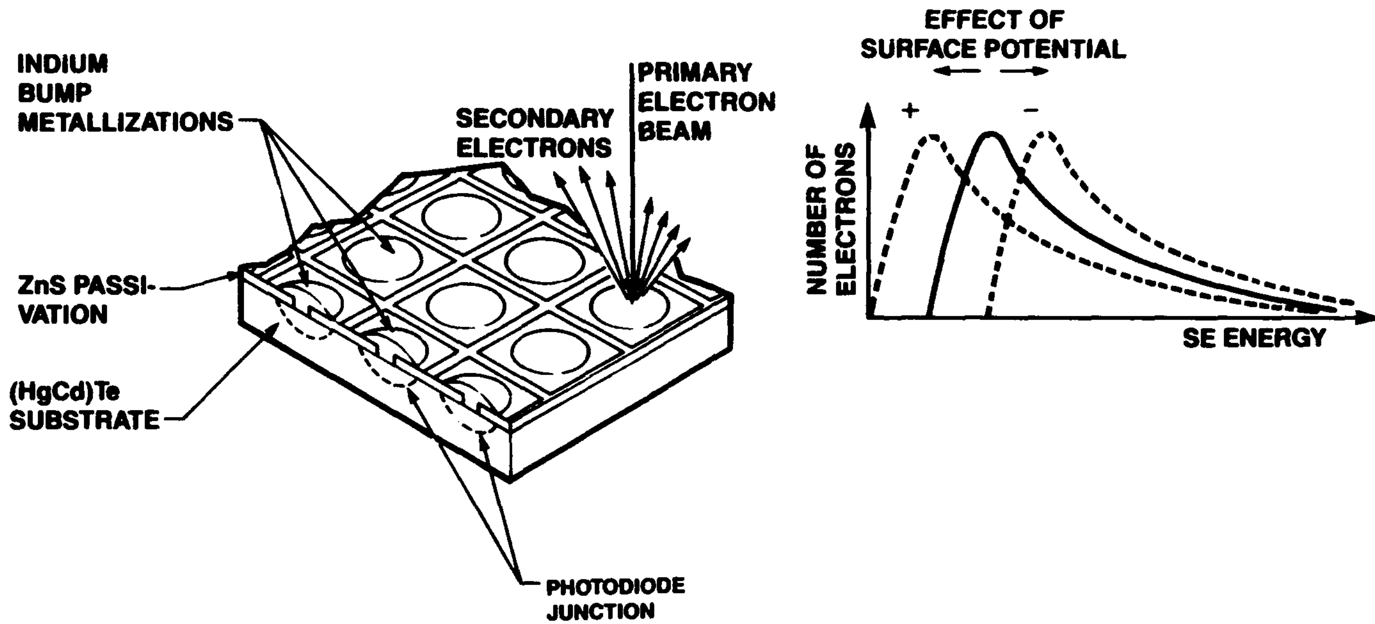

Figure 2-1. Principles of Voltage-Sensitive Electron-Beam Probing

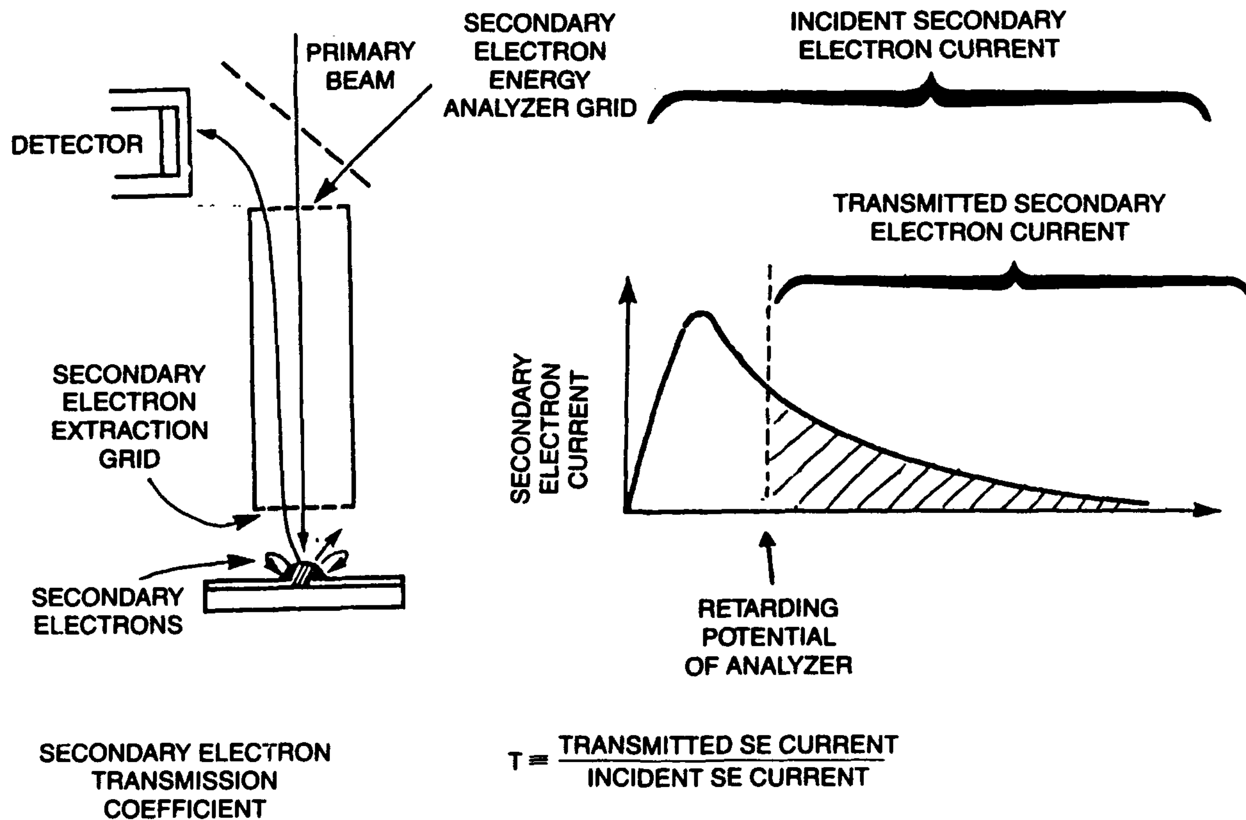

SECONDARY ELECTRON TRANSMISSION COEFFICIENT

$$T = \frac{\text{TRANSMITTED SE CURRENT}}{\text{INCIDENT SE CURRENT}}$$

Figure 2-2. Construction and Operation of Retarding-Field Secondary Electron Energy Analyzer

2.2 APPLIED BEAM TECHNOLOGY VOLTAGE PROBING SYSTEM

The system used in this work is the IL-200 voltage probing scanning electron microscope, manufactured by Applied Beam Technology, Inc., shown in Figure 2-3. It is based on a scanning electron microscope, model SS60, built by ISI. The microscope is fitted with a widebore objective lens. The SE energy analyzer needed for contactless voltage probing is of an in-the-lens design mounted inside the bore of the objective lens, as illustrated in Figure 2-4.

The bottom grid of the analyzer is an annular extraction grid which is held at 0.5 to 1 KV positive potential to pull SE's strongly up into the analyzer, independent of any local fields at the surface of the sample. The hole in the center of this grid is approximately 3 mm in diameter. The bottom surface of this grid is gold-plated. The body of the analyzer is a solid tube coated on the inside with a weakly conducting film to provide an electrostatically shielded environment. The retarding grid for SE energy analysis is located at the top of the analyzer. It is a phosphor bronze mesh with a hole cut out for the primary beam to pass through.

Since the measurement of zero-bias diode impedance requires application and detection of relatively small voltages (under 20 mV) the collection efficiency and energy resolution of the analyzer are important factors in obtaining adequate signal to noise ratio and throughput by this technique.

The performance characteristics of the in-the-lens energy analyzer design differ from that of earlier below the lens analyzer designs in two ways. The proximity of the first grid (extraction grid) to the microscope objective lens immerses the sample region in the residual magnetic field of the lens. The flux lines of this field are oriented along the axis of the electron column axis, so that SE's from the sample follow spiral paths which guides them along the column axis and up through the hole in the extraction grid regardless of their initial angle of emission. This is expected to increase the collection efficiency and optimize the sensitivity and signal to noise ratio of measurements based on SE emission.

Secondly, locating the analyzer inside the objective lens, higher in the electron column allows the analyzer to be long and narrow, thus allowing the SE's to approach the analyzer grid closer to normal incidence and be energy-analyzed more accurately. The in-the-lens analyzer design of the IL-200 system is claimed by ABT to provide as much as a factor of four advantage in signal to noise over below-the-

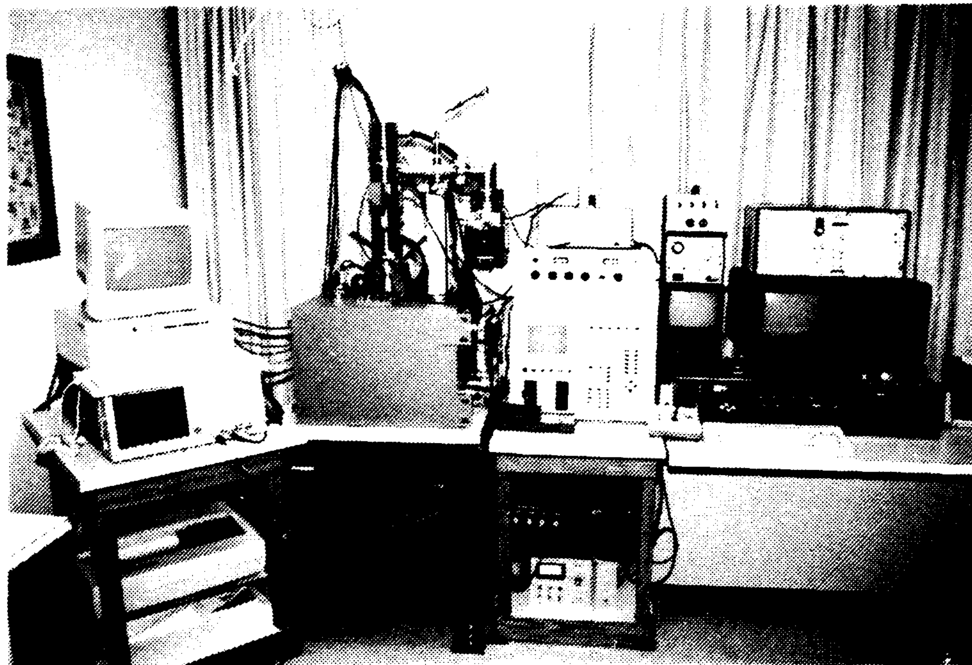

Figure 2-3. Applied Beam Technology IL-200 Voltage-Probing Electron Microscope System

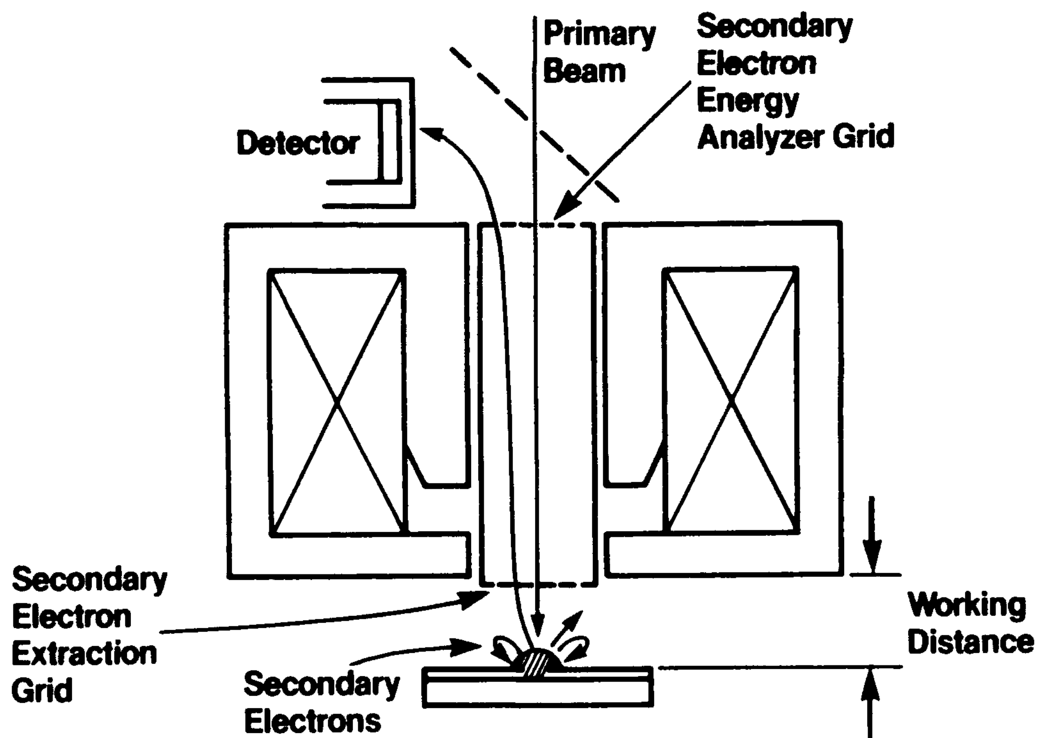

Figure 2-4. Configuration of Objective Lens and Secondary Electron Energy Analyzer in the IL-200 System

lens analyzers. This work was aimed at assessing the impedance measurement accuracy and throughput achievable in a voltage-probing scanning electron microscope system and the role played by the energy analyzer vs. other factors in determining this practical limit.

SE's which emerge from the energy analyzer are detected by a scintillator crystal and photomultiplier tube mounted on the side of the column above the analyzer as shown in Figure 2-5. The SE's are collected for detection by a negatively charged grid mounted just above the analyzer as shown in Figure 2-4. The primary electron beam can be blanked at rates ranging from a few kHz up to approximately 13 MHz in the IL-200 system by an electrostatic beam deflection system located at the top of the electron column, just below the electron gun, as shown in Figure 2-5. It consists of two electrode plates located on either side of the primary beam, separated by a gap of about 1 mm. Application of a 5 V differential between the electrodes deflects the primary electron beam sufficiently that it strikes one of the apertures further down in the electron column and is stopped.

Voltage probing in the ABT IL-200 system is handled by a controller also shown in Figure 2-5, which sets voltages on the analyzer grids, controls blanking of the electron beam if desired, sets the gain and zero offset of SE signal amplification, and samples the SE signal in synchronization with beam blanking when the blanked mode (i.e. pulsed mode) is used.

2.3 CURRENT CONTROL AND DEVICE VOLTAGE MEASUREMENT

Electron beam measurement of photodiode impedance differs from customary electron beam voltage probing of integrated circuits because there is no way to provide bias current to the devices under test other than through the charging effects of the probing electron beam itself. Thus a scheme is needed for controlling the bias current provided by the beam while simultaneously measuring the energy shifts in SE's which indicate shifts in device voltage. The level of bias current must not affect the voltage measurement except through the actual effect on the device voltage. The following is a description of the approach which was used in this program to achieve device voltage analysis while varying the beam current.

The photodiode array is mounted in the sample chamber of the SEM with the metallization for the photo diode elements accessible by the electron beam. An unbonded wafer or die is thus mounted with

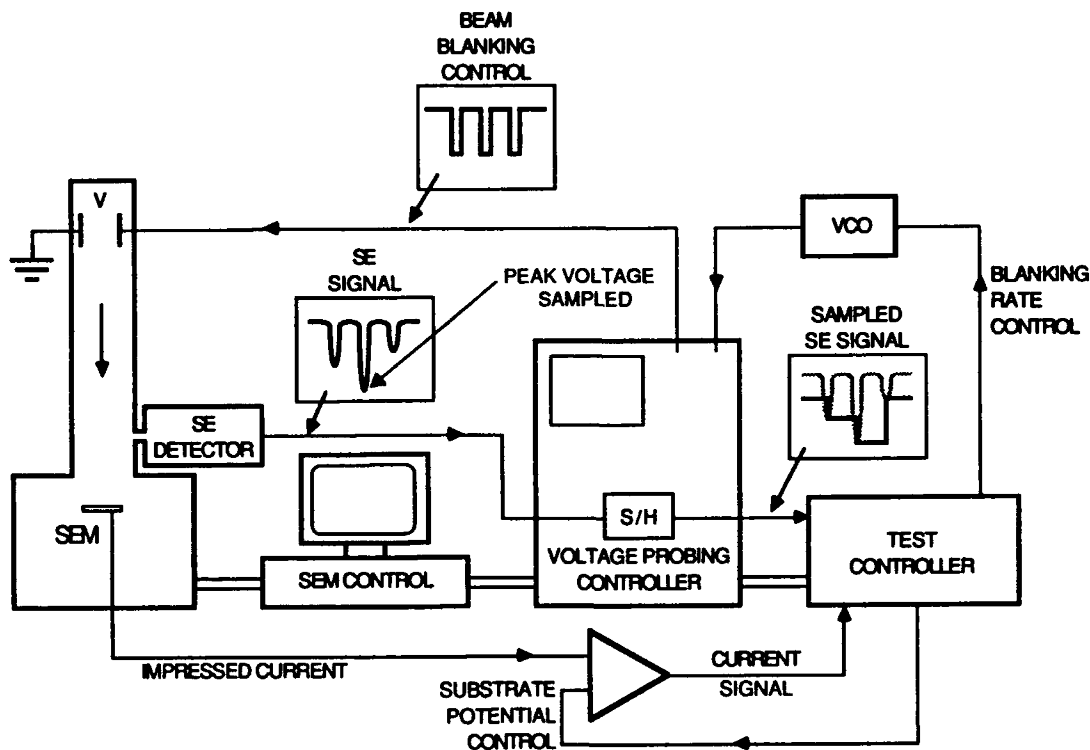

Figure 2-5. Configuration of IL-200 System and Dedicated Controller for Execution of Impedance Measurements

the bump bonding metallization facing upward toward the beam, while an array which is bump bonded to a ceramic carrier is mounted with the carrier metallization facing upward toward the beam. At the primary electron beam energies used (1 to 3 keV), primary electrons penetrate less than one micron into the metallization and thus do not affect any other layers of the device or package structure. As shown in Figure 2-5, a single hardwired electrical lead is connected from the substrate of the photodiode array to a virtual-ground input of a current-sensing operational amplifier. Bias current is applied to a selected photodiode by directing the electron beam to its metallization or package lead. The net bias current is the sum of the primary electron beam current (which is a negative current contribution) and an opposing current (positive) due to secondary electron emission. The overall sign of the resulting bias current (which we call the impressed current as proposed by Eberhart Menzel) is determined by whether the SE yield per primary electron is less than or greater than one.

The operational scheme for obtaining device bias voltage measurements at a selected impressed current value is indicated by the waveforms in Figure 2-5. The electron beam is operated in a blanked

mode. The duration of each beam pulse is identical under the control of the IL-200 controller while the pulse repetition rate is determined by a trigger signal applied externally by a voltage controlled oscillator (the VCO of Figure 2-5). The pulse repetition rates are intended to be sufficiently high compared to the diode RC response time that there is no significant charging or discharging of the diode bias during or between pulses. Under these conditions the diode develops a bias voltage which depends only on the average value of beam current and the diode impedance. The nature of this regime of pulse widths and repetition rates is derived and explained more fully in Appendix A. For measurements on MWIR devices, device RC time constants are on the order of 50-100 μs. This corresponds to minimum usable frequencies of 10 to 20 kHz which is easily satisfied with the present system. For LWIR devices, time constants are expected to be a few μs for high RoA devices and significantly shorter than 1 μs for low RoA devices. The range of blanking rates available in the IL-200 system as it stands (up to 13 MHz) is thus adequate for high RoA LWIR devices although probably inadequate to allow the impedance of low RoA LWIR devices to be resolved accurately.

Provided that the device RC time constant is not too short, then, the effective value of applied device current can then be controlled readily through the VCO control voltage. The average value of impressed current can be read out at the output of the current sensing amplifier after appropriate filtering.

The secondary electron signal at the output of the SE detector preamplifier consists of a pulse train due to the blanking of the primary electron beam. The timing of SE signal pulses is of course synchronized with that of the primary electron beam blanking pulses, aside from slight delays in generation and collection of SE's which are usually negligible. The amplitude of the SE signal pulses, however, is subject to the voltage contrast effect by the mechanism described in Section 2.1 and thus is sensitive to device bias voltage. A track and hold circuit in the IL-200 controller measures the peak amplitude of SE signal pulses; its sampling operation is synchronized to the same external signal which controls the beam blanking rate. The track and hold output signal, which appears as a monitor signal on the rear panel of the IL-200 controller, is thus sensitive to device bias voltage through the voltage contrast effect but is nominally insensitive to the beam blanking rate since it does not accumulate the effects of multiple SE signal pulses.

In summary, the device impressed current is selected using the VCO control voltage and relative changes in device bias are measured using the SE monitor signal.

2.4 IMPEDANCE MEASUREMENT PROCESS

Device impedance determinations were based on the results of two principal measurements. These are 1) calibration of the voltage contrast in the SE signal and 2) measurement of the variation of SE signal with a known variation in impressed current. Once again the term "SE signal" here means the signal at the IL-200 SE signal monitor, which is the output of the track and hold circuit described in Section 2.3 above, plus an adjustable offset. Calibration of the voltage contrast in the SE signal was carried out by modulating the potential of the entire sample under test (HgCdTe substrate and photodiode array) through the single substrate lead and sampling the SE signal. The modulation of the potential on the substrate lead was implemented by applying the desired voltage stimulus to the noninverting input of the current sensing operational amplifier; this voltage was then passed back to the substrate lead wire through the feedback action of the amplifier.

The voltage contrast calibration process was used to obtain a voltage contrast calibration factor defined as

$$g = \frac{1}{\text{SE signal}} \times \frac{\partial \text{SE signal}}{\partial \text{substrate voltage}} \tag{2-1}$$

In the ABT system this factor was found to range from 4% per volt to 12% per volt depending on adjustment of the analyzer grid voltage.

The second measurement (variation of SE signal with impressed current) was carried out by modulating the VCO control voltage (which in turn modulates the beam blanking rate and thus the impressed current) and measuring any associated variation in SE signal. The device dynamic resistance is then obtained from this measurement as follows:

$$R = \frac{1}{g \times \text{SE signal}} \times \frac{\partial(\text{SE signal})}{\partial(\text{impressed current})} \tag{2-2}$$

A test controller and controller software were developed to execute these measurements as well as other calibration, control and diagnostic functions. Extensive reliance was placed on automation of high speed test execution, signal sampling and signal recording because of the recurrence of transient effects requiring real-time recording or analysis of signals, and also because of the eventual need for a method capable of high throughput. An AT-compatible PC was selected for analog measurement, analog control, digital control and IEEE-488 communications with the remainder of the system.

Three analog measurement channels were used, assigned to sampling of 1) the SE signal, 2) the impressed current signal, and 3) a synchronization signal taken from the 60 Hz local power line. The first two of these channels appear in Figure 2-5. Two analog control (i.e., analog out) channels were used, assigned to control of 1) the VCO frequency (blanking rate) and 2) the substrate potential. These also appear in Figure 2-5. Four digital control lines were used to control operation of two integrating filters used for averaging of the SE and impressed current signals. An IEEE-488 communications channel shown in Figure 2-5 was used to communicate the following parameters and operating modes to the IL-200 controller:

1. Transition from raster scanned to stationary electron beam mode at specified x, y coordinates on the sample surface;
2. Initiation of blanked-beam mode (as opposed to continuous beam mode), with the blanking triggered by the extreme input;
3. Setting of the pulse width of beam blanking (time duration of primary beam pulses);
4. Setting of the gain and offset applied to the SE detector preamp signal.

The control program was written in Pascal. A schematic representation of the flow of data and control is shown in Figure 2-6. Approximately fifty procedures were developed for test execution, system initialization and calibration, file management, data manipulation and analysis and signal inspection; they were made accessible for execution in a user-interactive manner from a series of menus, as indicated in Figure 2-6. A file organization system for specification and documentation of test conditions and recording of test results was adopted. In this system, as shown in Figure 2-6, parameters for execution of a test run are specified through creation and editing of a run specification text file for each test run which is then stored on the controller hard disk. In this file, the specifying parameters are preceded by labels which make the file readable for editing by the user or interpretable by the controller for test execution.

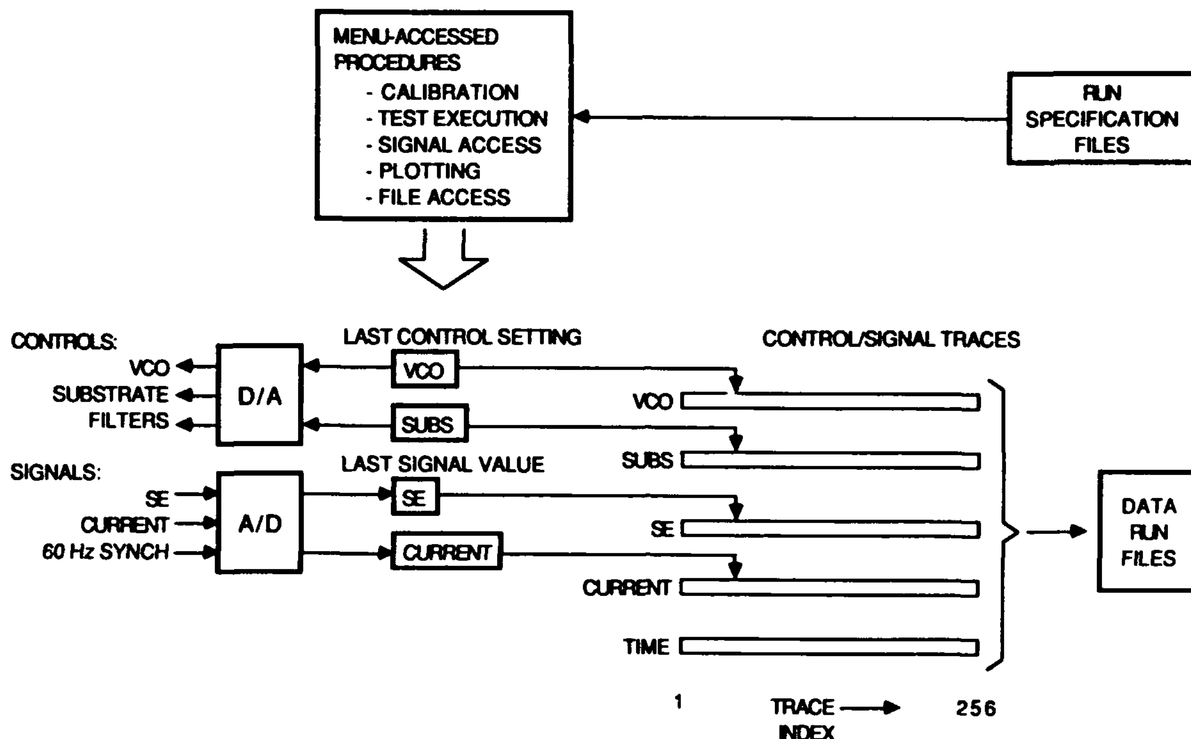

Figure 2-6. Schematic Diagram of the Flow of Data and Control Involved in Execution of the Test Controller Main Program

This system allows test specification to be reviewed for accuracy before it is used and automatically provides documentation of the conditions used for individual runs. Filenames for each of these run specification files as well as for free-format user notes and comments consist simply of the date on which the file was created, preceded by a two-letter prefix ranging from AA to ZZ which allows up to 676 files to be named on a given day. This naming system allows old runs or free-formatted user comments to be reviewed, searched or copied.

Under control of a chosen measurement procedure the various measured quantities and times of their measurement are recorded in a number of data arrays termed "traces", shown in Figure 2-6. These arrays of numbers are eventually saved to disk storage under a filename traceable to the run specification file. Various routines for checking on stability of signals, calibration of the voltage contrast effect and device impedance measurement were developed.

The most highly developed impedance measurement routine, used in tests toward the end of the program, executes the following sequence:

- Zero the VCO control voltage and substrate bias
- Let the electron beam pulse duration and the standby position of the electron beam.
- Position the beam at the location specified
- Modulate the substrate voltage and impressed current as implied by equations 1) and 2) for voltage contrast calibration and impedance measurement. The modulation of the two control voltages is done jointly in a common time interval to minimize the effects of drift but using modulation patterns which are orthogonal so that the effects can be separately determined in the next step.
- By a least-squares regression analysis determine the effects of substrate bias and impressed current on SE signal and determine the impedance.

The information resulting from this fitting process is a value of diode dynamic impedance at the average current value which occurred during the measurement. Since voltages are measured only in a relative sense by the electron beam technique, the basic form in which information is directly provided by the electron-beam technique is impedance at a specified device current rather than at a specified voltage.

2.5 COLD STAGE AND COLD RADIATION SHIELDING

Due to the cooling and background shielding requirements for accurate characterization of infrared photodiode performance, a liquid nitrogen cooled, shielded stage was set up in the IL-200 sample chamber. A cross-sectional view of this assembly is shown in Figure 2-7. It consists of a rectangular LN2 reservoir mounted above the floor of the sample chamber via a low thermal conductance support structure (bolts and main support platform made from nylon) and fitted with a sample holder whose temperature can be varied. The sample holder is built from a thin-walled stainless steel tube and a copper platform where samples are fastened down. Adjustment of the sample holder temperature is accomplished

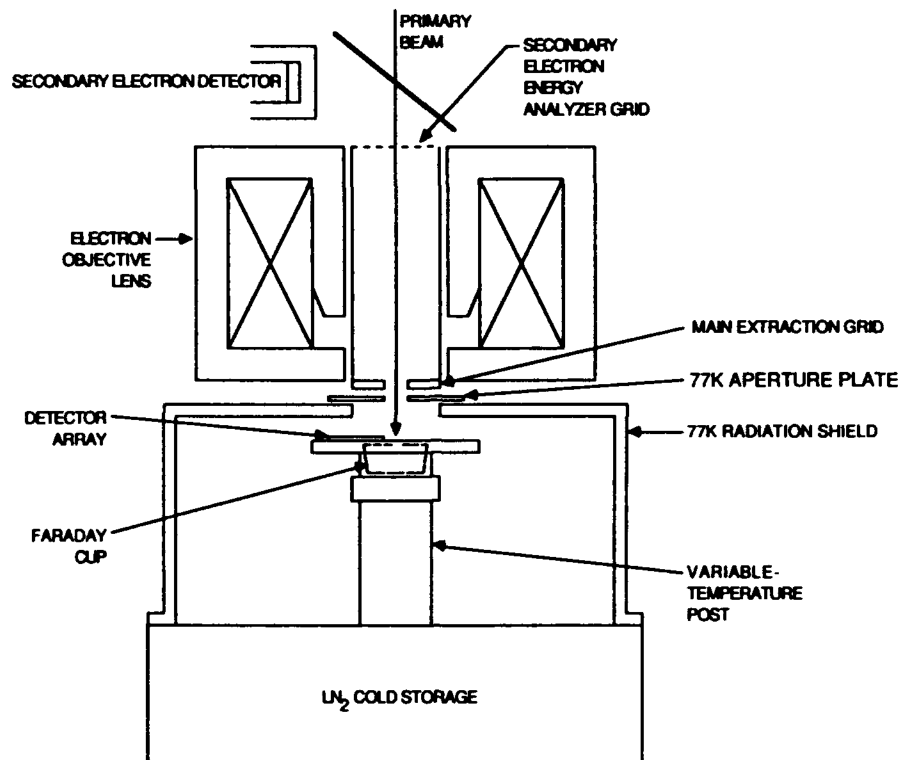

Figure 2-7. Configuration of Cold Stage and Cold Shielding

through an electrical resistance heater wound onto the thin-walled tube. Temperatures ranging from near liquid nitrogen temperature to approximately 180K were found to be accessible using this fixture.

Background radiation shielding of the sample mounting area is achieved by a cylindrical copper shield, approximately 4 inches in diameter, mounted directly onto the LN2 reservoir. The ceiling of this shield is continous except for a 1" diameter hole in the center. This hole is meant to allow installation of a final cold shield aperture piece which is electrically isolated from the rest of the sample chamber and which can be biased to improve SE extraction from the interior of the cold shield to the electron column. The 1" diameter hole without any added plate forms an aperture of approximately f/.2. An aperture plate with a 2.5 mm diameter opening was used in SE extraction efficiency tests (Section 3.4), forming an aperture of approximately f/2.

In order to allow alignment of the cold shield aperture with the center of the electron beam system field of view, the position of the entire cold stage assembly can be controlled and adjusted over a range of several millimeters by means of adjustment screws which locate the assembly relative to the left and back walls of the IL-200 sample chamber.

As indicated in Figure 2-7, a Faraday cup was incorporated into the cold stage for direct measurement or monitoring of primary electron beam current, especially after the occurrence of various instabilities in primary and impressed current were discovered.

2.6 VACUUM CONFIGURATION AND MEASUREMENT

Minimization of contaminant adsorption on probed metallization surfaces has been identified as an important factor in achievement of reproducible e-beam noncontact voltage measurements[1]. This is due to the tendency of high energy primary electrons to interact with any such contaminants and modify the secondary electron yield of the metallization being probed. Therefore effort was devoted to characterization and improvement of the vacuum conditions in the IL-200 system.

The configuration of electron column, pumping lines and vacuum gauge locations is shown in Figure 2-8. For vacuum purposes the system divides into the upper half of the electron column, pumped by an ion pump, and the sample chamber, pumped by a turbopump. The two regions are connected through two paths: 1) a weak link in the column (differential pumping aperture) and 2) a higher-conductance line outside the column which can be opened or valved off as desired. An ionization gauge can be connected to either region as shown in the figure. The sample chamber is turbopumped and thus water vapor is not expected to be pumped particularly efficiently. This is potentially important for IR detector probing because of the low sample temperatures and the possibility of water vapor adsorption on device metallizations as they are exposed to the beam. To assist in more rapid pumping of water vapor, a liquid-nitrogen temperature cold trap was installed in the sample chamber.Initial leakchecking of the system identified poor vacuum seals at two electrical feedthroughs at the top of the electron column (leading to the beam blanking plates). The vacuum seals at these feedthroughs were refurbished. Other seals where minor leaks were found (such as the main door to the sample chamber) were upgraded by

1. E-Beam Testing of PV HgCdTe Photodiode Arrays, Contract DAAB-7-89-C-F035, Hughes Santa Barbara Research Center, June 1988.

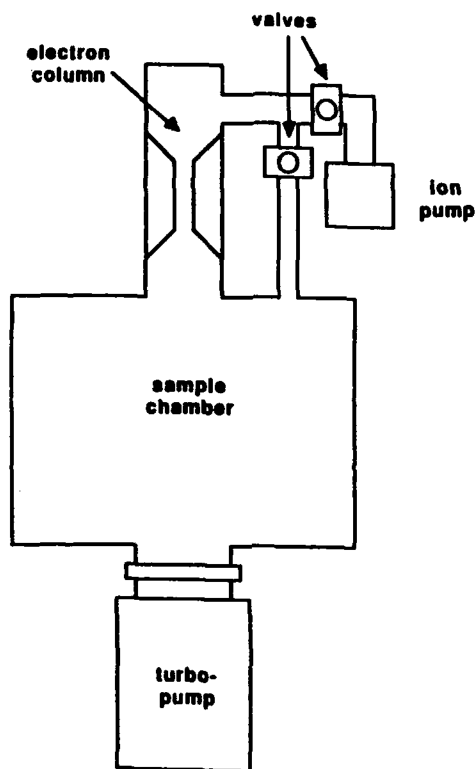

Figure 2-8. Vacuum Configuration of IL-200 Electron Column and Sample Chamber

installation of O-rings and gaskets of the lowest vapor pressure available. After these improvements the sample chamber was found to pump down to pressures in the mid-10^{-6} torr range in an overnight pump-down. The pressure at the gauge position between the electron column and the ion pump, was found to reach values in the high 10^{-7} range. Later in the program, as noted below, the differential pumping aperture in the electron column was removed to allow the higher-speed ion pump to pump the electron column more effectively.

SECTION 3
RESULTS AND DISCUSSION

In this section specific results from the development of the electron-beam contactless impedance measurement are presented and discussed. These are given in an order starting from characteristics of the basic aspects of the method and leading to the results of device impedance measurements. This does not correspond exactly to the order in which these results were obtained in the program since some basic aspects of the method were not necessarily identified early in the work.

3.1 CONTROL OF PRIMARY BEAM CURRENT

For measurement of low-impedance long wavelength detectors, impressed currents up to or somewhat in excess of 100 nA may be needed to establish bias voltage changes which can be resolved. Such magnitudes of impressed current were not initially achievable in the electron-beam system and modifications were made to the system and the operating procedure to maximize the primary current capacity. These included widening or removal of some apertures in the electron column and development of a current-based procedure for alignment of the electron gun.

The magnitude of impressed current available soon after system operation was established is shown in Figure 3-1. This data indicates that even at fairly high primary beam duty factors (up to 40% in this case) impressed currents were limited to about 0.5 nA or less. This current capacity was first increased through improvement of the electron beam alignment technique.

The process of electron gun alignment involves adjustment of two sets of x-y beam deflection coils (4 coils in all) so that the primary beam emerging from the electron gun can be guided into alignment with the rest of the electron optical column. In general two sets of x-y deflection are needed because the primary beam may be misaligned in either its location or its direction relative to the electron column. The first deflection thus "jogs" the beam over to cross the column axis just as it reaches the second deflection point, and the second deflection steers the beam direction to follow the column axis the rest of the way down.

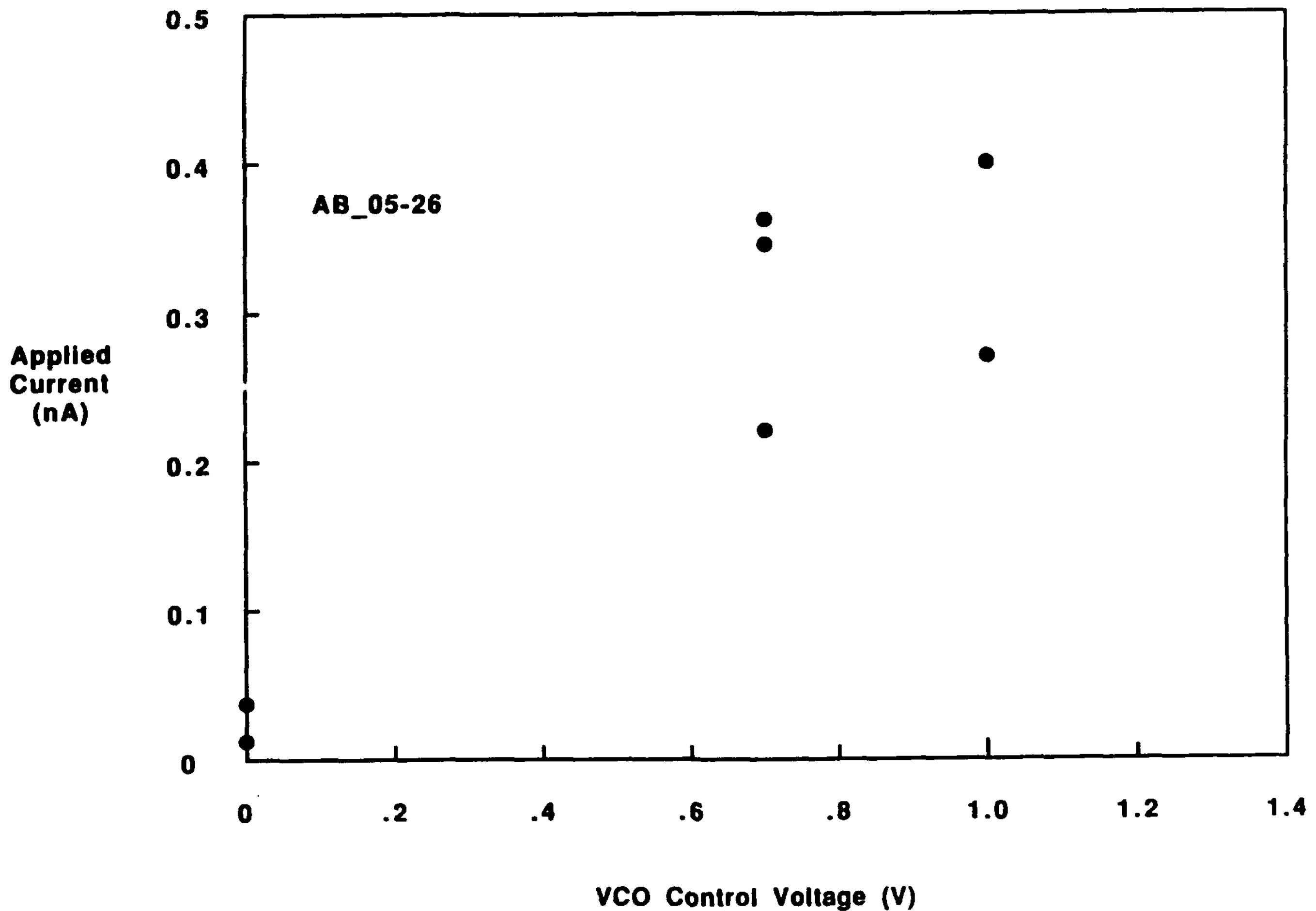

Figure 3-1. Impressed Current Capacity of the Electron Beam System in Initial Mode of Operation

An alignment facility commonly provided in SEMs relies on display of an image, referred to as the "filament image", which is based on the SE signal and generated by raster scanning of one set of the gun alignment coils. Typically the filament image appears as a bright circular spot, sometimes distorted, located somewhere in the display, at a position which roughly corresponds to the best deflection setting of whichever coils are scanned to generate the image. Gun alignment is then a rather subjective process consisting of adjustment of the four alignment controls until the filament image is judged to have the most circular shape possible and to be located in the center of the display.

The modified alignment procedure is based on direct observation of the primary beam current using the Faraday cup installed on the stage connected to the current-sensitive preamp, and consists of adjustment of the four individual beam alignment controls, as well as a fifth parameter, the bias on the electron gun Wehnelt grid, one at a time, in search of the conditions for an overall maximum in the beam

current arriving at the Faraday cup. This procedure led to new settings of these controls which would not have been found by the filament image method, and which provided a primary beam current of 46 nA. This corresponds to an impressed device current capacity of 3 nA (assuming a primary beam duty factor of 40% and an SE yield of 1.2).

Although this represents an improvement by a factor of six over the previously achieved values, it is still significantly below the current requirements stated above. Shortly after the adoption of the modified alignment technique, the beam current was increased further by widening the first aperture following the beam blanking plates, from 100 to 600 microns and by removing a differential pumping aperture further down in the column. These apertures had been installed in the system previously for reasons applicable to conventional voltage probing work but not to impedance measurements on IR photodiodes. The level of impressed current available after these changes is indicated by the data of Figure 3-2. These data

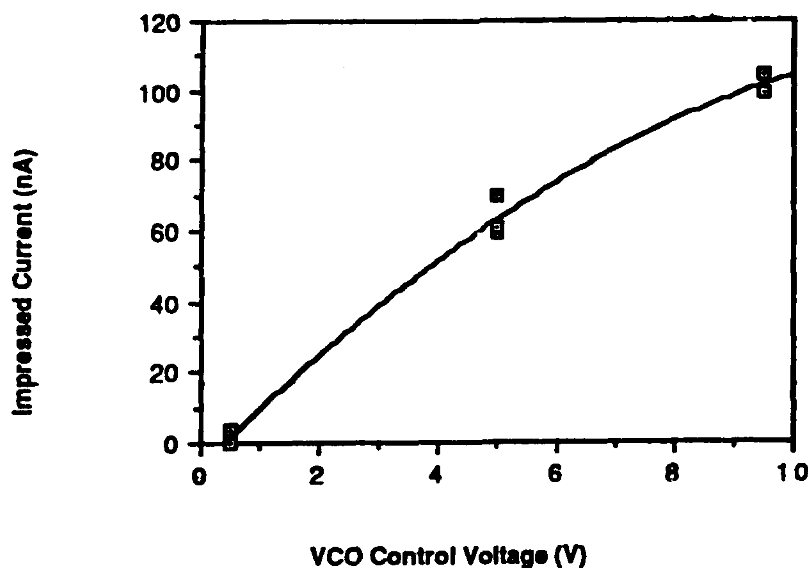

Figure 3-2. Impressed Current Capacity of the E-Beam System Following Improvements in Beam Alignment Procedure and Replacement of E-Beam Column Apertures. The maximum duty factor used was 22%, secondary electron yield 1.2 $\leq \gamma \leq$ 1.3, primary current at sample 600-700 nA. The blanking rate was 130 kHz/Vco Volt.

indicate that impressed currents over 100 nA are accessible using primary beam duty factors below 25%.

Instability in Primary Current Modulation per Unit Duty Factor

The time duration available for impedance measurement per detector element is limited to times near or below one second, either because of instabilities in SE yield discussed below in Section 3.2 or more generally due to the requirement of a rapid overall device screening rate. As stated above, this was the reason for the development of high-speed automated control and recording of test execution. As the test procedure became sufficiently automated that electron beam positioning and primary beam duty factor changes could be executed on short time scales, an unexpected instability in the primary current (not the SE yield) became apparent.

The instability appears as a drift in primary beam current following a sudden change in primary beam duty factor. An example of this behavior is shown in Figure 3-3. In this test the beam was first operated at a very low duty factor and positioned on the Faraday cup of the cold stage. After a few readings of average beam current were taken over a few tenths of a second, the beam duty factor was suddenly increased from near 0% to 18% and additional readings of average beam current collected. The average beam current jumped to a larger (that is more negative) value as expected, but then drifted to even larger values for several tenths of a second before stabilizing. The most likely origin of this drift is the presence of insulating contamination on surfaces in the electron column which gain or lose surface charge in response to changes in primary beam duty factor. The details of this explanation are as follows.

When the electron beam is blanked it is deflected by the blanking plates so that it strikes an aperture further down the electron column. Any insulating contamination on that aperture becomes charged by the beam, to a degree proportional to the fraction of time that the beam is off at the device under test (i.e., deflected). This charge buildup then distorts the path of the primary beam. If a low beam duty factor is used during both the initial beam alignment process and all subsequent measurement runs, this distortion is constant and is corrected during beam alignment and remains hidden.

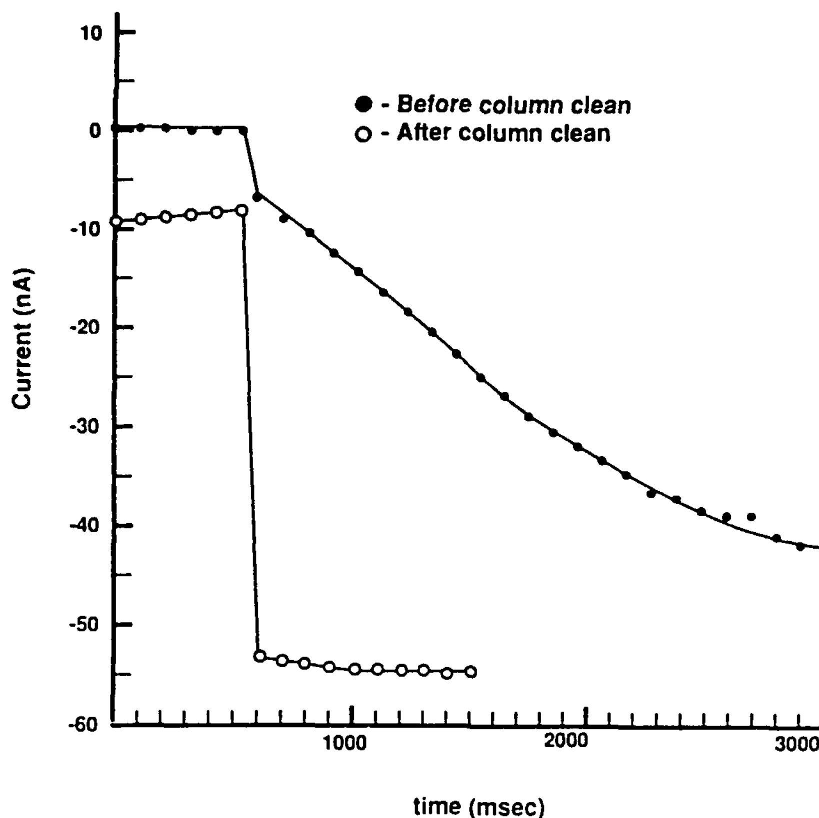

Figure 3-3. Instability in Response of Primary Current to Modulation of Beam Duty Factor and its Relation to Column Cleanliness

However, if a high beam duty factor is used (e.g., to supply current to a low-impedance device), the beam-off time fraction deviates significantly from 1, thus changing the charging conditions at apertures in the column, altering the beam alignment and reducing the primary beam current at the device under test.

The role of insulating surface contaminants in this effect is clearly based on two observations of primary current response before and immediately after cleaning of the column. The column cleaning process includes removing the SS60 column liner (a metal tube approximately 3 mm in inside diameter which surrounds the electron beam and also holds the column apertures), cleaning the inside surface of the liner with a diamond polishing compound and installing new molybdenum apertures in the liner. The results of the second primary current response test, also shown in Figure 3-3, indicate that the drift rate for the first few tenths of a second after the duty factor change is reduced to about 7% per second when the column has been cleaned. By comparison, the drift rate prior to column cleaning is on the order of 100% per second or higher depending on the current value chosen to reference the drift to. The pre-

The response of the beam current within a few ms of a duty factor change was also investigated but could not be recorded using the 60-Hz synchronized controller software. Relative drift rates ranging from 1300% per second to 100% per second just prior to and just after column cleaning, respectively, were observed.

3.2 CONTROL OF IMPRESSED CURRENT

The impressed current (the actual device current occurring in the measurement) is the sum of the primary current carried by the incoming electron beam and the opposing current carried by emitted secondary electrons. For the blanked-beam mode of operation used in this program the complete expression for the impressed current is

$$\text{impressed current} = (\text{blanking duty factor}) * (\text{dc primary current}) * (\gamma - 1) \quad (3\text{-}1)$$

where γ is the secondary electron yield. The degree of control over impressed current is obviously affected by all the factors, intentional or not, which govern the primary current and the secondary electron yield (γ).

The degree of control over impressed current varied widely at different times in the program. Instability in SE yield has been blamed as a likely source of this variability, since it is known to depend on sample composition, surface texture and surface condition. However, the additional occurrence of primary current instability reported in Section 3.1 above has not been mentioned in earlier reports and was not clearly isolated and corrected until relatively late in the program, so that the variability of SE yield alone cannot be isolated from much of the early data.

However some measurements of SE emission stability were obtained under stable primary current conditions near the end of the program. Figure 3-4 shows the degree of responsiveness and stability in the impressed current obtained after a sudden increase in primary beam duty factor, for the beam directed at three different locations on the cold stage: into the Faraday cup, onto a gold-plated lead of the de-

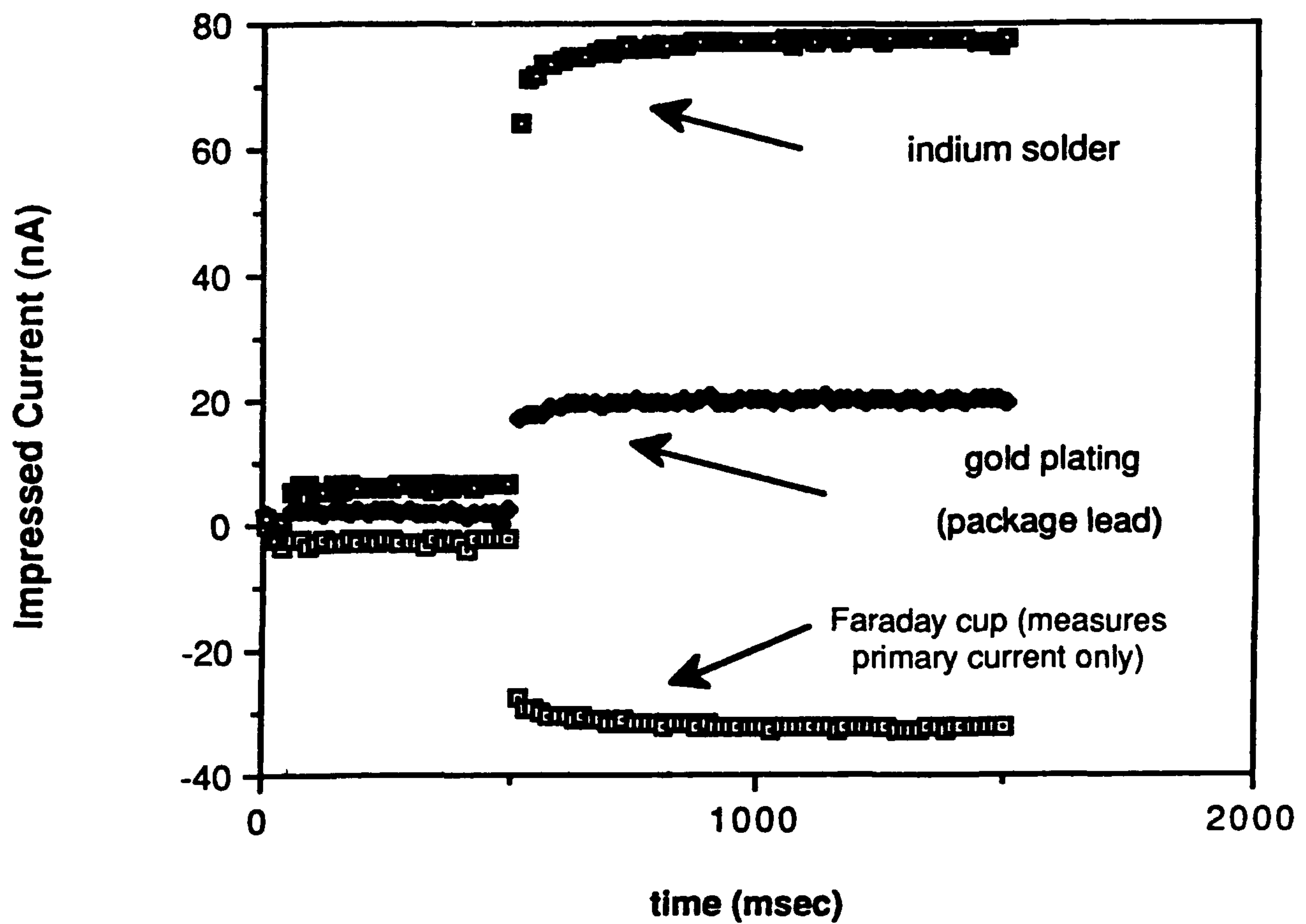

Figure 3-4. Stability of Impressed Current at Gold and Indium Surfaces, Under Clean Column Conditions

tector flatpack, and onto a portion of this lead which was coated with indium solder. These measurements were all taken within a time period of 30 minutes, when the system had undergone approximately 20 hours of operation following column cleaning. The primary current measured at the Faraday cup responds to within 85% of its ultimate value in the first 17 ms, followed by a drift rate of approximately 250% per second in the second 17 ms interval. These characteristics as well as those observed on the other two surfaces are summarized in Table 3-1.

Responsiveness And Drift Rate Of Primary Current And Impressed Currents Following A Fast Risetime Step In The Beam Blanking Duty Factor.

location	current after 1 second settling	percentage of final current after 17 ms	drift rate in 2nd 17 ms interval
Faraday cup	-33 nA	85%	250% /s
gold-plated package lead	20 nA	85%	150% /s
indium-soldered package lead	77 nA	83%	400% /s

The percentage of response in the first 17 ms after duty cycle change is comparable for the other two surfaces tried, although the impressed current using the indium surface settled more quickly, giving a higher rate of drift in the second 17 ms interval. The impact of drift at these rates on impedance measurement accuracy will be discussed in Section 4.

3.3 MWIR IV MEASUREMENTS

Approximately midway through the Phase I effort the feasibility of electron-beam based impedance measurements was tested on a MWIR detector array. A detector array bump-bonded to a 68-lead flat-pack was used. It was mounted on the platform of the variable-temperature post. Shielded electrical

leads from the array substrate and from the cathode of one selected detector element were connected from the appropriate package leads to the outside of the SEM sample chamber. These two leads allowed curve tracer measurement of the detector impedance for direct comparison with e-beam measurements. The electron column had been cleaned approximately 20 hours previous to this run, although the relationship between column cleanliness and control of primary current was not recognized at the time of these measurements. The system was operated at a primary energy of 1.5 keV and a beam pulse width of 200 ms. Beam blanking rates ranging from 13 to 260 kHz were used for this measurement. The main cold shield was installed with no added aperture plate so that the aperture diameter was 25 mm. The temperature was varied over the range 130 to 160 K.

In the version of the measurement software used here, modulation of impressed current and substrate voltage as described in section 2.4 were done in two separate time intervals each 700 ms long separated by a pause of 100 ms. Figure 3-5 shows the modulation of impressed current with VCO control voltage which occurred during the actual time period of the measurement. The primary beam duty factor corresponding to this range of VCO control voltage is 0 to 5%. The current response characteristics are stable to within 6% during test execution. Figure 3-6 shows the variation in SE signal produced by application of bias voltages, ranging from 0 to 2 volts, to the entire detector array through the substrate connection. This part of the run calibrates the voltage contrast effect.

The results of the electron beam measurements at 130 and 160 K are shown in Figure 3-7 as well as the results of in situ electrical measurements using a diode curve tracer. Because of the information on the device current at zero bias provided by the curve tracer, absolute current and voltage values could be obtained from the electron-beam measurement and located on an I-V plot and the shapes of the electron-beam and curve tracer I-V curves compared.

The detector short-circuit current due to background radiation was measured to be approximately 400 pA. This value is considerably lower than that expected (by about a factor of 35) for the large size of the aperture used (approximately f/.2). The most likely reason for the low background is that the underside of the extraction grid is gold-plated and mirrors the low-background conditions of the cold shield interior. The arrangement of extraction grid and cold shield opening which allows this to happen (when no added aperture plate is used) can be seen in Figure 2-7.

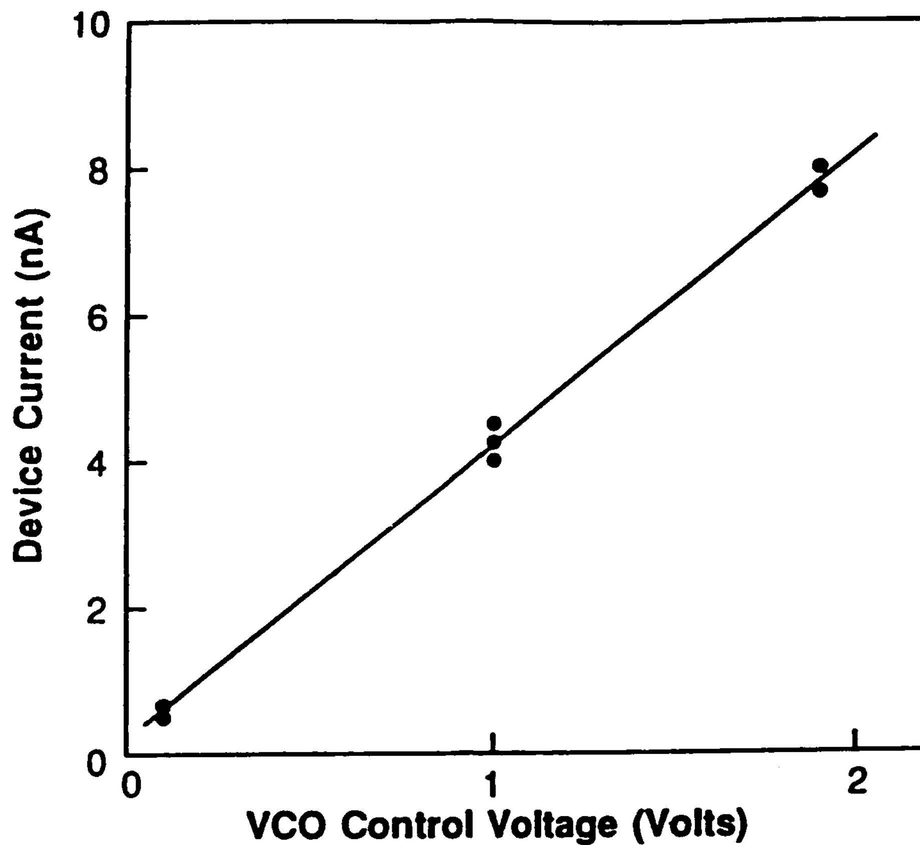

Figure 3-5. Dependence of Impressed Current on VCO Control Voltage as Achieved in MWIR Photodiode Impedance Measurement

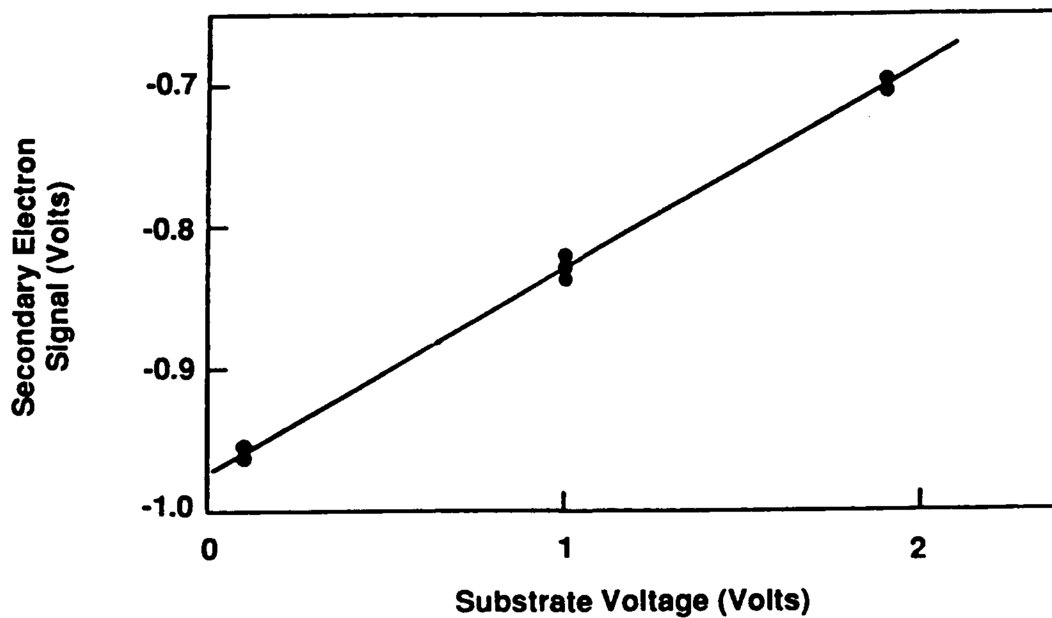

Figure 3-6. Dependence of SE Signal on Substrate Voltage as Observed During Calibration Phase of MWIR Photodiode Impedance Measurement. The baseline of the SE signal is at +1.3 volts. The voltage contrast calibration factor g for the above data was $g = [\partial V_{SE}/\partial V_{SUB}]/V_{SE} = [0.2/(1.9 - 0.5)]/(1.3 + 0.8) = 6.8\%$

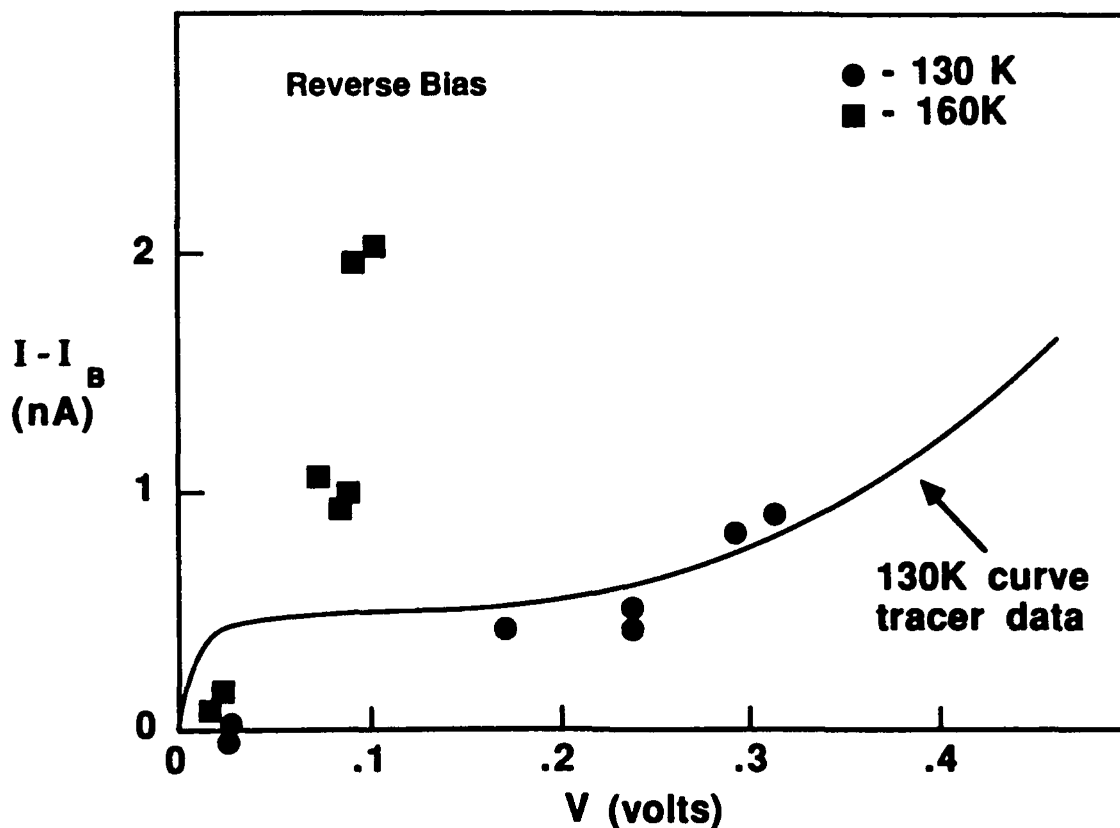

Figure 3-7. Comparison of Electron-Beam Measurements of MWIR Photodiode I-V Characteristics with an In Situ Hard-Wired Measurement

Under these conditions, then, the first 400 pA of positive impressed current (which is in the reverse bias direction) cancels the background photocurrent and puts the device at zero bias. The electron beam values of current and voltage shown in Figure 3-7 are plotted relative to the zero bias condition. Specifically, 400 pA is subtracted from the impressed current values and the voltage values are plotted relative to the e-beam voltage reading at 400 pA impressed current. The curve tracer results are also shown in Figure 3-7; the background photocurrent has also been subtracted from this data. The 130 K electron-beam data are in approximate agreement with the curve tracer results. The selected values of impressed current extend into the reverse saturation region of the diode characteristics, resulting in reverse bias voltages out to 0.15 V. Based on the curve tracer data, the detector zero-bias resistance in this case is 23 MΩ, and the dynamic resistance in the region probed by the electron-beam measurement is approximately 400 MΩ.

A second run was carried out at a temperature of 160 K At this temperature the photodiode zero-bias resistance seen by the curve tracer fell to 0.6 MΩ. The SE signal measurements also indicated very

much lower photodiode bias changes with impressed current than were seen in the 130 K data. These signal measurements are also shown on Figure 3-7, although an interpretation of these points as photodiode I-V values is not valid because at this impedance the diode RC time constant is estimated to be about 2 μs. This RC time constant is shorter than the repetition time of the beam blanking cycle. As described in Appendix A, under these conditions the output of the track and hold circuit becomes independent of the beam blanking duty factor, disabling the impedance measurement.

3.4 EFFECTS OF COLD SHIELDING ON SECONDARY ELECTRON COLLECTION AND ENERGY ANALYSIS

Allowable background radiation levels are much lower for LWIR photodiodes than for MWIR photodiodes. This forces the diameter of the 77 K electron beam electron beam aperture (shown in Figure 2-7) to be much less then were used in the MWIR device measurements discussed above. Measurements were made to estimate the effect of a small-diameter aperture on the achievable voltage contrast in the system.

A series of runs were carried out in which a packaged detector was mounted on the cold stage and the usual hardwired connection made to the array substrate through the appropriate package lead. The cold shield aperture plate with a 2.5 mm diameter opening was installed. In the runs, the cold shield aperture was held at +150 V while the electron beam was directed to a package lead and operated at constant duty factor (constant primary current) while a 0 to 1 V modulation was applied to the entire array through the substrate lead. The resulting modulation of the SE signal was then recorded at various settings of the SE analyzer retarding grid over the range 0 to 10 V. This process actually traces out the SE energy spectrum. The results are shown in Figure 3-8.

The relative voltage contrast in the SE signal (percent SE signal change per volt change in sample potential) reaches a maximum of 12% per volt at 3 V retarding grid potential. This value of relative contrast is in good agreement with values seen without aperturing, and indicates that the energy spectrum of SE's extracted through an aperture of this size is not distorted significantly from that first emitted from the sample surface. However analysis of the photomultiplier gain setting required to collect this data indicates that the aperture does have an effect on the overall efficiency of SE extraction into the analyzer.

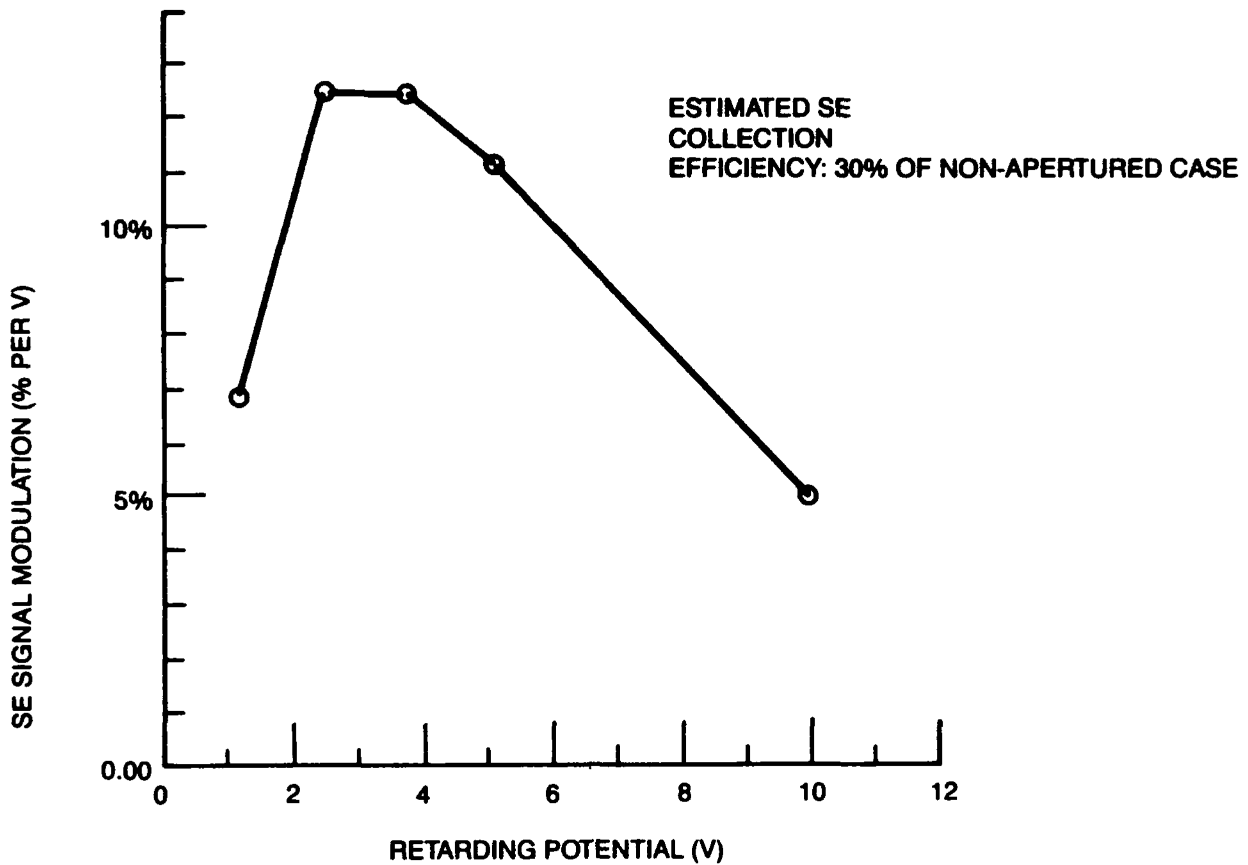

Figure 3-8. SE Energy Spectrum Observed While Extracting SE's Through a 2.5 mm Cold Shield Aperture

From the SE signal levels obtained in these measurements it appears that the extraction efficiency through the 2.5 mm diameter cold shield aperture is about 30%.

LWIR photodiodes will require a background radiation level of 5×10^{14} $cm^{-2}s^{-1}$ or less in order to keep the open circuit photovoltage below a few mV. (For example, a photodiode with R_0 = 1 M and area 2.5×10^{-5} cm^2 would develop an open circuit voltage of approximately 2 mV.) The apertures required to achieve this are small enough in diameter that the effects of the low-emissivity room temperature extraction grid mentioned in Section 3.3 will not come into play (the gold-plated portion would be out of the line of sight of the device under test). Thus standard formulas for background vs. aperture size are appropriate in this context. Based on the relationship

$$Q_b = \frac{Q_b(180°,\mathrm{LWIR})}{4 \times f^2} = 5 \times 10^{14}\ \mathrm{cm}^{-2}\ \mathrm{s}^{-1}$$

where f is the f-number, an f/20 aperture must be used.

To provide this at the present sample-to-aperture distance of 5 mm, the aperture diameter would have to be reduced to 0.25 mm. The collection efficiency through small-diameter apertures is expected to scale with the aperture area, in spite of the magnetic confinement effects mentioned in Section 2.2 (the diameter of the spiral path of a 5 eV electron is estimated to be several mm). The collection efficiency for a 0.25 mm aperture can be estimated from the results of the 2.5 mm data as follows:

$$\text{Collection efficiency of 0.35 mm aperture} = 30\% \times \frac{(0.25\ \text{mm})^2}{(2.5\ \text{mm})^2} = 0.3\%$$

Such a small aperture would also severely restrict the distance over which the electron beam could be scanned, limiting the field of view to about 250 μm x 250 μm. The implications of this result are discussed further in Section 4.

3.5 ASSESSMENT OF NOISE AND SYSTEMATIC ERROR

Limits on the accuracy of electron-beam based impedance measurements can be grouped into two categories: resolution (determined by signal-to-noise ratio and by the number of bits of analog to digital conversion) and systematic error. Tests were carried out to provide some information in both of these areas and allow estimates to be made of the accuracy achievable in impedance measurements within the constraints of the present system.

Resolution

The level of resolution adopted as a criterion for feasibility of the electron beam method was a "minimally resolved" impedance measurement, defined as 1) voltage measurements with 3 mV rms variance obtained at device voltage values of +10 mV and -10 mV above and below zero bias and 2) measurements of impressed current well enough resolved so as not to degrade the resolution of the impedance measurement further than the level imposed by the voltage resolution. Fluctuations in the primary current produce noise directly in the impressed current and also in the SE signal used for voltage measurements. The nature of noise in the primary current was therefore analyzed as well as the noise level in the SE signal at the monitor output from the IL-200.

Of the two requirements listed above, the requirement on voltage measurement resolution places the tightest restriction on allowable fluctuations in primary current. This is discussed further in section 4. The noise of the primary current was measured by directing the electron beam to the Faraday cup on the microscope stage. The current output of the Faraday cup was connected directly to the input of a spectrum analyzer of known input impedance (1 MΩ) and the voltage noise spectrum measured. This spectrum is shown in Figure 3-9. The measurements indicate that the excess noise in the primary beam current is dominated by residual interference at 60 Hz and harmonics (i.e., ripple) which totals about 0.1% of the beam current. By comparison the rms magnitude of primary beam shot noise is about 0.01% for a measurement bandwidth of 100 Hz.

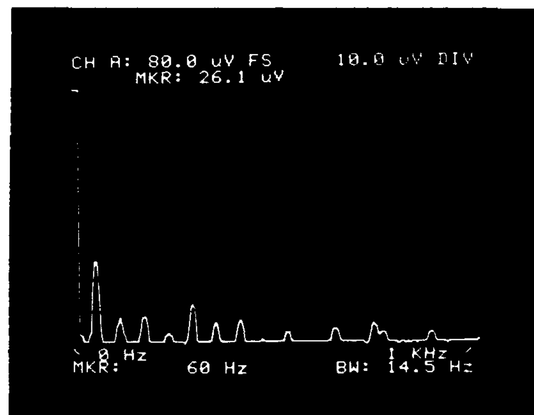

NOISE SPECTRUM OF PRIMARY CURRENT

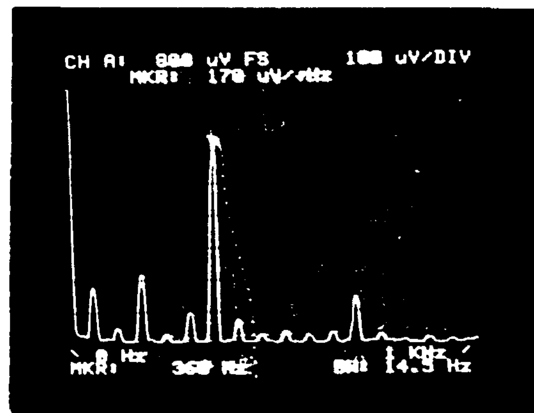

NOISE SPECTRUM OF SE SIGNAL

Figure 3-9. Noise Spectra Primary Current and SE Signal

The secondary electron signal for spectrum analysis was obtained as a voltage signal from the monitor output on the back panel of the IL-200 controller. Its noise spectrum is also shown in Figure 3-9. The analysis of the SE signal from the monitor output also shows excess noise at multiples of 60 Hz. The amplitude of this noise corresponds to about 1 part in 1000, similar to the level measured in the primary current. Thus the signal/noise ratio of the SE signal is not degraded below the "signal"/noise ratio of the beam current.

These levels of interference are somewhat higher than those desired for achievement of the minimally resolved impedance measurement described above. Fortunately the interference appears to be periodic at 60 Hz so that it can be rejected by synchronizing all sampling of current and SE signals with the phase of the local 60 Hz line voltage as mentioned in Section 2.4. Rejection of the 60 Hz interference by only one order of magnitude is adequate to bring it to a level comparable with the shot noise limit.

Systematic error

After the various instabilities in primary current and SE yield were identified and dealt with, systematic errors in the impedance measurement process were investigated in baseline measurements with the electron beam directed to a grounded metal surface, which is equivalent to a device of zero impedance. Either a gold-plated package lead or an exposed molybdenum surface of the Faraday cup was used as the grounded surface. Impedance measurements on such surfaces directly indicate the actual level of random noise and systematic error occurring in the impedance measurement. The completely developed impedance measurement program described in Section 2.4 was used. Results from one run are shown in Figure 3-10. The beam was operated in a blanked mode with pulse width of 20 ns and blanking rate varied from 1 to 4 MHz. The data points represent about 0.5 second of signal collection following automatic beam positioning and SE signal gain and offset adjustment. A reproducible variation of SE signal with impressed current shows up in these runs in spite of the known zero impedance, indicating a systematic error equivalent to -130 MΩ of impedance (i.e., an apparent negative voltage change for a positive impressed current).

This systematic error may well have been present in the MWIR photodiode IV data of section 3.3 but was not obvious there since the measurement operated in a region of the I-V characteristics where the diode dynamic impedance was several hundred MΩ.

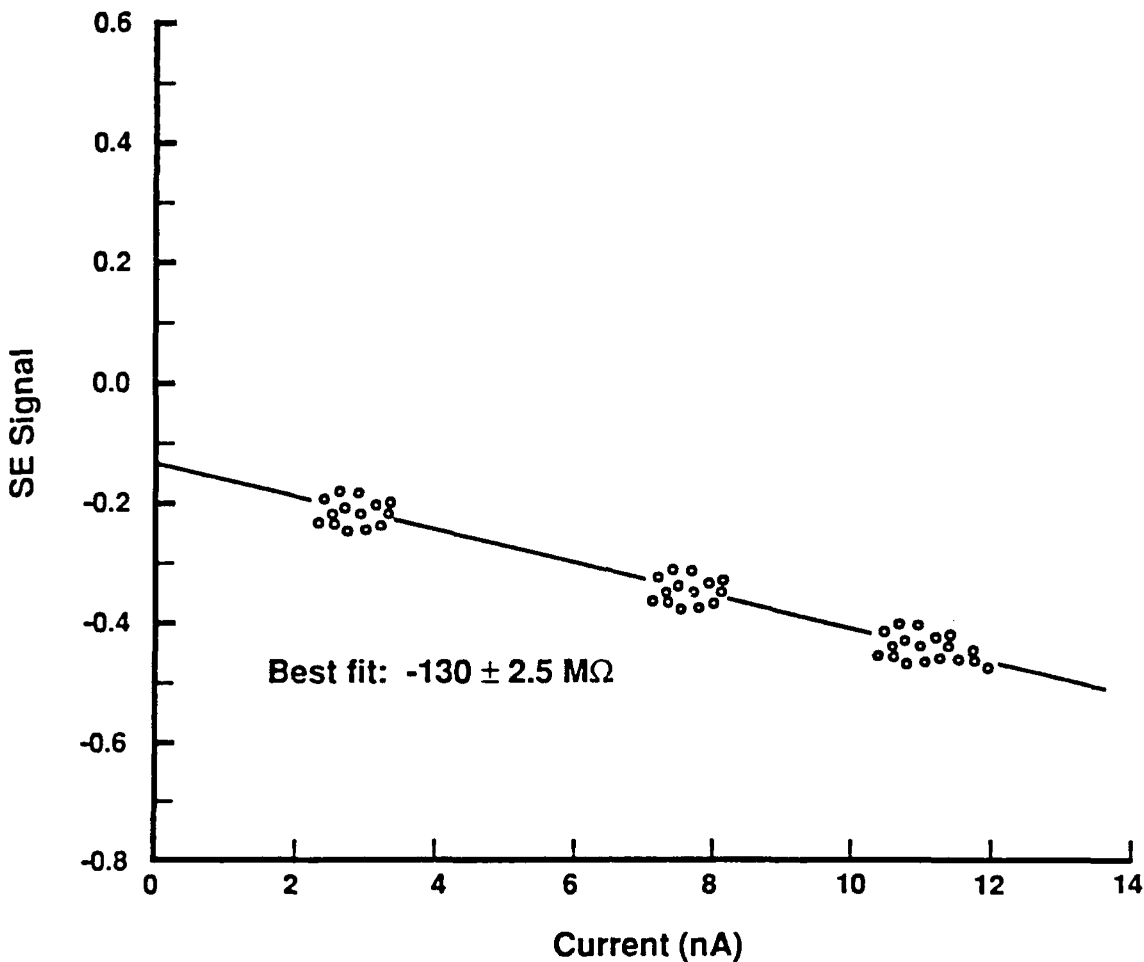

Figure 3-10. Assessment of Systematic Error of Electron Beam Impedance Measurement Based on Data Collected on a Grounded Surface

The false modulation of SE signal with impressed current was traced back as far as the output of the SE detector preamplifier. The behavior of the SE signal at that point is shown in Figure 3-11. When the system is operating in the blanked mode, the SE signal consists of a series of negative-going pulses, one for each primary electron beam pulse. The oscilloscope traces in Figure 3-11 show this pulse train at low and high repetition rates (pulses show up as single dots for the time base used in Figure 3-11). The effect which contributes to the systematic error in SE signal measurement is a negative shift in the SE preamplifier output (baseline and peak level) as the blanking rate is increased. The SE monitor signal used in the impedance measurements samples the peak level of the pulses and is thus susceptible to this shift. Expressed as a percent... ...ge in SE signal per unit duty factor, the magnitude of the shift in Figure 3-11 is 900%/unit duty factor.

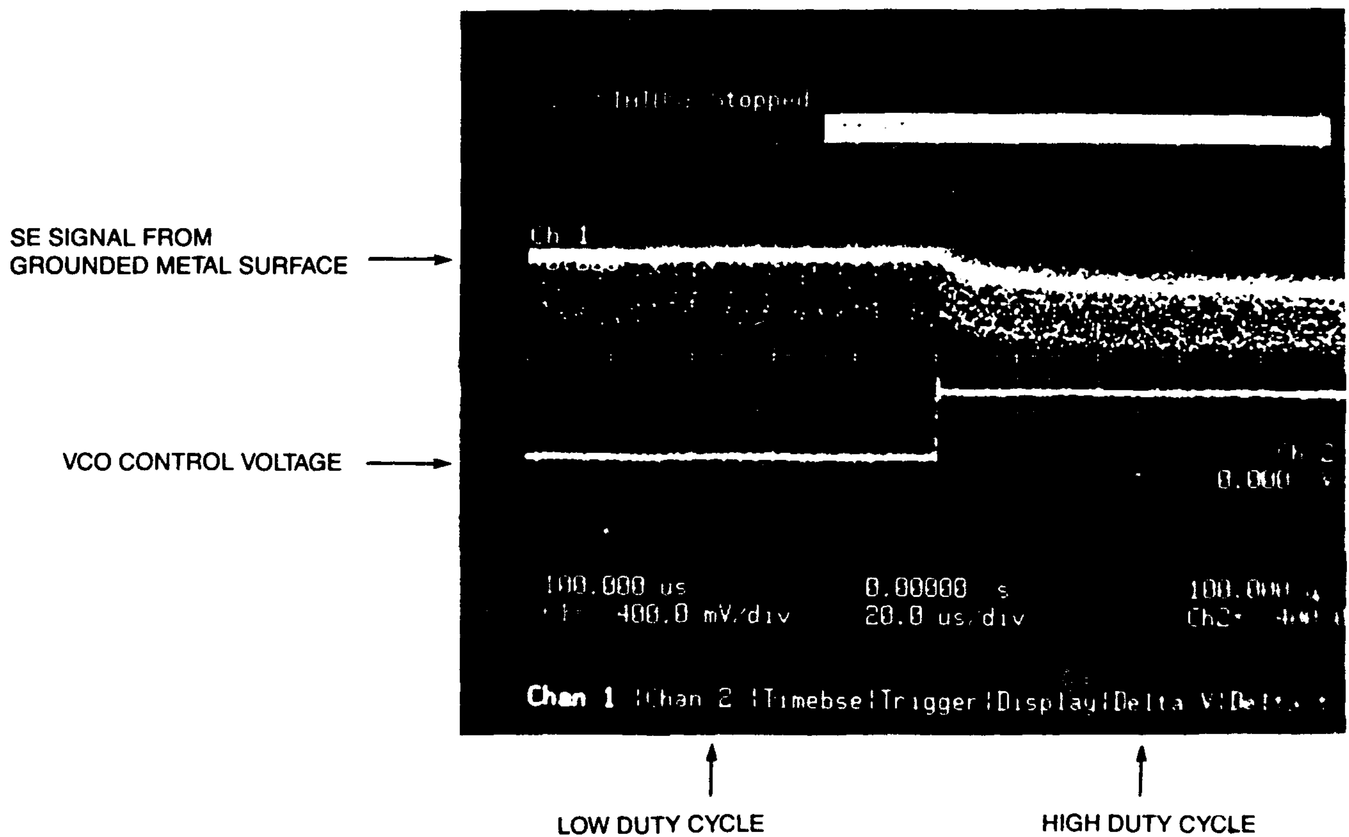

Figure 3-11. False Modulation of SE Signal Level with Beam Duty Factor

Further tracing of this false modulation effect would require disassembly of factory-sealed or relatively inaccessible parts of the photomultiplier and preamplifier. At the point in the program where the effect was identified and partially isolated, such an effort would have exceeded the resource and schedule constraints of the program.

SECTION 4
CONCLUSIONS AND RECOMMENDATIONS

This investigation has demonstrated the possibility of contactless impedance measurements at levels down to a few hundred Megohms using the electron beam method. Due to the unexpected appearance of drift in the primary current (section 3.1) and false modulation in the SE signal (section 3.5) a demonstration of impedance measurements at typical LWIR device values (1 Megohm or less) was not achieved within the scope of the program. In this section, the major sources of measurement error are summarized, as well as the specific requirements of additional development needed to achieve accurate measurement of sub-Megohm impedances.

The error sources in impedance measurement at zero bias can be grouped into 1) errors in voltage measurement and 2) error in locating the zero bias point (which cannot be done directly since contactless electron-beam-based measurements sample voltage changes and not absolute voltage values).

The specific error sources related to voltage measurement which have been identified in this investigation are

a) Shot noise in the SE current and in the impressed current (section 3.5),

b) Drift in the primary and secondary currents following a duty factor change (sections 3.1, 3.2),

c) Systematic error due to false modulation of the SE signal baseline (section 3.5), and

d) Systematic error due to incomplete settling of the device bias if the impressed current is modulated at a high frequency.

The impact of each of these sources on the accuracy of impedance measurement is given one by one below and summarized in Table 4-1.

a) **Shot Noise** --

For an impedance measurement based on modulation of device bias between two points on the device I-V curve, (denoted as I_1, V_1 and I_2, V_2), the measured impedance value is given by

$$R = \frac{(V_1 - V_2)}{(I_1 - I_2)} \qquad (4\text{-}1)$$

Table 4-1. Estimates of minimum achievable error contributions in measurements of MWIR and LWIR device impedances using the experimental e-beam system under typical 60 Hz-synchronized operating conditions. Values of other parameters are: signal collection time 300 ms total per impedance measurement; cold shield/analyzer transmission 30% for MWIR,.5% for LWIR; primary current relative drift rate 10 s^{-1}, SE yield 1.3; device capacitance = 2 pF; and SE voltage contrast calibration factor g = 12% / volt.

	MWIR 60 Hz	LWIR 60 Hz
R_o	25 MΩ	1 MΩ
I_1	15 pA	400 pA
I_2	800 pA	7 nA
V_1	-6.9 mV	0 mV
V_2	27.8 mV	30.7 mV
$t_{samp,1}$	17 ms	17 ms
$t_{samp,2}$	17 ms	17 ms
Error in R due to false modulation-of SE signal	-530 MΩ	-530 MΩ
Error in R due to drift in primary current/SE yield	1800 MΩ (depending on microscope column surface condition)	210 MΩ
RMS variance in R due to SE shot noise	3.5 MΩ	640 MΩ
Error in R due to background-induced bias shift	10.6 MΩ (46%)	250 MΩ (25%)
Error in R due to incomplete settling	150 kΩ (0.6%)	0.24 kΩ (0.024%)
RMS variance in R due to impressed current shot noise	940 Ω (0.004%)	1.3 Ω (0.001%)

The mean squared variation in measured impedance can be related to noise in the measured voltages or currents by differentiation of Eq. (4-1):

$$\langle \Delta R^2 \rangle = \frac{\langle \Delta V_1^2 \rangle + \langle \Delta V_2^2 \rangle}{(I_1 - I_2)^2} + R^2 \times \frac{\langle \Delta_1^2 \rangle + \langle \Delta I_2^2 \rangle}{(I_1 - I_2)^2} \tag{4.2}$$

Here the brackets mean averages and Δ means the deviation of a signal from its average value. The first term comes from random fluctuations in voltage readings; the two voltage deviations are squared before adding because they are not correlated with each another. The second term comes from fluctuations in the impressed current measured through the substrate connection.

The fundamental lower limit of noise in the measurements of V_1 and V_2 is determined by the shot noise in the current reaching the SE detector. This is referred to as the shot-noise limited voltage resolution. As shown in section 3.5, the SE signal from the IL-200 electron beam system operates near this limit except for residual 60 Hz pickup. The shot noise in the SE current arriving at the SE detector $I_{SE(det)}$ is related to operating conditions by

$$\langle \Delta I_{SE\,(det)^2} \rangle = 2 \;\; e \;\; I_{SE\,(det)} \Delta f \tag{4.3}$$

where e is the electron charge and f is the measurement bandwidth used to sample the voltage value. Fluctuations in samples of $I_{SE(det)}$ are equivalent to errors in measured voltage given by

$$\Delta V = \frac{\Delta I_{SE\,(det)}}{I_{SE\,(det)} \times g}$$

$I_{SE(det)}$ can be evaluated using Eq.(4-3) and $I_{SE(det)}$ can be expressed in terms of the magnitude of impressed current and the SE yield. The resulting expression for mean squared error in each measured voltage then turns out to be

$$\langle \Delta V^2 \rangle = \frac{2\ e}{T\ g^2\ t_{int}} \times \frac{\gamma - 1}{\gamma} \times \frac{1}{I_{imp}} \tag{4.4}$$

where V is the voltage value being measured (either V_1 or V_2), T is the net transmission coefficient of the SE analyzer and the cold shield aperture, g is the voltage contrast calibration factor as defined in Section 2.3, t_{int} is the total integration time for the voltage measurement, γ is the SE yield and I_{imp} is the impressed current supplied for the measurement (either I_1 or I_2 plus any current needed to cancel background photocurrent).

The resulting random error in impedance measurement from noise in voltage measurements according to Eq. (4-4) is evaluated and listed in Table 4-1 along with all the other error sources discussed below.

The fundamental lower limit of noise in the measurements of I_1 and I_2 is determined by the shot noise in the impressed current. This is given by an expression similar to Eq. (4-3), with I_{SE} replaced with I_1 or I_2. The mean squared error in measured impedance due to this noise source turns out to be

$$\langle \Delta R^2 \rangle = R^2 \times \frac{(|I_1| + |I_2|) \times 2\ e\ \Delta f}{(I_1 - I_2)^2} \tag{4.5}$$

b) **Drift in Primary Current and in SE Emission Coefficient –**

Drift in the primary beam current or in the SE yield during signal collection causes an error in device voltage sampling which appears as an error in impedance measurement given approximately by

$$\Delta R_{drift} \approx \frac{1}{2\ \Delta I_{mod}\ g\ f_{mod}} \times \frac{\partial \ln\ (I_p \times \gamma)}{\partial t} \tag{4.6}$$

where I_{mod} is the amount of current modulation used in the measurement ((I_1 - I_2) in this case), f_{mod} is the frequency of the current modulation factor including any delays to allow settling of the device bias

and I_p is the primary beam current. Eq. (4-6) is approximate by about a factor of two because the exact amount of error depends on the specific modulation pattern used as well as on whether the drift in (I_p * γ) changes with each duty factor change (as discussed in Sections 3.1 and 3.2) or proceeds at a constant rate.

c) **False Modulation of SE Signal --**

The magnitude of the false modulation effect in the SE signal was estimated in Section 3.5 at 900% per unit duty factor. The error in calculated device impedance which results from this effect can be estimated by applying Eq. (2-2):

$$R = \frac{1}{g \times \text{SE signal}} \times \frac{\partial\ (\text{SE signal})}{\partial\ (\text{impressed current})}$$

$$= \frac{1}{g \times \text{SE signal}} \times \frac{\partial\ (\text{SE signal})}{\partial\ (\text{duty factor})} \times \frac{\partial\ (\text{duty signal})}{\partial\ (\text{imp current})} \qquad (4.7)$$

$$\Delta R = \frac{1}{g} \times \frac{900 \text{ percent}}{\text{unit duty factor}} \times \frac{1}{I_p^0 \times (\gamma - 1)}$$

where I_p^0 is the primary electron beam current available at 100% duty factor (typically 700 nA). The estimated value of this impedance error based on these values is approximately 500 Megohms. The polarity of the effect turns out to give an error contribution in the negative direction as seen in section 3.5.

d) **Incomplete Settling of Device Bias --**

As is discussed below the possibility of current modulation frequencies as high as 30 kHz are considered in order to minimize errors due to drift. At high current modulation frequencies, an error contribution due to incomplete settling of the device bias may occur. This error contribution is systematic rather than random. It is convenient to express as a percentage error (e.g., 10% error for the case where the device bias settles only 90% of the way to its final value before a voltage reading is taken). It is given by

$$\frac{\Delta R}{R} = \frac{RC}{t_{samp}} \times \exp\left(\frac{-t_{set}}{RC}\right) \times \left(1 - \exp\left(\frac{-t_{samp}}{RC}\right)\right), \tag{4.8}$$

where t_{set} is the time allowed for settling of the device bias before the signal sample, t_{samp} is the duration of signal sampling and RC is the device RC settling time. An error contribution enters at each of the voltage readings (I_1, V_1 and I_2, V_2).

2) **location of zero bias**

Due to background radiation the device bias settles at a different value than that which would be determined by the impressed current alone. The dynamic resistance measured at the shifted bias condition is different from the value at zero bias. Approximating the device I-V characteristics as an exponential around zero bias, the dynamic resistance at the shifted bias point is

$$R = R_o \times \exp(-eV_{bg}/kT)$$

where V_{bg} is the background-induced shift in device bias.

As an example, for the MWIR device discussed in section 3.3, R_0 is 23 Megohm at 130 K, the shift V_{bg} is estimated to be 6.7 mV due to the 400 pA of background photocurrent, and the dynamic resistance at the shifted bias point is 12.4 Megohms which differs from R_0 by about 46%.

For an LWIR device the extent of this type of error will depend on the background radiation conditions achieved. The percentage error is likely to be comparable to the MWIR case since reducing it further would mean using apertures smaller than the f/20 aperture estimated in Section 3.4, which would tend to detract further from efficient SE collection. For the f/20 aperture the resulting shift in bias V_{bg} for a device with R_0 = 1 Megohm is estimated at 2 mV and the dynamic resistance is shifted to 0.75 Megohm, which represents an error of 25%.

All of the error contributions discussed here are evaluated for the operating conditions typically used in the experimental e-beam system and listed in Table 4-1 starting with the largest component.

The two dominant sources of error are 1) the false modulation of the SE signal baseline with blanking rate and 2) the drift in the primary current and/or SE yield. Elimination of the false modulation is obviously the first priority. Although the source of this effect was not identified, it seems unlikely to be a fundamental limitation to measurement accuracy. Even if the effect in the SE signal baseline cannot be completely eliminated through changes in detector or pre-amplifier design, the effect could be rejected further by a differential measurement of the peak height above the baseline using two track and hold circuits. However it is achieved, the ultimate requirement is that the coefficient of false SE signal modulation used in eq. (4-7), (900% per unit duty factor) be reduced to about 0.5% per unit duty factor.

The reduction of primary current drift by maintenance of clean surface conditions in the electron microscope column has been discussed in section 3.1. Reduction of the drift rate further by several orders of magnitude as suggested by the size of the error contribution on Table 4-1 would require additional fundamental development work which might involve changes in the column design, and could also present ongoing constraints in system maintenance procedures or in operating conditions.

Another probably easier approach to reducing drift error is to use substantially faster modulation of applied bias between the two points on the device I-V *curve* (I_1, V_1 and I_2, V_2). The eventual limitation on this approach is the error contribution of incomplete settling of the device bias, which grows with increasing frequency. However since this contribution is extremely small under the conditions used now there is considerable leeway to change the operating conditions in this direction.

The shot noise error contribution is the next lowest in magnitude and the first on the list where the error is less than the value being measured. Nonetheless for LWIR devices the percentage error is large so that the possibility of reducing it should be considered. The relatively large value in the LWIR case results from the small cold shield aperture and low efficiency of SE extraction as described in section 3.4.

Improvement of this situation will require redesign of the cold shielding and SE energy analyzer. One straightforward approach would be to make the SE energy analyzer part of the low-temperature cold shielding. Then the present aperture below the extraction grid could be eliminated and an aperture at the top of the analyzer used to determine the solid angle of room-temperature background radiation. Since the top of the analyzer is several times farther away from the sample surface than the aperture

used now, it could then be made several times larger in diameter than the estimate given in section 3.4, (specifically 2.5 mm as opposed to 0.25 mm) while keeping the background radiation level constant. An overall transmission of 5% is a reasonable design goal using this approach.

The potential amount of improvement in the overall LWIR device impedance measurement accuracy by 1) optimization of the modulation frequency and 2) improvements in drift and analyzer transmission have been estimated; the results are summarized in Figure 4-1. To obtain these results the error contributions from drift, shot noise and incomplete bias settling were combined at a given values of drift rate and analyzer transmission and then the modulation frequency and amplitude were adjusted to minimize the total error.

The noise and drift contributions were squared and added and the square root of the sum taken, since the sign of these two components are uncorrelated. The error due to partial device settling at high modulation frequencies was added directly to this result since it is systematic. Other parameter values in these estimates were kept the same as in Table 4-1, specifically: total signal collection time of 300 ms per impedance measurement; SE yield = 1.3; device capacitance = 2 pF; SE voltage contrast calibration factor g = 12% / volt; and I_{b} = 400 pA. Once again, it should be stated that these potential improvements would require reduction of the false SE modulation effect by over three orders of magnitude to be below the three error contributions which were included in these estimates.

The results indicate that even at the currently achievable levels of drift and analyzer transmission, the strategy of increasing the modulation frequency promises to improve the measurement accuracy by about three orders of magnitude, to error levels near 300 kΩ. The bias modulation frequency associated with this case (30 kHz) is beyond the range of the software-controlled signal-processing system developed here. Software-controllable analog units, such as phase-locked function generators for driving the VCO input and substrate potential in a coordinated way, and a dual gated integrator for demodulation of SE signal, would be needed. From that point the most rapid gains in accuracy appear to lie in improvement of the SE analyzer transmission. In the best case modeled, where both drift and analyzer transmission are improved by an order of magnitude, the estimated error levels drop to near 100 kΩ.

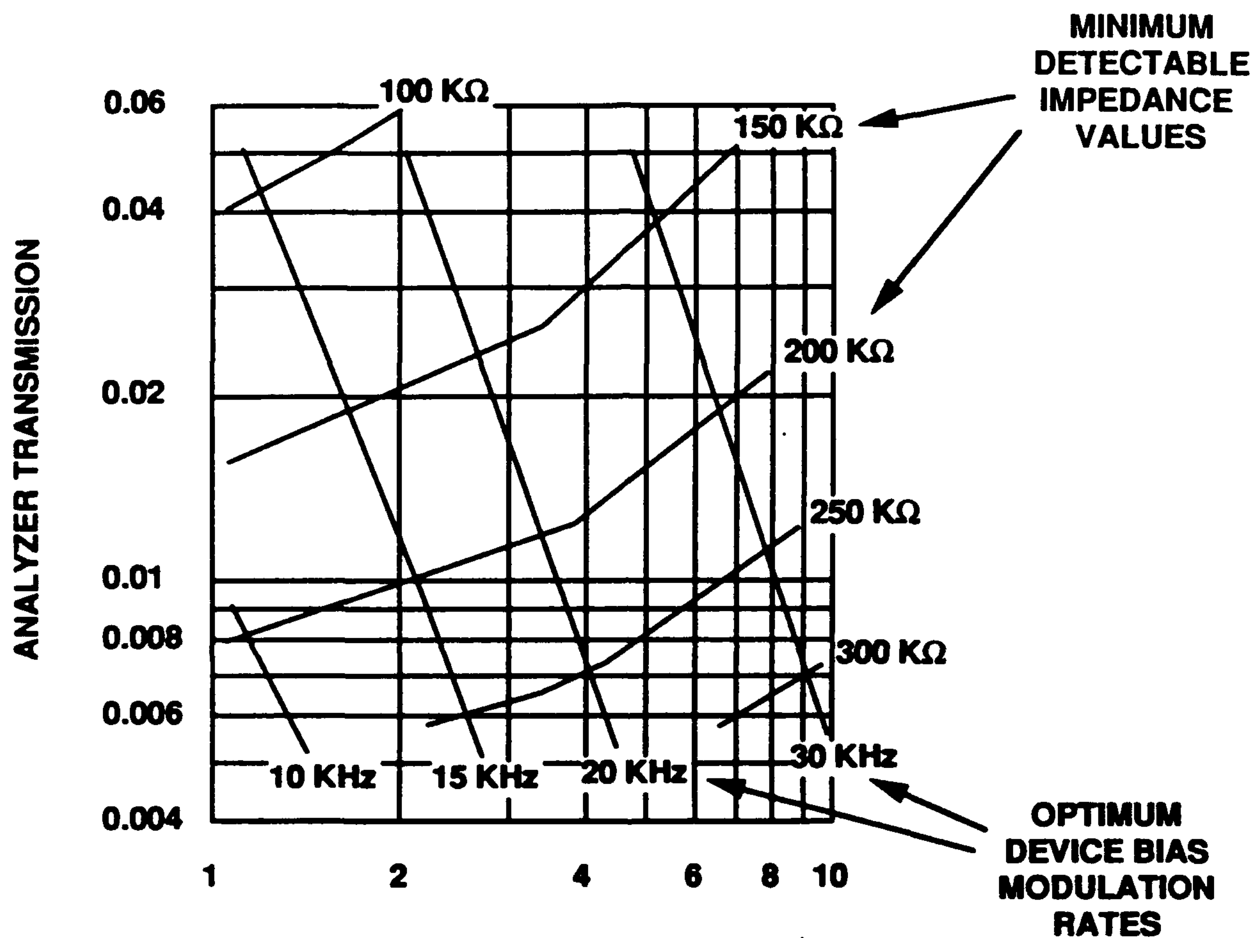

Figure 4-1. Estimated Levels of Total Impedance Measurement Error as a Function of 1) Primary Current or SE Yield Drift Rate and 2) Transmission of the Analyzer and Cold Shield, Assuming that the False Modulation of SE Signal is Eliminated. All of the error sources discussed in Section 4 are combined here except for the false modulation of the SE signal. Other parameter values are: signal collection time = 0.3 s; SE yield = 1.3; device capacitance = 2 pF; SE voltage contrast factor g = 12%/V and I_{bg} = 400 pA.

In summary, the feasibility of electron-beam based impedance measurements of LWIR photodiodes with sufficient accuracy for screening purposes depends on the success of further improvements in system components and operating conditions. Starting with the most significant, the necessary improvements are:

- Reduction of the false duty-factor-related modulation of the SE signal to.5% per unit duty factor either through improvement in the frequency response of the SE detector and preamplifier or through changes in the filtering or sampling of the SE signal to reject duty-factor-related modulation.
- Reconfiguration of the device bias modulation and SE signal sampling systems to move the frequency of modulation from 60 Hz to the 10 - 30 kHz range.
- Achievement of background levels below 10^{15} $cm^{-2}s^{-1}$ and SE extraction efficiencies near 5% through development of an integral cold shield and SE analyzer.
- Improvement in the column vacuum to allow all interior column surfaces to remain clean and well grounded during blanked-beam operation. The motivations here are first to reduce the drift in primary current as discussed above and second to make the relationship between duty factor and impressed current as reproducible as possible so that frequent readjustment of duty factor modulation amplitude is not required to maintain a desired level of impressed current modulation.

SECTION 5
SUMMARY

In this investigation, contactless I-V probing of IR diodes using a commercial voltage probing electron beam system was found to require a non-standard mode of operation, driven by an external controller, so that voltage measurements at variable applied current could be implemented. The minimum detectable impedance achievable in the resulting augmented electron beam system was found to be in the $10^8\Omega$ range, limited mainly by frequency-dependent baseline shift in the secondary electron signal at around 10 kHz. Other key results of the program were:

- Demonstration of dynamic impedance measurements of a 400 MΩ MWIR diode,
- Demonstration of automated beam positioning, signal calibration and impedance calculation,
- Analysis of random and systematic error sources indicating that aside from the present limitations due to the SE detection system, the electron beam based method should be capable of detecting and measuring impedances at or below 1 MΩ.

The system improvements needed to achieve the 1 MΩ detection and measurement capability were identified as:

- Development of specialized radiation shielding around the sample stage which maintains a background radiation level well below 10^{15} cm^{-2} s^{-1} while also achieving a secondary electron extraction efficiency of 5% or more.
- Reduction of the baseline shift in the secondary electron detection system to less than 2% of the SE signal pulse height per 100% modulation of the duty factor.
- Upgrade of the vacuum pumping in the electron beam column to maintain clean, well-grounded interior surfaces in the column for longer intervals, thus reducing maintenance requirements.
- Upgrade of triggering and signal sampling electronics (external to the electron beam system) to allow diode bias modulation at frequencies in the range 10 kHz - 30 kHz.

Should further development of electron-beam based voltage probing of LWIR photodiodes be pursued it is recommended that the next phase of effort concentrate on development of an e-beam system meeting these specifications, prior to further tests of automated measurements on photodiodes. Such an instrument development effort would likely be best undertaken in an environment specializing in e-beam systems.

APPENDIX A
DYNAMICS OF DIODE BIAS UNDER PULSED IMPRESSED CURRENT

In order for the pulsed impressed current technique described in section 2.3 to work as intended, certain relationships must hold between the pulse repetition rate and the internal discharge time of the diode (approximated here as RC, where R is the dynamic resistance and C the capacitance of the diode). In this appendix more details are given of the dynamics of diode charging and discharging and its relationship to the device voltage signal as it appears at the output of the track and hold circuit.

Figure A-1 depicts waveforms of pulsed impressed current versus time and the charging and discharging of diode bias which result. The duration of each current pulse is termed t_{on} and the time between pulses t_{off}. The voltage levels at the minimum and maximum of the voltage waveform are labeled V_{lo} and V_{hi}; they occur at the beginning and the end, respectively, of each impressed current pulse.

Secondary electrons are emitted from the point of impact of the electron beam, throughout the entire impressed current pulse. The secondary electron signal used for the measurement is taken from the output of a track and hold circuit in the IL-200 system controller. In between impressed current pulses, this circuit holds the SE signal associated with the peak diode bias voltage reached during the last pulse. Since the values of duty factor used in this method are always fairly low, (i.e., this circuit spends most of the time holding rather than tracking), the time average of the track and hold output signal will be determined primarily by V_{hi} rather than by V_{lo}.

During an impressed current pulse, the time dependence of diode bias is given by:

$$\frac{\partial V}{\partial t} = \frac{I_{imp}(t) - I_{leak}(V)}{C} \qquad \text{(A-1)}$$

$I_{imp}(t)$ is the pulsed impressed current applied to the diode and I_{leak} (V) is the reverse leakage of the diode. The dependence of I_{leak} on V is not a simple function so we parameterize it in the linear form

$$I_{leak}(V) = I_O + V / R$$

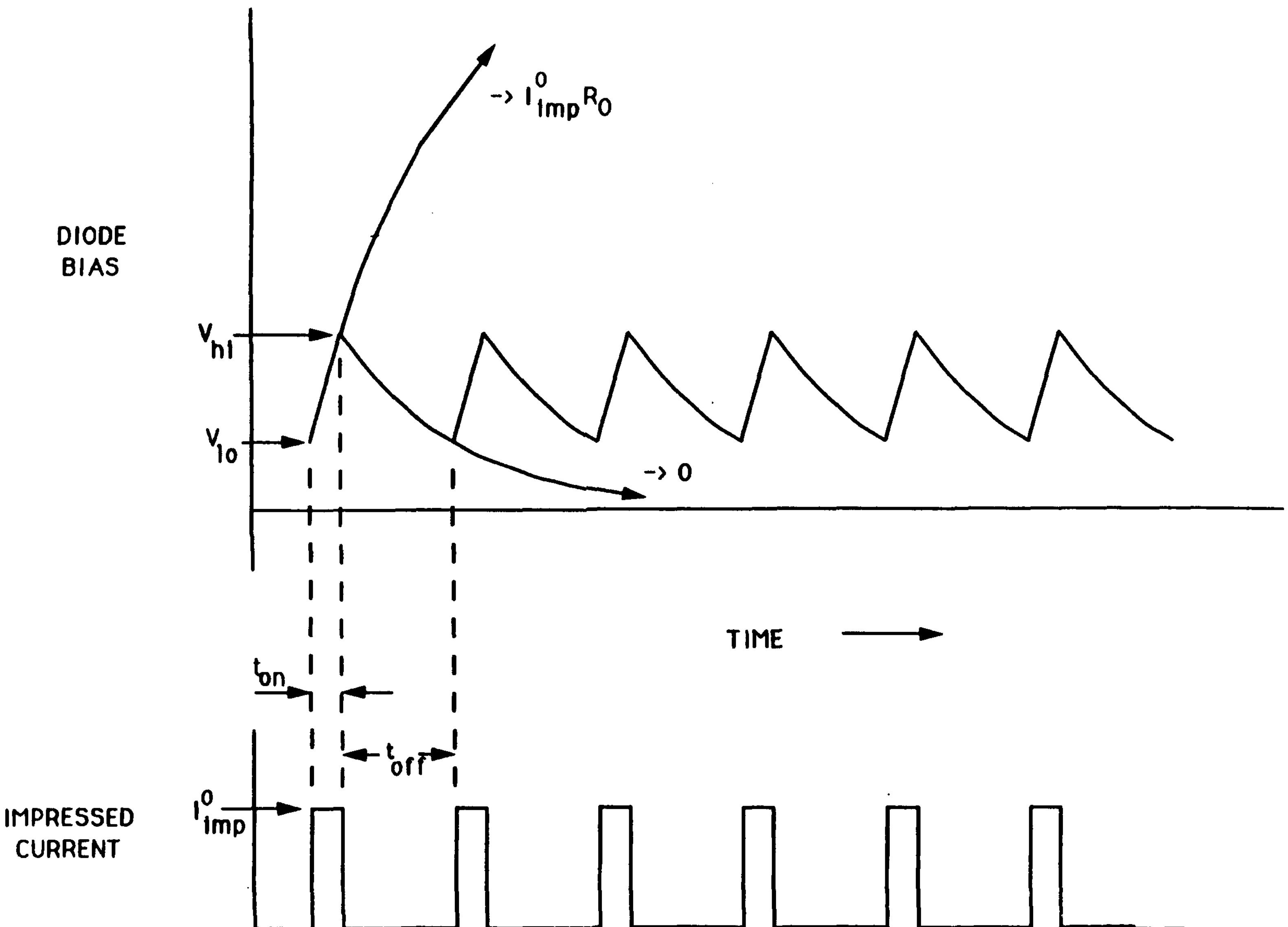

Figure A-1. Pulsed Impressed Current versus Time and the Resultant Charging/Discharging of Diode Bias

Here I_0 may have physical significance such as background current or it may be just the I-axis intercept of a linear fit to part of the diode I-V characteristics.

Integration of Eq. A-1 gives

$$V_{hi} = V_{lo} \exp(-t_{on}/RC) + (I_{imp} - I_0) R [1 - \exp(-t_{on}/RC)]$$

and

$$V_{lo} = V_{hi} \exp(-t_{off}/RC) - I_0 R [1 - \exp(-t_{off}/RC)].$$

Solving for V_{hi} gives

$$V_{hi} = I_{imp} R \times \frac{[1 - \exp(-t_{on}/RC)]}{[1 - \exp(-(t_{on} + t_{off})/RC)]} - I_o R$$

Three different situations may occur depending on the relative magnitudes of RC, t_{on} and t_{off}. The expression for V_{hi} can be approximated by different expressions for these three cases.

Case 1: For the case where both t_{on} and t_{off} are significantly less than RC, V_{hi} follows the relation

$$V_{hi} = I_{imp} R \times \frac{t_{on}}{t_{on} + t_{off}} - I_o R$$

In this case the effect of the pulsed impressed current on the track-and-hold output signal is equivalent to that of a dc applied current of I_{imp} * duty factor. The pulse duration time and repetition rate must be in this regime in order for the variable duty cycle method described in section 2.3 to work correctly.

Case 2: For the case where $t_{on} << RC$ but $t_{off} >> RC$, the situation is described by the relationship

$$V_{hi} = I_{imp} R \times \frac{t_{on}}{RC} - I_0 R = I_{imp} \times \frac{t_{on}}{C} - I_0 R$$

In this regime the increase in diode bias at the end of each impressed current pulse is governed only by the diode capacitance and not by its resistance, and the diode bias recovers essentially to the open-circuit value between pulses.

Case 3: Finally, if both t_{on} and t_{off} are significantly *greater than RC, the expression for* V_{hi} approximates to

$$V_{hi} = (I_{imp} - I_0) R$$

In this regime the diode bias reaches a steady-state condition, determined by the diode resistance, during each impressed current pulse. As in case 2, the diode bias recovers to the open-circuit value between pulses.

An important aspect to note about cases 2 and 3 is that the track and hold output signal becomes independent of impressed current duty factor. Such signal behavior could be misinterpreted as a low device impedance or a short.

APPENDIX C
SAW TESTING

8807-06

SAW Evaluation of IR Diode Detector Arrays

Technical Report Under
Purchase Order No. 7351068A

prepared for

Honeywell
2 Forbes Road
Lexington, MA 02173

by

S. A. Reible*
A. Bers†
J. H. Cafarella*

30 June 1988

"Distribution authorized to U.S. Government agencies only. Other requests for this document shall be referred to CNV&EO."

*MICRILOR, Inc,
17 Lakeside Office Park
North Avenue
Wakefield, MA 01880

†Consultant
Professor at MIT
Department of Electrical and Computer Science
Cambridge, MA 02139

TABLE OF CONTENTS

SECTION	TITLE	PAGE
1	INTRODUCTION AND SUMMARY	1-1
2	ACOUSTOELECTRIC INTERACTIONS	2-1
2.1	SAW DELAY LINES	2-1
2.2	OVERVIEW OF ACOUSTOELECTRIC (AE) INTERACTIONS	2-3
2.3	ACOUSTOELECTRIC CURRENT/VOLTAGE	2-4
2.4	CONVOLVER INTERACTIONS	2-5
2.5	STORED CHARGE INTERACTIONS	2-7
2.6	SAW RF PROBE	2-7
3	PHYSICAL STRUCTURES	3-1
3.1	GAP TECHNOLOGY	3-1
3.2	WAVEGUIDING	3-1
3.3	FILLING FACTOR LOSS	3-3
3.4	SENSE/GROUND PLATES	3-5
3.5	PHYSICAL DESIGNS	3-7
	3.5.1 Convolver Structure	3-7
	3.5.2 Proposed Configuration for Stored Charge Readout	3-9
	3.5.3 Physical Configurations for SAW rf Probe	3-9
4	MODELS	4-1
4.1	SAW FIELD	4-1
4.2	COUPLING FROM SAW ADJACENT DIODE ARRAY	4-1
4.3	DIODE ARRAY AS A SAW CONVOLVER/STORAGE CORRELATOR	4-1
4.4	DIODE CHARGING DYNAMICS	4-1
4.5	GENERATION OF PROBE FIELD	4-1
5	SIGNAL PROCESSING CONSIDERATIONS	5-1
5.1	SIGNAL-TO-NOISE REQUIREMENTS	5-1
5.2	BASIC MEASUREMENT	5-1
5.3	SIGNAL-TO-NOISE IMPROVEMENT	5-1
5.4	TRANSFORM TECHNIQUES	5-2
6	PROPOSED SAW FOLLOW-ON EFFORT	6-1
7	CONCLUSION	7-1
8	REFERENCES	8-1

LIST OF APPENDICES

APPENDIX	TITLE	PAGE
I	SURFACE ACOUSTIC WAVE (SAW) ON A PIEZO ELECTRIC	I-1
I.A	LINEAR PROPAGATION AND TRANSDUCTION	I-1
I.B	NONLINEAR EFFECTS ON PROPAGATION	I-3
I.C	REFERENCES	I-5
II	LINEAR COUPLING FROM A SAW TO AN ADJACENT DIODE ARRAY	II-1
II.A	SAW PROPAGATION IN THE PRESENCE OF A SEMICONDUCTING SURFACE	II-1
II.B	EQUIVALENT CIRCUIT FOR DIODE EXCITATION BY SAW	II-6
II.C	REFERENCES	II-7
III	DIODE ARRAY AS A SAW CONVOLVER/STORAGE CORRELATOR	III-1
III.A	NONLINEAR (VARACTOR) ACTION OF THE DIODES	III-1
III.B	THE DEGENERATE SAW CONVOLVER	III-3
III.C	THE STORAGE CORRELATOR MODE	III-5
III.D	REFERENCES	III-7
IV	DIODE CHARGING DYNAMICS	IV-1
IV.A	"FAST" DIODE CHARGE DYNAMICS	IV-2
IV.B	CHARGING DYNAMICS FOR A P+N DIODE	IV-3
IV.C	REFERENCES	IV-5
V	HIGH FREQUENCY E-FIELD PROBES WITH SAWS	V-1
V.A	E-FIELD PROBE BY ELASTIC NONLINEARITY	V-1
	V.A.1 Diode D-Field from the Nonlinear Elastic Prove	V-2
V.B	E-FIELD PROBE BY ELECTRON NONLINEARITY	4-8
	V.B.1 Diode D-Field from the Nonlinear Semiconductor Probe	V-8
V.C	REFERENCES FOR APPENDIX V	V-13

LIST OF ILLUSTRATIONS

FIGURE	TITLE	PAGE
1-1	RF Potentials at Diode Surface as a Function of Air Gap Spacing	1-4
1-2	SAW Charge Storage/Readout	1-6
1-3	SAW RF Probe	1-6
2-1	SAW Generation by Interdigital Electrodes	2-1
2-2	SAW Generation by Interdigital Electrodes	2-2
2-3	Acoustoelectric Interactions	2-3
2-4	Piece Parts for an AE Signal Processing Device	2-5
2-5	Convolver Interaction	2-6
2-6	Diode Charging/Readout	2-8
2-7	SAW RF Probe	2-9
3-1	Rail Support Structure	3-4
3-2	Short Pulse/Long Pulse Convolution	3-6
3-3	Electrical Output/Ground Connections	3-7
3-4	Piezoelectric Plate for Convolver Measurement	3-9
3-5	Composite Convolver Structure (End View)	3-10
3-6	Piezoelectric Substrate for Stored Charge Readout	3-11
3-7	Composite Convolver Structure	3-12
3-8	GaAs Substrate for RF Probe	3-12
3-9	Modeling of SAW RF Probe Interactions	3-13
I-1	Piezoelectric Surface	I-2
I-2	Electrical coupling to and from a SAW	I-4
II.1	Diode Array Adjacent to a Piezoelectric Surface	II-2
II.2(a)	Open-circuit voltage and for the equivalent circuit of Figure II.1(c)	II-3
II.2(b)	Acoustic coupling capacitance for the equivalent circuit of Figure II.1(c).	II-4
II.3	Short-circuit, normal electric displacement field in the equivalent circuit of Figure II.1(c)	II-5
III.1	Set-up for convolution and/or correlation of two SAW Signals	III-2
III.2	Equivalent circuit for calculating output power to load (R_L) from open-circuit plate voltage (V_3) produced by SAW's shown in Figure III.1.	III-5
III.3	(a) Plate signal excitation and (b) its equivalent circuit	III-6
IV.1	One dimensional p+n abrupt junction diode regimes with applied electric displacement field D(t) due to SAW's	IV-1
V.1	Convolution of SAWS Pulses	V-2
V.2	E-Field Probe Nonlinearly Generated	V-3
V.3	Model structure for calculating the normal D-Field at the diodes	V-4
V.4	Counterpropagating SAW's with gaussian pulse signals	V-5
V.5a	Normalized, (short-circuit) normal D-Field, D_p, at diodes	V-6

LIST OF ILLUSTRATIONS (CONTINUED)

FIGURE	TITLE	PAGE
V.5b	Normalized, (short-circuit) normal D-field, D_p, at diodes	V-7
V.5c	Normalized, (short-circuit) normal D-field, D_p, at diodes	V-7
V.6	E-Field probe nonlinearly generated by SAWs in semi-insulating GaAs with ion-implanted semiconductor strips	V-9
V.7	Model structure for calculating the normal D-Field..................................	V-10
V.8a	Normalized, (short-circuit) normal D-field, D_p, at diodes	V-11
V.8b	Normalized, (short-circuit) normal D-field, D_p, at diodes	V-11
V.8c	Normalized, (short-circuit) normal D-field, D_p, at diodes	V-12

LIST OF TABLES

TABLE	TITLE	PAGE
2-1	SAW Alternatives	2-5
3-1	Ion Implanted Waveguides on $LiNbO_3$	3-2
3-2	Waveguide on $LiNbO_3$ Formed by Titanium In-Diffusion	3-3
3-3	Waveguides on $LiNbO_3$ Formed by Narrow Support Rails	3-5
3-4	Physical Parameters for AE Measurement Alternatives	3-8
6-1	Comparison of Measurement Techniques	6-1
6-2	SAWS Measurement Instrument	6-2

SECTION 1
INTRODUCTION AND SUMMARY

Three types of nonlinear acoustoelectric interactions in piezoelectric/diode-array structures were explored for measuring individual diode parameters in IR detector arrays. The three alternatives explored include: 1) Convolution interactions in detector materials and IR diodes, 2) the readout of stored charge patterns in IR-diode arrays, and 3) an acoustically generated radio frequency (RF) probe of IR diodes.

The first two alternatives considered employ the electric fields generated by surface acoustic waves (SAW) on a piezoelectric substrate to generate nonlinear interactions in adjacent (separated by a narrow air gap) IR diodes. The output signal generated by these interactions can provide a measurement of significant IR material and diode parameters. Such convolver and charge-readout types of SAW interactions have undergone significant development during the past decade for signal processing components

These particular acoustoelectric interactions provide moderately large output signals but require relatively small gap spacings, typically less than 1 mm, between the piezoelectric substrate and the semiconductor. This is due to the fact that the piezoelectric fields generated by the SAW vary rapidly in phase in the direction of propagation and, therefore, decay rapidly with distance from the surface of the piezoelectric substrate. The exponential fall-off of the piezoelectric fields in the direction perpendicular to the surface of the piezoelectric substrate is depicted in Figure 1-1.

Convolution-type interactions measure the mobility and density of free carriers near the surface of the semiconductor. These interactions produce an output signal which is perpendicular to the plane of the semiconductor. Convolver interactions have the advantage of providing large output signals (to -30 dBm) which are spectrally separated from the two input frequencies; the output frequency is equal to the sum of the two input frequencies. This eliminates most problems associated with spurious signals being generated by the SAW. Carrier mobility and density information would be highly desirable to possess before the fabrication of the diode arrays and SAW, therefore, should be largely looked upon as a sensitive, nondestructive material evaluation technique.

The second type of acoustoelectric interaction, which was explored in depth, utilizes nonlinear effects with fixed or stored charge in the detector diodes. This interaction is often termed a charge-storage/ charge-readout process. The technique provides a contactless measurement of the resistance (R) of individual diodes by observing the decay time constant of the stored charge. A measurement of this type on an IR diode array is depicted in Figure 1-2.

To charge the diode array, a large RF signal of sufficient amplitude to slightly forward bias the diodes is applied to one (or) two SAW transducers. This introduces a small amount of stored charge across the depletion capacitance of the diode. After the large amplitude SAW wave is removed, the diodes remain slightly reversed biased (e.g., several mVs).

A small-amplitude, short-duration read SAW is then introduced onto the piezoelectric substrate. The read SAW provides an output signal which varies with the amplitude of the stored charge in the diode array. Without additional signal processing, the spatial resolution of this measurement is determined by the duration of the read SAW. With signal processing techniques the resolution of the readout process can be smaller than the duration of the SAW read pulse.

The decaying of the stored charge in the diode array is directly observed with multiple SAW reads. This provides a contactless measurement of the diode time constant (RC_d). Both the resistance R and depletion capacitance C_d of the diode are highly nonlinear and depend upon the amount of stored charge (or correspondingly the potential) across the diode. For moderate amounts of stored charge, and hence, small (e.g., <2 mV) diode potentials, the diode resistance approaches its unbiased value (R_0). Since, values for C_d are fairly well known, acoustic measurement of the stored charge decay rate at small reverse bias levels provides a measure of the diode parameter R_0 which we desire to extract.

The output signal for the charge-readout process appears at the same center frequency as the SAW read signal, and hence, spurious signals can be a potential problem. Since the overall process involves two nonlinear interactions, charge storage and read, it is inherently less efficient than the convolution process, and provides smaller output signals. If necessary, signal processing techniques can be implemented to improve the signal-to-noise (S/N) ratio of the readout process.

A significant improvement in the readout sensitivity can be obtained by storing a charge pattern with a spatial frequency. This can be implemented by utilizing two SAWs, a long-CW or coded waveform and a short, counterpropagating strobe, in the charge-storage step. Alternatively, a spatially-varying charge pattern could be introduced by selectively discharging (or charging) the detector array with IR radiation. Since, a spatially varying charge pattern must encompass a minimum of two or three diodes, the spatial resolution of the readout process is also limited to a minimum of three diodes. However, signal processing techniques utilizing multiple scans can overcome this limitation.

During the exploration of various SAW measurement alternatives a new SAW measurement concept was developed. This concept, which we term a SAW RF probe, utilizes an interaction between two large amplitude, counterpropagating SAW waves to generate a short, but spatially uniform RF field at twice the frequency of the SAW waveforms. This RF field is used to probe (measure) the stored charge in individual IR diodes via its modulation of the depletion capacitance.

For efficient operation, a weakly piezoelectric, but highly nonlinear GaAs substrate, as depicted in Figure 1-3, would be utilized to generate the localized RF probe fields. The limitations associated with the weak piezoelectricity of GaAs would be overcome with an appropriate SAW transducer design. Relatively high (e.g., 300 MHz) SAW frequencies would be employed with moderate fractional SAW bandwidths. Selected ion-implanted regions in the GaAs substrate would provide free electrons for the desired nonlinear interactions for the generation of the RF probe fields. Electrical nonlinearities in the GaAs are much stronger than the mechanical nonlinearities encountered in insulating piezoelectric such as lithium niobate or quartz.

In this proposed measurement technique, the depletion capacitance would be first modulated by placing a small charge across the diode terminals. This charge would be introduced on the diodes by utilizing a short, high-voltage pulse through the gap capacitance to instantaneously forward bias the diodes in the array. The RF probe field would be then employed to place a small RF potential across the depletion capacitance of individual detector diodes. The resultant RF current flowing from the SAW interaction region through the series combination of depletion capacitance, gap, and piezoelectric capacitances to a ground plane would be measured a sequential number of times as the stored charge decays. The magnitude of this current flow would be modulated as the magnitude of Cd varies with the amount of stored

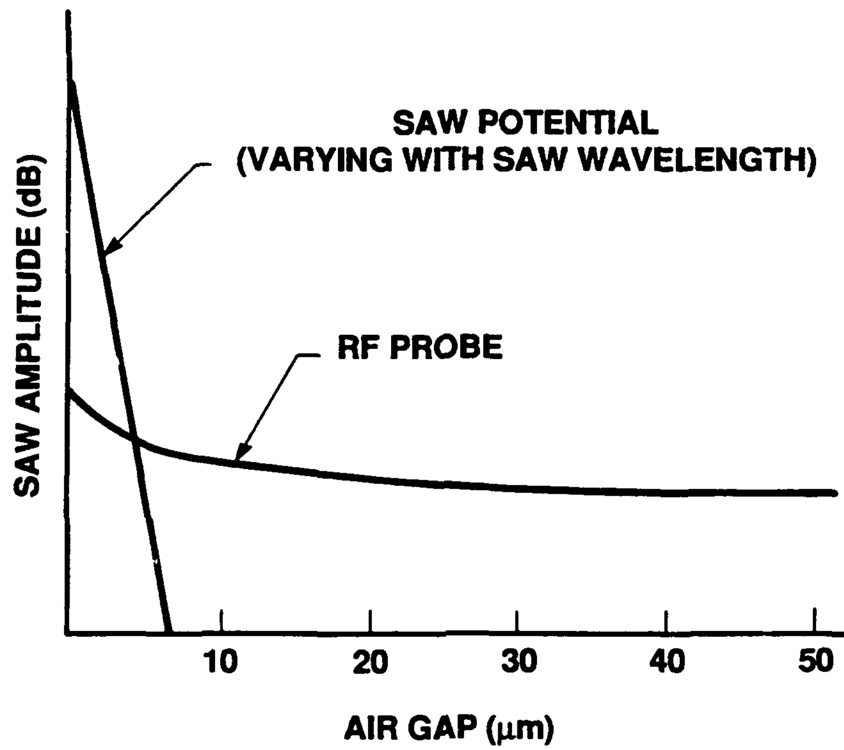

Figure 1-1. RF Potentials at Diode Surface as a Function of Air Gap Spacing

charge remaining on the individual diodes. With multiple SAW reads, the local discharge of the depletion capacitance Cd would be observed and provide a measure of R_oC_d (and R_o).

A major advantage of this technique is that because the RF probe field decays slowly with distance from the surface of the piezoelectric, much like the field from a phased antenna, the semiconductor-piezoelectric gap spacing can be as much as an order of magnitude larger (e.g. 3 to 30 μm) than for the more traditional acoustoelectric interactions. In addition, as is also true of the other types of SAW interactions explored, the location of the probe field can be electronically stepped or scanned, facilitating rapid electronic measurements. Spatial SAW pulses as short as 50 μm could be utilized to generate the RF probe field providing single diode resolution.

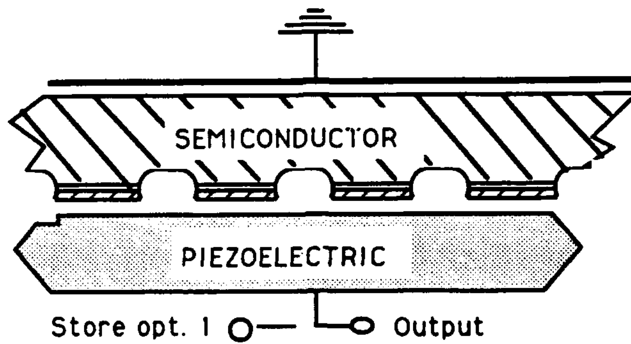

CHARGE STORAGE

Option 1 Voltage Spike Perpendicular to diode plane

Option 2 Convolution of 2 Oppositely directed waveforms

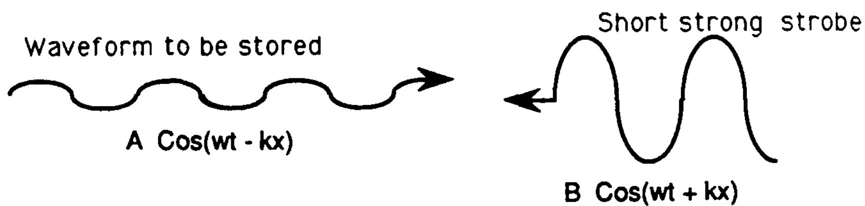

SUCESSIVE READOUT

C Cos(2wt - 2kx)

Figure 1-2. SAW Charge Storage/Readout

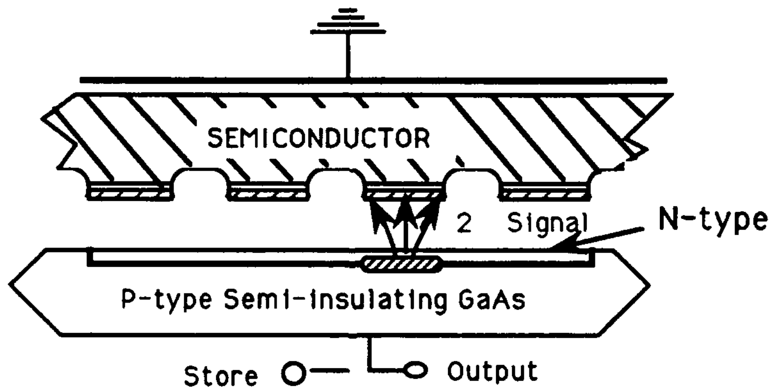

CHARGE STORAGE

Voltage Spike perpendicular to diode plane

SUCESSIVE READOUT

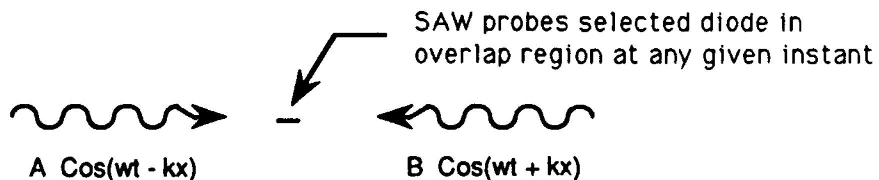

Figure 1-3. SAW RF Probe

SECTION 2
ACOUSTOELECTRIC INTERACTIONS

2.1 SAW DELAY LINES

Sound waves in the atmosphere travel about a million times more slowly than electromagnetic waves. Almost the same sluggishness prevails for sound waves in crystal. There, however, the slowness becomes an exploitable virtue; launching acoustic signals on the surface of a solid, engineers can capture almost 100,000 times as much information in the same distance of travel as would be the case for electromagnetic structures. Thus, there will be 100,000 times as many acoustic wavelengths as there would be electromagnetic wavelengths on the device surface. For example, at 1 GHz and with an acoustic propagation velocity of 3,000 m/s, the signal has a wavelength of 0.0003 cm. An acoustic device, one centimeter long, can be packed with more than 30,000 wavelengths of information-carrying signal. Such inherent resolution or concentration of information opens the door to many opportunities.

Envision a miniature wafer of piezoelectric material, a material such as lithium niobate, that responds mechanically to electrical pressure (and electrically to mechanical pressure). At one end, fingerlike, interdigital electrodes, as sketched in Figure 2-1, convert an electromagnetic wave into mechanical (acoustic) energy via the piezoelectric effect. The strength of this interaction is quantified in terms of an electromagnetic coupling constant (K^2). Lithium niobate has a relatively large coupling constant, meaning that relatively few fingers (conceptually equivalent to antenna elements) can efficiently convert the electromagnetic energy into acoustic energy. The acoustic energy propagates away from the source in two major directions, hugging the surface of the crystal.

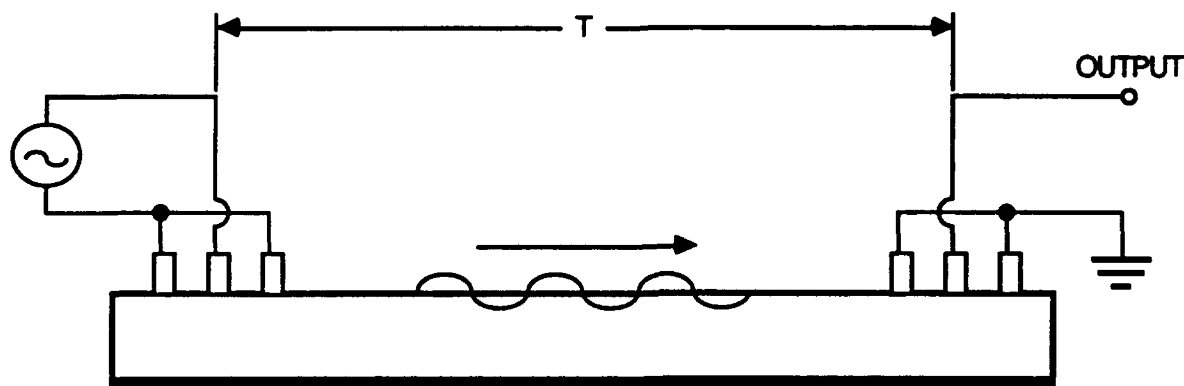

Figure 2-1. SAW Generation by Interdigital Electrodes

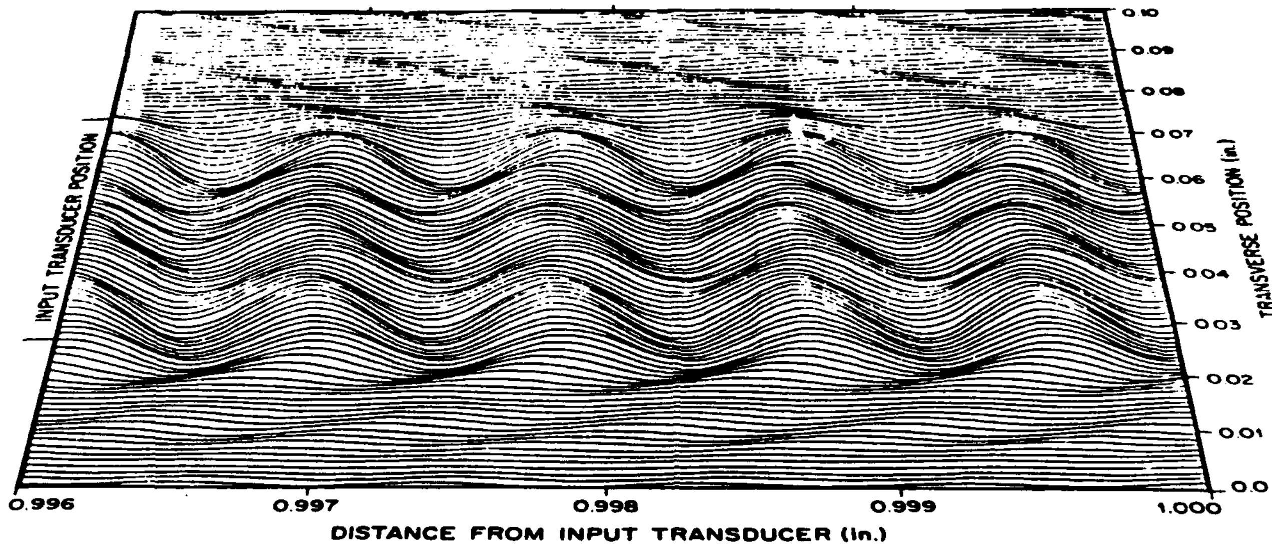

Figure 2-2. SAW Generation by Interdigital Electronics

The two propagation directions are perpendicular to the length of the transducer fingers. Typical lengths for the transducer fingers on lithium niobate are 66 wavelengths, with 2 to 10 finger pairs being utilized for each transducer, depending upon the desired bandwidth.

The presence of the top and bottom surfaces on the crystal forms an acoustic waveguide. The acoustic energy launched by the transducers has both shear and longitudinal components. As in the case of electromagnetic waveguides several multimoded waveguide solutions exist. One of these solutions is a shear wave with horizontal polarization (SH). This solution exists because at the free surface of the crystal the energy of the SH wave only scatters into itself. Other possible solutions might be vertically polarized shear partial waves or longitudinal partial waves. However, for a crystal with free surfaces, solutions for these two waves do not exist individually. Solutions do exist when these two modes are coupled and these solutions are called Lamp waves.

When a crystal is many wavelengths thick, the Lamb wave solution no longer has a significant interaction with both surfaces. In this case the acoustic energy hugs one or both of the crystal surfaces. This is the standard surface acoustic wave solution which is usually referred to as a SAW or a Rayleigh wave. This is the wave which will be used for non destructive testing and read out of the infrared detector arrays. A profile of a propagating SAW, measured with an electrostatic probe which detects the electric fields associated with the mechanical wave, is shown in Figure 2-2. Most of the acoustic energy of the SAW is carried mechanically, yet the mechanical height of the wave is only about 10^{-10} meter for an input power of about 100 mW.

With standard interdigital transducers, a surprisingly large fraction (80 to >99%) of the total acoustic energy appears as SAW waves. However, the remainder of the acoustic energy is transduced into bulk modes which can be a serious source of spurious.

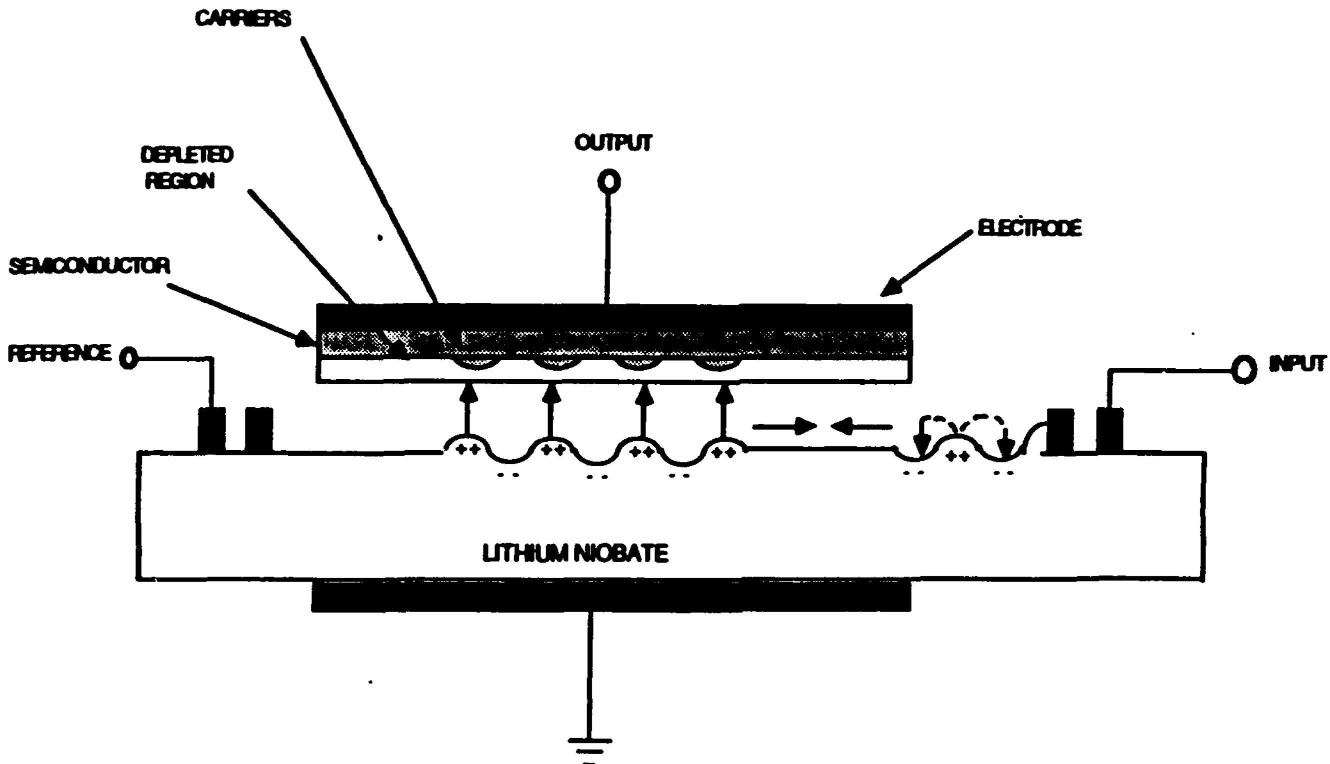

Figure 2-3. Acoustoelectric Interactions

2.2 OVERVIEW OF ACOUSTOELECTRIC (AE) INTERACTIONS

The interaction between acoustic waves and electrons in solids has been the object of numerous theoretical and experimental studies. Initially, great interest in this interaction was stimulated by the observation that in an applied electric field, drifting electrons can amplify a piezoelectrically active acoustic wave. This was demonstrated by several laboratories in the early 1970s but never became a practical device concept because of inherent inefficiencies in the interaction and reduced acoustic propagation loss as piezoelectric substrates and acoustic device technology became better developed.

A somewhat similar interaction occurs when a semiconductor with free carriers near its surface is brought within close proximity to a SAW delay line. The propagating SAW "drags" free electrons along its propagation path generating acoustoelectric currents (or potentials) along the length of the semiconductor. This interaction can provide a sensitive measure of the density and mobility of the free carriers near the surface of the semiconductor.

At the same time, interest developed in combining the enhanced nonlinearities afforded by semiconductors with the signal storage capabilities of piezoelectric delay lines. Subsequently, essential signal processing functions were demonstrated with structures employing a SAW delay line coupled through an intervening air gap to a semiconductor, of the type sketched in Figure 2-3. Devices which perform functions, such as convolution, correlation, and matched filtering exist in well-engineered forms providing signal processing for waveforms having bandwidths to 200 MHz and time-bandwidth (TB) products to 2000. The piece parts (metal package, piezoelectric substrate, and mounted silicon strip) for one of these acoustoelectric signal processing components is shown in Figure 2-4.

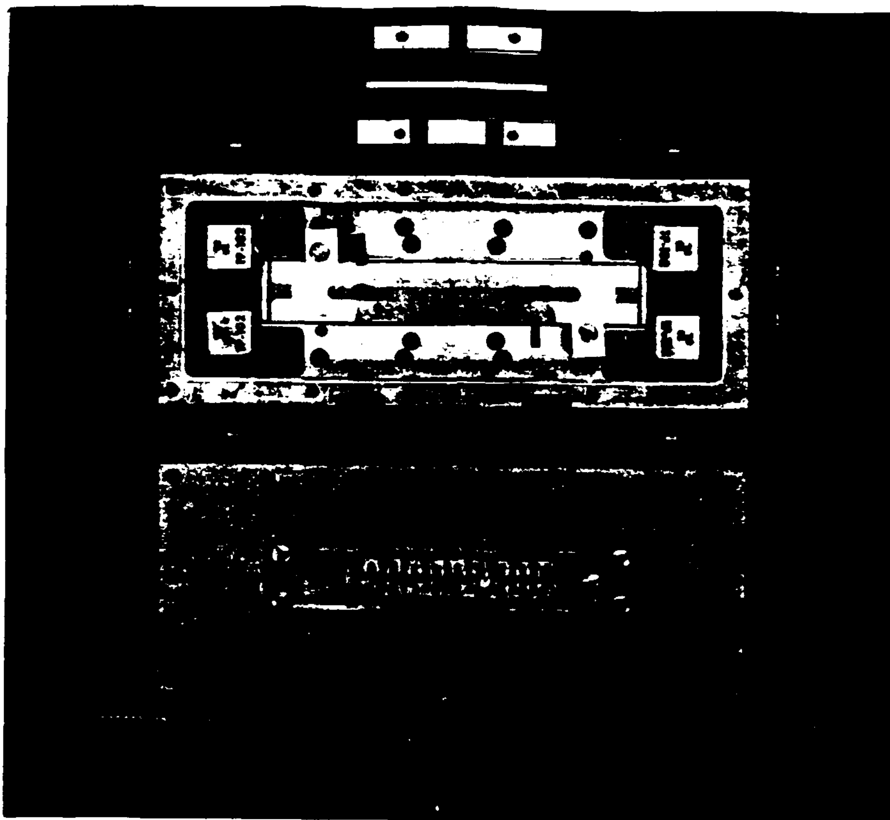

Figure 2-4. Piece Parts for an Acoustoelectric Signal Processing Device

More recently, interest has been directed at the potential of employing acoustoelectric interactions for the nondestructive evaluation (NDE) of semiconductor materials and diode arrays. It is the evaluation and read out of infrared detector arrays which the remaining discussion herein will address.

Three particular nonlinear interactions in piezoelectric/diode array structures appear to have the most hope of meeting program requirements for measurement of individual diode parameters such as R_0C_d. The three alternatives include: 1) convolution interactions in detector materials and diodes, 2) the readout of stored charge patterns in IR diode arrays, and 3) an acoustically generated rf probe of IR diodes. The material or diode parameters which each might best measure are summarized in Table 2-1.

2.3 ACOUSTOELECTRIC CURRENT/VOLTAGE

The space-charge-coupled interaction of a surface acoustic wave in a piezoelectric material with a semiconductor surface placed in proximity to its surface gives rise to SAW attenuation. This attenuation is related to the distance to the semiconductor surface and its conductivity. Relative change in semiconductor surface potential or carrier density can be measured using this attenuation data. Models exist which predict this attenuation for bulk semiconductors as well as semiconductors with depleted surfaces. In general, this attenuation increases with frequency, going approximately as the square of the increase in frequency. The mobility of carriers in a semiconductor layer can be determined by measuring the acoustoelectric current (or voltage) which accompanies the interaction between the carriers and piezoelectric surface waves.[3] This measurement is direct, not needing the carrier density to find the mobility. By using sufficiently high frequency

Table 2-1. SAW Alternatives

Parameter	Techniques		
	Convolution	**Charge Readout**	**High Freq. Probe**
SAW Freq. (MHz)	30 to 70	30 to 70	150 to 300
Gap Height (μm)	~1	~1	3 to 20
Measured Parameters	μ, Nd	Spectral Sens. R_oC_d	Spectral Sens. R_oC_d
Output Power to kTB (dB)	>60	>40	>20
Signal Processing Required	No	Desirable	Yes
Signal Resolution (μm)	150 to 300	150 to 300	35 to 100
Line Scan	Yes	Yes	Yes

*Potentially large S/N ratios would allow resolution to be improved with signal processing techniques.

SAW waves, the effects of surface states on mobility measurements can be made negligible. For these two reasons, such surface mobility measurements have distinct advantages over the usual field-effect method.

However, measurements which provide high spatial resolution are difficult with this technique. The output signal is the result of AE interactions over the length of the SAW signal. When the SAW is pulsed to produce short interactions, the output appears as a small dipole in a large conductive plate, the IR semiconductor wafer in this case. This causes a severe shorting effect on the signal, producing significantly smaller output signals. For these reasons measurement of AE attenuation and longitudinal AE currents and voltages is not considered a viable technique for the evaluation of IR detector materials and detector arrays at moderate to high resolutions.

2.4 CONVOLVER INTERACTIONS

Convolution interactions have the advantage of providing large output signals (to -30 dBm) which are spectrally separated from the two input frequencies; the output frequency is equal to the sum of the two input frequencies. These interactions produce an output signal which is perpendicular to the plane of the semiconductor. This allows the output parasitics associated with the conducting surface of the semiconductor to be localized. However, for this interaction the output signals which emerge are mostly dependent upon the mobility (μ) and density (N_d) of the charge carriers in the semiconductor.

Convolver interactions are depicted in Figure 2-5. Two counterpropagating SAW waves having potentials ϕ_1 and ϕ_2 are introduced on the piezoelectric substrate. These potentials

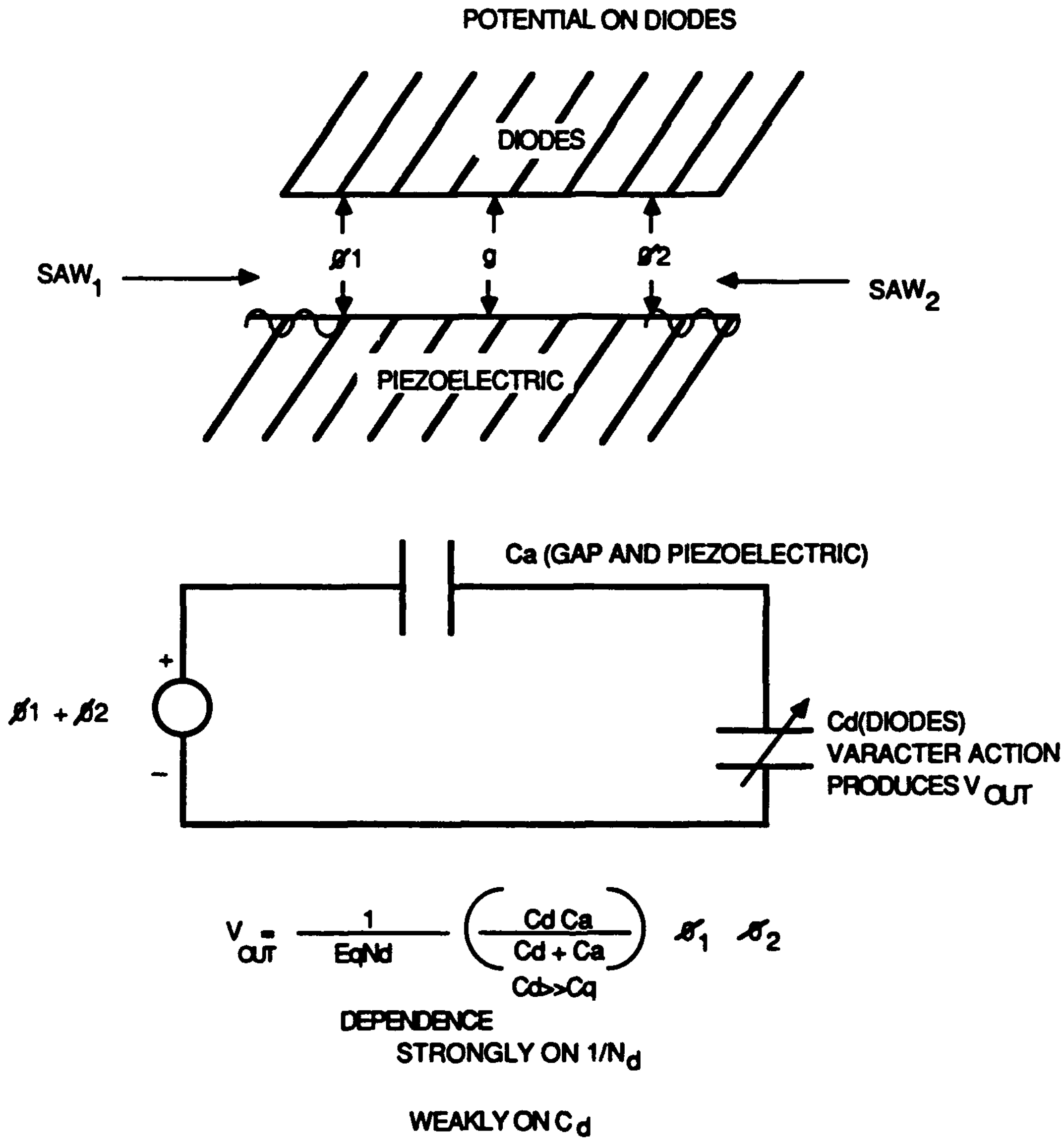

Figure 2-5. Convolver Interaction

are impressed across the series capacitance (C_a) associated with the gap spacing and the insulating piezoelectric substrate as well as the depletion capacitance (C_d) associated with the diodes in the detector array. The varactor action of the diodes produces a voltage across the diodes which is proportional to the product of the two SAW potentials as given by:

$$V_{out} = 1/\epsilon_q N_d \, [C_d \, C_a/C_d + C_a)] \phi_1 \phi_2 \qquad (1)$$

Since the capacitance C_a associated with the gap and piezoelectric is much smaller than the depletion capacitance C_d, the output potential is only weakly dependent upon the carrier density N_d. Hence, AE convolver interactions can provide a sensitive, contactless measurement of the surface doping profile in semiconductors.

2.5 STORED CHARGE INTERACTIONS

In the proposed charge readout process, the diodes are first charged via an acoustoelectric interaction. The duration, or lifetime, of the stored charge pattern in the diode array depends upon the RC time constant of the diode. The resultant charge pattern is then read out via multiple acoustic-read interactions. The output signal appears at the same center frequency as the acoustic read signal, and hence, acoustic read spurious can be a potential problem. In addition, since this process involves two nonlinearities, charge storage and read, it is inherently less efficient than the convolution process.

Charging and readout of stored charge in an IR diode array is depicted in Figure 2-6. First, a large signal is applied to the SAW transducers to generate a SAW wave of sufficient amplitude tc :lightly forward bias the diodes. This introduces a small amount of stored charge across the depletion capacitance of the diode. After the large amplitude SAW wave is removed, the diodes remain slightly reversed biased (i.e., several mVs). A small-amplitude, short-duration read SAW is then introduced onto the piezoelectric substrate. The read SAW provides an output signal proportional to the amplitude of the stored charge pattern in the diode array. Without additional signal processing, the spatial resolution is determined by the duration of the read SAW. With signal processing techniques the resolution of the readout process can be significantly greater than the duration of the SAW read pulse. With multiple read signals the decay constant of the stored charge pattern can be directly observed. This provides a contactless measurement of the time constant R_oC_d.

Both the resistance R and depletion capacitance C_d of the diode are highly nonlinear and depend upon the amount of stored charge (or correspondingly the potential V_d) across the diode. For moderate amounts of stored charge, and hence, small (<2 mV) diode potentials, the diode resistance approaches its unbiased value R_o. Since values for C_d are fairly well known, acoustic measurement of the stored charge decay rate for small V_d provides an indirect measure of Ro.

A signific ant improvement in the signal output levels can be obtained by modulating the stored charge with a spatial k pattern.[12] This can be provided by shining light through a grating pattern positioned over the back side of the semiconductor array. The light can be used to either selectively introduce charge into particular diodes or to discharge diodes which have been acoustically precharged.

2.6 SAW RF PROBE

During the exploration of various SAW measurement alternatives, a new SAW measurement concept was developed. This concept utilizes an interaction between two large amplitude SAW waves to generate a spatially uniform rf field at the surface of a weakly nonlinear piezoelectric as depicted in Figure 2-7d.

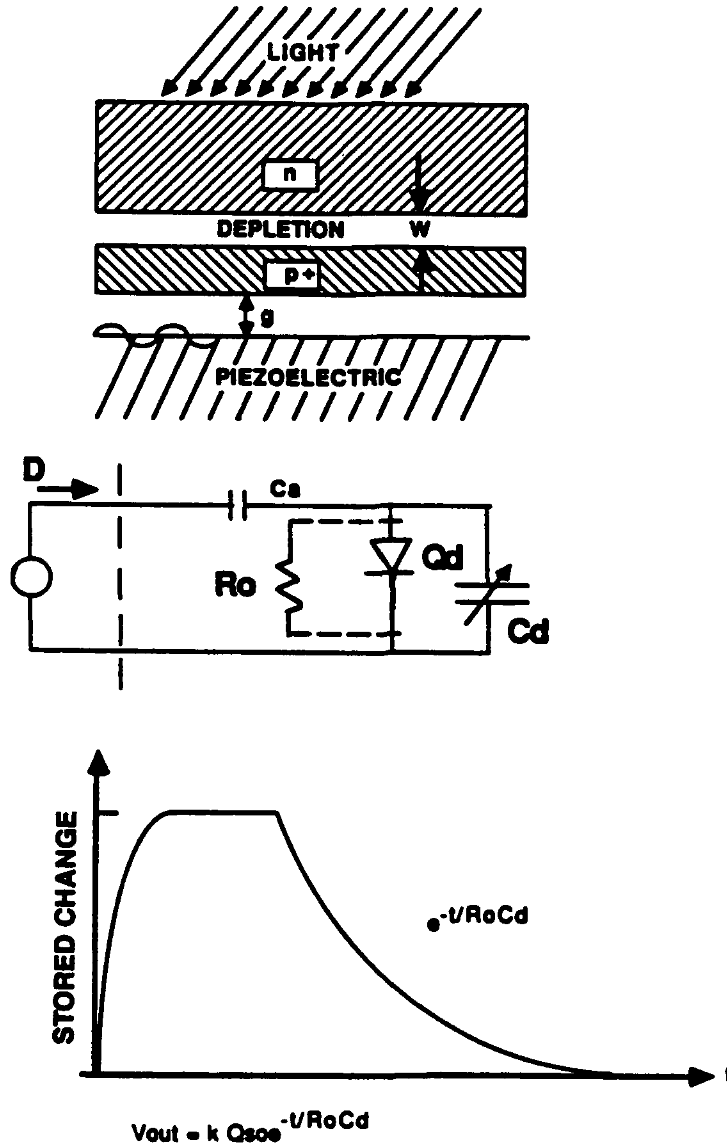

Figure 2-6. Diode Charging/Readout

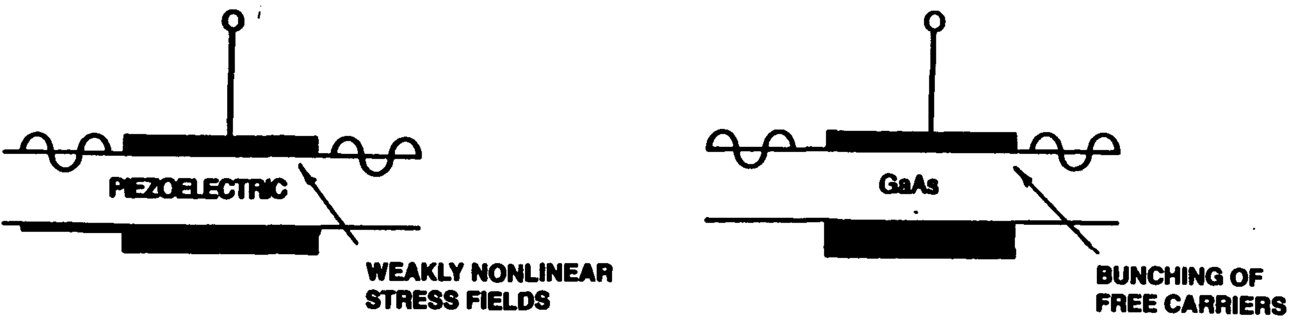

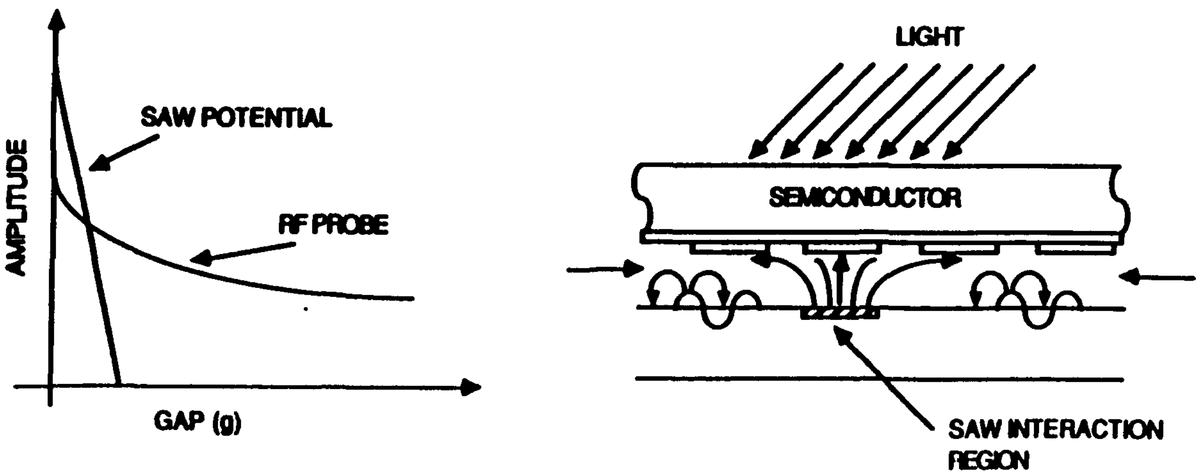

Figure 2-7. SAW RF Probe

During the early seventies structures employing this type of interaction were developed to produce wideband convolvers on lithium niobate substrates. In this case, however, a metal plate was deposited on the surface of the substrate to collect the local signal produced by the nonlinear interaction between a reference and signal SAW as depicted in Figure 2-7a. To increase device efficiency the magnitude of the nonlinear interaction was enhanced by compressing the SAWs into very narrow apertures and guiding the beam compressed SAWS with some type of $\Delta V/V$ waveguide.

More recently, weakly piezoelectric GaAs has been employed to realize highly efficient signal processing devices. While the stress-induced nonlinearities of insulating piezoelectric substrates, such as lithium niobate, are very weak, the free electrons in semiconductor piezoelectric provide much stronger nonlinearities as depicted in Figure 2-7b. Such devices can provide moderate rf probe fields with considerably smaller SAW input signals.

In the proposed measurement technique, the depletion capacitance would be locally modulated by placing a small dc charge across the diode terminals. This dc charge would be introduced on the diodes by acoustic or optical interactions. The rf fields generated by this interaction would be employed to place a small rf potential across the depletion capacitance of individual detector diodes.

The resultant rf current flowing through the series combination of depletion Cd gap and piezoelectric capacitances Ca would be measured by placing a sense electrode on the bottom surface of the piezoelectric substrate. With multiple SAW pulses, the local discharge of the Cd can be measured.

SECTION 3
PHYSICAL STRUCTURES

3.1 GAP TECHNOLOGY

Most of the energy in a SAW is carried by the mechanical wave. Nominally 1% or less of the energy is carried by the electrical fields associated with the SAW. Because the electrical field associated with the SAW varies rapidly in the direction of propagation, the strength of the piezoelectric field falls rapidly with distance from the surface of the piezoelectric. The distance at which reasonable electrical coupling to the SAW can be obtained is somewhat frequency dependent, being somewhat larger at low frequencies (i.e., 10 to 50 MHz). In general, this spacing is limited to distances of about 1 μm. With spacings of this magnitude the IR detector material and arrays to be evaluated must have fairly uniform surfaces and be free of particulate contamination to carry out acoustoelectric evaluation with reasonable sensitivity and resolution.

Gap-coupled signal processing devices utilizing SAWs have undergone extensive development during the seventies. This highly-developed technology includes support, waveguiding, and packaging structures for the establishment, maintenance and stabilization of uniform air gaps.[10] Similarly, techniques have been developed for the cleaning and handling of piezoelectric crystals and semiconductors prior to their assembly in gap-coupled structures. This technology is available and can be utilized on to implement similar configurations for the AE evaluation of IR detector arrays and materials.

3.2 WAVEGUIDING

The energy in elastic surface waves can be concentrated in a lateral direction by means of a guiding structure placed on the substrate surface.[7-8] The simplest structures consist of either overlaid strips or raised ridges extending along the direction of propagation. In the overlay type of elastic waveguide, guiding results from the use of a strip of material having a characteristic shear velocity lower than the Rayleigh velocity of a free substrate surface. Thus modes of propagation arise, because of a decreased local phase velocity, which are confined to the region of the overlaid strip and which have a phase velocity less than the Rayleigh velocity of the substrate, and thus, do not radiate either bulk waves into the substrate or Rayleigh waves laterally onto the free surface beyond the overlaid region.

When the thickness of the overlaid strip is much less than the characteristic wavelengths, the propagation behavior of the dominant waveguide modes can be determined by a perturbation analysis; this analysis gives rise to results which agree well with experiments on thin strips. Since the acoustic wave propagates in media having slightly different phase velocities, the waveguides are somewhat dispersive. This is often not a problem, and in particular for this application, since we hope to employ fairly short pulse widths to interact with only several diodes at one time.

Thin metal film overlays are often employed as waveguiding structures on piezoelectric substrates.[7] However, the metal shorts out the piezoelectric fields associated with the SAW and cannot be employed for the type of interactions desired herein. An alternative approach is to employ thin dielectric overlays, such as zinc oxide or silicon nitride.

Implantation of ions in piezoelectric substrates induces a change in the SAW velocity as a consequence of modification of the crystalline structure of the substrate. In quartz for example, an increase of velocity is produced by ion implantation. For lithium niobate a decrease of velocity is induced by ion bombardment.

Table 3-1. Ion Implanted Waveguides on $LiNbO_3$*

	Guide #1	Guide #2
Dopant (4Het/cm2) at 100 keV	6×10^{15}	1.5×10^{16}
Frequency (MHz)	150	150
Bandwidth (MHz)	11	11
Beam Compression	Horns	Horns
ΔV/V	1%	1.36%
Guide Widths (μm)	60 ($2.6\lambda_R$) 80 ($3.5\lambda_R$) 14 ($5\lambda_R$)	50 ($2.2\lambda_R$) 66 ($2.9\lambda_R$) 88 ($8.8\lambda_R$)
Guide Length	21 mm	21 mm
Delay Line Loss (db)	10.5	10.5

*P. Harteman, et al, Thomson CSF

A group at Thomson-CSF have achieved SAW guides with excellent characteristics by ion planting a narrow channel,[9] (slow region) on the surface of a lithium niobate substrate. The characteristics of these waveguides are summarized in Table 3-1. A horn pattern was used to compress the acoustic energy from a 186 μm transducer aperture into the nominal guide width. Acoustic power distribution profiles were determined with a laser probe for different distances from the input transducer, the diameter of the focused laser spot being about 10 μm for good resolution. Typical results indicated that with a nominal 80 μm wide channel, at a center frequency of 150 MHz 90% of the acoustic energy was concentrated within a 120-μm width. With the guide the insertion loss of the delay line was 10.5 dB; without the guide the insertion loss increased to about 17 dB due to diffraction effects.

The in-diffusion of metals (Ti, Ni, and Cr) into lithium niobate produces an increase in the SAW velocity with no additional loss. Metallic in-diffusion offers the possibility of fabricating SAW guides by making the regions just outside of the intended guide have a larger propagation velocity than the undiffused region. Such guides have been realized with widths of 2, 3, 4, 6, and 8 Rayleigh wavelengths (λ_R) by indiffusion of titanium films.[10] Experimental data on these waveguides is summarized in Table 3-2.

A mechanical support for maintaining a uniform, stable air gap has been developed[6] for AE convolvers and other AE signal processing devices. In this structure, space rails are formed by ion beam milling the surface of the lithium niobate delay line. The semiconductor is pressed

Table 3-2. Waveguides on $LiNbO_3$ Formed by Titanium In-Diffusion*

Parameter	Value
Frequency	240 MHz
No. Finger Pairs	20.5
Beam Compression	None
ΔV/V	1.5%
Guide Widths	2, 3, 4, 6 & 8 λ_R
Propagation Loss	0.5 dB/cm
Path Length	1.5 mm
Delay Line Loss	≈20 dB

*J.F. Weller, et al; Naval Research Laboratory

firmly against the rails and held in position by a spring pressure assembly as sketched in Figure 3-1. The presence of the semiconductor resting on the support rails stiffens the structure, resulting in higher propagation velocities under the rails. Therefore, the acoustic wave prefers the slower-wave region between the support rails. In this manner, the rails establish well-defined waveguide modes which can propagate with minimal loss. However, the excitation of several modes by the incident acoustic beam can introduce amplitude ripple in the frequency response of the devices. By carefully choosing the location and spacing of the rails in the acoustic beam path, waveguide moding effects and acoustic scattering losses were reduced to negligible levels (< 1 dB).[11]

Experimental results on the use of these support rails is summarized in Table 3-3. Theoretical calculations indicate that such structures would support a well-defined acoustic mode at rail spacings of 3 to 4 Rayleigh wavelengths (λ_R). However, experimental rail structures manufactured to the present time have supported one or more acoustic modes when the rail spacing was about $8\lambda_R$ or larger. When the rail spacing was reduced to 4 λ_R substantial acoustic energy leaked from the guide. Therefore, support rails can provide both mechanical support and the acoustic guiding for moderate waveguide widths. When both narrow waveguides and mechanical support required a combination of two structures (i.e., rails and diffused waveguides) may be required.

3.3 FILLING FACTOR LOSS

The simplest way to perform moderate resolution convolution (or charge readout) measurements via an acoustoelectric interaction is to insert a short rf pulse, the scanning pulse, at one end of a gap-coupled SAW delay line, and a long pulse at the other end of the delay line as depicted in Figure 3-2. The magnitude of the convolution output as a function of time corresponds to the density and mobility of the carriers in the particular region of the semiconductor where the AE interaction is taking place.

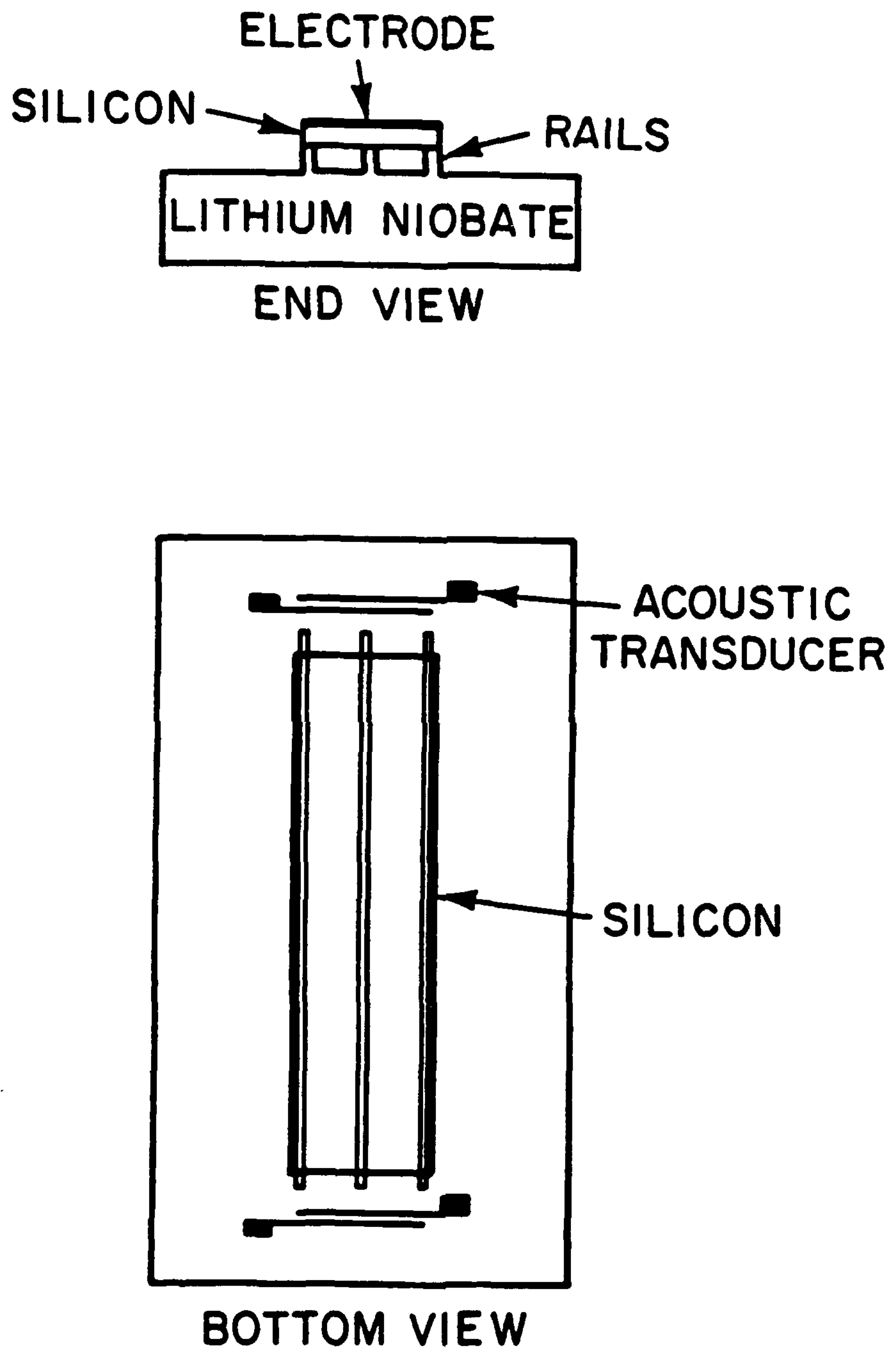

Figure 3-1. Rail Support Structure for Establishing and Maintaining a Uniform Air Gap in Acoustoelectric Devices

Table 3-3. Waveguides on $LiNbO_3$ Formed by Narrow Support Rails

Frequency		300 MHz	
Wavelength		11.7 μm	
Guide Length		35 mm	
Rail Spacing (λ_R)	**Rail Width (λ_R)**	**Excess Loss (dB)**	**Amplitude Ripple (dB)**
31.7	0.34	<1.0	<1.0
12.7	0.34	1.5	<3.0
8.8	0.17	2.0	<2.0
8.8	0.56	4.7	<2.0
4.4*	0.17	22	4 to 9

*Acoustic beam was not guided in this structure

One inherent limitation of this technique is that the scan pulse must be short in order to obtain adequate resolution. Yet, the inactive portion of the detector array capacitively loads the desired output. The reduction in output power is given by

$$P_r = P_o - 20 \log T/W, \quad (2)$$

Where T is the total length of the semiconductor region being electrically scanned and W is the length of the short or scanning pulse. Since it is difficult to obtain dynamic ranges (maximum output power over the thermal noise floor or spurious level, whichever is the largest) of more than 40 to 60 dB, this technique is unlikely to obtain resolution greater than about 0.01 T without signal processing. In addition to signal processing techniques to improve the inherent resolution, an alternative approach is to employ multiple sense planes to intercept the desired signal in more localized regions of the semiconductor. This approach will be discussed in the next section.

3.4 SENSE/GROUND PLATES

Two output terminals must be provided for an AE measurement. In the case of AE signal processing components, the usual technique was to provide a ground plate on the bottom or adjacent top surface of the piezoelectric substrate. The second output adjacent lead (carrying the rf signals in this case) consisted of an ohmic contact to the back surface of the semiconductor. To minimize capacitive loading, the semiconductor was diced into narrow strips and packaged so as to be at a sufficient distance from the sides of the metal package. This type of output circuit configuration is not the optimum structure for the evaluation of IR detector arrays.

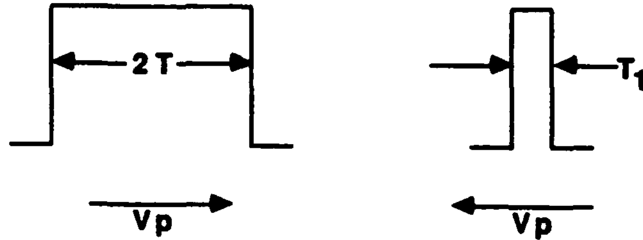

TIME RESOLUTION	T_1
SPATIAL RESOLUTION(Ro)	Vp/T
INPUT BANDWIDTH (BW)	$1/T_1$

EXAMPLE FOR $LiNbO_3$

Vp	~3400 m/sec
B	~10 MHz
R_o	~340μm

POTENTIAL RESOLUTION WITH SIGNAL PROCESSING

$$\approx \frac{Vp/T_1}{\sqrt{S/N}}$$

A S/N RATIO OF 20 dB GIVES A RESOLTION ~35μm

Figure 3-2. Short Pulse/Long Pulse Convolution

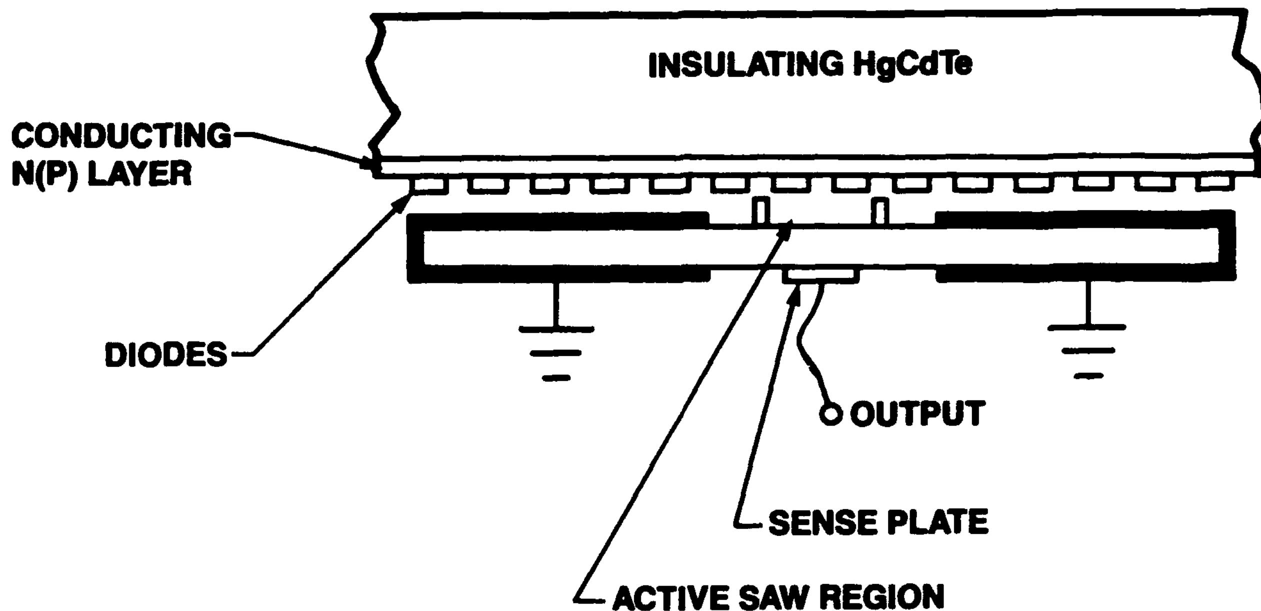

Figure 3-3. Electrical Output/Ground Connections

For the evaluation of IR detector arrays it is very desirable to test whole wafers before dicing. Also, for the evaluation of IR detector materials, entire wafers must be examined. The second constraint is that the IR detector arrays are often fabricated on semi-insulating wafers; this makes it impossible to place a conducting contact on the back side of the wafer. The capacitance across depth of the wafer is probably too small to provide reasonable output signals.

The first epilayer which is deposited on the IR wafers is common to all of the contacts on one side of the detector diodes, as depicted in Figure 3-3. This allows one to envision the placement of a large ground plate on the top surface of the piezoelectric substrate. Field lines between this ground plate and many inactive diodes on the wafer would provide a low impedance ground path through their depletion capacitance to the back contact of the diodes which are being probed by the SAW. Sense plates for sampling the rf potential on the front contact of selected IR diodes can be realized by fabricating metal patterns on the reverse side of the piezoelectric substrates. The filling factor loss can be dramatically reduced by utilizing multiple sense plates which divide the diodes in a particular line scan into multiple sections.

3.5 PHYSICAL DESIGNS

Separate physical designs were explored for the three alternative AE evaluation techniques. These are summarized in Table 3-4.

3.5.1 Convolver Structure

An example of a piezoelectric plate design which could be employed for convolver type measurements is shown in Figure 3-4. Here the acoustic beam generated by the interdigital fingers is divided into multiple channels and guided by silicon monoxide (SiO) rails which have been

Table 3-4. Physical Parameters for AE Measurement Alternatives

	Convolver	Stored Charge	RF Probe Piezoelectric	RF Probe GaAs
Center Freq. (fo)	70 MHz	70 MHz	150 MHz	360 MHz
Wavelength	50 μm	50 μm	24 μm	8 μm
Bandwidth (B)	25 MHz	25 MHz	40 MHz	40 MHz
Transducer Aperture	32	30	60	60
Beam Compression Ratio	None	10	15	5
Acoustic Channels				
Number	4	1	1	1
Guide	Rails	Ion Implant	Ion Implant	Dielectric Overlay
Width	4 /200 μm	3 /150 μm	4 /100 μm	12 /100 μm
Length	1 cm	0.54 cm	0.48 cm	
Gap Height (g)	1 μm	1 μm	5 μm	5 μm
Substrate Thickness (d)	0.5 mm	0.5 mm	0.5 mm	<0.5 mm
Sense Plates				
No.	4/parallel	6/series	8/series	8/series
Length	8 mm	0.9 mm	0.6 mm	

deposited on the the surface of the piezoelectric substrate. Because of the relative high efficiency of convolver interactions in semiconductors, there is no significant reason to concentrate all the acoustic energy into one narrow channel.

More significant considerations are obtaining adequate transverse resolution and reducing filling factor loss. These particular problems can be handled by placing narrow sense plates under each of the acoustic channels. Since the sense plates are electrically isolated, each channel can be read out independently without loading the adjacent channel. Resolution in the longitudinal direction can be obtained by utilizing long pulse/short pulse interactions.

The composite structure for evaluating IR semiconductor materials and IR diode arrays via convolver interactions is sketched in Figure 3-5. The height of the air gap is fixed by the silicon monoxide support rails. The uniform air gap is maintained by applying uniform spring pressure to the back surface of the semiconductor.

Transverse spatial resolution of the measurement is set by the spacing between the support rails which must be at least 4 SAW wavelengths. Figure 3-5 depicts SAW operation at about 70 MHz where the corresponding SAW wavelength is about 50 μm. This would provide a transverse resolution of 40 ns (i.e. ~ 120 μm). AE convolvers have been successfully realized at center frequencies to 500 MHz. Operation at this frequency would provide a transverse resolution of about 30 μm.

Longitudinal spatial resolution of the measurement is set by duration of the short pulse. For example, pulses of duration 40 ns (i.e. ~ 120 μm) would be accommodated by device bandwidths of 25 MHz. In this example it corresponds to a fractional SAW bandwidth of 25%, which is

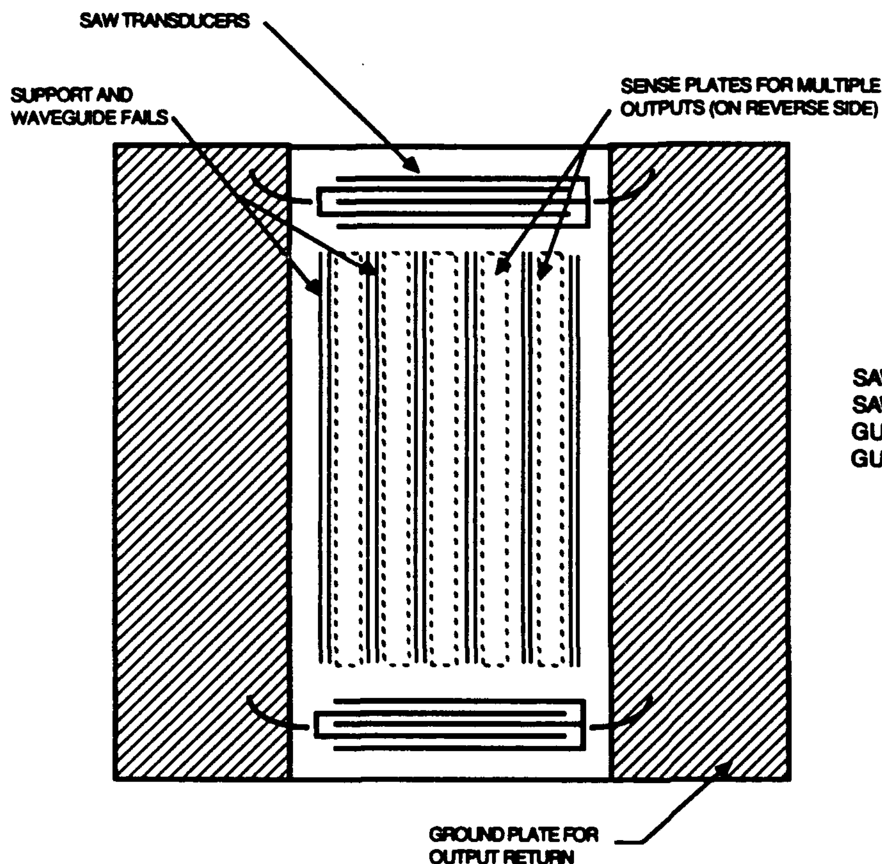

Figure 3-4. Piezoelectric Plate for Convolver Measurement

readily obtainable with lithium niobate delay lines. As in the case for the transverse resolution, increasing the SAW center frequency would result in a corresponding increase in longitudinal resolution.

3.5.2 Proposed Configuration for Stored Charge Readout

The piezoelectric substrate configuration proposed for the readout of stored charge in IR detector arrays is sketched in Figure 3-6. The structure employs a diffused waveguide for compressing the acoustic beam and guiding the SAW.

Multiple sense plates are employed along the length of the SAW guide to segment diodes being probed by a particular pulse into groups. This would significantly reduce the filling factor loss associated with capacitive loading by inactive diodes without generating the need for mechanical stepping in two directions. The need for further segmentation of the line scan is generated by the requirement that the potential induced across the diodes must be limited to several mV to provide a reasonable measure of R_o.

The composite configuration to be employed is similar to the one sketched in Figure 3-7. This particular structure was developed to process return waveforms from a radar system. This device coherently overlays multiple returns from a radar target as stored charge in a silicon diode array. The stored charge is then read out with a sense SAW.

3.5.3 Physical Configurations for SAW rf Probe

In this proposed measurement, nonlinearities in insulating or semiconductor piezoelectric substrates would be employed to generate uniform rf fields in a localized region of the substrate. These rf fields would be employed to measure the decay constant associated with individual

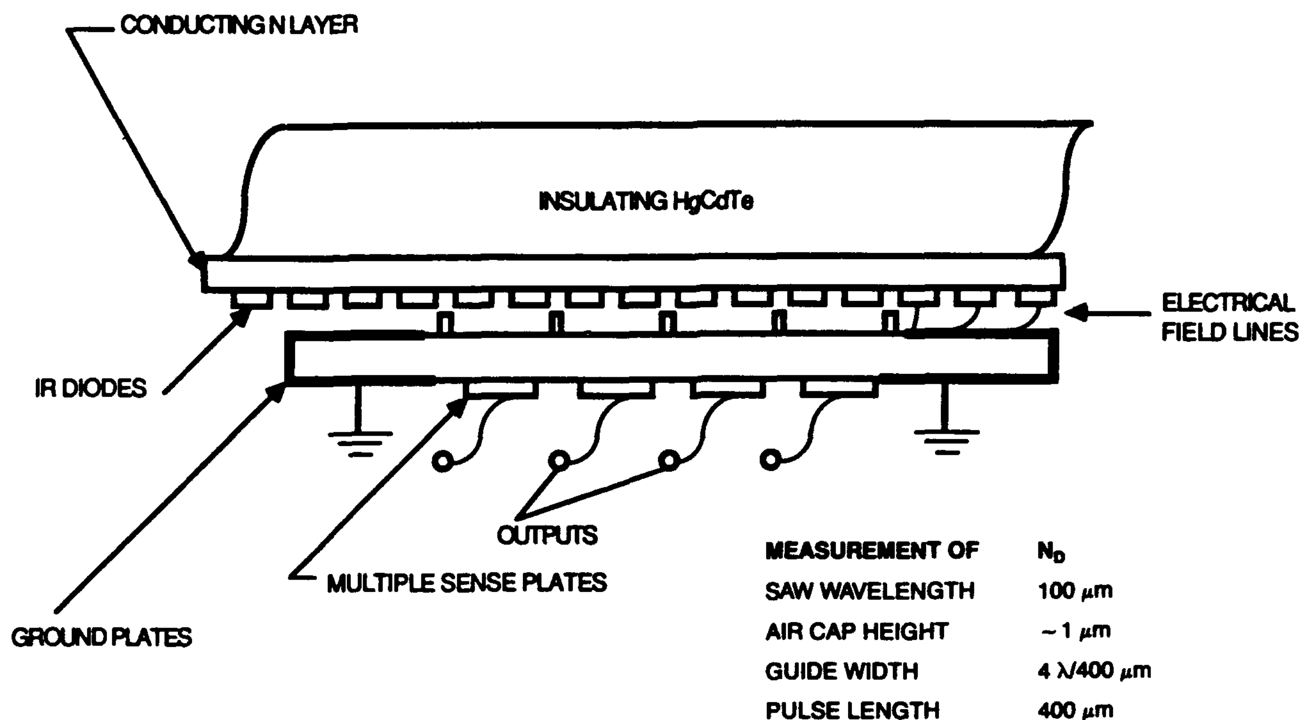

Figure 3-5. Composite Convolver Structure (End View)

diodes in an IR detector array. The location of the SAW-generated rf field can be rapidly stepped by changing the relative timing between the SAW pulses generated at opposite ends of the SAW substrate.

In comparison with the configuration for stored charge readout depicted in Figure 3-6, the gap spacing would be increased to 3 to 10 μm so that the SAW nonlinearities in the piezoelectric would dominate over those associated with the IR semiconductor. To provide rf fields of adequate strength, the applied acoustic energy must be increased and the beam compressed into relatively narrow acoustic beam widths. The sense plate would also be segmented in the longitudinal direction to reduce the filling factor loss.

Insulating piezoelectric substrates such as lithium niobate, with their inherently large electromechanical coupling constants, can provide delay lines with very large fractional bandwidths. However, the mechanical nonlinearities associated with the propagating SAW are weak. For piezoelectric GaAs substrates, on the other hand, the dominant nonlinearity is associated with the bunching of free electrons. This nonlinearity is about two orders of magnitude larger than the nonlinearity associated with lithium niobate. Hence, with GaAs substrates, less acoustic drive power or less beam compression is required to generate the same level of rf field.

A two-channel configuration for the GaAs substrate for a SAW rf probe is depicted in Figure 3-8. Shown is a semi-insulating GaAs substrate with local regions converted into a semiconductor by ion implantation. With this technique the acoustoelectric losses under the transducer and horn region of the substrate will be minimum. In regions such as under the diode array, where we desire strong nonlinear interactions, the ion implanted areas supply the free electrons. At the same time, the ion implanted region will supply the conducting sense plates for measurement of the rf current. With

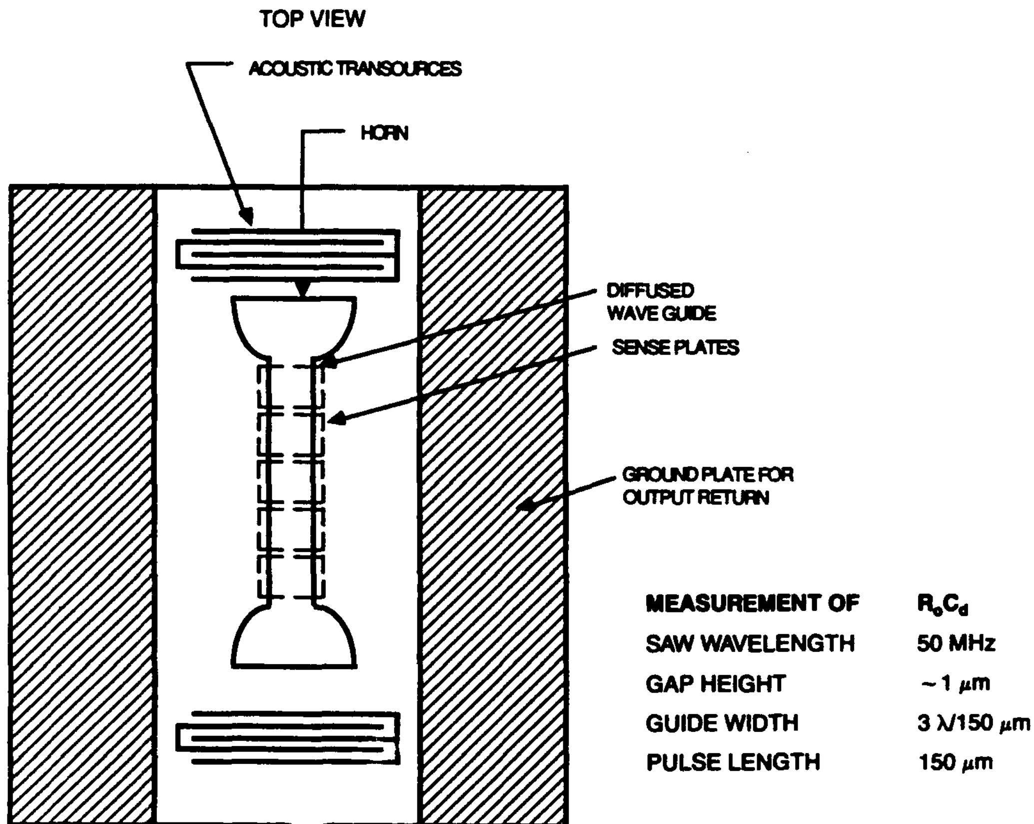

Figure 3-6. Piezoelectric Substrate for Stored Charge Readout

the remainder of the substrate remaining semi-insulating, parasitic capacitances which would reduce the output signal are minimized. The sensed rf output current will vary with the depletion capacitance, which is a function of the stored charge, of the individual diodes being probed. By observing the rf current over multiple read scans the time constant R_0C_d is determined.

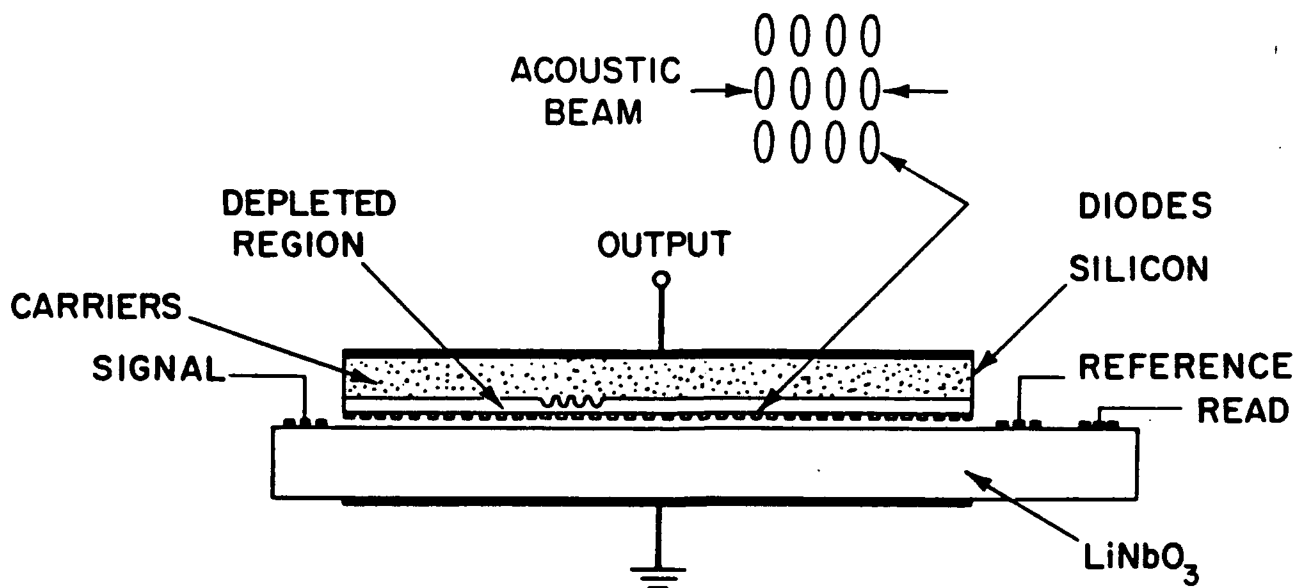

Figure 3-7. Composite Convolver Structure

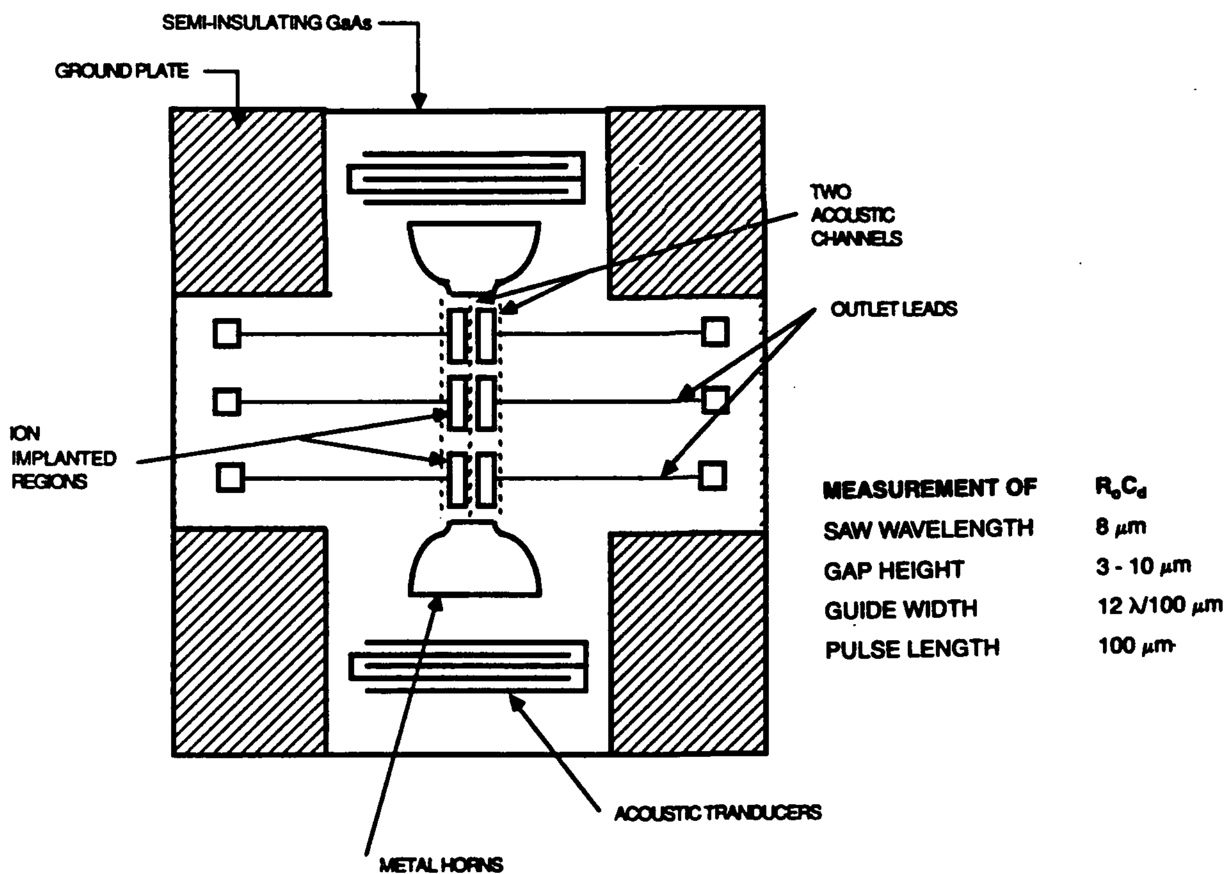

Figure 3-8. GaAs Substrate for RF Probe

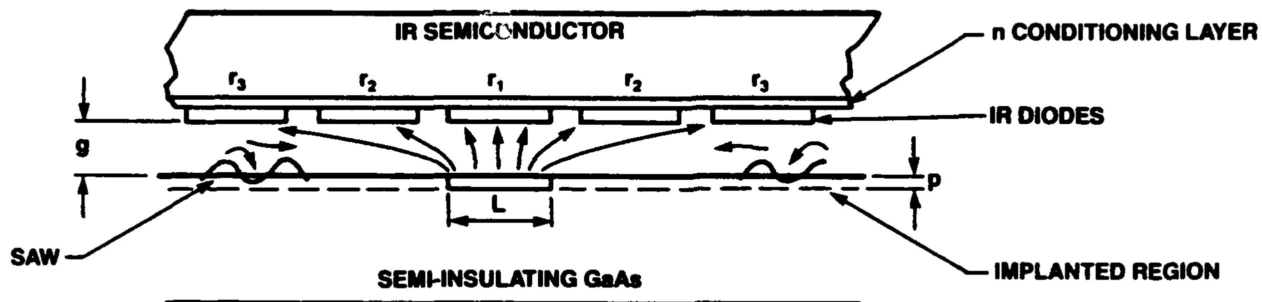

Normalized Displacement Field (Appendix V)

$$D = \int_0^\infty x\, e^{-x2/2}\, \frac{Jo(r_x x)}{G_s(g_n x, d_n x, p_n x)}\, dx$$

Figure 3-9. Modeling of SAW RF Probe Interactions

SECTION 4
MODELS

4.1 SAW FIELD

The generation of the SAW field on piezoelectric substrates is discussed and analyzed in Appendix I. High quality piezoelectric substrates, such as quartz and lithium niobate, provide low loss low dispersion propagation of SAW waves. Most of the energy of a propagating SAW is carried by the mechanical portion of the wave. However, with input powers of +20 dB, the electrical potential on the surface of the SAW plate can readily reach several volts. Such electrical potentials are more than adequate for any of the SAW measurement techniques which we explored for the evaluation of IR detector materials in diodes.

4.2 COUPLING FROM SAW TO ADJACENT DIODE ARRAY

The coupling between the propagating SAW and diode array is theoretically explored in Appendix II. Because the SAW field is rapidly varying in the direction of propagation, the strength of field falls rapidly with distance from the surface of the piezoelectric substrate.

4.3 DIODE ARRAY AS A SAW CONVOLVER/STORAGE CORRELATOR

Acoustoelectric interactions between two counter-propagating SAWS and the resultant convolver output are theoretically examined in Appendix II. Also examined in this appendix are AE interactions between a propagating SAW and stored charge in an adjacent diode array.

4.4 DIODE CHARGING DYNAMICS

The generation of stored charge patterns in an IR diode array are theoretically examined in Appendix IV.

4.5 GENERATION OF PROBE FIELD

Theoretical results on the generation of an rf probe field by two interacting SAWs is provided in Appendix V. The results show that the rf probe field drops moderately over the first few μm of distance from the surface of the piezoelecric but then falls very slowly over significantly larger spacings. Indications are that spacings of 3 to 20 μm would provide adequate potential for the evaluation of individual diodes.

SECTION 5
SIGNAL PROCESSING CONSIDERATIONS

5.1 SIGNAL-TO-NOISE REQUIREMENTS

We have described several characterization measurements which might be utilized to examine properties of HgCdTe diode arrays in various stages of fabrication. In this section we consider the accuracy of these measurements. For this discussion it is appropriate to let the quantity measured be called "x" since the signal-processing aspects do not depend upon whether we are measuring carrier density or diode capacitance. In any case we shall determine that some electrical output signal is proportional to the quantity x of interest. We may thus write

$$V_{out} = K_x \tag{3}$$

where K is the appropriate proportionality constant. It will normally be required to assume that x deviates by only a small amount relative to some average value to guarantee linearity in the measurement. Thus, in measuring the diode capacitance through an air gap, x includes a "delta C over C" parameter which relates a change in output voltage to a relative change in diode capacitance.

Invariably there is an output voltage fluctuation due to thermal noise; this causes measurements to be inaccurate at some level. Since the output signal voltage is proportional to the parameter to be measured, the thermal noise is equivalent to a fluctuation in the desired quantity. To measure a quantity accurately, it must be true that the output signal voltage is large compared to the thermal fluctuating voltage. The accuracy of the measurement is approximately the reciprocal of the signal-to-noise ratio (SNR). For example, a 5% accuracy requires 30 dB SNR. If a convolution measurement were used to measure the uniformity in doping level of a wafer, then the convolution voltage at the output must be 30 dB above the thermal noise floor.

5.2 BASIC MEASUREMENT

While the convolution measurement is estimated to directly provide SNRs that enable accurate measurements to be performed, the charge-readout and rf probe measurements generally will not be strong enough. The analysis of interactions carried out under this contract has resulted in an estimate for the SNR of the readout signal of +40 dB. This estimate includes a 20 dB filling factor loss which corresponds to the situation when 1 out of 10 elements in a line array are being instantaneously probed.

5.3 SIGNAL-TO-NOISE IMPROVEMENT

There are several means for increasing SNR when the basic measurement does not provide sufficient accuracy. Two are considered here: one for enhancing the SNR during a readout, the other for averaging successive readouts.

To provide spatial profiles of doping density or diode capacitance, a wideband signal must be used. If the probing signal is a simple pulse, and the output signal is too weak for the desired accuracy, then the probing signal might be replaced by a chirp waveform. Since the peak field in the interaction is limited, use of a chirp produces the same advantage as when it is used in a pulse-recompression radar. When the chirp waveform at the device output is recompressed. the output SNR is increased by the time-bandwidth product (TBP) of the chirp. This occurs because the output is then equivalent to having used a readout pulse TB times larger in peak power than the actual level. For practical measurement systems, a TBP of 20 to 30 dB is feasible.

Another approach to SNR enhancement is to perform the readout repetitively, averaging the results. To avoid excess hardware complexity, this averaging should be carried out noncoherently. In this case, if the initial SNR is small, the SNR is improved by approximately the square root of the number of cycles averaged. This approach is very cost effective compared to the pulse-compression approach since little extra hardware is required. However, since the basic measurement cycle must now be repeated many times, this approach can greatly extend the time required to measure a wafer.

For the strawman systems considered in this study, only averaging was considered because this resulted in very reasonable wafer characterization times (still dominated by mechanical repositioning) with simpler hardware requirements than the chirp-enhanced approach.

5.4 TRANSFORM TECHNIQUES

So far we have discussed the simplest situation - that of a short pulse scan of the stored charge. This is equivalent to scanning a semiconductor with an electron beam of small diameter. In such a device the signal-to-noise (S/N) ratio decreases as the time taken to scan one spot in the image is decreased, i.e., as the definition is increased. We now consider the possibility of using more complicated waveforms of long-time duration (the line time) to scan one line of the image. In this case, if we feed the output into a correctly designed matched filter, as in radar systems, it is possible to obtain a short pulse signal corresponding to a spot in the image, i.e., to take an inverse transform of the scanning signal. As in radar, such matched filter pulse compression techniques give rise to an improvement in the signal-to-noise ratio because any spot in the image is now scanned for the line time rather than the spot time.

As an example, when two linear f-m chirp signals are inserted into opposite ends of the device with frequencies $\omega_\sigma = \omega_1 + at$, $\omega_r = \omega_2 - bt$, respectively; they give rise to two waves with a linear variation of frequency and a square law variation of phase. Using the center of the device as a reference, we find that the phase of the resultant product signal is,

$$\phi(z,t) = (\omega_1 + \omega_2)t + (\omega_2 - \omega_1)\frac{z}{v} + \frac{a}{2}\left(t - \frac{z}{v}\right)^2 - \frac{b}{2}\left(t + \frac{z}{v}\right)^2 \tag{4}$$

With a grating filter with $K = (\omega_1 - \omega_2)/v$, the output signal due to a carrier density variation $n(z)$ along the length of the devices, caused by illumination with light is,

$$F(t) = e^{j(\omega_1 + \omega_2)t} \int n(x) \left[e^{j\frac{a-b}{2}\left(t^2 + \frac{z^2}{v^2}\right)} e^{-j(a+b)\frac{tz}{v}} \right] dz \tag{5}$$

When a = b, the output as a function of time is the spatial Fourier transform of the carrier density, and hence of one line of the illumination. By using an acoustic convolver, matched chirp filter, or a digital processor, and inserting this signal in the proper way, an inverse Fourier transform of the response of the detector array can be obtained.

The Fourier transform technique is merely one example of a wide range of signal processing techniques which can be applied for acoustic nondestructive testing of imager arrays, not only to improve the sensitivity but also the bandwidth and definition.

In the more general case a unequal to b, a Fresnel transform is obtained. In this case, a chirp output with a chirp rate a - b and a bandwidth $B_s = (a - b)T_c/2\pi$ is obtained from one spot at

z_0 in the response of the detector array n(z). The response can be reconstructed by inserting the output signal into a suitable matched filter, match to a chirp with a rate a - b. If the time length of the chirps is T_c, the minimum resolvable spot d_s size is

$$ds = 2 \pi v/(a + b)T_c \quad (6)$$

where v is the propagation velocity of the SAW wave. The effective scan velocity along the detector array becomes

$$v_s = v(a - b)/(a + b) \quad (7)$$

Thus an arbitrary scan velocity can be obtained. The number of resolvable spots is still $N = L_d/d_s$, where L_d is the length of the imager array.

SECTION 6
PROPOSED SAW FOLLOW-ON EFFORT

A detailed conceptual design and procedure for an automated nondestructive "test" facility utilizing piezoelectric acoustic waves can be developed. The goal is to develop a design for a test facility capable of evaluating a 120 x 16 element HgCdTe diode array operating in the medium (5 - 6 μm) and moderately long (8 - 10 μm) spectral region with high throughput and reliability. In general SAW techniques cannot be utilized to measure R_0C_d when the diodes have submicrosecond storage times. Such storage times are common when the wavelength sensitivities of the diode arrays are 12 microns and longer. The design will include sufficient detail to allow fabrication of the test station based solely on the information provided in the design.

A comparison chart of the possible SAW measurement techniques is given in Table 6.1. While SAW/diode interactions have the SAW advantage of providing higher output power levels than the rf probe technique, the requirement for 1-micron gap spacings must be considered a serious drawback. The rf probe concept, on the other hand, has inherently smaller output levels, but has the advantage of operating with much larger (about 10x) gap spacings. This removes considerable stress on the mechanical jigging and on the surface smoothness which must exist on the IR detector wafers which are to be evaluated.

The projected development expense and production cost of the various SAW measurement alternatives is given in Table 6.2. The technology for SAW/diode interactions has undergone considerable development for signal processing applications. Similarly, considerable effort has gone into developing a gap technology for providing uniform, stable gap spacing in signal processing components. However, this technology will require considerable further development to accommodate the need for whole wafer measurements and the requirement for mechanical stepping in one or two dimensions. A more serious constraint is that even after the initial development of the mechanical jigging, the cost per instrument will remain inherently high because of the accuracy to which the gap spacing must be set.

Table 6-1. Comparison of Measurement Techniques

	SAW/DIODE INTERACTIONS		RF PROBE	
	CONVOLVER	STORED CHARGE	PIEZOELECTRIC	GaAs
Center Freq (MHz)	35	70	150	360
SAW Wavelength (μm)	100	50	24	8
Bandwidth (MHz)	> 10	25	> 40	> 40
Beam Compression	NONE	10	20	8
Gap Spacing (μm)	~1	~1	3-10	3-10
Measured Parameters	Nd	RoCd	RoCd	RoCd
Output Amplitude Above KTb(dB)*	> 40	> 20	-20	0
Signal Processing Req.	No	Desirable	Yes	Yes
Potential Resolution(μm)	50-300	150-300	35-100	35-100

* Includes at least a 20 dB filling factor loss associated with capacitive loading of output by inactive diodes. Assumes sectioned output with 100 diodes per line scan.

The rf probe concept, on the other hand, has not been experimentally demonstrated, and therefore the development time will be inherently longer, and perhaps more risky. While considerable signal processing will be required in conjunction with the rf probe, the cost of existing digital signal processing technology will be moderate when one considers the computation rates that are required for this particular application. In the case of the mechanical jigging, the potential problems are alleviated to a considerable extent by the larger gap spacing, but still must be considered nontrivial. The SAW components, in contrast, can be manufactured with moderate cost once the initial development is completed. In addition, with the reduced constraints on the mechanical jigging, the production cost rf probe instrument is expected to be relatively moderate in comparison with electron beam diode testing which require an expensive vacuum and instrument setup. For this reason, MICRILOR recommends the rf probe concept for further development including experimental verification of the modeling results and an instrument design.

Table 6-2. SAWS Measurement Instrument

	SAW/DIODE INTERACTIONS		RF PROBE	
	CONVOLVER	STORED CHARGE	PIEZOELECTRIC	GaAs
Measurement (MHz)	Nd	RoCd	RoCd	RoCd
Sensitivity	GOOD	GOOD	GOOD	GOOD
Component Proximity	~1 μm	~1 μm	3 - 10 μm	3 - 10 μm
Single/Multiple Diodes	MULTIPLE†	MULTIPLE†	SINGLE	SINGLE
Resolution	400 μm	150 μm	100 μm	100 μm
Linescan	YES	YES	YES	YES
Signal Processing Time*	N.A.	20 ms	20 s	0.2 s
Test Speed	HIGH	VERY GOOD	GOOD	GOOD
Production Cost/Inst.**	$300K	$300K	$200K	$200K

* Per line scan of about 100 diodes

** Estimated cost/instrument after initial development effort

† At least three diodes

SECTION 7
CONCLUSION

The results of this study indicate that convolver interactions are the optimum SAW technique for rapid measurement of carrier density variations in IR detector materials. By keeping the carrier frequency relatively low (i.e., ≤ 100 MHz), the gap spacing can be held to 1 μm or perhaps even larger, depending upon the readout efficiency desired. Convolver interactions have inherently large dynamic ranges alleviating any requirement for post signal processing.

Techniques for SAW readout of stored charge in silicon diode arrays have undergone extensive development for imager applications. By reading out the stored charge in IR detector arrays with SAW techniques over multiple scans, the decay time constant R_oC_d can be directly measured. Since the depletion capacitance C_d is fairly well known in these detector arrays, variations in the observed time constant is mostly dependent upon R_o. Knowledge of the diode zero-bias R_o resistance provides a direct indication of detector sensitivity D^*.

Unfortunately, SAW readout of stored charge in detector arrays requires fairly close gap spacings (i.e., ≈ 1 μm) to insure adequate sensitivity. This puts serious constraints on the surface uniformity of the IR detector arrays and the mechanical jigging required. During the investigation of stored charge, a new SAW measurement concept was developed which does not require direct interaction of the rapidly varying SAW fields with the IR diodes.

The new concept, termed SAW rf probe, uses a nonlinear interaction between two counterpropagating SAW waves to generate a short, but spatially uniform rf probe field. This probe field extends out from the surface of the piezoelectric substrate much like the signal from a phase-array antenna. Now the IR diodes can be located 10 to 20 μm from the surface of the piezoelectric substrate and still provide a measurement of the depletion capacitance C_d of individual detector diodes. Since this C_d varies with the amount of stored charge in the diode array, multiple scans provide a measurement of R_oC_d.

The location of the probe field can be stepped by changing the relative timing between the two SAW impulses used to generate the rf probe field. Hence this technique, as in the case of SAW convolver and SAW stored charge readout, can provide rapid line scans for the evaluation of IR detector materials and diodes.

The SAW rf probe concept has been modeled as part of the work described herein, but the models have not been experimentally verified. Because of the significant potential of this technique, this experimental work should be carried out as a follow-on effort.

The SAW techniques described above can provide measurement resolutions of 35 to 100 μm which should be adequate for most IR diode arrays. There is an inherent tradeoff between resolution and sensitivity. However, signal processing techniques, such as coherent overlay of multiple scan pulses, can provide dramatic improvements in readout sensitivity.

SECTION 8
REFERENCES

1. B.A. Auld, "Acoustic Waveguides," Acoustic Fields and Waves in Solids, Vol. II, New York: John Wiley and Sons, 1973, pp. 63-220.
2. A. Bers, "Interactions Between Acoustic Surface Waves and Electrons in Solids," *Invited Proceedings 1970 Ultrasonics Symposium,* New York: IEEE, 1970, pp. 138-172.
3. A. Bers, J.H. Cafarella, and B.E. Burke, "Surface Mobility Measurement Using Acoustic Surface Waves," Appl. Phys. Lett., Vol. 22, No. 8 pp. 399-401, April, 1973.
4. F.J. Leonberger, J.H. Cafarella, R.W. Ralston, E. Stern and A.L. McWhorter, "Acoustoelectrically Scanned Gap-Coupled Si-Diode-Array/$LiNbO_3$ Imaging Devices," *1977 Ultrasonics Symposium* Proc., New York, IEEE, 1977, pp. 456-459.
5. F.J. Leonberger, R.W. Ralston and S.A. Reible, "Gap-Coupled InSb/$LiNbO_3$ Acoustoelectric Convolver Operating at 77 K," Appl. Phys. Lett., Vol. 33, No. 6, pp. 484-486 (1978).
6. S.A. Reible, "Acoustoelectric Convolver Technology for Spread-Spectrum Communications," IEEE Trans. on Microwave Theory and Techniques, Vol. MTT-29, No. 5, 1981, p. 463.
7. R. Schmidt and L.A. Coldren, "Thin Film Acoustic Surface Waveguides on Anisotropic Media," IEEE Trans. on Sonics and Ultrasonics, Vol. SU-22, No. 2, pp. 115-122, March, 1975.
8. L.A. Coldren and D.H. Smithgall, "Thin Film Slot Waveguides and Arbitrary Cross Section," IEEE Trans. on Sonics and Ultrasonics, Vol. SU-22, No. 2, pp. 123-130, March, 1975.
9. P. Hartemann, P. Cauvard, and D. Desbois, "Ion-Implanted Surface-Acoustic-Wave Guides on Lithium Niobate," Appl. Phys. Lett., Vol. 32, No. 5, pp. 266-268, March, 1978.
10. J.F. Weller, J.D. Crowley, and T.G. Giallorenzi, "Surface Acoustic Waveguides on $LiNbO_3$ formed by Titanium In-Diffusion" Appl. Phys. Lett., Vol. 31, No. 3, pp. 146-148, August, 1977.
11. S.A. Reible, "Transverse Modes in Gap-Coupled Surface-Wave Devices," Appl. Phy. Lett., Vol. 34, No. 1, January, 1979.
12. F.J. Leonberger, J.H. Cafarella, R.W. Ralston, E. Stern and A.L. McWhorter, Acoustoelectrically Scanned Gap-Coupled Si-Diode Array/$LiNbO_3$ Imaging Devices, *1977 Ultrasonics Symp. Proc.*, IEEE, pp. 456-459.
13. S.A. Reible and I. Yao, "An Acoustoelectric Burst-Waveform Processor" *1980 Ultrasonic Symp. Proc.* New York: IEEE, 1980, pp. 133-138.

APPENDIX I
SURFACE ACOUSTIC WAVE (SAW) ON A PIEZOELECTRIC

SAWs on piezoelectrics have electric fields associated with them that extend into the free space above the piezoelectric surface. It is through these fields that electrical signals can be coupled to and/or from such waves for useful purposes. Since SAWs are typically five orders of magnitude slower than free-space electromagnetic waves, the electrical excitation of SAWs on piezoelectrics allows the creation of electric fields having very high spatial resolution. Thus, at a frequency of 300 MHz, while a free-space electromagnetic wave has a wavelength of 1 meter a SAW typically has a wavelength of 10 microns.

In the following we summarize the global, analytic description of SAWs on piezoelectric that will be useful in this study. We consider both linear and nonlinear propagation characteristics.

I.A LINEAR PROPAGATION AND TRANSDUCTION

Consider first the free surface of a piezoelectric on which a SAW is propagating in a beam of width w, as shown in Figure I-1. Since the phase velocity of the SAW is much less than the speed of light, the electric field associated with the piezoelectric SAW is quasi-electrostatic and hence describable by an electric potential ($\vec{E} = -\nabla\Phi$). The potential in the free-space above the piezoelectric surface is then given by

$$\Phi_o = \phi_p \exp(-ky) \exp [j(wt - kz)] \quad (1)$$

where we have assumed a single wave with wavenumber $k = \omega/v_f \equiv k_f$ at a radian frequency $\omega = 2\pi f$; v_f is the phase velocity of the free-surface SAW on the piezoelectric. On most piezoelectrics of interest (e.g., $LiNbO_3$) SAWs are essentially dispersionless and weakly damped. As an example, SAWs on YZ-$LiNbO_3$ have the following approximate, linear propagation characteristics [1]:

- Free-surface phase velocity,

  $v_f \approx 3.5 \times 10^5$ cm/s

- Free-surface dispersion parameter,

  $\delta/k \approx (2 \text{ to } 10) \times 10^{-4}$ at 100 MHz

  mostly due to surface roughness and scaling with frequency;

- Free-surface spatial attenuation rate

  $\alpha \approx 3 \times 10^{-3}$/cm at 100 MHz

  i.e., approximately 3×10^{-2} dB/cm, mostly due to lattice anharmonisticity and scaling like frequency squared.

Thus, for most of our considerations we can neglect dispersion and attenuation of free SAWs.

The relationship between the SAW power flow and the associated free-space potential is then determined by two characteristic parameters of the piezoelectric:

- The change in phase velocity when an infinitesimally thin, perfect conductor is deposited on the piezoelectric surface (and thus shorts out the free-space field)

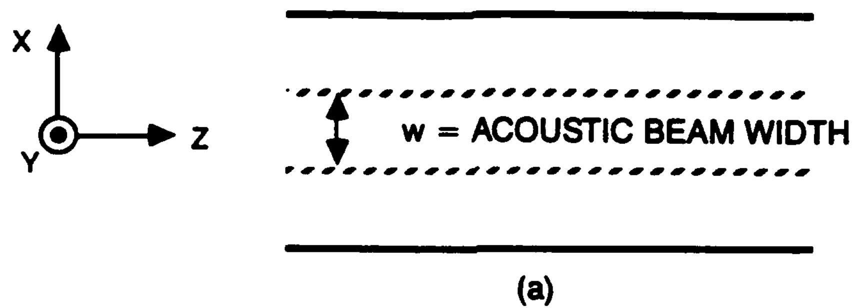

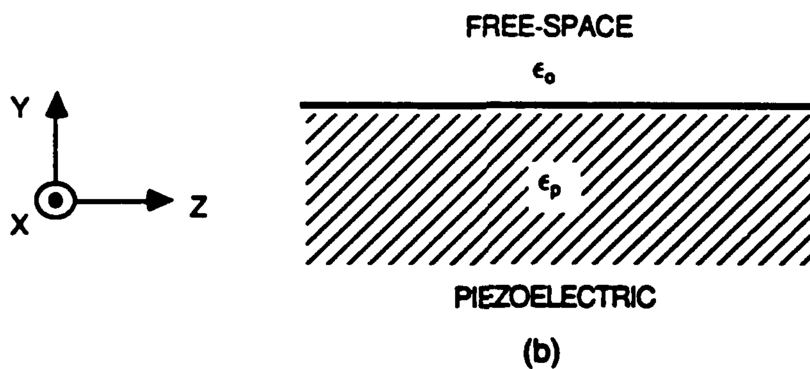

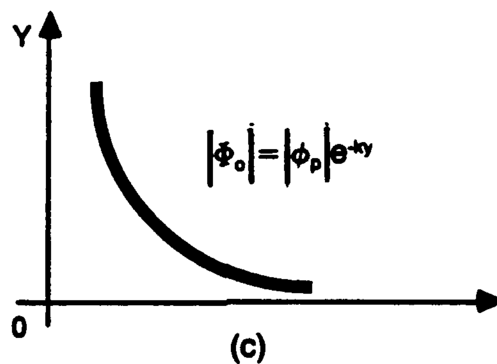

Figure I-1.

(a) Top-view of piezoelectric surface on which a SAW is propagating in the z-direction within a uniform beam of width w in x.

(b) Front view of piezoelectric free surface.

(c) Electric potential of SAW in free-space above the piezoelectric surface.

$$(\Delta v/v) \equiv (v_f - v_s)/v_f \tag{2}$$

- The effective permittivity of the piezoelectric material (which is in general anisotropic)

$$\epsilon_p = (\epsilon_{yy}\,\epsilon_{zz} - \epsilon_{yz})^{1/2} \tag{3}$$

where the elements are the components of the stress-free permittivity tensor of the piezoelectric.

With these, we find [2]:

$$S_a = [(\epsilon_p + \epsilon_o)/4]\ \omega|\phi_p|^2/(\Delta v/v) \tag{4}$$

where S_a is the acoustic power per unit width in x (Watts/m) also known as the acoustic sheet power density; the total power in the SAW is of course $P = S_a w$. Taking again YZ-$LiNbO_3$ as an example, we have approximately,

$$(\Delta v/v) \approx 2.3 \times 10^{-2}$$

and

$$\epsilon_p \approx 50\,\epsilon_o$$

At a given frequency and for a given acoustic power in a SAW equation (4) allows us to determine the potential in the free-space above the piezoelectric surface.

The conversion of an electrical signal into a SAW, and the reverse, is usually achieved by means of a set of interdigital transducers (metal strips) placed on the surface of the piezoelectric, as shown in Figure I-2. We need not concern ourselves with the details of these transduction processes; they are well-described in the literature [3], [4].

I.B NONLINEAR EFFECTS ON PROPAGATION

For a single SAW the principal effect is the generation of second (and higher) harmonic signals which may be undesirable. Experimentally, deviations from linearity are found to set in at acoustic power densities ($P/w\lambda = S_a/\lambda$) of about 1 W/mm² for Y-Z $LiNbO_3$ (1). Thus for beam width of 100λ, 1 W/mm² corresponds to 21 dBm of acoustic power at 100 MHz but only to 1 dBm of power at 1 GHz.

Second-harmonic generation can, however, be reduced by increasing the dispersion (e.g., by overlays on the acoustic beam). This introduces a dephasing in the nonlinear interaction which is therefore weakened. The condition for this is [5]:

$$(L_2\delta)^2 \equiv \frac{\pi\,\omega^2 v_a^2}{|K|^2 P}\left(\frac{w}{\lambda}\right)\left(\frac{\delta}{k}\right)^2 >> 4 \tag{5}$$

where L_2 is the scale length for the growth of the second harmonic amplitude relative to the initial amplitude in the fundamental, and $|K|$ is the nonlinear coupling constant for second-harmonic generation; it scales like ω^2. For Y-Z $LiNbO_3$, one finds approximately [6]:

$$|K| \approx 4 \times 10^9 \text{ meter/(sec)}^2 (\text{W})^{1/2} \quad @\ 100 \text{ MHz}$$

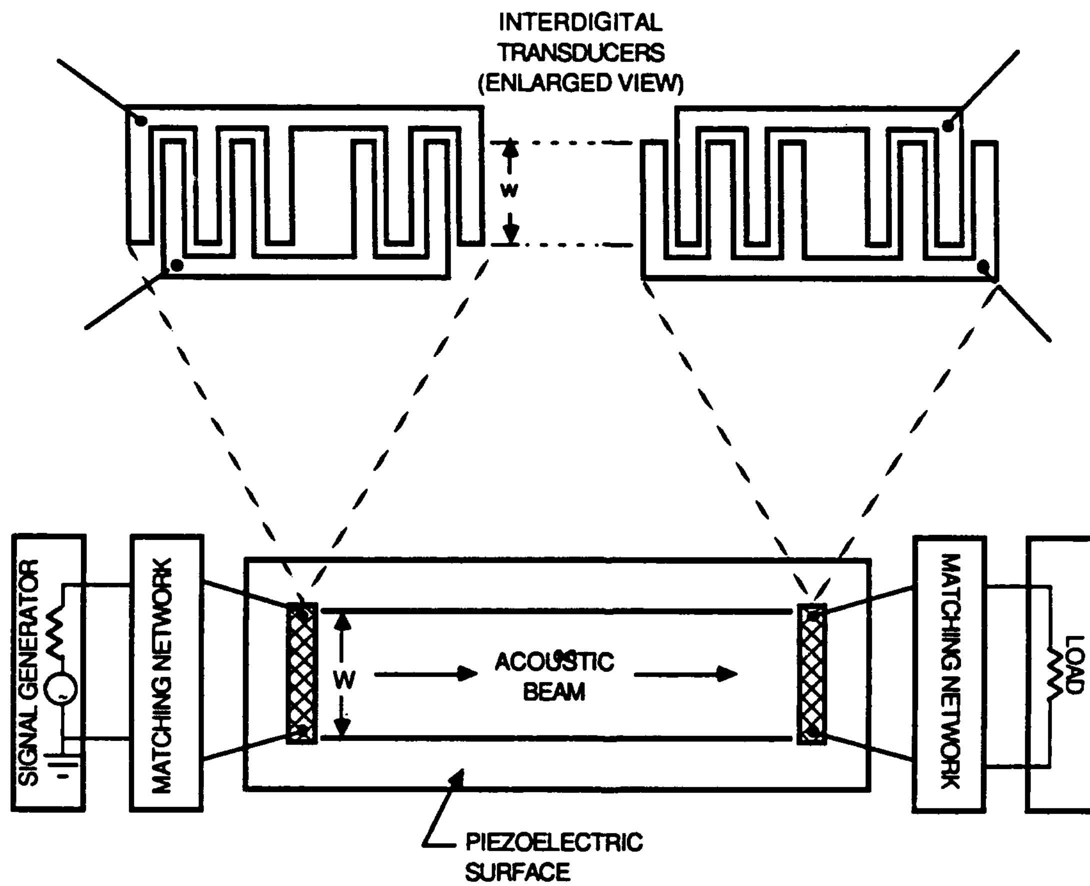

Figure I-2. Electrical coupling to and from a SAW by means of interdigital transducers placed on the surface of a piezoelectric

With this, equation (5) allows one to determine the needed dispersion (δ), for a given acoustic power (P), so that second-harmonic generation remains negligible.

For two counterpropagating SAWs nonlinearity can lead to very useful interactions and field generations which are discussed in Appendix IV.

I.C REFERENCES

[1] R.C. Williamson, *1974 Ultrasonics Symposium Proceedings,* IEEE Cat. #74 CHO 896-1SU, p. 321.

[2] A. Bers, *1970 Ultrasonics Symposium Proceedings,* IEEE Cat. #70, C69 SU pp. 138-172.

[3] W.R. Smith, H.M. Gerard, J.H. Collins, T.M. Reader, and H.J. Shaw, IEEE Trans, MTT-17, No. 11, 856 (1969).

[4] H. Engan, IEEE Trans, ED-16, No. 12, 1014 (1969).

[5] A. Bers, Special Summer Program in SAW Devices, M.I.T. June, 1979.

[6] N.P. Vlannes and A. Bers, *1980 Ultrasonics Symposium,* IEEE Nov. 1980 pp. 356-361, and J. Appl. Phys. 53, 372 (1982).

APPENDIX II
LINEAR COUPLING FROM A SAW TO AN ADJACENT DIODE ARRAY

For the purposes of this study we are interested in describing how a SAW on a piezoelectric interacts with an array of diodes on a surface which is adjacent, parallel, and facing the piezoelectric surface, as shown schematically in Figure II.1(a). Since the coupling between the two surfaces occurs through the free-space gap region g, and the fields are quasi-electrostatic, we can consider the situation as being represented equivalently as in Figure II.1(b). Here, the piezoelectric dynamics are represented by a surface-wave, dispersive dielectric function $\epsilon_{pp}(k,\omega)$, appropriate to giving the electric displacement normal to the piezoelectric surface; similarly, the dynamics of the electrons at the diode array are assumed to be described by $\epsilon_{se}(k,\omega)$ at a semiconducting surface. This defines a field coupling problem. The coupling from a SAW to the free electrons can be conveniently represented by an equivalent circuit derived from the open-circuit ($\epsilon_{se}=0$) voltage (ϕ_s^{oc}) and the short-circuit ($\epsilon_{se}=\infty$) current density ($j\omega D_s^{sc}$) normal to the surface s, per unit of SAW sheet power density (S_a) on a piezoelectric and under the diode array. This is sketched in Figure II.1(c), where the equivalent source capacitance per unit area is just $(D_s^{sc}/\phi_s^{oc})=C_a$. With this equivalent circuit we can then find the response of the diode array to a SAW.

To establish the parameters of the equivalent circuit in Figure II.1(c), we need to solve the linear field problem in Figure II.1(b) and from this determine: (a) the potential ϕ_p for a given SAW sheet power density (S_a); and (b) the potential ϕ_s per unit ϕ_p. The details of these calculations were carried out some years ago [1]. Here we summarize the results.

II.A SAW PROPAGATION IN THE PRESENCE OF A SEMICONDUCTING SURFACE

A semiconductor surface near a piezoelectric surface modifies the propagation characteristics of SAWs on the piezoelectric. The propagation constant of such waves will now be complex; the real part being different from the free-surface value described in Appendix I, and the imaginary part giving the wave attenuation due to power dissipated by the free electrons to which the SAW field is now coupled.

For wave-fields propagating in the z-direction, having their (t,z)-dependence as $\exp[j(\omega t-kz)]$, the quasi-electrostatic fields in the piezoelectric ($y\geq 0$), in the free-space gap ($0\leq y\leq g$), and in the semiconductor ($y\geq g$), take on simple exponential forms with y. Matching the tangential E-fields at $y=0$ and $y=g$, as well as the normal D-fields, with the use of $\epsilon_{pp}(k,\omega)$ and $\epsilon_{se}(k,\omega)$, it is readily found that the dispersion relation for the SAW in the presence of the semiconductor can be written as:

$$\epsilon_{pp}(k,\omega) = -\epsilon_{eff}(k,\omega) \tag{1}$$

where

$$\epsilon_{eff}(k,\omega) = \epsilon_o \frac{\epsilon_{se}(k,\omega) + \epsilon_o \tanh kg}{\epsilon_o + \epsilon_{se}(k,\omega) \tanh kg} \tag{2}$$

is the effective, normal dielectric function at the piezoelectric surface. To order $(\Delta v/v)$, defined in Appendix I, the solution of (1) for the propagation constant k is found to be given by:

$$\frac{k-k_s}{k_f} \approx -\left(\frac{\Delta v}{v}\right) \frac{\epsilon_p + \epsilon_o}{\epsilon_p + \epsilon_{eff}(k_f,\omega)} \tag{3}$$

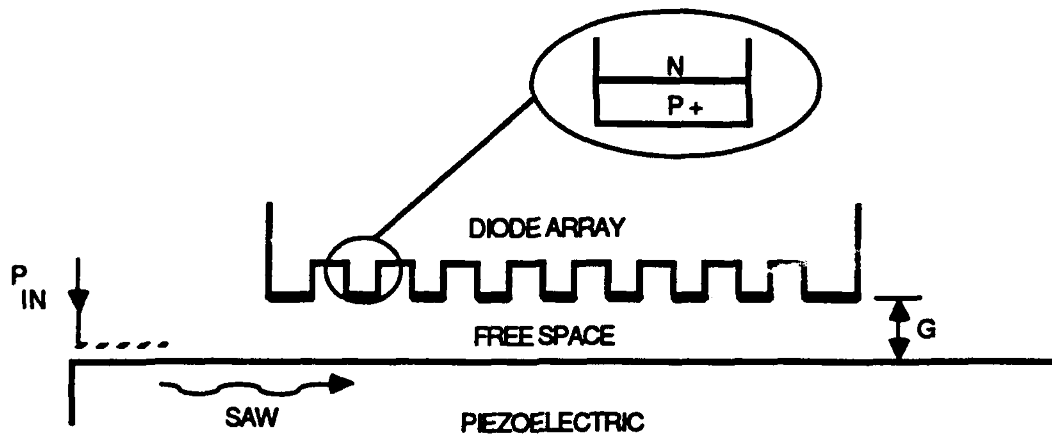

(a) Diode array adjacent to a piezoelectric surface on which a SAW is launched by an external electrical signal applied to an interdigital transducer.

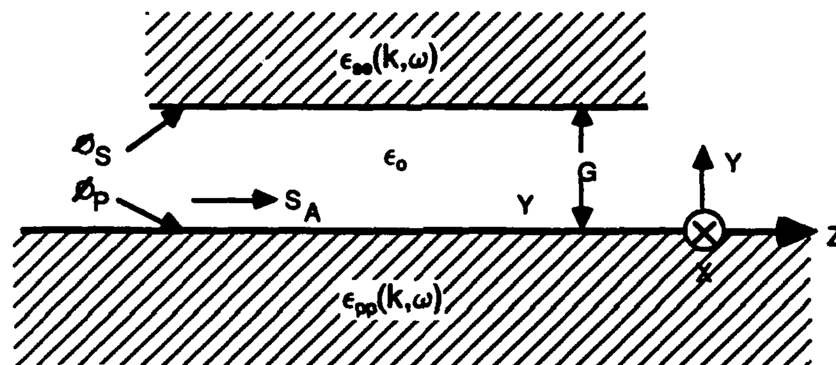

(b) Field problem set-up for calculating the linear coupling between a SAW on a piezoelectric and an adjacent semiconductor.

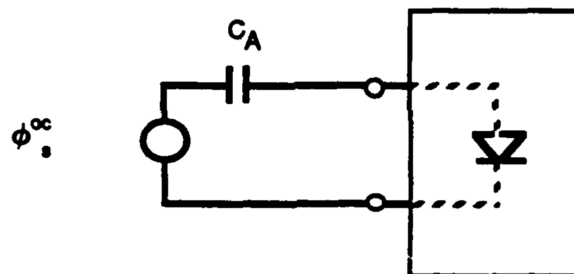

(c) Equivalent circuit used for calculating the diode array excitation by an adjacent SAW on a piezoelectric.

Figure II.1

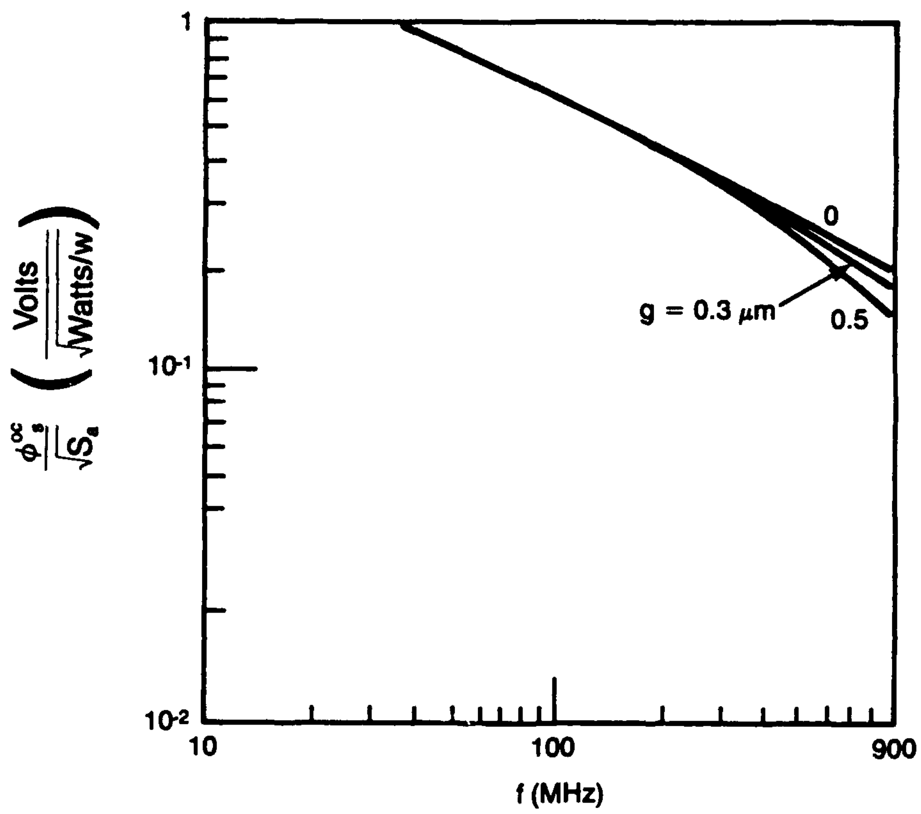

Figure II.2(a) Open-circuit voltage and for the equivalent circuit of Figure II.1(c). The calculation shown is for a SAW on YZ - $LiNbO_3$.

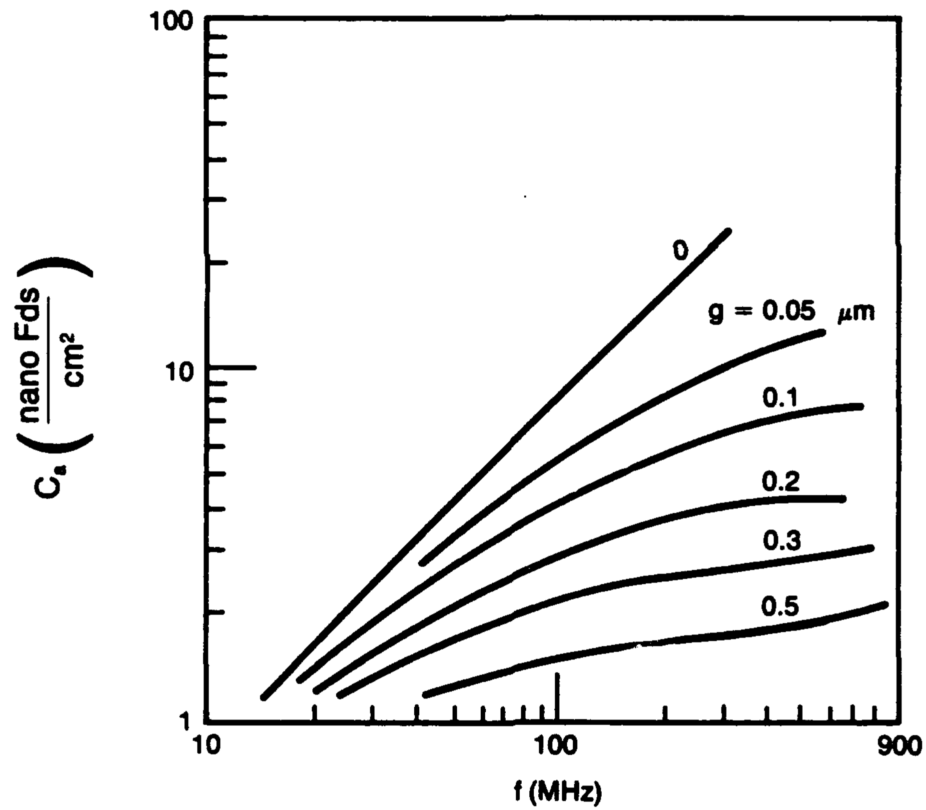

Figure II.2(b) **Acoustic coupling capacitance for the equivalent circuit of Figure II.1(c). The calculation shown is for a SAW on YZ - $LiNbO_3$.**

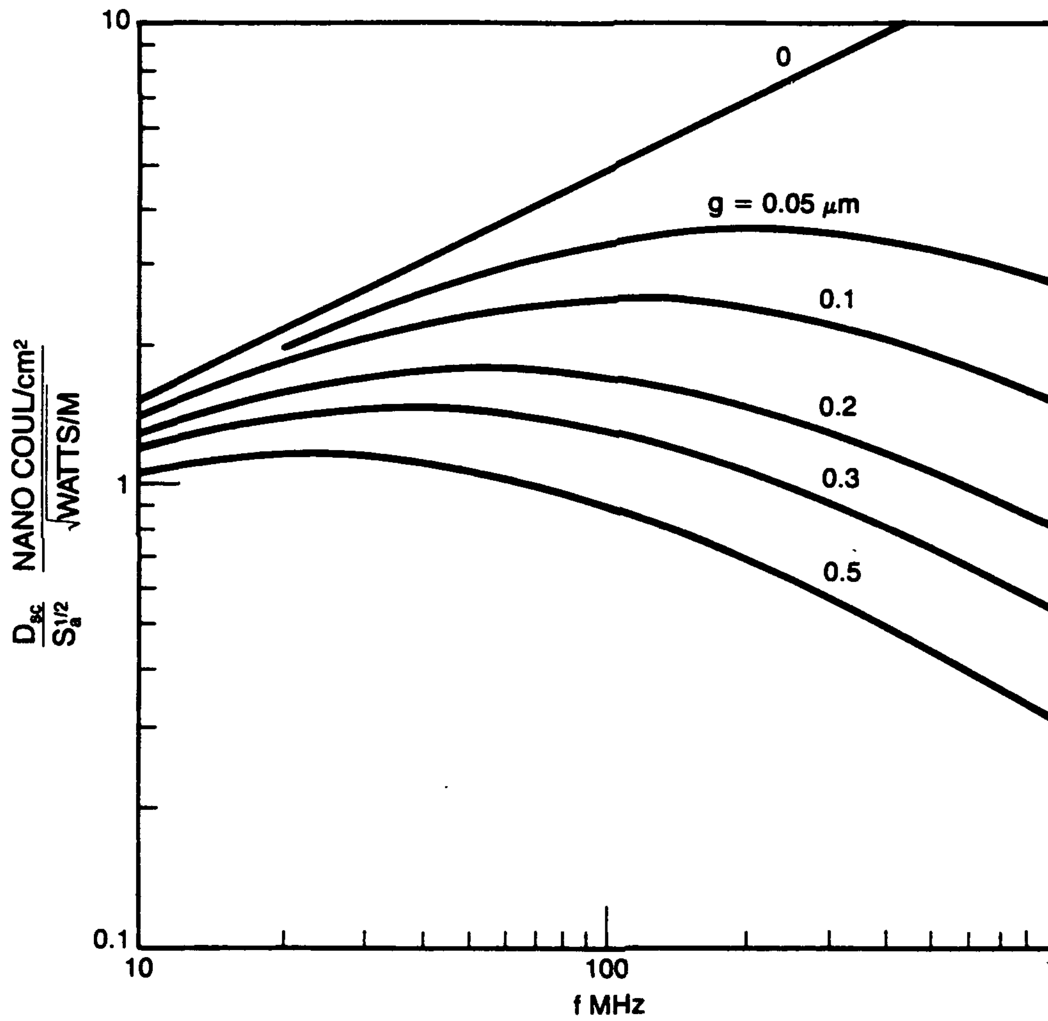

Figure II.3 Short-circuit, normal electric displacement field in the equivalent circuit of Figure II.1(c). The calculation shown is appropriate to a YZ-$LiNbO_3$ SAW.

where $k_f = (\omega/v_f)$ and $k_s = (\omega/v_s)$ are, respectively, the free-surface and shorted-surface SAW propagation constants, as described in Appendix I. For a relatively high conductivity semiconductor, appropriate for modeling the diode array, the normal dielectric function is approximately given by:

$$\epsilon_{se}(k,\omega) \approx \frac{\epsilon_s}{k\lambda_D}\left(1-j\frac{\omega/\omega_\sigma}{k\lambda_D}\right) \tag{4}$$

where ϵ_s is the dielectric constant of the semiconductor, λ_D is its Debey length, and $\omega_\sigma = \sigma_0/\epsilon_s$ is its conductivity frequency (the inverse dielectric relaxation time). The real part of the propagation constant, k_r, is determined from (3):

$$\frac{k_r-k_s}{k_f} = R_e\left(\frac{k-k_s}{k_f}\right) = (\delta k_r) \tag{5}$$

together with (2) and (4). The decay rate of the fields is given by exp $(-k_i z)$ with

$$k_i = k_f \, \mathrm{Im}\left(\frac{k-k_s}{k_f}\right) \tag{6}$$

For a relatively high conductivity semiconductor the attenuation per wavelength will be small, i.e., $k_i << k_r$, and $k_r = k_f$.

By the same electrodynamics techniques as described in Appendix I and its ref. [2], the acoustic power (per unit width in x, sheet power density) can again be related to the electric potential at the surface of the piezoelectric, now in the presence of the semiconductor. One thus finds

$$S_a = \frac{(\epsilon_p + \epsilon_o)}{4} \; \omega \, |\phi_p|^2 \; \frac{(\Delta v/v)}{(\delta k_r)^2} \tag{7}$$

Note, of course, as the semiconductor is removed (by either letting $g \rightarrow \infty$, or setting $\epsilon_{se} = \epsilon_o$) (7) reduces to (4) of Appendix I, as it should, and $k = k_f$.

II.B EQUIVALENT CIRCUIT FOR DIODE EXCITATION BY SAW

From the field solution described in sub-Section II.A, we readily establish the potential at the semiconducting sheet to be

$$\phi_s = \epsilon_o \phi_p / (\cosh kg)\,(\epsilon_o + \epsilon_{se} \tanh kg) \tag{8}$$

and for weak damping we can let $k \approx k_r$, from here on. The normal component of the electric displacement field at the semiconductor surface is

$$D_y\,(y=g) = \epsilon_{se}\, k\phi_s \equiv D_s \tag{9}$$

The open-circuit conditions are obtained with $\epsilon_{se} = 0$. Using this in (2), (3), (7) and (8) we find

$$\frac{\phi_s^{oc}}{S_a^{1/2}} = \frac{2\left[\frac{(\epsilon_p + \epsilon_o)}{\omega}\left(\frac{\Delta v}{v}\right)\right]^{1/2}}{(\cosh kg)\,(\epsilon_p + \epsilon_o \tanh kg)} \tag{10}$$

This gives the open-circuit voltage, for a given acoustic sheet power density in the SAW under the diodes, which enters into the equivalent circuit of Figure II.1(c).

The short-circuit conditions pertain to letting $\epsilon_{se} \rightarrow \infty$, then (2), (3), (7), and (9) give:

$$\frac{D_s^{sc}}{S_a^{1/2}} = \epsilon_o k \frac{2 \left[\frac{(\epsilon_p + \epsilon_0)}{\omega} \left(\frac{\Delta v}{v} \right) \right]^{1/2}}{(\cosh kg)\,(\epsilon_o + \epsilon_p \tanh kg)} \tag{11}$$

This gives the short-circuit current density ($j\omega D_s^{sc}$), for a given acoustic sheet power density in the SAW under the diodes.

Finally, the acoustic coupling capacitance in the equivalent circuit of Figure II.1(c) is given by the ratio of (11) to (10):

$$C_a = \epsilon_o k \frac{\epsilon_p + \epsilon_o \tanh kg}{\epsilon_o + \epsilon_p \tanh kg} \tag{12}$$

Equations (10) and (12) are plotted in Figure II.2 and (11) is plotted in Figure II.3, all as functions of frequency and for various values of g, assuming parameters appropriate to $LiNbO_3$ as a piezoelectric and $k \approx k_f$ as given in Appendix I.

So far, in the spirit of the representation in Figure II.1(b), we have considered the diodes to form a continuum, i.e., at each point along the surface of ϵ_{se}. In reality, the diodes are each of finite extent as shown in Figure II.1(a). Hence, diodes of finite extent δ along z, with $\delta < \lambda$ of the acoustic wave, will be excited by the SAW fields averaged over δ. It is easy to show that this average reduces the point-fields, that drive the diodes, by a factor

$$F = \frac{\sin(\pi\delta/\lambda)}{(\pi\delta/\lambda)} \tag{13}$$

Thus, both (10) and (11) become multiplied by F.

II.C REFERENCES

[1] A. Bers and J.H. Cafarella, unpublished work, Lincoln Laboratory, MIT, 1974.

APPENDIX III
DIODE ARRAY AS A SAW CONVOLVER/STORAGE CORRELATOR

In this appendix we explore the possibility of probing the diode array through either the convolution of two counterpropagating SAWs via the nonlinear diode depletion capacitances, or through the storing of charge in the diodes by a SAW along, and a voltage signal across, the diodes. In either case a light beam may also apply a signal charge to the diodes through a grating.

Consider an array of diodes on a surface that is brought in close proximity to the surface of a piezoelectric, as shown in Figure III.1. On the surface of the piezoelectric, SAWs can be launched (see Appendix I) from either or both ends of the piezoelectric toward the region where the diode array is present. In addition a plate signal may be applied across the diodes, and/or a light signal through a grating in the plate. Due to the launched SAWs, electric fields will exist in the region between the piezoelectric and the diode array, as described in Appendix II. The rf electric displacement field normal to the diodes will induce charge flow in the diodes. Through their depletion capacitances, the diodes act as nonlinear elements and produce a voltage which is proportional to the square of the electric displacement field. In particular, two counterpropagating SAW signals can thus produce a diode voltage at their sum frequency, which gives the convolution of the signals. If the frequencies of the SAWs are the same, the convolution of the signals is uniform in space and can be picked up by the simple parallel plate circuit, as shown in Figure III.1.

In the following we give the analysis of the nonlinear process described above, as well as the input/output analysis of such a convolver and its relation to the diode parameters that can thus be probed.

III.A NONLINEAR (VARACTOR) ACTION OF THE DIODES

Consider, for illustration purposes, a one-sided step-junction diode (e.g., with doping densities $N_A >> N_D$, as for a p^+-n diode). The voltage across its depletion layer (of cross sectional area A) depends upon the surface charge [1]:

$$V_d = \frac{(Q_d/A)^2}{2\epsilon q N_D} \tag{1}$$

In equilibrium $Q_d = qN_d d_o A \equiv Q_o$, where $d_o = (2\epsilon V_b/qN_D)^{1/2}$ is the depletion width and $V_b \approx (\kappa T/q)\ln(N_A N_D/n_i^2)$ is the built-in voltage; V_d is then, of course, equal to V_b. The nonlinear relationship between voltage and charge represented by (1) is the basis of the Varactor action of the diode.

In the presence of SAW fields there will be a component of the electric displacement field normal to the diode (p^+) surface, as described in Appendix II; we denote it as D(t). Hence, the diode charge will be

$$Q_d(t) = Q_o - AD(t) + Q(t) \tag{2}$$

where Q(t) is the charge lost from the surface by the diode current. The time variation of D(t) is given by the high-frequency (ω) of the SAW (typically, $\omega > 10^8$Hz. As we shall see in Appendix IV, the time scale over which Q(t) varies is given by $R_o C_{do}$ of the diode; this we assume is much longer than ω^{-1}, or any signal envelope duration. Hence, for the high-frequency fields of the SAW we can take the diode voltage to be

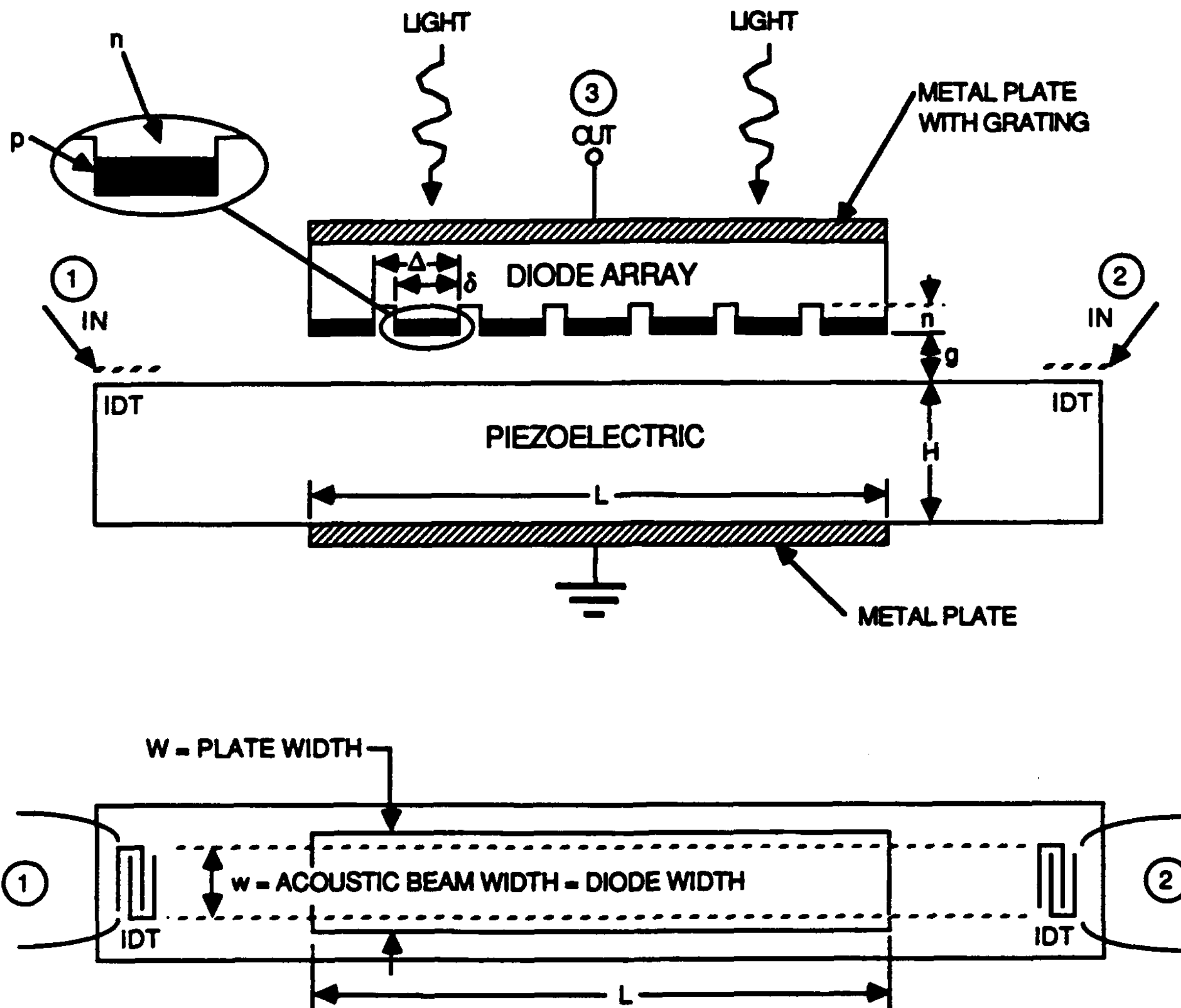

Figure III.1. Set-up for convolution and/or correlation of two SAW Signals 1 and 2 in interaction with a diode array; The output is then at 3. The same set-up can also be used to store charge in the diodes with either light and/or signals applied to the plate 3 and one of the transducers; the stored charge can then be read with signals applied subsequently to the plate and the output appearing at the IDT's

$$V = \frac{D^2}{2\epsilon q N_D} \quad (3)$$

The quadratic dependence on D shows that the diode can be used as a loss-free mixer of SAW fields. Thus consider the D-field due to two SAWs, D_1 at (ω_1, k_1) and D_2 at (ω_2, k_2). The second order term from (3) will have a diode voltage at

$$\omega_3 = \omega_1 + \omega_2 \quad (4)$$

$$k_3 = k_1 + k_2 \quad (5)$$

which we can write as

$$V_3 = \frac{D_1 D_2}{\epsilon q N_D} \quad (6)$$

This forms the basis for convolving or correlating SAW signals.

III.B THE DEGENERATE SAW CONVOLVER

For two counterpropagating SAWs at the same frequency ($\omega_1 = \omega_2 = \omega$, $k_1 = -k_2$) we have $\omega_3 = 2\omega$ and $k_3 = 0$; this is the "degenerate" case from (4) and (5). In this case, where the SAWs overlap underneath a set of the diodes, the diode response (4) is uniform in space and can therefore be detected simply by an integrating plate over this particular set of diodes from the array, as shown in Figure III.1. Using the equivalent circuit of Appendix II for the diode excitation, we have from (6)

$$V_{2\omega} = \frac{1}{\epsilon q N_D} \left(\frac{C_d C_a}{C_d + C_a} \right)^2 F^2 \phi^{oc}_{s+} \phi^{oc}_{s-} \quad (7)$$

where we have written $V_3 = V_{2\omega}$ to indicate that we are considering the degenerate case, C_d is the diode depletion layer capacitance [1] $C_d = [\epsilon_q N_D/2(V_b\text{-}V)]^{1/2}$, C_a is the acoustic coupling capacitance given in Appendix II, F is the factor accounting for the finite extent of the diodes (also given in Appendix II), and the $\pm$ subscripts on ϕ^{oc}_s denote, respectively, the forward and backward traveling SAWs. The output voltage can then be written as

$$V_o = \frac{1}{L} \int_o^L V_{2\omega} \, dz \quad (8)$$

where the set of diodes producing $V_{2\omega}$ is within $0 \leq z \leq L$. Since the integrand in (8) contains the product of $\phi^{oc}_{s+} \phi^{oc}_{s-}$, the output plate voltage will give the convolution/correlation of signals carried by the SAWs [2, 3].

Suppose that the two external, electrical excitations of the SAWs are given by, respectively, $\psi_{\pm}(t)\, e^{j\omega t}$ signals, where $\psi_{\pm}(t)$ are slowly-varying (compared to ω^{-1}) envelopes. The counterpropagating SAWs will then create electrical potentials in the diode integration region:

$$\phi_{p+} = |\phi_{p+}| \psi_+(t-\frac{z}{v}) \; e^{-\alpha z} \quad \text{for } z>0 \quad (9)$$

and

$$\phi_{p-} = |\phi_{p-}| \, \psi_- \, (t + \frac{z-L}{v}) e^{\alpha(z-L)} \quad \text{for } z < L \tag{10}$$

where α is the linear attenuation rate of the SAW due to the presence of the diode array ($\alpha \equiv k_i$ given by (6) in Appendix II), and v is the phase velocity of the SAW as modified by the presence of the diode array (i.e., $v = \omega/k_r$, with k_r given by (5) in Appendix II). Thus, the plate output voltage (6) can finally be written as

$$V_o = M \sqrt{S_{a+} S_{a-}} \; C_{\psi_+\psi_-} \tag{11}$$

where

$$C_{\psi_+\psi_-} = \int \psi_+(\tau) \; \psi_-(2t \frac{L}{v} - \tau) \frac{v}{L} \; d\tau \tag{12}$$

is the convolution of the signal envelopes ψ_+ and ψ_-, and

$$M = \frac{e^{-\alpha L}}{\epsilon q N_D} \left(\frac{C_d C_a}{C_d + C_a} \right)^2 F^2 \quad \left(\frac{\phi_s^{oc}}{S_a^{1/2}} \right)^2 \tag{13}$$

is the so-called "merit factor" (volts/watt/meter in x) of the convolution process: ($\phi_s^{oc}/S_a^{1/2}$) is given in Appendix II by (10) and Figure II.2.

We note that for $C_a >> C_d$, $M \sim C_d^2/N_d$ becomes independent of carrier concentration and inversely proportional to the potential across the diode depletion region. In the opposite limit of $C_d >> C_a$, we have $M \sim 1/N_d$ and independent of the depletion capacitance.

The power output of the convolver, to an external load, can be determined from an approximate output equivalent circuit. Again, for illustrative purposes, we show such an output equivalent circuit in Figure III.2 related to the configuration shown in Figure III.1. (The more practical design discussed in the text will, of course, have different dimension parameters for its equivalent circuit.) Referring to Figures III.1 and 2, since V_3 is essentially the output, open-circuit voltage appearing across the depletion region of each diode, C_p is the capacitance between the diodes and the metal ground plate below the piezoelectric, and C_s is the capacitance of the diode array substrate to ground. Using the output equivalent circuit, we can calculate the output power P_3 to the load, and hence the overall "power transfer factor" for the convolver device: $F_T = P_3/P_1P_2$ where P_1 and P_2 are the electrical input powers to the SAW transducers. It is common practice to express this in dBm:

$$(F_T)_{dBm} = 10 \log \frac{P_3(mW)}{P_1(mW) \; P_2(mW)} \tag{14}$$

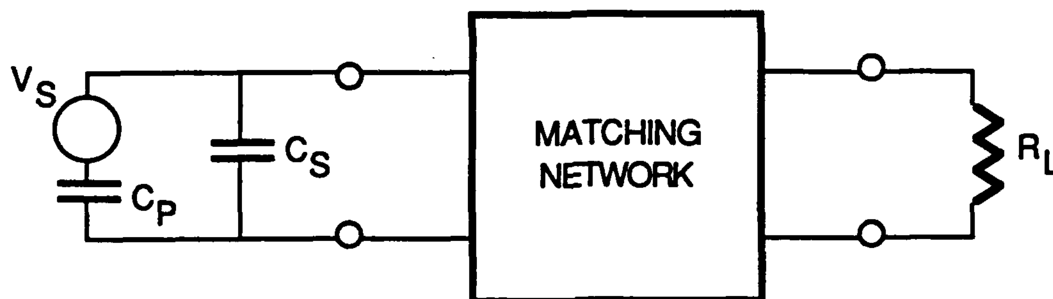

$$C_P = \frac{\epsilon_{pn} W}{H+g} L \frac{\delta}{\Delta} \; ; \; C_s = \frac{\epsilon_{pn} W}{H} L \frac{\left(1 - \frac{w}{W}\frac{\delta}{\Delta}\right)}{1 + \frac{\eta}{H}\frac{\epsilon_{pn}}{\epsilon_o}}$$

Figure III.2. Equivalent circuit for calculating output power to a load (R_L) from open-circuit plate voltage (V_s) produced by SAW's shown in Figure III.1. THe formulas for the capacitances C_P and C_s pertain to the configuration shown in Figure III.1

III.C THE STORAGE CORRELATOR MODE

Charge can also be stored in a diode array by means of simultaneously applying a SAW field signal from an adjacent piezoelectric and a plate signal. This is the basic means by which charge storage is achieved in a diode memory correlator [4]. A signal applied to the plate of the system shown in Figure II.1 affects the diodes in a rather obvious manner, as illustrated in Figure III.3a; its equivalent circuit is shown in Figure III.3b, where C_p is the capacitance due to the piezoelectric and air gap and R_s is the lumped resistance due to the diode array substrate.

The charge stored in the diodes when a plate signal and SAW signal are applied simultaneously is given by

$$Q_d \sim \int V_d^P(t) \; \psi^s\left(t - \frac{z}{v}\right) dt \qquad (15)$$

The charge distribution on various diodes can thus be varied with the use of various signal shapes.

The diode time constant can be inferred from the decay of the stored charge. This can be obtained by reading out the stored charge as a function of time. There are two possible read-outs. The first is where the output appears at the plate when a SAW readout signal is applied. The second is where the output appears at one of the acoustic ports in response to a plate readout signal. All of these involve well known signal processing techniques [3] and each can be optimized for probing the diodes in an array by proper choice of signal shapes.

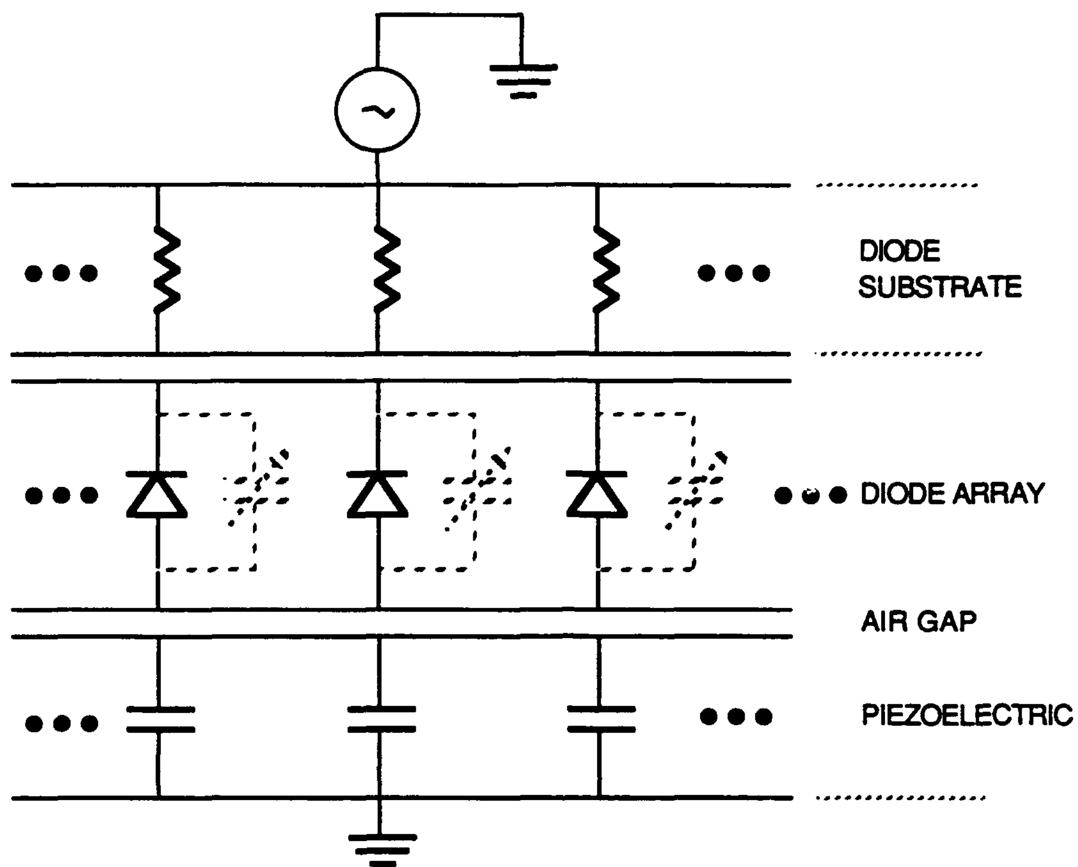

(a)

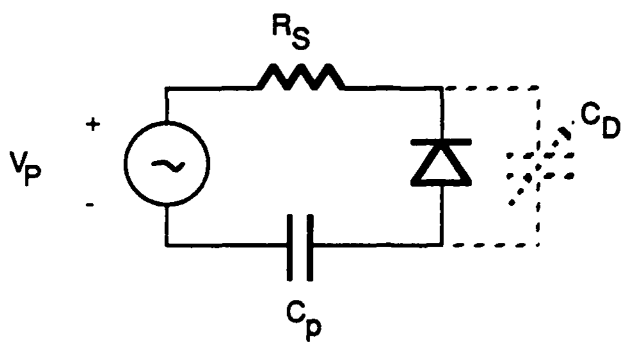

(b)

Figure III.3. (a) Plate signal excitation and (b) its equivalent circuit

The crucial element in these types of probing is the charging dynamics of the diodes of interest. This is dealt with in the Appendix IV.

III.D REFERENCES

[1] See, e.g., S.M. Sze, *Physics of Semiconductor Devices.* 2nd edition, John Wiley and Sons, Inc. 1981.

[2] A. Bers and J.H. Cafarella, *1974 Ultrasonics Symposium Proceedings,* IEEE Cat. # CHO 896-1 SU, pp 778-787.

[3] J.H. Cafarella, *1978 Ultrasonics Symposium Proceedings,* IEEE Cat. # 78 CH 1344-1 SU.

[4] K. Ingebritsen, R.A. Cohen and R.W. Mountain, Appl. Phys. Lett. *26,* 596 (1945).

APPENDIX IV
DIODE CHARGING DYNAMICS

In this appendix we give the analysis that describes the charging of diodes by SAWs. In particular, we relate this charging process to the equilibrium diode time constant $\tau_{do} = R_o C_{do}$ which we seek to probe with SAWs. As detailed in Appendixes I-III and V, SAWs can be made to produce locally an electric displacement field normal to the surface of the diode array. This normal electric displacement field, D(t), creates charge flow in the diode and changes the voltage across the diode. For our analysis we consider the one-dimensional p^+n diode configuration as illustrated in Figure IV.1. A similar analysis, for somewhat different purposes, and with much of the important details missing, can be found in [1].

The voltage across the depletion layer of a p^+n diode and the diode charge were introduced in Eqs. 1 and 2 of Appendix III. With these, the voltage across the diode is simply

$$V(t) = V_b - V_d = \frac{Q_o^2 - (Q_o - AD + Q)^2}{2\epsilon q N_D A^2} \qquad (1)$$

Furthermore, Q(t) and V(t) are related through the dynamics of charge flow in the diode. It is convenient to distinguish two types of charging dynamics: "fast" and "slow". In a "fast" diode its I-V characteristic is established instantaneously. In a "slow" diode, typical of p^+n junction diodes, account must be taken of their transient charging dynamics. For simplicity we consider first the "fast" diode charge dynamics. This will be followed by the more general analysis from which the conditions for a "fast" diode behavior in the charge dynamics can be established in detail.

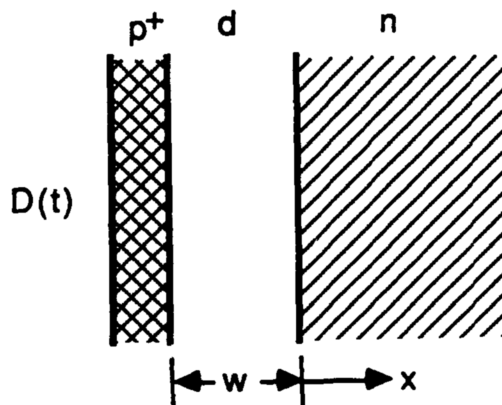

Figure IV.1 One-dimensional p^+n abrupt junction diode regimes with applied electric displacement field D(t) due to SAW's.

IV.A "FAST" DIODE CHARGE DYNAMICS

Assuming that the diode current is

$$I(t) = I_s \left[e^{qv(t)/\kappa T} - 1 \right] \tag{2}$$

we have

$$\frac{dQ}{dt} = I_s \left[e^{\beta V(t)} - 1 \right] \tag{3}$$

where V(t) is given by (1), and we have abbreviated $(q/\kappa T) \equiv \beta$. As we shall see, the time scale over which Q changes is long compared to $(2\pi/\omega)$, hence, averaging (3) over the fast time scale $(2\pi/\omega)$ we obtain

$$\left(\frac{dQ}{dt} \right)_{SLOW} \approx I_s \left[\left\langle e^{\beta V(t)} \right\rangle - 1 \right] \tag{4}$$

where angular brackets indicate the averaging process.

For acoustic signals of interest (see Appendix I), and typical diodes, we have $A|D| << 2Q_o$ and hence also typically $Q^2 << Q_o^2$. Under these conditions we can ignore the $(AD)^2$ term in (1) and find,

$$\beta V \approx \frac{1}{Q_T} \left[\left(1 + \frac{Q}{Q_o} \right) AD_a \sin\omega t - Q \right] \tag{5}$$

where we have taken $D(t) = D_a \sin\omega t$ and set $Q_T \equiv (\kappa T/q)\, C_{do}$ with $C_{dc} = \epsilon A/W_o$ the equilibrium depletion capacitance. Carrying out the time averaging over $(2\pi/\omega)$ we find

$$\left\langle e^{\beta V(t)} \right\rangle = e^{-\frac{Q}{Q_T}}\, I_o \left[\left(1 + \frac{Q}{Q_o} \right) \frac{AD_a}{Q_T} \right] \tag{6}$$

where $I_o[x]$ is the modified Bessel function of order zero. Noting that $AD_a >> Q_T$ we can use the asymptotic form for $I_o[x >> 1]$ and obtain from (6)

$$\left\langle e^{\beta V(t)} \right\rangle \approx \frac{e^{-\frac{Q}{Q_T}}\, e^{\left(1 + \frac{Q}{Q_o} \right) \frac{AD_a}{Q_T}}}{\sqrt{2\pi \frac{AD_a}{Q_T}}} \tag{7}$$

where we have ignored (Q/Q_o) compared to one in the square-root but not in the exponential. Using (7) in (4) we arrive at the slow-time scale differential equation for Q:

$$\frac{dQ}{dt} \approx I_s \left(\alpha\, e^{-\gamma Q} - 1 \right) \tag{8}$$

where

$$\alpha \equiv \frac{e^{AD_a/Q_T}}{\sqrt{2\pi\, AD_a/Q_T}} \tag{9}$$

and

$$\gamma \equiv \frac{1 - (AD_a/Q_o)}{Q_T} \tag{10}$$

Equation (8) can be solved for Q(t) giving

$$\gamma Q(t) = \ln\left[\alpha - (\alpha - 1)\, e^{-t/\tau_Q}\right] \tag{11}$$

where

$$\tau_Q = \frac{1}{\gamma I_s} = \frac{(\alpha T/qI_s)C_{do}}{1 - (AD_a/Q_o)} = \frac{R_o C_{do}}{1 - (AD_a/Q_o)} \tag{12}$$

Equation (11) exhibits how the diode equilibrium relaxation time R_oC_{do} enters into the stored charge. Monitoring Q can thus give $\tau_{do} \equiv R_oC_{do}$ of the diodes. For $t << \tau_Q$ we have approximately

$$Q \approx Q_T \ln\left[1 + \alpha \frac{t}{\tau_Q}\right] \tag{13}$$

When the external signals are switched off the diode starts to discharge through its leakage current I_s and the observed storage time gives an estimate of $Q/I_s \sim R_oC_{do}$.

IV.B CHARGING DYNAMICS FOR A P+N DIODE

We now reconsider the charging dynamics with a finite minority carrier lifetime τ_p. Let the hole concentration on the n-side be $p_n = p_{no} + p_{n1}(x,t)$ where $p_{no} = n_i^2/N_D = N_A \exp(-\beta V_b)$ and $p_{n1}(x,t)$ is due to V(t) and satisfies the diffusion equation,

$$\frac{\partial p_{n1}}{\partial t} - D_P \frac{\partial^2 p_{n1}}{\partial x^2} = \frac{p_{n1}}{\tau_P} \tag{14}$$

(D_p = diffusion constant for holes), subject to the boundary conditions:

$$p_{n1}(0^+,t) = p_{no}\left[e^{\beta V(t)} - 1\right] \tag{15}$$

$$p_{n1}(\infty,t) = 0 \tag{16}$$

We assume diffusion in a semi-infinite medium, which is appropriate for times less than the storage times, and thus

$$Q(t) = -qD_p \int_o^t \partial p_{n1}(0^+,t') \frac{\partial p_{n1}(0^+,t')}{\partial x}\, dt' \tag{17}$$

Taking the Laplace transform (e^{st}) of (14) through (17) we find

$$Q(s) = R(s)\, P_o(s) \tag{18}$$

where

$$R(s) = \frac{q}{s}\sqrt{D_p\left(s + \frac{1}{\tau_p}\right)} \tag{19}$$

and $P_o(s)$ is the Laplace transform of $p_{n1}(0^+,t)$. Whence we find

$$Q(t) = \int_o^t r(t-\tau)\, p_{n1}(0^+,\tau)\, d\tau \tag{20}$$

where

$$r(t) = q\sqrt{\frac{D_p}{\pi}}\left[\frac{e^{-t/\tau_p}}{\sqrt{t}} + \sqrt{\frac{\pi}{\tau_p}}\ \mathrm{erf}\sqrt{\frac{t}{\tau_p}}\right] \tag{21}$$

This is the general relationship between Q(t) and V(t) which enters through $p_{n1}(0^+,\tau)$ given by (15); V(t) is in turn related to Q(t) through (1).

We now consider the same amplitude inequalities as in sub-Section IV.A: $A|D| << 2Q_o$ and $Q^2 << 2Q_o^2$, so that (20) becomes approximately

$$Q(t) \approx p_{no}\int_o^t\left[\exp\left(\frac{AD(\tau)}{Q_T} - \frac{Q(\tau)}{Q_T}\right) - 1\right] r(t-\tau)\, d\tau \tag{22}$$

Now, letting $D(t) = D_a \sin\omega t$ and noting that r(t) and Q(t) change slowly on the time scale of $(2\pi/\omega)$ we can (as in sub-Section IV.A) average (22) over the fast time scale of $(2\pi/\omega)$ and obtain from it a differential equation for the slow-time evolution of Q(t):

$$\frac{dQ}{dt} \approx \left[I_o\left(\frac{AD_a}{Q_T}\right) e^{-Q/Q_T} - 1\right] p_{no}\, r(t) \tag{23}$$

where, as before, $I_o(y)$ is the modified Bessel function of order zero. Equation (23) can be solved to give

$$Q(t) = Q_T \ln\left\{I_o\left(\frac{AD_a}{Q_T}\right) - \left[I_o\left(\frac{AD_a}{Q_T}\right) - 1\right]\exp\left[\frac{\sqrt{\tau_p/\pi}}{\tau_{do}}\ g(t)\right]\right\} \tag{24}$$

where we have noted that $qp_{no}\sqrt{D_p/\tau_p} = I_s$ the p^+n diode saturation current, $Q_T/I_s = R_oC_{do} \equiv \tau_{do}$, and

$$g(t) = \sqrt{t}\, e^{-t/\tau_p} + \sqrt{\pi}\,\tau_p\left(\frac{t}{\tau_p} + \frac{1}{2}\right)\mathrm{erf}\sqrt{\frac{t}{\tau_p}} \tag{25}$$

For $t >> \tau_p$

$$\frac{\sqrt{\tau_p/\pi}}{\tau_{do}}\ g(t) \approx \frac{t}{\tau_{do}} \tag{26}$$

and (24) reduces, essentially, to the "fast" diode result (11). Thus the "fast" diode result (13) is applicable to p^+n diodes for $\tau_p << t << \tau_{do}$.

For $t << \tau_p$

$$\sqrt{\frac{\tau_p/\pi}{\tau_{do}}}\ g(t) \approx \frac{2}{\tau_{do}}\sqrt{\frac{\tau_p}{\pi}}\ t \qquad (27)$$

which gives (24) a time-dependence that is much different from (11) but still involving the $\tau_{do} = R_o C_{do}$ of interest.

Finally, we note that typically $(AD_a/Q_T) >> 1$ and $\sqrt{\tau_p/\pi}\, g(t) << 1$ so that (24) is approximately

$$Q(t) \approx Q_T \ln\left[1 + I_o\left(\frac{AD_a}{Q_T}\right)\frac{\sqrt{\tau_p/\pi}}{\tau_{do}}\ g(t)\right] \qquad (28)$$

For $t >> \tau_p$ (28) reduces, essentially, to the "fast" diode result (13).

IV.C REFERENCES

[1] M. El-Nokali and E.L. Adler, IEEE Trans. on Sonics and Ultrasonics, SU-27, 38 (1980).

APPENDIX V
HIGH FREQUENCY E-FIELD PROBES WITH SAWs

In the preceding appendixes we explored the use of SAWs interacting with an adjacent array of diodes for probing the characteristics of its individual diodes. It was shown that the diodes could be used as a nonlinear medium to convolve/correlate SAW signals and thereby generate locally uniform fields that could be readily detected. When these nonlinearly generated fields depend upon the diode doping, or depletion capacitance, and/or the diode equilibrium time constant, these interactions give useful diagnostic means for the diodes of the array. However, since the electric fields associated with high-frequency SAW's decay exponentially at a very fast rate [$\sim \exp(-ky)$, $k=\omega/v_a$, see Appendix I] from the piezoelectric surface, a disadvantage of such interactions is that the diode array must be brought into very close proximity to the piezoelectric.

In this appendix we look at a different way of probing the diodes, a way that circumvents the above difficulty. Here we explore generating a localized, uniform ($k=0$) electric field by nonlinear interactions of SAWs in a piezoelectric or semiconductor *outside* the diode array system. Such electric fields, which we call "E-field probes with SAWs," decay only due to their finite spatial extent, which is much larger than the wavelength of the SAWs used to produce them. For this type of probe, the separation between the diode array and the piezoelectric or semiconductor surface, on which the probe field is produced, can be much larger than in the case when the diodes themselves are used as the nonlinear medium. Thus we can achieve a mechanically more practical diagnostic system for probing diode arrays. In the following we describe and analyze two such novel probe systems.

V.A E-FIELD PROBE BY ELASTIC NONLINEARITY

The simplest way of generating a high-frequency electric field probe with SAWs is to make use of the nonlinear properties of the piezoelectric (e.g., $LiNbO_3$) on which SAWs propagate. Thus, if two counterpropagating (ω, $\pm k$) SAW pulses are launched from transducers at opposite ends of a piezoelectric, as shown in Figure V.1, in the region where the pulses overlap, they will produce, via an appropriate quadratic nonlinearity, a localized electric polarization field at frequency 2ω. This is the interaction in a degenerate elastic convolver for SAWs — by now a highly developed signal processing device [1,2]. The strength of this nonlinear interaction can be appraised from known measurements on such convolvers. For YZ-$LiNbO_3$ the figure of merit ($M = V_{2\omega}/\sqrt{S_{a+}S_{a-}}$, see Appendix III) is found in the range $M \approx 10^{-4}$ to 10^{-5} V/W/meter of beam width. This is about one to two orders-of-magnitude smaller than the figure of merit for SAW convolvers employing free electrons, in an adjacent semiconductor or diode array, as the nonlinear mixing medium (see Appendix III).

The manner in which an array of diodes could be diagnosed by such an E-field probe is sketched in Figure V.2. The diode depletion capacitance could be changed with external light, for example, and this change would then be detected with the E-field probe. The sensitivity of such a measurement can be estimated with the aid of the equivalent circuit shown in Figure V-2(c). Assuming an equilibrium diode depletion capacitance $C_D \approx 2$pF, a gap spacing of 10 μm, as shown and YZ - $LiNbO_3$, we find $Cg = 10^{-2}$pF and $C_L = 10^{-1}$pF. Thus with $Cg << C_L << C_D$,

$$V_{out} \approx V_{2\omega}\frac{Cg/C_L}{1 - Cg/C_D} \qquad (1)$$

and

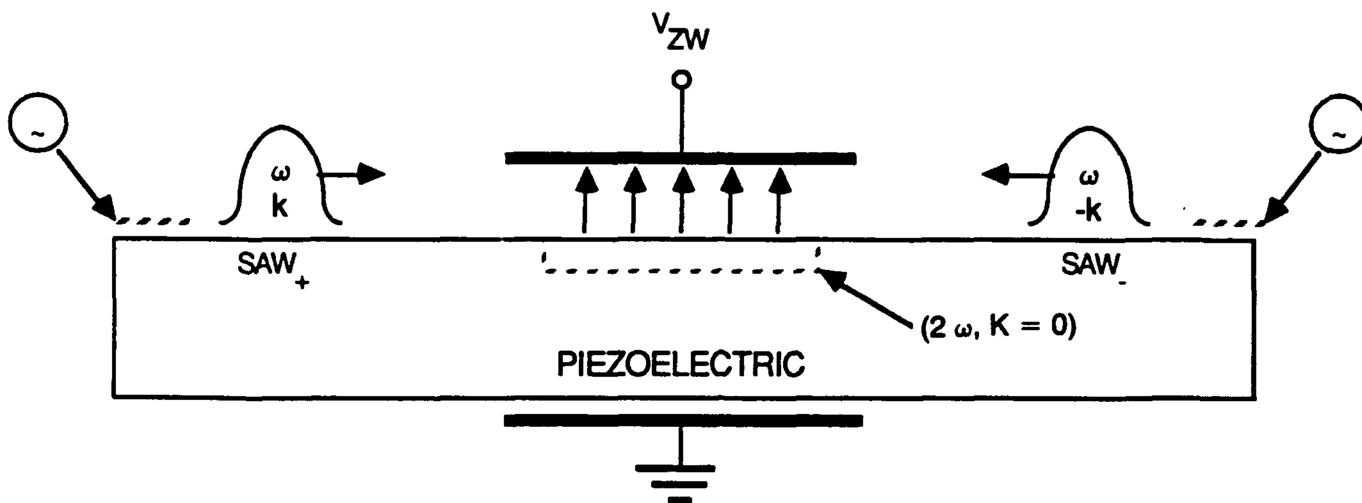

Figure V.1 Convolution of SAW pulses on a piezoelectric and the resultant E-Field to a metal plate above the surface.

$$\delta V_{out} \approx V_D \frac{C_g}{C_L} \left(\frac{\delta C_D}{C_D}\right) \tag{2}$$

Assuming $V_D \approx 2mV$, so that the diode is not driven too far from equilibrium, we find for $(\delta C_D/C_D)$ = 0.1, $\delta V_{out} \approx 20\mu V$. The rms noise voltage at the output is $\approx (4\kappa T/2\pi C_L)^{1/2}$ which at 77 K is about $80\mu V$. Hence, with some 10 to 20 dB of signal processing, which can be easily implemented (see text), small changes in depletion capacitance should be readily measurable.

The required SAW power densities, and total powers, can also be estimated. Using the known figure of merit for YZ - $LiNbO_3$, $M \approx 5x10^{-5}$ and V_D = 2mV, which for the above parameters entails $V_{2\omega} \approx 0.4V$, we find a required SAW sheet power density $S_a \approx 10^4 W/m$. Choosing a beam width of 100 μm ($\approx$ diode diameter), and a frequency of 150 MHz ($\lambda \approx 25\mu m$), the acoustic power required is $\approx$ 1W; the acoustic power density is then $\approx 4x10^8 W/m^2$. Recalling from Appendix I that linear excitation is limited to power densities of $\approx 10^6 W/m^2$, we require beam compressions of $\approx$ 100. This is achievable [2] with dispersive overlays so that second harmonic SAW generation (see Appendix I) is negligible.

V.A.1 Diode D-Field from the Nonlinear Elastic Probe

In probing the diodes we are interested in the normal electric displacement field at the diode surface (see Appendixes III and IV). Given that an elastic convolver-type interaction can create a localized polarization field on the surface of the piezoelectric, we now seek to determine the (short-circuit) normal D-field this will produce at the surface of the diodes.

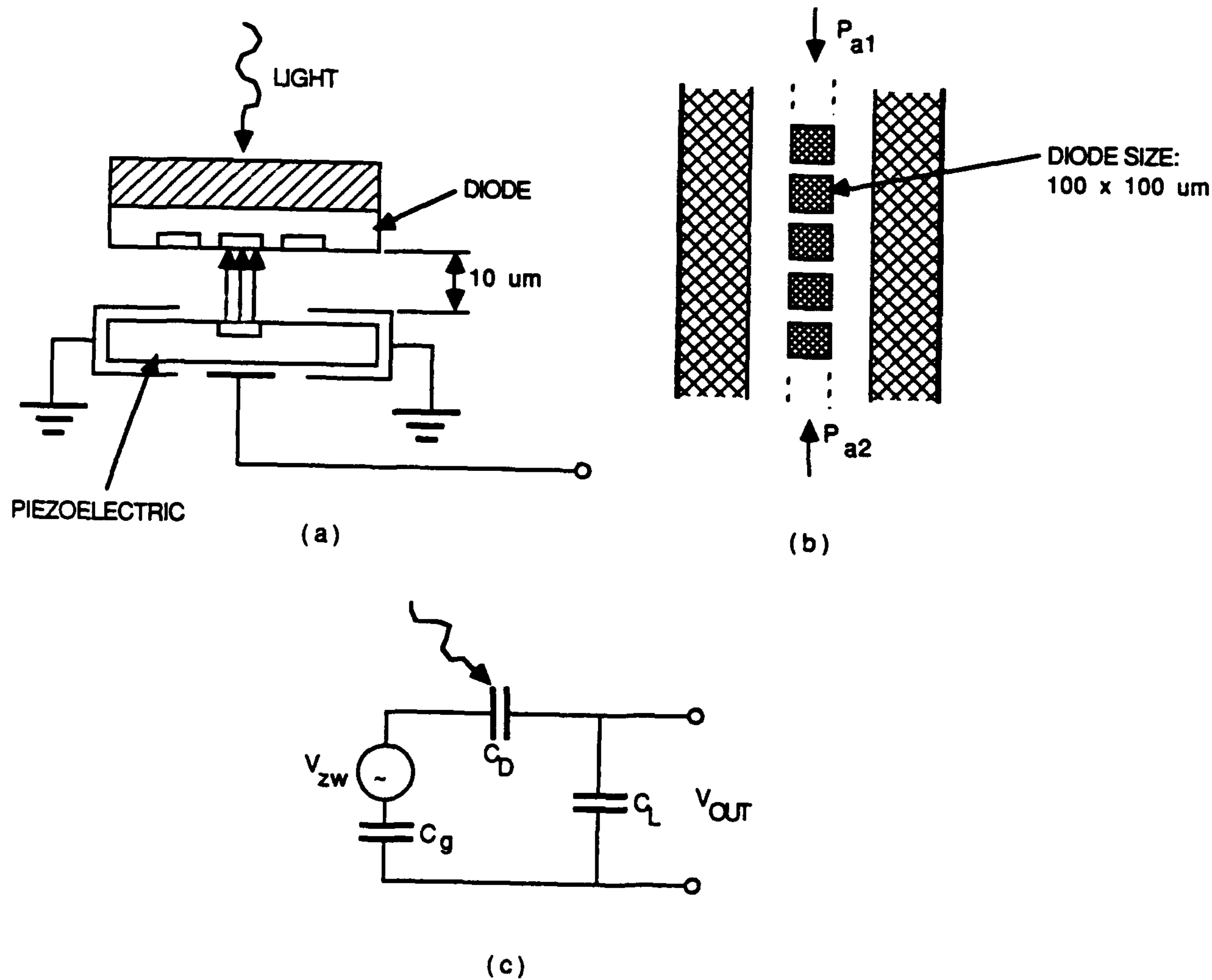

Figure V.2 (a) E-field probe nonlinearly generated by SAW's on a piezoelectric, adjacent to a diode array. (b) Top view. (c) Equivalent circuit for calculating output.

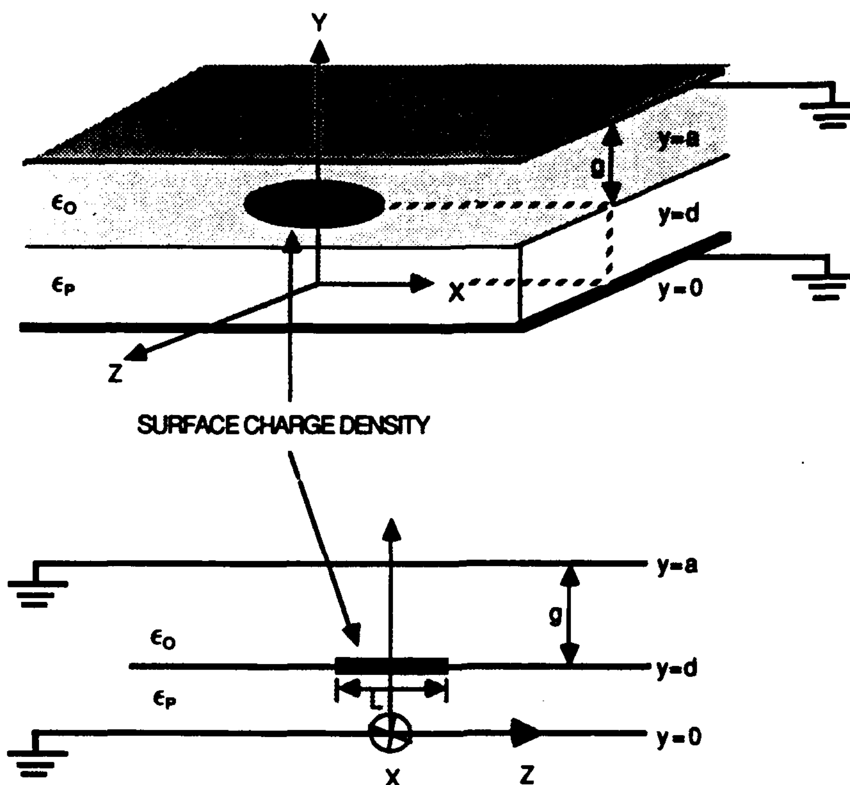

Figure V.3 Model structure for calculating the normal D-Field at the diodes due to a surface charge density on an adjacent piezoelectric.

From the simplest model of the elastic nonlinear interaction for the convolver [3], we can find the approximate magnitude of the nonlinear polarization:

$$P_{NL} \approx \frac{\epsilon_p}{\lambda} \; M \; \sqrt{S_{a+} S_{a-}} \tag{3}$$

We take this polarization to be a localized surface charge density on the piezoelectric surface, as shown in Figure V.3. To be definite, assume that the two counterpropagating SAW signals have gaussian pulse shapes, and the SAW beam shape is also gaussian, as shown in Figure V.4, so that the resultant nonlinear surface polarization charge has a symmetric, two-dimensional gaussian structure

$$\sigma(r) = \sigma_p e^{-r^2/2L^2} \tag{4}$$

where $r^2 = x^2+z^2$. (Note that, since in the nonlinear interaction the beam width becomes squared, the SAW pulse widths were chosen to be half the beam width.)

The electrostatic field problem for the configuration given in Figure V-3 is readily solved by Fourier-Bessel transform techniques [4]. The electric potential in the free space (ϵ_o) and in the piezoelectric (ϵ_p), satisfying the boundary conditions at y = o and y = a, are:

$$\Phi_p(r,y) = \int_o^\infty \alpha \; J_o(\alpha r) \; \phi(\alpha) \; \frac{\text{sh} \; \alpha y}{\text{sh} \; \alpha d} \; \frac{d\alpha}{2\pi} \tag{5}$$

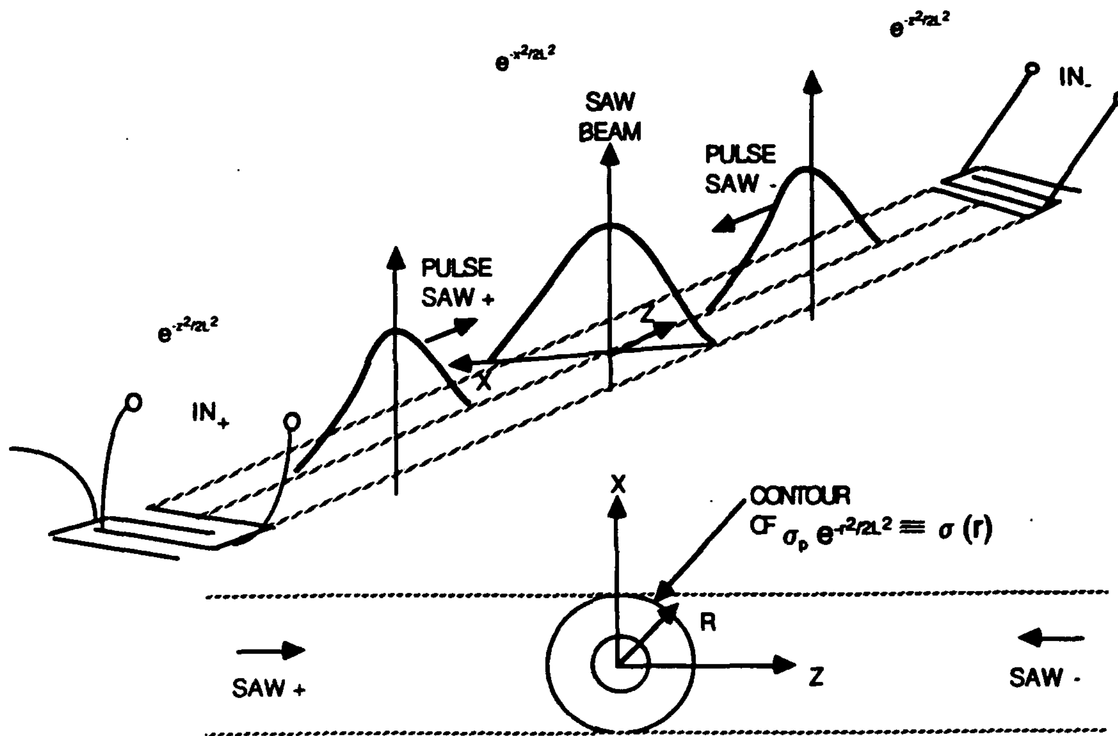

Figure V.4 (a) Counterpropagating SAW's with gaussian pulse signals, and with a gaussian beam shape, which will nonlinearly produce a symmetric, two-dimensional gaussian surface charge (b).

$$\Phi_p(r,y) = \int_0^\infty \alpha\ J_o(\alpha r)\ \phi(\alpha)\ \frac{\text{sh}\ \alpha(a-y)}{\text{sh}\ g}\ \frac{d\alpha}{2\pi} \tag{6}$$

where J_o is the ordinary Bessel function of order zero and sh is the hyperbolic sine function. Further, letting

$$\sigma(r) = \int_0^\infty \alpha\ J_o(\alpha r)\ S(\alpha)\ \frac{d\alpha}{2\pi} \tag{7}$$

$$S(\alpha) = \int_0^\infty J_o(\alpha r)\ \sigma(r)\ 2\pi r\ dr \tag{8}$$

and applying the boundary condition at y = d, we find

$$\phi(\alpha) = \frac{S(\alpha)/\epsilon_0\alpha}{\text{cth}\ \alpha g + K_p \text{cth}\ \alpha d} \tag{9}$$

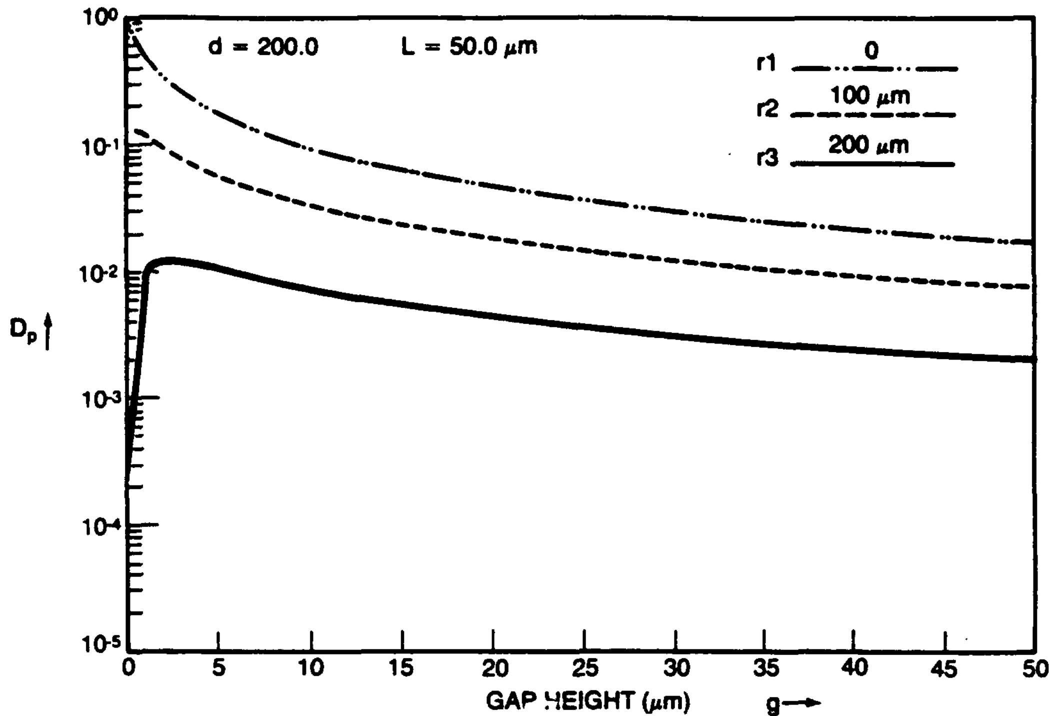

Figure V.5a Normalized, (short-circuit) normal D-Field, D_p, at diodes (see Figure V.3) as a function of gap height g, and for three radial $[r = (x^2 + z^2)^{1/2}]$ positions. Calculations based upon Eqs (11) and (12), with $K_p = 50$, d = 200 μm. (a) L = 50 μm

where cth is the hyperbolic cotangent function, and $K_p = \epsilon_p/\epsilon_o$. Defining the normalized (short-circuit) normal D-field on the diodes as

$$D_p = \frac{D_y(y=a,r)}{\sigma_p} = -\frac{\epsilon_o \partial \Phi_o}{\sigma_p \, \partial y}\bigg|_{y=a} \tag{10}$$

and using (4) in (8), we obtain

$$D_p = \int_o^\infty \xi e^{-\xi^2/2} \frac{J_o(r_n \xi)}{G_p(g_n \xi, d_n \xi)} d\xi \tag{11}$$

where

$$G_p = (\text{ch } g_n\xi) + Kp(\text{sh } g_n\xi)(\text{cth } d_n\xi) \tag{12}$$

and we have normalized all lengths to L: $r_n = r/L$, $g_n = g/L$, $d_n = d/L$ and $\xi = \alpha L$. Note that for $g_n = 0$ (no air gap), $G_p = 1$ and $D_p = \exp(-r_n^2/2)$, as would be expected.

Figures V.5a-c show the variation of D_p as a function of g, at three different radii, for a fixed value of d (d = 200 μm) and L = 50 μm in Figure V.5a, L = 100 μm in Figure V.5b, and L = 150 μm in Figure V.5c. From these results we can make two observations. First, in all cases the rate of decrease in D_p with increasing gap height decreases rapidly; in fact, above a certain gap (which increases with L) the decrease in D_p is very slow. Second, as L increases the spread in D_p with radius decreases. Thus for a 100 μm diameter diode, choosing L = 50 μm may give a too rapid decrease of D_p

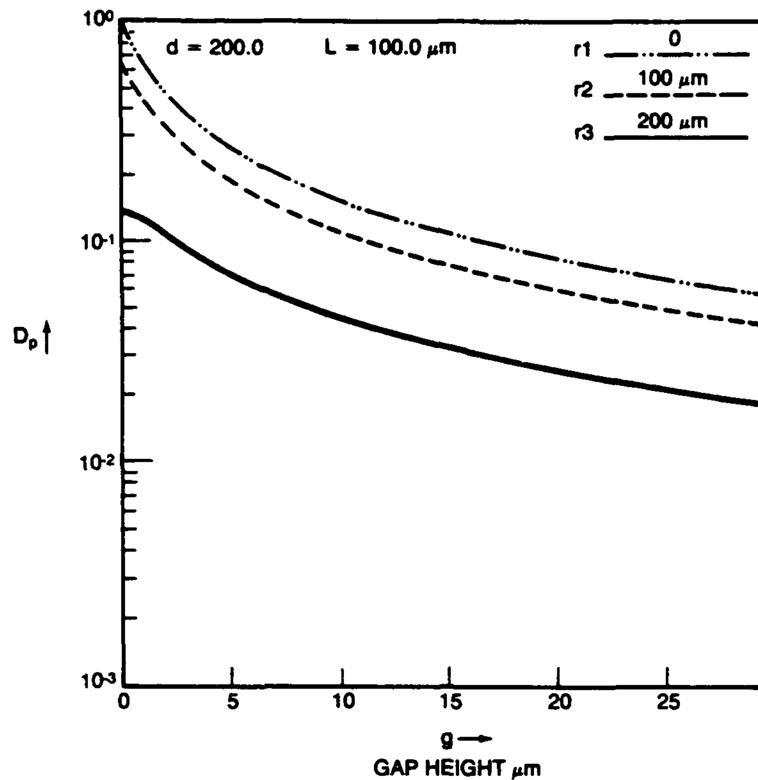

Figure V.5b Normalized, (short-circuit) normal D-Field, D_p, at diodes (see Figure V.3) as a function of gap height g, and for three radial $[r = (x^2 + z^2)^{1/2}]$ positions. Calculations based upon Eqs (11) and (12), with $K_p = 50$, $d = 200\ \mu m$.
(b) $L = 100\ \mu m$

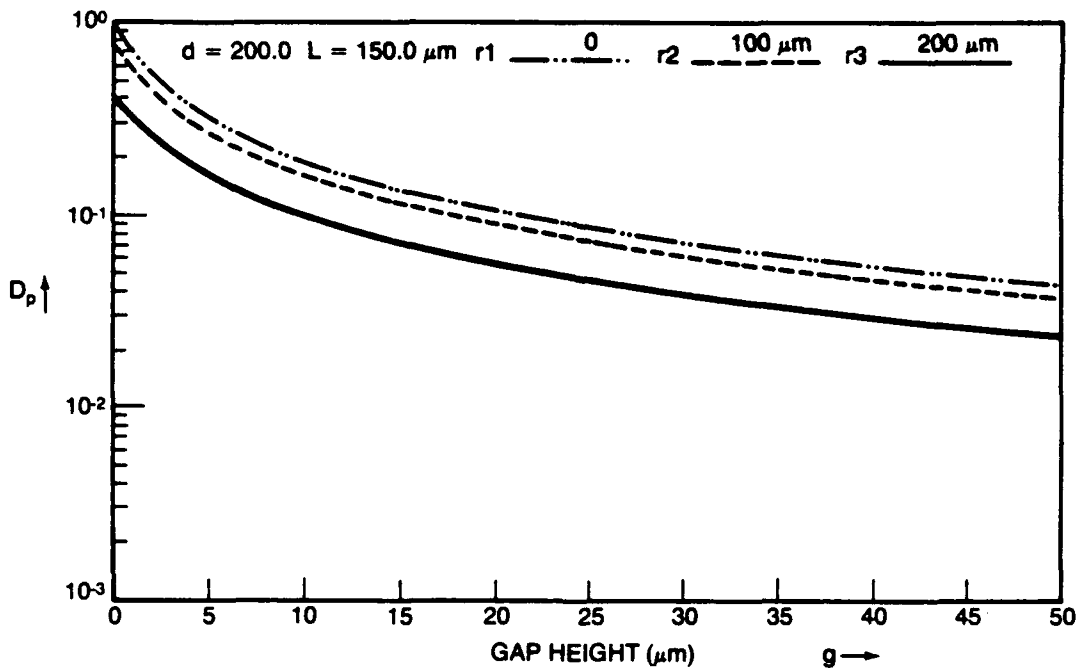

Figure V.5c Normalized, (short-circuit) normal D-Field, D_p, at diodes (see Figure V.3) as a function of gap height g, and for three radial $[r = (x^2 + z^2)^{1/2}]$ positions. Calculations based upon Eqs (11) and (12), with $K_p = 50$, $d = 200\ \mu m$.
(c) $L = 150\ \mu m$

with radius over a single diode. On the other hand, with L = 150 μm there is not enough of a decrease of D_p with radius, so that D_p may drive more than one diode. Clearly, for a desired probe resolution a compromise must be sought. From other calculations, not shown, as d is increased, for a fixed L, the different r-curves come closer together, as in the figures shown when L is increased.

Finally, since a diode will respond to the total charge induced on its surface, we calculate the total charge in a given radius $r = r_o$, at $y = a$, normalized to total charge on the piezoelectric surface:

$$Q_n(r_o) = \frac{\int_o^{r_o} D_y(y = a,r)\ 2\pi r\ dr}{2\pi L^2 \sigma_p} = \int_o^{r_{on}} D_p r_n dr_n \tag{13}$$

Using (11) this is readily found to be

$$Q_n(r_o) = r_{on}\int_o^{\infty} e^{-\xi^2/2} \frac{J_1(r_{on}\xi)}{G_p(g_n\xi, d_n\xi)} d\xi \tag{14}$$

For $g_n = 0$, $G_p = 1$ and (14) evaluates to $Q_n(r_o) = 1\text{-}\exp(-r^2_{on}/2)$ as might be expected. For finite g_n (14) can be evaluated numerically just as easily as (11) was. Unfortunately, due to lack of funds this was not done.

V.B E-FIELD PROBE BY ELECTRON NONLINEARITY

In a piezoelectric semiconductor two counterpropagating SAW pulses can also produce a localized electric field by convolver action through the nonlinearity in the free electron dynamics. Such is the case in GaAs, for example. Signal processing SAW convolvers have been successfully built using epitaxial n-type GaAs grown on n^+ and semi-insulating substrates [5,6]. For (100)-cut, [100]-propagating GaAs, the convolver merit factor is found to be $M \approx 1\text{-}3\times10^{-3}$ V/W/meter of beam width, i.e., about two orders-of-magnitude larger than for an elastic convolver on YZ-$LiNbO_3$, as was already remarked.

For the purpose of generating an E-field probe, semiconducting regions would have to be ion-implanted into semi-insulating GaAs. SAWs on (100)-[110] GaAs have their electric potentials peaked near the surface, about half of a SAW wavelength below it [5]. Since reliable ion-implants can be made to depths of 5 μm or less, such an E-field probe will require using rather high-frequency SAWs. For example on (100)-[110] GaAs at f = 360 MHz the SAW $\lambda \approx 8\mu$m, which should be adequate. A schematic of the configuration for such a probe is shown in Figure V.6. The equivalent circuit for calculating the output, the sensitivity to δC_D, and the required SAW power densities, are similar to what we showed in sub-Section V.A, but, of course, with parameters relevant to the GaAs configuration in Figure V.6. We therefore do not detail these calculations here again.

V.B.1 Diode D-Field from the Nonlinear Semiconductor Probe

The convolution of two counterpropagating SAWs in the implanted semiconductor layer can also be viewed as generating a localized charge layer at frequency 2ω. For SAW pulse shapes and SAW beam width as shown in Figure V-4, we then consider the electrostatic field problem in the configuration of Figure V-7, where the surface charge layer at y = d is taken to be

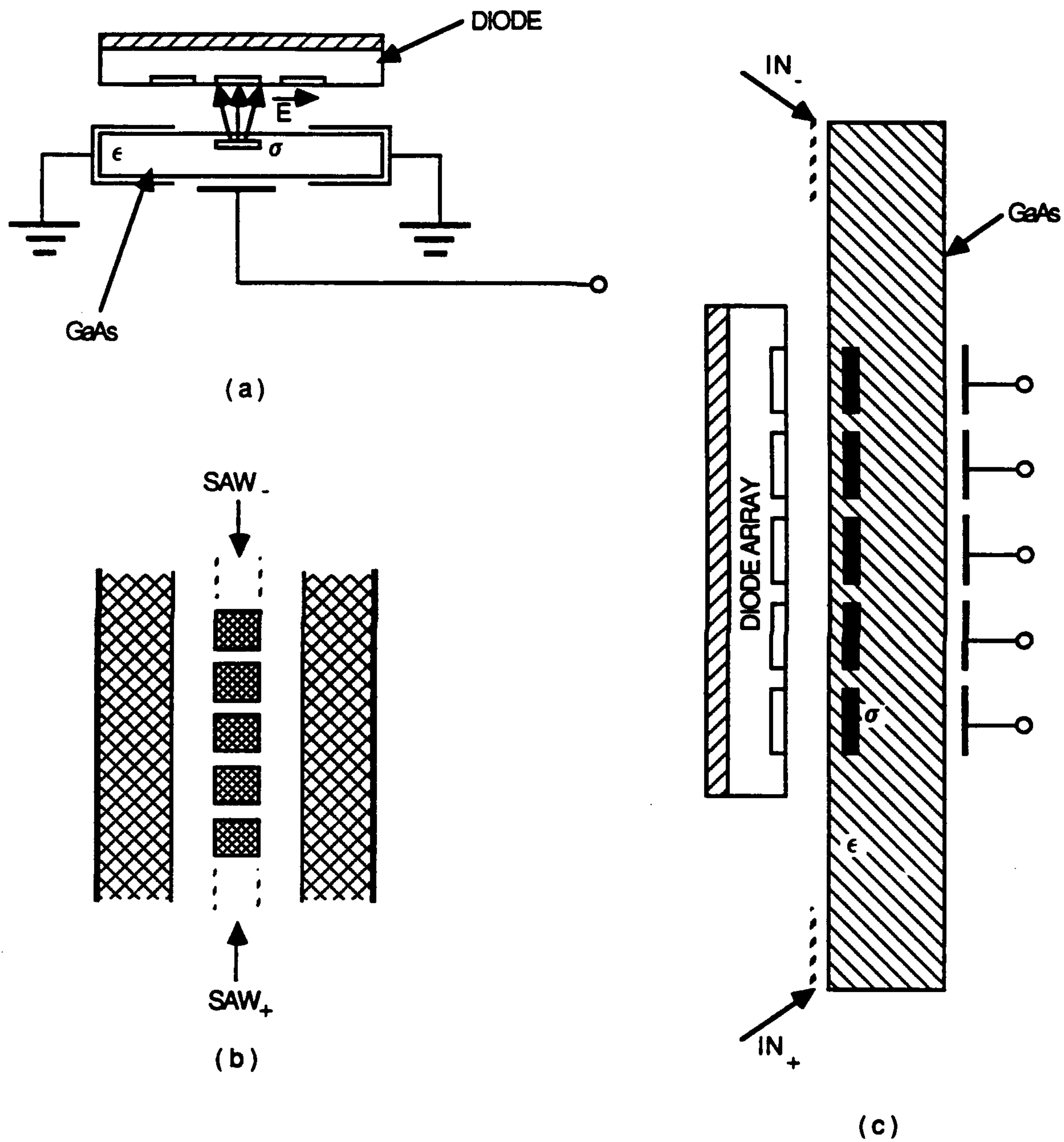

Figure V.6 (a) E-Field probe nonlinearly generated by SAWs in semi-insulating GaAs with ion-implanted semiconductor strips. (b) Top view. (c) Side view.

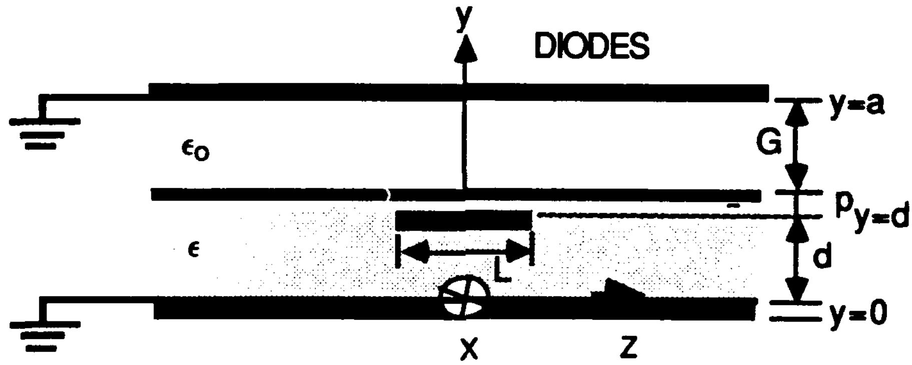

Figure V.7 Model structure for calculating the normal D-Field at the diodes due to a surface charge layer generated below the surface of a semi-insulating adjacent material.

$$\sigma(r) = \sigma_s\, e^{-r^2/2L^2} \tag{15}$$

Following along lines similar to the analysis described in subsection V.A.1, and accounting for the additional boundary condition, we now find the normalized (short-circuit) normal D-field to be given by

$$D_s = \frac{D_y(y = a,r)}{\sigma_s} = \int_o^\infty \xi\, e^{\xi^2/2} \frac{J_o(r_n\xi)}{G_s(g_n\xi, d_n\xi, p_n\xi)} d\xi \tag{16}$$

where

$$G_s = (\mathrm{ch}\ g_n\xi)(\mathrm{ch}\ p_n\xi) + K(\mathrm{sh}\ g_n\xi)(\mathrm{sh} p_n\xi)$$

$$+ [K(\mathrm{sh}\ g_n\xi)(\mathrm{ch}\ p_n\xi) + (\mathrm{sh}\ p_n\xi)(\mathrm{ch} g_n\xi)](\mathrm{cth}\ d_n\xi) \tag{17}$$

and again all dimensions have been normalized to L.

Figures V-8a-c illustrate the behavior of D_s as a function of gap height at three different radii, and for three values of L: (a) 50 μm, (b) 100 μm, and (c) 150 μm. For all of these curves the implant depth (p = 5 μm) and the semi-insulating GaAs layer thickness (d+p = 10 μm) were kept constant; $K = (\epsilon/\epsilon_o) = 13$ was taken as appropriate for GaAs. Extensive numerical integrations of (15) were again not carried out due to lack of funds. We note that the general trends are similar to the piezoelectric probes. For small g, D_s drops rapidly but then becomes essentially constant; hence, if the nonlinear surface charge amplitudes are significantly large, large gaps become practical. (Note that

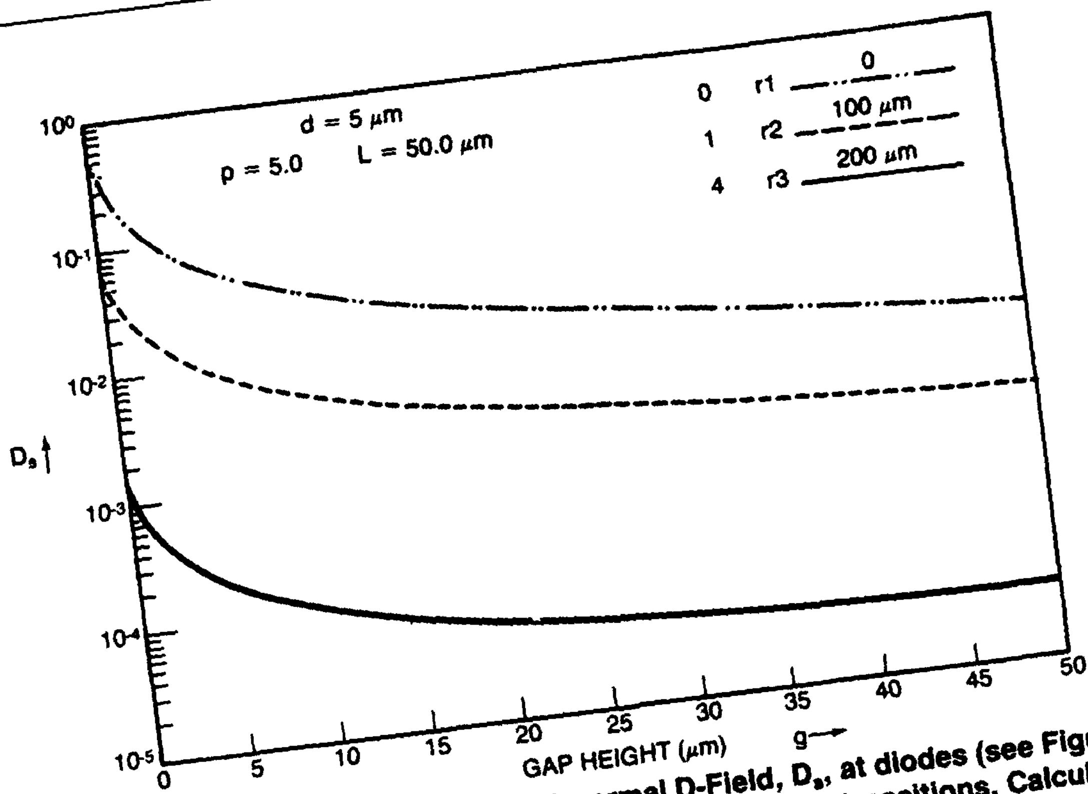

Figure V.8a Normalized, (short-circuit) normal D-Field, D_s, at diodes (see Figure V.7) as a function of gap height g, and for three radial $[r = (x^2 + z^2)^{1/2}]$ positions. Calculations based upon Eqs (16) and (17), with K = 13, p = 5 μm and d = 5 μm.
(a) L = 50 μm

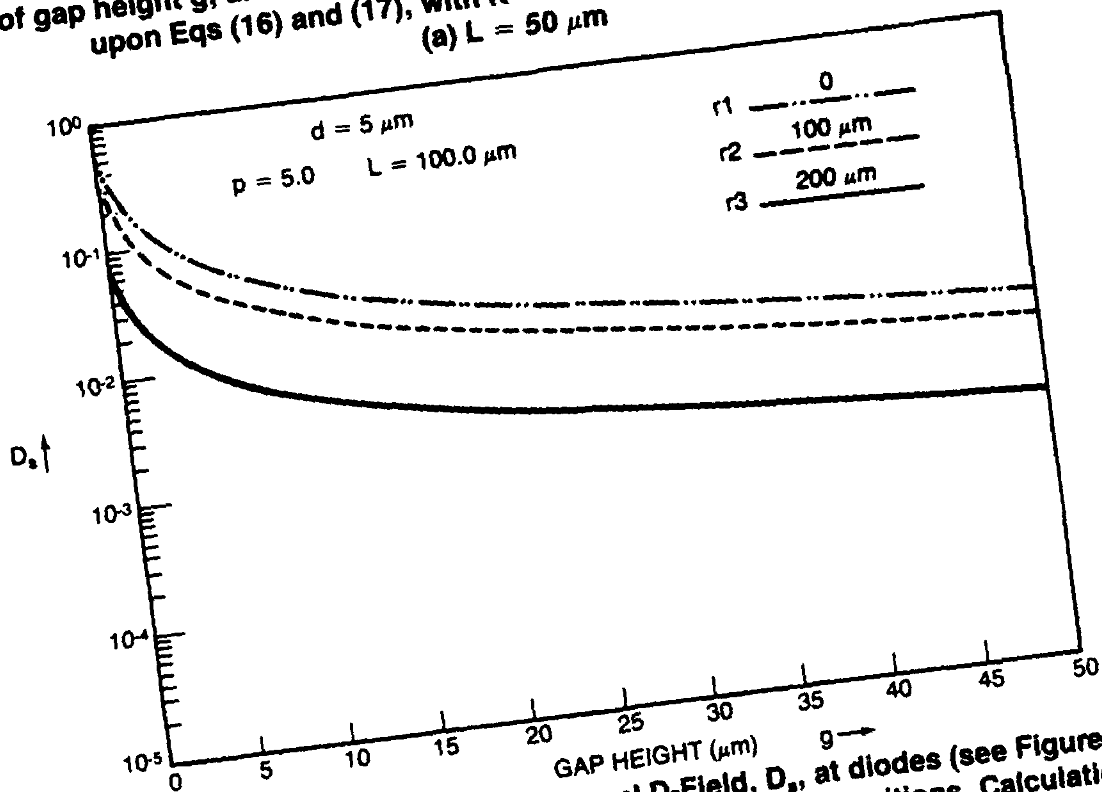

Figure V.8b Normalized, (short-circuit) normal D-Field, D_s, at diodes (see Figure V.7) as a function of gap height g, and for three radial $[r = (x^2 + z^2)^{1/2}]$ positions. Calculations based upon Eqs (16) and (17), with K = 13, p = 5 μm and d = 5 μm.
(b) L = 100 μm

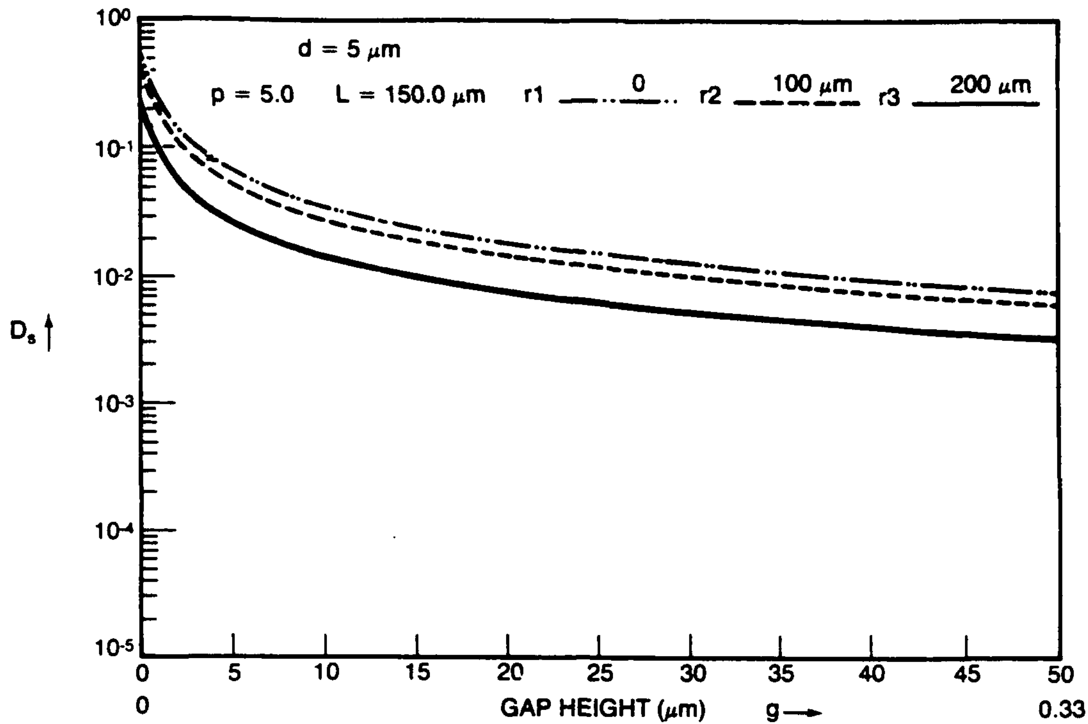

Figure V.8c Normalized, (short-circuit) normal D-Field, D_s, at diodes (see Figure V.7) as a function of gap height g, and for three radial $[r = (x^2 + z^2)^{1/2}]$ positions. Calculations based upon Eqs (16) and (17), with K = 13, p = 5 μm and d = 5 μm.
(c) L = 150 μm

we expect $\sigma_s >> \sigma_p$ since $M_s >> M_p$). Probe resolution depends again on the choice of L (i.e., the implanted nonlinear SAW interaction region); too small an L may give inadequate excitation of even a single diode, while too large an L may not allow resolving an individual diode. Because of the required finite depth of implantation, the values of D_s for g = 0 are reduced from what they would be if p were zero. Finally, as mentioned in the case of the elastic probe, one should calculate the total charge induced on a diode by integrating (16), as was done in (13). Again, because of limitations in funds and time, this was not done. It is hereby recommended that such calculations should be carried out for a continuation of this work, and in particular in relation to the design of a feasibility experiment for producing and testing such probes.

V.C REFERENCES FOR APPENDIX V

[1] R.B. Thompson and C.F. Quate, J. Appl. Phys. *42*, 907 (1971).

[2] Ph. Defranould and C. Maerfeld, Proc. IEEE *64*. 748 (1976).

[3] M. Luukkala and J. Surakka, J. Appl. Phys. *43*, 2510 (1972).

[4] J.D. Jackson, *Classical Electrodynamics*, second edition, John Wiley & Sons 1975, Chapter 3.

[5] T.W. Grudkowski, M.L. Report No. 2440, W.W. Hansen Lab., Stanford Univ., Stanford, Calif. 1975.

[6] T.W. Grudkowski, C.K. Motress, M. Gilden and J.F. Black, IEEE Trans. MTT-29, 1348 (1981).

APPENDIX D
OPTICAL TESTING

APPENDIX D
OPTICAL TESTING

The possibilities of using optical, or optical and electrical testing techniques for RoA determination are investigated in this section. It will be assumed that the n-type base layers are not Shockley Read recombination limited; therefore the excess majority and minority carrier lifetimes and concentrations are comparable. The FPA diodes to be evaluated are configured for typical back n-side illumination for IR detection. The front p-side may, or may not already have a metallization bump at the center with the remaining surface area passivated.

As noted earlier, electrical test techniques are considered essentially contactless as far as the probing of individual diodes is concerned, if the electrical contacts are n-side ground contacts placed at the periphery of the FPA unit that is being tested. Two types of testing approach may be used, these are:

- Measurement of probing signals proportional to the total number of excess carriers induced in the n-region and relating these to the RoA.
- Measurement of the frequency response in the number of modulated excess carriers and relating this to the space charge discharge time $\tau_{RC} = (RoA)\, C_j$.

Frontside photogeneration is preferred for either type of measurement approach because the analysis is simpler. The excess carrier frequency response for a thin diode, or a diode in which $\tau_{RC} >> \tau_p$ is given by equation 3.21. This equation is modified to

$$\Delta\bar{n}(\omega) = RoA\left[\frac{1}{(RoA)_{diff}} + \frac{C_j}{\tau_p}\right]\frac{\bar{Q}\tau_p}{(1+\omega^2(\tau_p+\tau_{RC})^2)^{1/2}} \qquad 1$$

If the base material thickness, lifetime, interface recombination and junction capacitance do not vary much across the diode array, then $\Delta\tilde{n}(\omega)$ can be directly related to the RoA of each diode. For good diodes with RoA ~ 100 ohms cm^2, $C_j \sim 6 \times 10^{-8}$ F/cm^2 $\tau_{RC} \sim 6\mu s >> \tau_p$. Then, at low frequencies.

$$\Delta\bar{n} = \bar{Q}\tau_{RC} = \bar{Q}(RoA)\,C_j \qquad 2$$

In addition, if measurements are performed in the presence of a high background photo-bias (Q_o ~ high 10^{16} photons/cm^2-s range), the lifetime may also be obtained since τ_{RC} can be considerably reduced, i.e.

$$\tau_{RC} = (RA)\,C_j = \frac{(RoA)\,C_j}{(1 + e\,(RoA)\,Q_o/(kT/e)} \qquad 3$$

to levels well below the excess carrier lifetime τ_p.

When $\tau_{RC} \lesssim \tau_p$, and the RoA is significantly below its diffusion limit, the diode impedance may be much more difficult to assess. The problem is then similar to that of evaluating the recombination parameters S, τ in a single thin n-type layer when the measured effective lifetime τ_{eff} depends on both, i.e., $\tau_{eff} = \tau/(1 + S\tau/L)$.

1. RoA EVALUATION BY OPTICALLY MODULATED ABSORPTION

The possibility of monitoring the excess carrier concentration $\Delta\tilde{n}\,(\omega)$ by either of two different OMA approaches is evaluated in this section. The technique, variously referenced as Optically Modulated Absorption (OMA) or Light Induced Modulation of the Absorption (LIMA) has been applied to the evaluation of several direct and indirect gap semiconductors. The technique has been applied to HgCdTe using probe beams for monitoring the absorption and transmission changes with energy both below the energy gap* and around the energy gap.†

Case 1 Probe Energy Around The Bandgap Energy

The possibility of using a probe beam with energy close to the bandgap energy has been investigated and found to be unlikely because the probe beam itself also results in some photogeneration. Since optical modulations are generally small and the probe beam intensity must be low the sensitivity of this technique is not good.

---

*. Lifetime Measurement in $Hg_{0.7}Cd_{0.3}Te$ by Population Modulation, Appl. Phys. Lett., 38, 261 (1981).
†. Photoabsorptance and Electron Lifetime Measurements in HgCdTe, J. Vac. Sc. Tech. 3, 259 (1985).

OMA measurements on large area p-on-n LWIR HgCdTe double layers have confirmed the significant influence of the junction space charge modulations at lower backgrounds.* However, the lowest modulated flux levels that could be used for non-delineated wafer sized diode evaluation with a comparable intensity probe beam are predicted to be around 5×10^{15} photons/cm^2 s. When the complication of a limited diode area is added it is recognized that this technique must probably be excluded.

Case 2 Probe Beam Energy Below the Bandgap Energy

Carrier concentration changes also produce changes in the optical absorption below the bandgap. The following examines the possibility of monitoring those absorption changes with a probe beam with a wavelength around 16 µm.

The hole absorption cross-section σ_p in LWIR HgCdTe at 77 K and around 16 µm is much greater than for electrons with $\sigma_p \sim 2.5 \times 10^{-15}$ cm^2.† Low photogeneration modulations with $\tilde{Q} \approx 10^{15}$ photons/cm^2 s and diode τ_{RC} values around 6 µs will result in excess hole modulations on the p-side similar to the electron modulations on the n-side $\Delta\tilde{p} \approx 6 \times 10^9$/cm^2 s. These carrier modulations will in turn result in small modulations in the transmitted intensity $\tilde{I}_t$ of a probe beam given by

$$\frac{\Delta\tilde{I}_t}{I_t} = -\sigma_p \Delta\tilde{p} = -1.5 \times 10^{-5} \qquad (4)$$

A 16 µm probe beam focussed on a good diode with 10 µW of transmitted energy should therefore be modulated by about 150 pW. Under these conditions, a 20 Hz measurement bandwidth and a 50% quantum efficiency in a 16 µm radiation sensing detector the BLIP limited S/N ratio will be about 40. To achieve this S/N ratio, the testing detector would have to be cooled below 77 K in order that it not be thermally limited.

Since the analysis indicates that a below bandgap energy probe approach should work, the practical details of a possible test approach are briefly assessed. The pump beam could be a short wavelength laser imaged with known photon flux on the layer, but not on the metallization if this is already

---

*. Optical Evaluation of LWIR HgCdTe p-on-n Double Layers, IRIS Materials Group Meeting, NPGS, Monterey, August 12, 1989

†. Optical Absorption Below the Absorption Edge in $Hg_{1-x}Cd_xTe$, J. Appl. Phys., 54, 2041 (1983).

present. The probe beam could be a CW 16 μm CF_4 laser.* This simple type of gas laser is preferred over a tunable lead salt diode laser system which is complicated, less reliable and does not provide good beam quality. The probe laser, although focussed, would still effectively flood illuminate the diode due to the considerable diffraction spread at 16 μm. The transmission modulations would be picked up by a long cut-off wavelength detector cooled below 77 K and positioned behind the n-side of the FPA unit.

2. RoA EVALUATION BY PHOTOLUMINESCENCE (PL)

The presence of excess carriers may also be monitored by PL if the lifetime of the base layer is known. However, there is a subtle difference between the OMA techniques and PL technique. Absorption and conductivity modulations of the base layer depend on the **total** number of excess carriers. In contrast the PL technique depends on the departure of carrier concentrations from their thermal equilibrium values. The modulation of the n-layer thickness in this case is a negligible effect. The PL emission rate can be expressed as

$$\bar{Q}_{PL}(\omega) = W_r \times \Delta\tilde{n}(\varpi) = \frac{1}{\tau_r} \times \left(\frac{RoA}{RoA_{diff}}\right) \frac{Q\tau_p}{(1+\varpi^2(\tau_p+\tau_{RC})^2)^{1/2}} \qquad 5$$

where W_r, τ_r are the radiative transition rate and lifetime, and the same base layer restrictions $d_n/L_{po} << 1$ or $\tau_{RC} >> \tau$ still exists to obtain the simplest form for $\Delta\tilde{n}(\omega)$.

For a diffusion limited diode and low frequency

$$\bar{Q}_{PL} = \bar{Q}(\tau_p/\tau_r) \qquad 6$$

The number of PL emitted photons which escape through the AR coated substrate backside and are collected by a test detector can now be expressed as

$$\tilde{N}_{PL} = \bar{Q}_{PL} \times \eta_{sa} \times \mathrm{Sin}^2(\theta/2) \qquad 7$$

*. Continuous Wave 16 μm CF_4 Laser, IEEE QE-19, 10, 1469 (1983)

where the PL collection FOV half angle $\theta/2$ is limited to 17 degrees by total internal reflections at larger angles, and η_{sa} is the average PL self absorption coefficient estimated to be 0.3 for a 15 µm thick base layer.

We will assume all the escaping radiation is collected, τ_p has been determined with a frequency response rolloff at high Q_o bias levels, and τ_r is constant. If τ_r = 20 µs then

$$\tilde{N}_{PL} \approx 10^{-3}\tilde{Q} \qquad 8$$

This means that only about 1 in 10^3 photogenerating pump photons end up producing a collected PL photon. If $\tilde{Q} = 10^{15}$ photons/cm^2-s and the detector area is 10^{-4} cm^2, the rms PL signal power would be only 1 pW.

The analysis indicates that a PL approach is unlikely to be useful for good RoA diodes, and particularly diodes with much smaller dimensions. However, the technique may be useful for quickly identifying diodes with very low RoA when much higher photon fluxes can be used. From an engineering test setup and operating point of view, the PL technique is probably one of the simplest to implement.

3. LATERAL PHOTO INDUCED MODULATION EFFECTS

When a light spot is scanned across a diode a lateral photocurrent will flow as shown in Figure D-1 and a photovoltage develops, except when the diode and illumination are uniform and centered symmetrically. These effects have long been recognized.* More recently the techniques have been refined and frequently referred to as OBIC or LBIC (Optical or Laser Induced Currents)

When the junction impedance R_o is much greater than the cap or base layer lateral resistance R_c, R_B the forward diffusion current will be uniformly distributed across the diode area. This is the typical situation with LWIR diodes and it is easy to show that the maximum lateral voltage at either sample edge is given by

$$\tilde{V}_{lpv} = \tilde{I}_{ph} \times R_B/2 = e\eta\ \tilde{Q}\ R_B/2 \qquad 9$$

and R_B is the sheet resistance value of the higher resistance layer. The measurement then does not reflect a value for R_o, except for the case of drastically low R_o values.

*. A New Semiconductor Photocell Using Lateral Photoeffect, Proc. IRE, 45, 474 (1957)

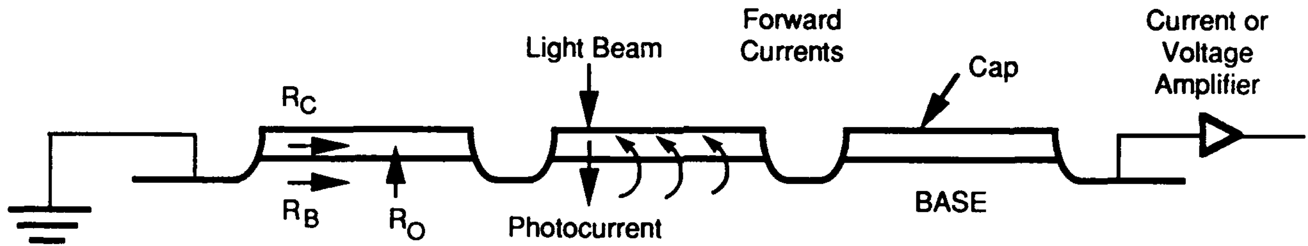

Figure D-1. Section Through a Diode Illuminated by a Narrow Strip of Light Whose Length Equals the Diode Width

4. RoA EVALUATION FROM PHOTO-CONDUCTIVITY MODULATIONS

The same pump beam that produced the lateral effects can also produce a transverse increase of the n base layer resistance as the space charge layer width decreases and the effective thickness of the n-region increases. This effect is independent of the position of the pump beam for typical area diodes.

Table 3-1 gives the expressions for the magnitudes of the excess carrier concentrations. For an estimate of the magnitude of the conductivity modulation we consider an FPA which on the whole provides diodes with RoA values of typically 100 Ωcm^2, the junction capacitance near zero bias is $Cj \sim 6x10^{-8}$ F/ cm^2 and the lifetime in the 15 micron thick base layer is 1 μs. From equation 3.8 we see that a pump beam with flux $Q = 2x10^{14}$ photons/cm^2-s would not provide an excessive background. The fractional modulation in the base layer transverse conductivity G would be largely space charge modulation controlled with

$$\Delta G/G = n\Delta d/nxd = Q\ (RoA)\ Cj\ /\ nxd \sim 0.1\% \qquad 10$$

This result applies to a single isolated diode. Further sensitivity analysis of conductivity modulation measurements for FPA diode evaluation depends largely on the mxn FPA diode configuration and the location of the base layer ground pads. For large tightly packed mxm staring arrays where all the base layer sides are grounded there is little chance of extracting individual diode signals out of thousands of surrounding diodes. However, for smaller linear arrays, there is a good possibility of diode evaluation with

the appropriate distribution of grounds, and particularly if some of the grounds can be floated during the test routine. Further quantitative analysis of these possibilities was not pursued due to limitations in program funding.

APPENDIX E
UV PROBING

APPENDIX E
UV PROBING

The possibility of IR FPA 1-V probing based on UV induced photoelectron emission (as opposed to energetic primary E-beam emission) came to our attention early in the program. Although the UV technique appeared in several respects to be simpler and more sensitive than the E-beam technique, we did not pursue it because a quick means of evaluating the technique was not available until near the completion of the program. At that time a new company which had developed a commercial UV probing system was identified; the company was Ultraprobe located at Laguna Hills in California. Ultraprobe collaborated with Loral in the evaluation of several simple resistors representing diode impedances in the MWIR range. The following reports the preliminary findings.

DISCUSSION OF TECHNIQUE

In the UV probe technique light either from a laser[1] or a lamp[2] is focussed to a small spot on the metallized part under investigation. The light spot can be smaller than 1 μm in diameter In comparison to the ~1 KeV incident electrons in the E-beam technique the UV photons cause much less disruption of the surface being probed and therefore most of the work function instabilities which seriously limit the E-beam probe accuracy are effectively avoided.

Figure E-1 shows the components of the UV prober developed by Ultraprobe. A high pressure gas lamp is used as a source due to its inherent stability, ruggedness and low maintenance. Filters and beam splitters are used to remove unwanted wavelengths in the visible and the IR. A special reflective microscope has been designed to achieve a very small spot size with sufficient UV flux to produce measurable photoelectrons.

Secondary electron detection is simplified because the primary UV beam is not charged. This allows greater flexibility in the electron collection methods. Biased grids and plates can be positioned very close to the sample without affecting the primary beam, this is not the case of E-beam instruments.

---

1. "Energy and Time Resolved Photoemission in a Promising New Approach for Contactless IC Testing," Microelectronic Engineering 5, 547 (1986).
2. "Noncontact Voltage Measurement of VLSI Currents by Photo-Electron Simulation and Detection," International Symposium for Testing and Failure Analysis, Oct. 1988.

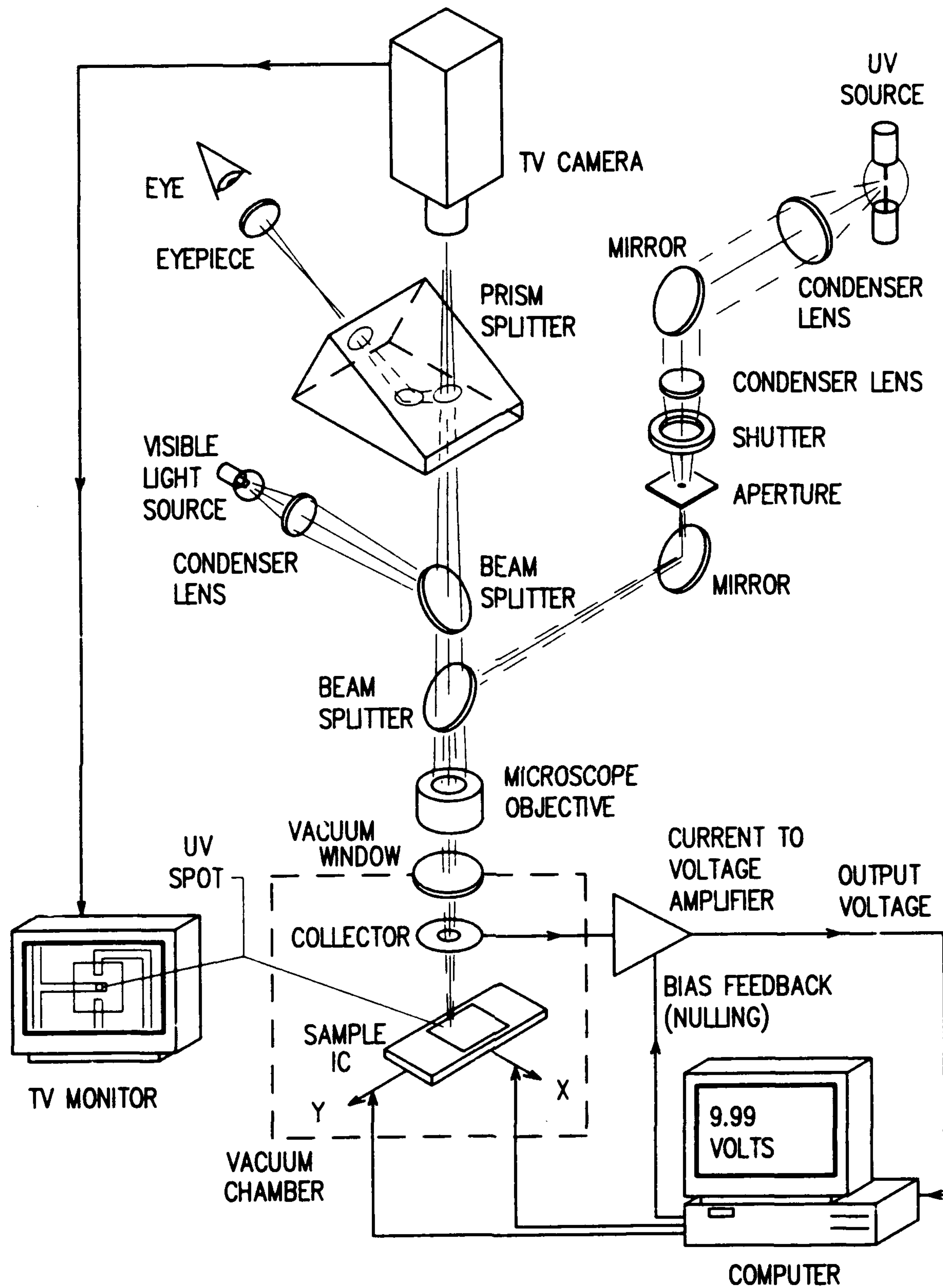

Figure E-1. Schematic of Ultraprobe's UV Probing System

The wavelength of the UV light is selected such that its energy is greater than the work function of the diode metal contact surface. The surface voltage is determined by analyzing the energy spectrum of the secondary electrons collected by a collector grid. The bias current is simply the electron current flowing through the circuit.

The UV technique requires a voltage calibration before 1-V measurements similar to that used in the E-beam technique. For calibration the same device metallization is first UV probed at a fixed UV flux and photoelectron emission level with the metallization at ground potential. The so-called nulling voltage on the collector is swept from an initial positive value that attracts all electrons to the least negative value that repels the most energetic electrons. These measurements which determine the system S-curve at zero bias are shown in Figure E-2. If the metallization potential is lowered slightly the potential on the collector grid needed to collect the same photocurrent as that obtained previously at zero bias is lowered by approximately the same amount. The relationship between the metallization voltage and the collector nulling voltage is then determined from the most sensitive part of the S-curve, i.e., the inflection point where $\partial^2 I/\partial Vnull^2=0$. The calibration data of Figure 2 indicate a calibration factor C_{cal} given by

$$C_{cal} = \partial Vnull/\partial V \text{ metal-surface} \sim (0.082/0.1) = 0.82 \text{ V/V}$$

The reason for C_{cal} not being unity is attributed to the fact that the nulling voltage is determined not only by the energy of the photoelectrons but by their emission trajectories.

When the calibration is complete the UV beam can be moved to similar metallization on a non-grounded diode in order to make a metal surface potential measurement at the same current.

PRELIMINARY RESULTS

Figure E-3 shows the preliminary results taken on 2 resistors with the beam incident on the Pb,Sn soldered leads. The analysis of these measurements is based on a photo-current close to 1 nA which was emitted from an appropriate 100 μm dia area of the resistor leads.

10^8 Ω Resistor Measurement

$$\Delta Vnull = 0.068 \text{ V} \rightarrow \Delta Vresistor = 0.08 \text{ V} \rightarrow R = \Delta Vresistor/I \sim 8\times10^7 \Omega$$

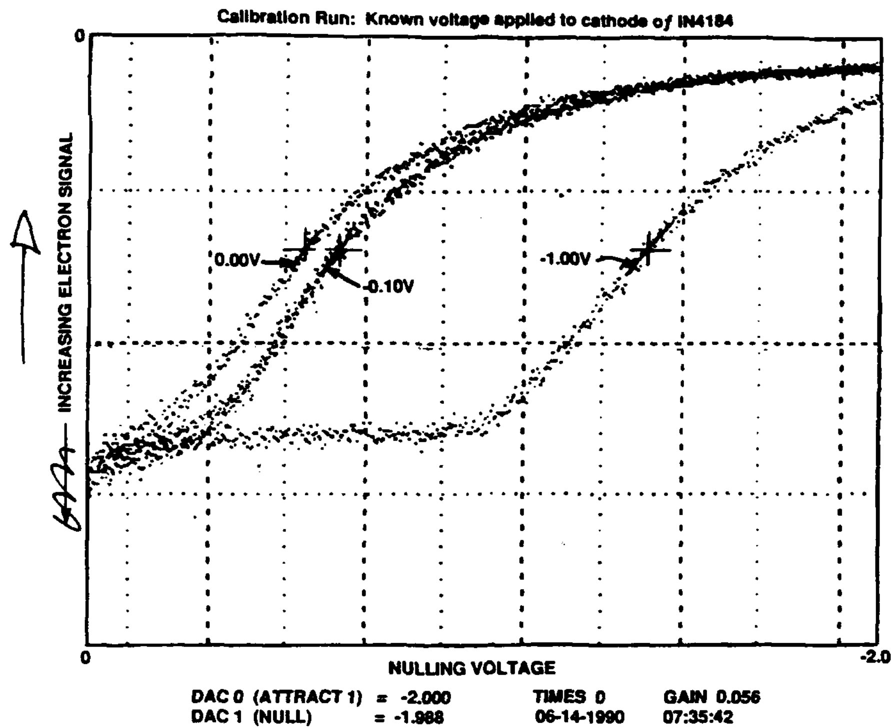

Figure E-2. Calibration for Collector Nulling Voltage Change Required to Reproduce Photocurrent Signal at 3 Different Substrate Biases. Note distortion of S curve at the large substrate voltage bias change.

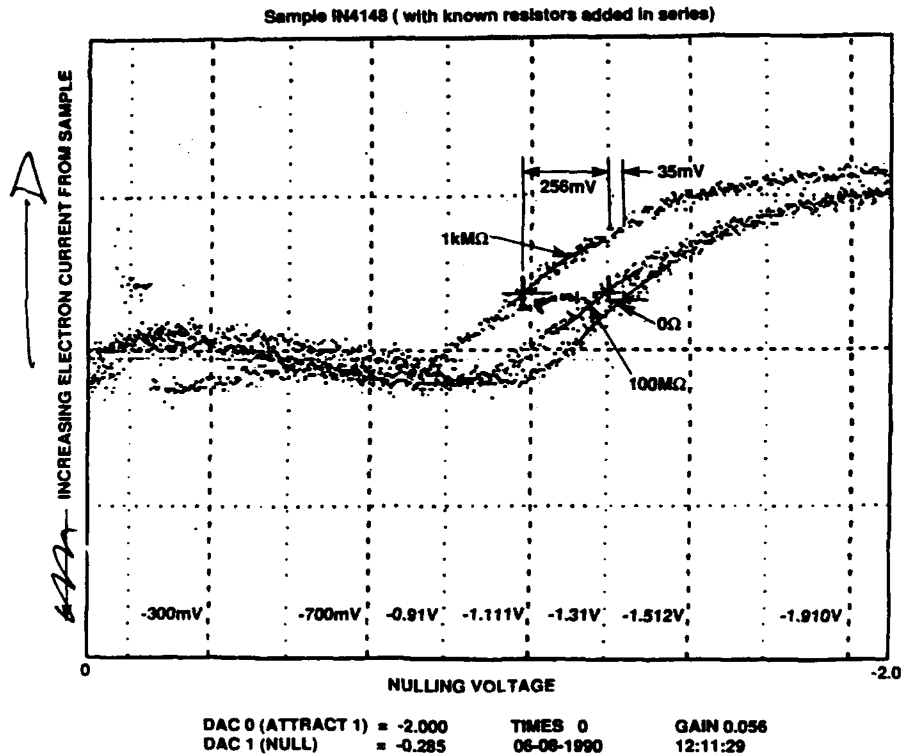

Figure E-3. S Curves with Shorted, $10^8\Omega$ $10^9\Omega$ Resistors between the UV Probed Surface and Ground

$10^9\ \Omega$ Resistor Measurement

ΔVnull = 0.026 V $\longrightarrow$ ΔVresistor = 0.32 V $\longrightarrow$ R = ΔVresistor/I ~ $3 \times 10^8 \Omega$

DISCUSSION

It should be noted that the Ultraprobe UV probing system test approach used was far from optimum for low voltage resistor impedance measurements. At the time the resistors were evaluated the UV probing system was configured for very high frequency AC measurements of VLSI voltage levels. In this mode voltage resolution degraded in favor of time resolution. The system was operated in the pulsed mode where each electron leaving the sample was counted individually and represented 5 ns of the waveform being acquired. The data was taken using a sampling oscilloscope which is very inefficient in collecting signal.

The voltage resolution of the Ultraprobe system in resistance measurements was about 20 mV. In another test configuration Ultraprobe achieved a voltage resolution of 3 mV. With **$2 \times 10^6 \Omega$** diode impedance and 3 mV voltage limit 1 nA of photo-current is required from a metallization area with typical dia of 20 µm. This photo-current density appears somewhat higher than what can be achieved using the brightest incoherent light sources or without some special high photo-electric efficiency metallization.

While UV CW ion lasers could stimulate more than sufficient photocurrent in a sub-micron spot these lasers appear to be much too expensive, large and unreliable (short tube life between replacements) to justify use in an E-beam system. It is likely that an alternate much cheaper, compact and more reliable solid state UV source may appear in the next few years. UV electroluminescence has been observed in a number of wide gap semiconductors such as AlN and BN. Laser operation in such materials and possibly diamond, is expected in the future. Such a development should make photo-electric probing of LWIR diodes possible.

Most LWIR diode processing includes a passivating overcoat of some material, frequently the passivating layer is ZnS. Short wavelength radiation which is transmitted through the ZnS can produce trapped charge states at the HgCdTe/ZnS interface which degrade the diode impedance. However, if the UV radiation is of sufficiently short wavelength around 250 nm it will be completely absorbed at the pas-

sivation layer surface and the interface problem from stray UV photons not focussed on the metallization spot will be avoided.